Regulation of pericyte contractility in health and disease

Chanawee Hirunpattarasilp

A thesis submitted to University College London

for the degree of Doctor of Philosophy

Department of Neuroscience, Physiology and Pharmacology

University College London

August 2021

Abstract

Pericytes regulate blood flow by constricting and dilating capillaries, especially in the brain, which requires a controlled supply of oxygen and energy substrates, and where the majority of the vascular resistance is in the capillaries. This thesis explores cerebral pericyte contractility in health and disease.

I showed that pericytes can be identified reliably by bright-field imaging and that the pericyte-specific dye Neurotrace 500/525 in fact preferentially labels pericytes on higher capillary branch orders. Raising pericyte $[Ca^{2+}]_i$ evokes a maximum capillary constriction near pericyte somata where pericyte circumferential processes originate, but adjustment of capillary wall tone by longitudinal processes of pericytes on higher order capillary branches may also regulate blood flow.

In Alzheimer's disease (AD) pericytes contract and reduce brain blood flow. The involvement of reactive oxygen species in amyloid β (Aβ)-induced pericyte contraction was assessed. I demonstrated that NADPH oxidase 4 (NOX4) and hydroxyl radicals mediate this process. A combination of NOX4 and endothelin A receptor blockers, or C-type natriuretic peptide, prevented Aβ-induced constriction, suggesting therapeutic approaches to AD targeted at pericytes.

Hyperoxia often occurs in clinical situations. In rodent and human brain slices, I showed that hyperoxic perfusion causes capillaries to constrict and pericyte $[Ca^{2+}]_i$ to increase. In rat but not human pericytes, this process was inhibited by blocking 20-HETE production, suggesting a role of 20-HETE in hyperoxic pericyte contraction.

Cerebral blood flow decreases in COVID-19 patients, in which the SARS-CoV-2 virus binds to angiotensin converting enzyme 2 (ACE2). In the brain I showed that ACE2 is mainly expressed in pericytes. I found that the receptor binding domain (RBD) of the SARS-CoV-2 spike protein potentiates the capillary constriction evoked by

angiotensin II, by reducing ACE2 activity, leading to more activation of AT1 receptors by angiotensin II. My results suggest that pericytes could play a role in the neurological complications of COVID-19 and that the AT1R blocker losartan might prevent this.

Impact statement

The brain relies heavily on blood flow to provide energy substrates because it has almost no reservoir of those nutrients and yet has a considerable demand for energy to power neural computation. In addition, the blood supply needs to accommodate the changing energy demand of different brain regions, in accordance with the activities of those areas at any specific time. Imbalance of energy demand and cerebral blood flow can cause disturbances to normal brain function, as seen in ischaemic stroke and Alzheimer's disease. Despite the importance of cerebral blood flow regulation, not much is known about the role of contractile cells called pericytes in controlling blood flow at the capillary level, but this is crucial since the capillaries confer the most hydraulic resistance to the intracerebral circulation. The knowledge from my thesis on "Regulation of pericyte contractility in health and disease" will serve as a foundation for further understanding of cerebral blood flow control and molecular signalling pathways affecting pericytes. Moreover, the methodology I have developed can be applied to study blood flow regulation in other organs, such as the heart or kidneys, which also contain a large number of pericytes.

Studying pericyte dysfunction in pathologies might lead to new potential therapeutic approaches to diseases that currently have no definite treatment. For instance, I found that amyloid β (Aβ) induces pericyte contraction and capillary vasoconstriction via NADPH oxidase 4 (NOX4) and hydroxyl radical generation, leading to the reduced cerebral blood flow found in the preclinical stage of Alzheimer's disease. Reversal of Aβ-evoked pericyte contraction could be achieved using a combination of a NOX4 inhibitor and an endothelin receptor blocker, so reactive oxygen species and pericytes might be interesting candidates to target for Alzheimer's disease therapy. In my study of the effects of a high oxygen level on pericytes, I found

that hyperoxia causes pericyte constriction through an increase in 20-HETE production. This might be related to the poorer neurological outcome seen in critically ill patients receiving hyperoxia. Furthermore, I showed that the receptor-binding domain (RBD) of COVID-19 potentiates capillary vasoconstriction evoked by angiotensin II and that this constriction can be inhibited by an angiotensin II receptor type 1 blocker. These data might be used to develop a treatment for neurological complications of COVID-19 in the future.

Some parts of my thesis have been disseminated at neuroscience conferences and at more clinically related conferences, in the form of poster and oral presentations. The results were also published as peer-reviewed papers. In addition, I have trained a number of students and post-docs in the lab, thus supporting the next generation of researchers.

Statement of the candidate's contribution to this thesis

The work in this thesis is presented in five results chapters. All of the experiments, data analysis, figure production and writing were primarily performed by Chanawee Hirunpattarasilp (with normal supervisorial input from Prof. David Attwell), with his contribution to each project as described below.

(1) Contractile properties of pericytes (Chapter 3)

Most of the planning, execution and analysis of bright-field imaging and immunohistochemistry studies were performed by Chanawee Hirunpattarasilp, with the exception of a live bright-field imaging experiment to describe contractility of Neurotrace 500/525 labelled pericytes and an immunohistochemistry experiment to explore the uptake mechanism of this dye (see Section 3.3.3-3.3.4), which were done in collaboration with an undergraduate student (Heidy Chen) being supervised by Chanawee Hirunpattarasilp, who contributed 70% to the experiments. *In vivo* surgery studies were executed and analysed by Chanawee Hirunpattarasilp with initial guidance from Dr. Lila Khennouf and original analysis programmes from Dr. Lorena Arancibia-Carcamo.

(2) Alzheimer's disease (AD) and pericyte contractility (Chapter 4)

The confirmation of Amyloid beta (Aβ) oligomeric preparation (see Section 4.3.1) was performed by Chanawee Hirunpattarasilp (40%) in collaboration with Dr. Pablo Izquierdo (60%). Aside from the bright-field imaging experiments in Section 4.3.3., which were done by Dr. Ross Nortley and in Section 4.3.7, which were performed by Chanawee Hirunpattarasilp (75%) and Dr. Nils Korte (25%), all bright-field imaging work was planned, executed and analysed by Chanawee Hirunpattarasilp. *In vivo* experiments on AD mice (see Section 4.3.2) were performed by Dr. Nils Korte but the analysis was done by Chanawee Hirunpattarasilp and Dr. Nils

Korte. The overall contribution for the *in vivo* experiment for Chanawee Hirunpattarasilp was 25%.

(3) Hyperoxia and pericyte contractility (Chapter 5)

All bright-field imaging and immunohistochemistry studies in this Chapter were planned, executed and analysed by Chanawee Hirunpattarasilp. The calcium imaging experiment (see Section 5.3.2) was done by Chanawee Hirunpattarasilp with help from Dr. Thomas Pfeiffer, who performed the slicing procedure and contributed to 25% of the work.

(4) COVID-19 and pericyte contractility (Chapter 6)

Bright-field imaging studies were performed by Chanawee Hirunpattarasilp (60%) in collaboration with Dr. Greg James (40%). The immunohistochemistry for ACE2 was planned, executed and analysed by Chanawee Hirunpattarasilp. The death analysis (see Section 6.3.8) was performed by Chanawee Hirunpattarasilp (50%) and Dr. Felipe Freitas (50%). Synthesis of RBD and mutated RBD-Y489R was done by Prof. Ray Owens (Oxford University).

Acknowledgements

First and foremost, I would like to thank my supervisor, Prof. David Attwell, without whom this PhD would not have been possible. I am grateful for his tremendous guidance, support, patience and kindness. I could not have asked for a better supervisor.

I would like to also thank all past and present lab members of the Attwell lab, who have taught me so much and made me feel at home since I first came to the lab: Dr. Lorena Arancibia-Carcamo, Dr. Marc Ford, Dr. Vasiliki Kyrargyri, Dr. Ross Nortley, Dr. Felipe Freitas, Dr. Nils Korte, Dr. Pablo Izquierdo, Dr. Lila Khennouf, Dr. Thomas Pfeiffer, Dr. Tania Quintela-Lopez, Dr. Jonathan Lezmy, Dr. Greg James, Dr. Hiroko Shiina, Dr. Anna Barkaway. I feel very fortunate to have met you all.

I would like to thank Miss Huma Sethi, Prof. Ray Owen and Dr. Nat Na-ek for their collaboration and generosity.

I am extremely grateful to Prof. HRH Princess Chulabhorn, Prof. Chirayu Auewarakul, Prof. Claudio Stern and the Faculty of Medicine and Public Health, The HRH Princess Chulabhorn College of Medical Science (PCCMS) for giving me the opportunity to study for my PhD.

I want to thank all my friends who supported and encouraged me and kept me entertained over the last four years.

Finally, I would like to thank my family, particularly my father, my mother and my sister, for their unconditional love and support.

Contents

List of figures

List of tables

Chapter 1: Introduction

1.1 Overview

Brain pericytes, which are contractile cells on the abluminal surface of capillaries, have been recently identified as major regulators of cerebral blood flow (CBF), matching blood supply to the energy demands of the brain (Hall *et al.*, 2014; Gould *et al.*, 2017). Although there are increasing numbers of studies on pericytes, there is still a large knowledge gap about pericyte physiology and the impact of these cells, especially in the context of pathologies that disturb normal regulation of CBF. In this thesis, which aims to address this gap, I have investigated the following aspects of pericyte function.

(i) The contractility of pericytes. Conflicting claims about pericyte contractility have been shown to mainly reflect differences in the definition, classification and methods for identification of pericytes (Attwell *et al.*, 2016). In this section, I investigated the use of bright-field microscopy and a putative pericyte-specific dye, Neurotrace 500/525 (Damisah *et al.*, 2017), to identify pericytes and examined the role of pericytes, both at the arteriolar end and in the middle of the capilllary bed, in regulating CBF.

(ii) The role of pericytes in Alzheimer's disease (AD). Most studies on vascular effects of amyloid beta (Aβ) have focused on cerebral arteries and arterioles (Niwa *et al.*, 2001; Paris *et al.*, 2003) and capillaries, which confer most of the intracerebral flow resistance (Gould *et al.*, 2017), have been mostly ignored in AD. In this section, I studied the effect of Aβ on pericyte contractility and the contribution of oxidative stress to that process.

(iii) The role of pericytes in hyperoxia. Hyperoxia causes decreased CBF and leads to poorer brain function in patients with conditions such as cardiac arrest, ischaemic stroke and subarachnoid haemorrhage (Janz *et al.*, 2012; Li *et al.*, 2019; Fukuda *et*

al., 2019; López *et al.*, 2019), but the effect of high oxygen on cerebral pericytes has not yet been studied. In this section, I investigated the association between high oxygen exposure and pericyte contractility, and the underlying mechanisms.

(iv) The role of pericytes in COVID-19. COVID-19 is a pandemic disease that mainly causes respiratory symptoms, but neurological symptoms and CBF deficits have been reported (Helms *et al.*, 2020; Ellul *et al.*, 2020; Wildwing & Holt, 2021). In this section, I investigated the contribution of cerebral pericytes to CBF deficits in COVID-19 and the underlying pathophysiology.

1.2 Brain energy use

Although the human brain weighs only 2% of the body's mass, it uses 20% of the resting body's oxygen consumption (Sokoloff, 1960; Rolfe & Brown, 1997). Most of the energy expenditure in the human brain is used to power the grey matter, in which the calculated ATP and glucose consumption (7.0×10^{19} ATP/s and 0.31 μmol of glucose/g/min for the whole cerebrum in the awake resting state) are approximately twice that in the white matter (Yu *et al.*, 2018). The ATP used in the grey matter is expended mostly on synaptic transmission (48.5%), resting potentials (19.9%), housekeeping tasks (10.6%), action potentials (8.7%), presynaptic calcium (8%), and glutamate and GABA recycling (4.3%) (Yu *et al.*, 2018). The housekeeping activities include actin polymerisation and depolymerisation, microtubule turnover, protein and lipid synthesis, microglial activity and mitochondrial proton leak (Engl & Attwell, 2015). This means that most of the energy (~70%) is spent on signalling processes. In contrast, 4.01×10^{19} ATP/s and 0.19 μmol/g/min of glucose are used by the white matter in the whole cerebrum, the majority (~80%) of which is used for non-signalling processes (Yu *et al.*, 2018). Overall, the brain consumes a large amount of body

energy and expends it mainly on signalling in the grey matter and non-signalling processes in the white matter.

The major oxidative fuel for energy consumption in the brain is glucose, with a global oxygen-glucose index (OGI) of ~5.5 in resting human brain (Blazey *et al.*, 2018). The OGI is the ratio of the cerebral metabolic rate of oxygen (CMR_{O_2}) to the cerebral metabolic rate of glucose (CMR_{glu}), so complete oxidation of glucose should give an OGI of 6 in theory. The suboptimal OGI of 5.5 observed is thought to be due to lactate production, the pentose phosphate shunt pathway and glycogen turnover (Dienel, 2019).

Glucose is normally the main energy source for the brain but oxidative substrates, such as lactate, pyruvate, ketones and galactose can also be used to supply energy (Schurr, West & Rigor, 1988; Fowler, 1993; Dienel, 2019). However, it is still unclear whether these energy substates can replace glucose. In some studies, lactate supports synaptic function of neurons when glucose cannot be used (Schurr, West & Rigor, 1988; Fowler, 1993). Nevertheless, other studies have shown that replacing glucose with lactate reduces field potentials (Cox & Bachelard, 1988) and causes synaptic transmission loss in brain slices (Chih *et al.*, 2001).This discrepancy might arise from different preparation methods because rapidly prepared brain slices, but not slowly prepared tissues, show loss of synaptic activity after replacing glucose with lactate (Okada & Lipton, 2007). In *in vivo* situations, lactate alleviates hypoglycaemic symptoms in some studies (Veneman *et al.*, 1994; King *et al.*, 1998; Maran *et al.*, 2000) but not in others (Sokoloff, 1996). However, recent findings suggest that the amount of lactate taken up by the brain during hypoglycaemia is not enough to correct the energy deficit (Lubow *et al.*, 2006; Herzog *et al.*, 2013) but lactate might regulate brain metabolic and neuronal activity instead (Herzog *et al.*,

2013). A small amount of brain glycogen stored in astrocytes and lactate derived from the astrocyte-neuron lactate shuttle may supplement glucose utilisation during increased neuronal activity, but this is also under debate (Rich, Harris & Brown, 2019). The astrocyte-neuron lactate shuttle hypothesis (ANLSH) states that glutamate from neuronal synaptic transmission is taken up by astrocytes via Na^+-coupled glutamate transporters. The glutamate undergoes an ATP-dependent reaction to form glutamine, which is then released into the extracellular space for recycling to neurons. Astrocytic glucose uptake and glycolysis are triggered by the uptake of glutamate into astrocytes and by the energy needed to reverse the increase in intracellular Na^+ concentration accompanying the uptake. This leads to lactate being produced and released into extracellular space for neurons to use as an energy supply (Magistretti & Pellerin, 1999; Mason, 2017; Rich, Harris & Brown, 2019). The ANLSH is supported by experiments showing that glial glutamate transporters mediate increased astrocytic glucose utilisation and lactate release in the developing cortex (Voutsinos-Porche *et al.*, 2003) and that lactate is generated within the brain *in vivo* during neuronal activation (Sampol *et al.*, 2013). A mathemathical model also supports the idea that activated neurons take up lactate (Aubert *et al.*, 2005). On the other hand, lactate uptake is estimated to be too slow to be used for fuel (Dienel & Hertz, 2001) and a decreased lactate concentration is found at the onset of neural activity (Mangia *et al.*, 2003). Another mathematical model also suggested that glycogenolysis in astrocytes does not provide lactate but preserves extracellular glucose to be used by neurons (DiNuzzo *et al.*, 2010). Hence, the role of the ANLSH, as well as other energy substrates, is still controversial.

Since most of the ATP used by the brain comes from glucose oxidation (Dienel, 2019), the normal human brain needs a large quantity of glucose (CMR_{glu} = 0.25

μmol/g/min) and oxygen (CMR_{O_2} = 1.5-1.9 μmol/g/min or 3.3 – 4.2 ml/100 g/min) (Dienel, 2019). Assuming that the human brain weighs around 1,400 g (Jerison, 1973), it uses around 91 g of glucose and 68-86 litres of oxygen per day at the standard temperature and pressure at sea level (Dienel, 2019). Thus, the human brain relies on a substantial supply of oxygen and glucose, which cannot be stored, to function.

During neuronal activity (termed functional activation of the brain), the utilisation of glucose and oxygen increases. The CMR_{glu} and CMR_{O_2} rise by 51% and 5% in human visual cortex during visual stimulation (Fox *et al.*, 1988). The disproportionate increment of glucose and oxygen consumption during brain activation results in a decreased OGI, which indicates an increase in non-oxidative breakdown of glucose such as aerobic glycolysis (lactate production even though oxygen is present) and the pentose shunt pathway (Dienel, 2012). Moreover, the changes in glucose metabolism are brain region-specific, depending on the task performed. For example, when subjects opened their eyes, increased glucose usage was detected in primary visual cortex, motor cortex and cerebellum, but decreased metabolism was observed in the frontal cortex (Hahn *et al.*, 2016). Therefore, the glucose demand is different in each brain region at different times.

An adequate supply of glucose and oxygen is needed for the brain to function normally. In hypoglycaemia, neuroglycopenic symptoms occur when the glucose level falls to 54 mg/dl. A glucose level of 50 mg/dl causes a functional brain failure, manifesting as cognitive impairment, behavioural changes and seizures (Cryer, 2007). Coma may occur when the glucose level decreases below 50 mg/dl and prolonged severe hypoglycaemia can cause brain death (Cryer, 2007). Exposure to high altitude, thus reducing brain oxygen supply, causes headache, nausea/ vomiting, dizziness, impaired cognitive functions and even loss of consciousness (as fast as in 15 s at an

altitude higher than 16,000 m) (Bärtsch & Swenson, 2013; Lumb & Pearl, 2017). Upon cessation of the CBF that supplies both glucose and oxygen to neurons and glia cells, local cortical activity stops within seconds, resulting in loss of consciousness in the case of global cerebral ischaemia (Lee *et al.*, 2000). Finally, irreversible neuronal death is triggered after 5 minutes of CBF cessation (Lee *et al.*, 2000).

Because the brain has a spatially and temporally dynamic metabolism, without any significant energy substrate reserves, a precise control of local CBF to match brain energy requirements is extremely important (Iadecola, 2017). This process of fine-tuning brain blood flow according to neuronal activity is named neurovascular coupling (Iadecola, 2017).

1.3 Cerebral vasculature

The cerebral vasculature is separated into two parts, namely the macrovasculature, which includes cerebral arteries and veins, and the microvasculature, which includes arterioles, capillaries and venules (Coelho-Santos *et al.*, 2020).

1.3.1 Macrovascular blood supply of the cerebrum

The brain is supplied by two main circulatory pathways (Shah & Jeyaretna, 2018). The carotid system supplies the majority of the cerebrum apart from the occipital and the inferior surfaces of the temporal lobes, hence this system can be called the anterior circulation (Shah & Jeyaretna, 2018). The vertebrobasilar system, or the posterior circulation, provides blood supply to the occipital and temporal (inferior surfaces) lobes of the cerebrum, the cerebellum, the brainstem and the upper part of the spinal cord (Shah and Jeyaretna, 2018; Fig. 1.1).

The anterior circulation originates from two main arteries, the left and right internal carotid arteries (ICAs), which arise from the left and right common carotid arteries respectively. The left common carotid artery derives directly from the aortic arch, but the right common carotid artery originates from the brachiocephalic trunk connected to the aortic arch. The two ICAs run within the carotid sheath from their origins without giving off any branches in the neck, enter the skull through carotid canals in the temporal bones and anastomose with the posterior circulation to form the circle of Willis (Fig. 1.1), although this completely anastomosing variant is only found in 11.9% of the population (Hindenes *et al.*, 2020). The ICAs terminate to form the anterior and middle cerebral arteries. The anterior cerebral arteries (ACAs) supply medial parts of frontal and parietal lobes. The middle cerebral arteries (MCAs) provide blood to most of the frontal, parietal and temporal lobes except for the ACA territories and the occipital and inferior parts of the temporal lobes, which are supplied by the posterior cerebral arteries (PCAs) (Netter, 2014; Shah & Jeyaretna, 2018).

The posterior circulation derives from the left and right vertebral arteries, which are the first branches of the subclavian arteries on both sides. The vertebral arteries enter the foramen magnum after running in the transverse foramens of C1-6 vertebra. They then merge together at the caudal part of the pons to form the basilar artery, which form the circle of Willis and terminates into left and right posterior cerebral arteries (PCAs). The PCAs give branches to supply the occipital and inferior surfaces of the temporal lobe (Netter, 2014; Shah & Jeyaretna, 2018).

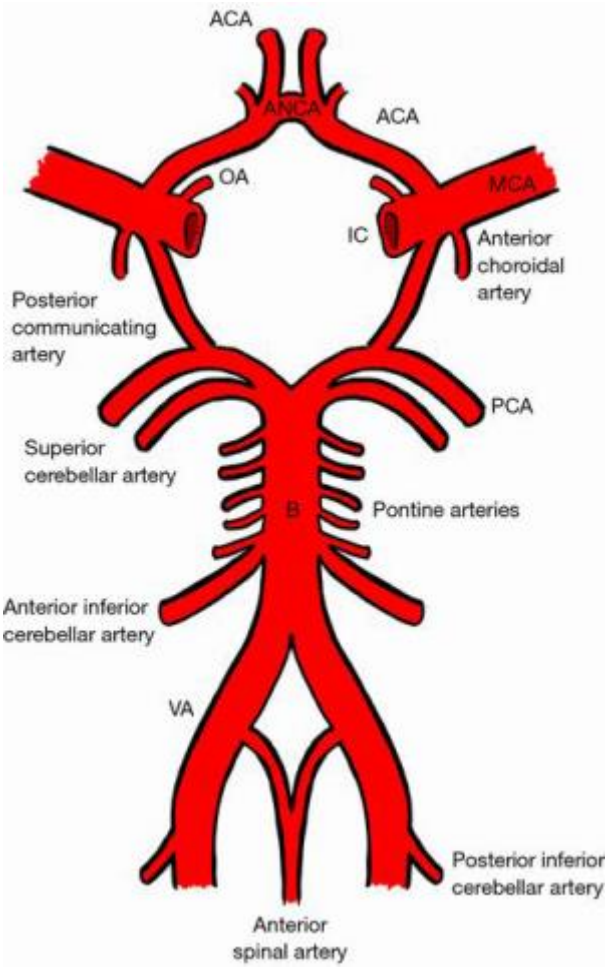

Figure 1.1: The Circle of Willis.

This figure is from Shafafy *et al.* (2017).

VA, vertebral artery; B, basilar artery; PCA, posterior cerebral artery; IC, internal carotid artery; MCA, middle cerebral artery; ACA, anterior cerebral artery; ANCA, anterior communicating artery; OA, ophthalmic artery.

1.3.2 Microvascular blood supply of the cerebrum

The three major cerebral arteries (ACA, MCA and PCA) run inside subarachnoid spaces along the surface of the brain and give off branches to form pial arteries and arterioles, to create a microvascular network outside the cerebrum called the leptomeningeal network, which helps to shunt blood to functionally active or ischaemic areas (Iadecola, 2017; Coelho-Santos *et al.*, 2020). This network gives rise to penetrating arterioles, which run perpendicular to the brain surface and dive into the cerebrum before branching off and terminating as capillaries to allow exchange of substances between blood and the brain tissue (Iadecola, 2017).

The brain microvasculature has distinct histologic characteristics depending on the region of the vessels. A pial arteriole has a diameter of tens to hundreds of microns in humans (Duvernoy, Delon & Vannson, 1981) and consists of an endothelial tube covered by elastic laminae, multiple layers of vascular smooth muscle cells (vSMCs) and an adventitial layer with a mesh of perivascular nerves from peripheral autonomic and sensory ganglia. This innervation allows pial arterioles to constrict and dilate to modulate CBF. Branching from a pial arteriole, a penetrating arteriole has a diameter of 10 – 240 μm in humans (Duvernoy, Delon & Vannson, 1981) and comprises an endothelial layer, a less prominent elastic lamina than in pial arterioles, and a thinner layer of vSMCs. In the upper cortex layers, these arterioles are surrounded by the Virchow-Robin space, which is connected to the subarachnoid space and separates the vascular basement membrane from the glia limitans. This perivascular space is filled with cerebrospinal fluid, perivascular macrophages and perivascular nerves. In lower cortical layers, the arterioles are covered with only one complete or discontinuous layer of vSMCs and glia limitans without the Virchow-Robin space. These vessels are controlled by axon terminals or dendrites from interneurons,

subcortical nuclei and brainstem nuclei. Capillaries are less than 10 μm in diameter and are covered with pericytes instead of vSMCs (see Section 1.4), astrocytic endfeet and occasionally neural processes (Iadecola, 2017; Coelho-Santos *et al.*, 2020).

Blood pressure within different sections of the cerebral circulation has been studied in anesthetised cats using a micropipette pressure system (Stromberg & Fox, 1972). At a low systemic blood pressure (SBP) of 50 mmHg, vascular resistance, calculated by the pressure drop, was 39% in arteries upstream of the leptomeningeal network, 21% in pial arteries/arterioles and 40% in vessels downstream of the pial network. However, at a higher SBP of 180 mmHg, the resistance was 33% in major arteries, 15% in pial vessels and 52% in downstream vessels. This resistance distribution is consistent across species (De Silva & Faraci, 2016). Hence, penetrating arterioles and capillaries hold the most resistance in the cerebral circulation and cerebrovascular responses occur mainly at these sites (Stromberg & Fox, 1972), potentially because these vessels receive direct inputs from axon terminals and are believed to be regulated by neuronal activity (Iadecola, 2017).

Direct measurement of resistance in the intracerebral microcirculation to distinguish the contribution of penetrating arterioles and capillaries is not feasible (Iadecola, 2017) and computer analyses have yielded different results. The majority of studies show that most of the vascular resistance in the cerebral microcirculation is in capillaries (Boas *et al.*, 2008; Hall *et al.*, 2014; Gould *et al.*, 2017; Peyrounette *et al.*, 2018; Rungta *et al.*, 2018; but see Schmid *et al.*, 2017; Sweeney, Walker-Samuel and Shipley, 2018), and the regulation of blood flow in capillaries is mediated by contraction and relaxation of pericytes (Hall *et al.*, 2014; Attwell *et al.*, 2016).

1.4 Pericytes

1.4.1 Overview of pericytes

A pericyte is a bump-on-a-log shaped cell located on the abluminal surface of endothelium with a prominent spatially isolated nucleus, and with processes running along and around the vessels (Fig. 1.2) (Hirschi & D'Amore, 1996; Armulik *et al.*, 2011; Cheng *et al.*, 2018). They were first discovered in the 1870s by Eberth (1871) and Rouget (1873) as cells which surround capillary endothelium and are embedded in the basement membrane. However, they were only named "pericytes" 50 years later by Zimmerman and Zimmermann (1923) who characterised them into three subtypes, namely; (i) pre-capillary pericytes, which are a transitional form between vSMCs and capillary pericytes resting on pre-capillary arterioles; (ii) capillary pericytes, which are found in the mid-capillary beds; and (iii) post-capillary pericytes found on post-capillary venules. Pericytes, which in fact are present on capillaries throughout the body, were suggested to be contractile in the early studies, and indeed a Nobel prize was awarded to Augustus Krogh in 1920 for his discovery of contractile cells on skeletal muscle capillaries.

In the brain, with advances in imaging techniques, it has been found that the mural cells of vascular beds have a continuum of phenotypes from the arteriolar end to the venular end (Armulik *et al.*, 2011; see Section 1.4.3). This may cause the variations found in the definition of pericytes and of the vascular segments across different studies (Uemura *et al.*, 2020). For instance, the proximal branches of penetrating arterioles were considered to be capillaries in most studies (Hall *et al.*, 2014; Attwell *et al.*, 2016; Cai *et al.*, 2018; Rungta *et al.*, 2018; Grant *et al.*, 2019), but they were defined as pre-capillary arterioles in others (Hartmann *et al.*, 2015; Hill *et al.*, 2015). The mural cells on these branches were also specified either as pericytes

(following the definition of Zimmermann & Zimmermann (1923): Hall *et al.*, 2014; Cai *et al.*, 2018; Rungta *et al.*, 2018), smooth muscle-pericyte hybrid (Hartmann *et al.*, 2015) or vSMCs (Hill *et al.*, 2015; Vanlandewijck *et al.*, 2018). Figure 1.3 shows different naming of mural cells in the capillary bed (Uemura *et al.*, 2020).

In this thesis, I will use the definition of Zimmermann & Zimmermann (1923) and Attwell *et al.* (2016), and consider the proximal branches of penetrating arterioles and the mural cells on them as capillaries and pericytes respectively.

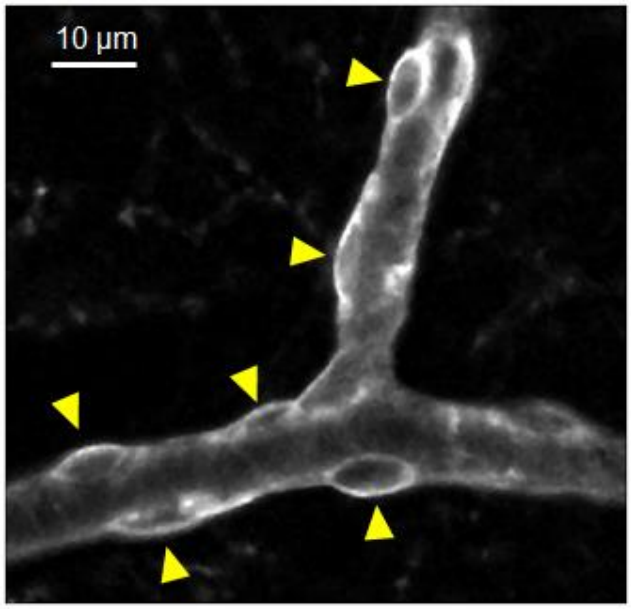

Figure 1.2: Pericyte morphology.

Confocal image of rat cortical pericytes (yellow arrows) with a bump-on-a-log morphology on capillaries, labelled by Isolectin B4.

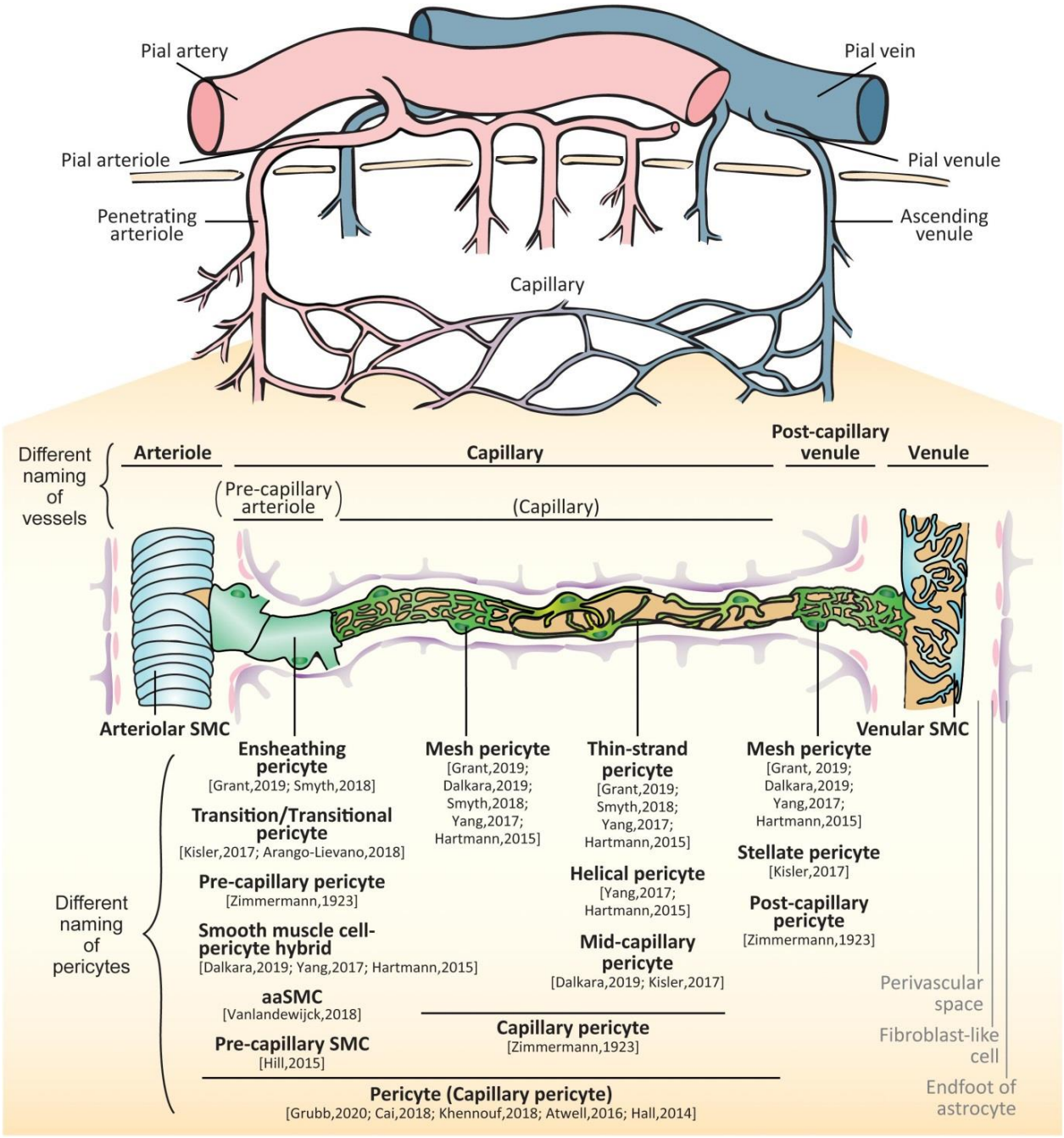

Figure 1.3: Brain vessels and mural cells.

This figure and figure legend are from Uemura *et al.* (2020). The pial arterioles branch from pial arteries which follow the outer rim of the brain along the meninges. The arterioles penetrate perpendicularly into the brain parenchyma (penetrating arteries) and further split into smaller arterioles. As their diameters and constituent cell types are changed, the vessels make a transition to capillaries. The capillaries join to form venules that collect into pial venules and further into pial veins. In the small vessels,

there are two types of mural cells separately located outside of endothelial layer: vascular smooth muscle cells (SMCs) and pericytes. SMCs are localized at the arteries, arterioles, venules and veins whereas pericytes are localized at the capillaries and post-capillary venules. The proximal capillary branches coming off penetrating arterioles are sometimes called pre-capillary arterioles. The subtypes of pericytes are differently called: ensheathing pericytes, transitional pericytes, pre-capillary pericytes, smooth muscle cell-pericyte hybrids, arteriole SMC (aaSMCs), or pre-capillary SMCs within a few branches close to arterioles; capillary pericytes, mesh pericytes, thin-strand pericytes, helical pericytes, or mid-capillary pericytes in the middle part of capillary; and mesh pericytes, stellate/stellate-like pericytes, or post-capillary pericytes in the post-capillary venules.

1.4.2 Identification of pericytes

The gold standard for identification of pericytes is proposed to be through ultrastructural analysis (Trost *et al.*, 2016). In mature tissue, pericytes and their processes are surrounded by a basal lamina which is connected to the endothelial basement membrane (Sims, 1986). This feature is key to separating pericyte processes from those of fibroblasts. However, ultrastructural analyses may not always be practical in experimental settings (Trost *et al.*, 2016).

Important structures that may help separate pericytes from vSMCs are the soma and shape of processes. Pericytes have isolated prominent bump-on-a-log shaped somata with thin processes of less than 2 μm in diameter, whereas vSMCs have inconspicuous cell bodies with broader processes (as large as 7 μm in diameter) (Attwell *et al.*, 2016; Uemura *et al.*, 2020).

Because there are subtypes of pericytes with different features (Cheng *et al.*, 2018; Grant *et al.*, 2019; Uemura *et al.*, 2020), one needs to consider anatomical position, morphology and protein expression to correctly identify a pericyte. The absence of endothelial cell markers, such as CD31 or von Willebrand factor (vWF), and other mesenchymal cell markers are also needed for differentiating pericytes from other cell types (Armulik *et al.*, 2011; Cheng *et al.*, 2018).

1.4.3 Classification of pericytes

Penetrating arterioles give off first branch order capillaries, which split into second branch order capillaries, which split into 3rd branch order capillaries, and so on. At present, pericytes are mainly divided into three groups, depending on capillary branch order.

(i) Proximal capillary pericytes. This subgroup of pericytes is found on 1st to 4th branch order capillaries (Hartmann *et al.*, 2015; Rungta *et al.*, 2018; Grant *et al.*, 2019).

These cells have prominent somata and have multiple circumferential primary processes around the vessel, resulting in ~95% vessel coverage (defined as the ratio of the area of lectin-labelled vessels covered by pericytes to the total area of the lectin-labelled vessels) similar to what is found for vSMCs (Sims, 1986; Grant *et al.*, 2019). These pericytes express a high level of α-smooth muscle actin (αSMA), although it is less than that in vSMCs (Alarcon-Martinez *et al.*, 2018; Grant *et al.*, 2019) . A transcriptomic analysis of these cells also shows expression of smooth muscle protein 22-α (*Tagln*) similar to that found in arterial SMCs, but not of calponin 1 (*Cnn1*), which is highly expressed in arterial SMCs or sulfonylurea receptor 2 (*Abcc9*), which is predominant in other subgroups of pericytes (Vanlandewijck *et al.*, 2018). Although Vanlandewijck *et al.* (2018) categorised these cells as arteriolar SMC clusters, they show prominent somata on vessel segments branching off vSMC-covered arterioles, and thus they are classified as low branch order capillary pericytes based on Zimmermann & Zimmermann (1923) and Attwell *et al.* (2016). These proximal capillary pericytes are vital for neurovascular coupling and for regulation of CBF (Hall *et al.*, 2014; Cai *et al.*, 2018; Rungta *et al.*, 2018; see Section 1.4.4).

(ii) Mid-capillary pericytes. This group of pericytes is on higher-order capillaries (starting at the 5th branch order: Grant *et al.*, 2019). This type of mural cell can be categorised according to morphology into 2 subgroups, termed mesh and thin-strand pericytes (Hartmann *et al.*, 2015; Grant *et al.*, 2019). Mesh pericytes exhibit a net-like appearance that surrounds capillaries and provides ~70% vessel coverage, whereas thin-strand pericytes are longer in length, exhibit thin primary processes along the vessel and provide only ~50% vessel coverage (Hartmann *et al.*, 2015; Grant *et al.*, 2019). Transcriptomic analysis suggested that mid-capillary pericytes do not express αSMA or calponin 1 but they express *Abcc9* (Hartmann *et al.*, 2015; Vanlandewijck *et*

al., 2018; Grant *et al.*, 2019). However, some studies have observed αSMA in these cells (Bandopadhyay *et al.*, 2001). Moreover, mid-capillary pericytes also express *Ggt1* (Gamma-Glutamyltransferase 1) and *Kcnj8* (an inward-rectifying K^+ channel subunit) which are specific to these cells (Chasseigneaux *et al.*, 2018). A Nissl dye, NeuroTrace 500/525, has been suggested to label these non-contractile pericytes *in vivo* (Damisah *et al.*, 2017); however, not much information on the properties of this dye is known. These mural cells are important in maintaining the blood-brain barrier (BBB) (Armulik *et al.*, 2010; Attwell *et al.*, 2016) and they might play a role in modulating CBF (Rungta *et al.*, 2018; Hartmann *et al.*, 2021).

(iii) Post-capillary pericytes. This pericyte subgroup near the venular end of capillary is numerous and has a spidery anatomy, showing long narrow anastomosing processes with distal cytoplasmic swellings and a relatively large stellate soma (Sims, 1986; Armulik *et al.*, 2011; Yang *et al.*, 2017). These mural cells express *Abcc9* and a very small amount of αSMA and are speculated to modulate immune cell transmigration into the brain parenchyma (Attwell *et al.*, 2016; Uemura *et al.*, 2020).

1.4.4 Pericyte contractility and neurovascular coupling

Pericyte contractility has been proposed since the discovery of this cell type (Eberth, 1871; Rouget, 1873) and is supported by several lines of evidence. An ultrastructural analysis reveals that bands of actin, myosin and tropomyosin, which are filaments used in contraction, can be found beneath the plasma membrane, near the nucleus and in the cells' peripheral extensions in the heart and the brain (Lebeux & Willemot, 1978; Sims, 1986); however, these studies do not specify which subtype of pericytes were studied. Transcriptomic data also supports the expression of contractile filaments in pericytes, particularly the ones near the arteriolar end of the capillary bed (Vanlandewijck *et al.*, 2018; Zeisel *et al.*, 2018). Contraction and dilation of pericytes

has been observed in cell culture (Lee *et al.*, 2010), brain slices (Peppiatt *et al.*, 2006; Hall *et al.*, 2014), *in vivo* animal experiments (Cai *et al.*, 2018; Khennouf *et al.*, 2018; Rungta *et al.*, 2018) and even in live human brain slices (Nortley *et al.*, 2019). This contractility has also shown to be related to intracellular calcium level inside the cell (Khennouf *et al.*, 2018; Rungta *et al.*, 2018; Nortley *et al.*, 2019). Recent studies have support the importance of pericyte contractility. In an optogenetic mouse model, activation of channelrhodopsin-2 specifically expressed in pericytes led to an 8% reduction of capillary diameter and a 42% decrease in capillary red blood cell (RBC) flow (Nelson *et al.*, 2020).

Pericytes have been suggested to play an important role in neurovascular coupling. Dilation of capillaries precedes that of arterioles (Hall *et al.*, 2014; Kisler *et al.*, 2017b; Cai *et al.*, 2018; Rungta *et al.*, 2018), implying that capillaries dilate actively rather than responding passively to an increase in local pressure caused by upstream dilation of arterioles. The percentage diameter change is also larger in 1st and 2nd branch order capillaries than that in arterioles (Hall *et al.*, 2014; Khennouf *et al.*, 2018). This means that the proximal capillary pericytes respond earlier and with a larger magnitude of dilation to neuronal activity when compared to SMCs on arterioles. Moreover, because capillaries provide the most resistance within the brain vasculature (Boas *et al.*, 2008; Hall *et al.*, 2014; Gould *et al.*, 2017; Peyrounette *et al.*, 2018; Rungta *et al.*, 2018), pericyte contraction and relaxation can cause large changes in CBF. Indeed, a neurovascular coupling defect has been shown in pericyte deficient mice (Kisler *et al.*, 2017b).

Neurovascular decoupling and CBF deficits caused by pericyte dysfunction can be found in various neurological diseases (Cheng *et al.*, 2018). In ischaemic stroke, pericytes constrict and die in rigor (Hall *et al.*, 2014), causing the no-reflow

phenomenon that prevents blood from reaching the ischaemic area despite a successful revascularisation of the upstream occluded arteries (Hauck *et al.*, 2004; Yemisci *et al.*, 2009). Pericyte contraction in cortical spreading depression, which occurs during migraine attacks (Charles & Baca, 2013) and in traumatic brain injury (Hartings *et al.*, 2011), leads to the cortical oligaemia found in these conditions (Khennouf *et al.*, 2018). These cells are also involved in ictal blood flow restriction in epilepsy that contributes to ictal neurodegeneration (Leal-Campanario *et al.*, 2017).

Most studies of pericyte contractility focus on proximal capillary pericytes (Cai *et al.*, 2018; Khennouf *et al.*, 2018; Rungta *et al.*, 2018) because they express most αSMA, provide the most vessel coverage, and have the most circumferential processes (which are needed to change capillary diameter) among all types of pericytes (Sims, 1986; Grant *et al.*, 2019). The proximal capillary pericytes on the first branch order have the largest initial intracellular Ca^{2+} decrease compared to vSMCs on arterioles and pericytes from other branch orders during spreading depolarisation, leading to vasodilation (Khennouf *et al.*, 2018). Pericytes on the first capillary branch order in the glomerulus of the olfactory bulb also dilate vessels more than arterioles (Rungta *et al.*, 2018). As mentioned above, first-order capillaries also dilate faster than arterioles during neuronal stimulation (Hall *et al.*, 2014; Cai *et al.*, 2018), further emphasising the role of proximal capillary pericytes in neurovascular coupling.

Nevertheless, mid-capillary bed pericytes have also been proposed to regulate CBF. Hartmann *et al.* (2021) showed that depolarisation of mid-capillary bed pericytes leads to capillary constriction. However, given that this subtype of pericytes, especially thin-strand pericytes, extend their processes primarily along (rather than around) the vessels (Hartmann *et al.*, 2015; Grant *et al.*, 2019), the force created by the contraction of these processes may lead to contraction along the vessel axis rather than

vasoconstriction. Another theory is that these pericytes contract to reduce passive dilation of vessels (Lee *et al.*, 2010) but more information is needed to quantify the importance of this theory. In addition, at least in the retina, mid-capillary pericytes mediate propagation of vasoactive signals from neurons to proximal capillary beds and feeding arteries (Kovacs-Oller *et al.*, 2020). They can also modulate blood flow by regulating endothelial tube growth (Cheng *et al.*, 2018).

The mechanism underlying contraction of pericytes is assumed to be analogous to that of vSMCs (Hamilton, Attwell & Hall, 2010; Sweeney, Ayyadurai & Zlokovic, 2016). Increased intracellular calcium concentration activates calmodulin to trigger myosin light chain kinase (MLCK) (Webb, 2003). Phosphorylation of myosin light chain (MLC) by MLCK leads to coupling of myosin and αSMA to induce contraction (Mizuno *et al.*, 2008; Lee *et al.*, 2010). On the other hand, myosin light chain phosphatase (MLCP) converts phosphorylated MLC back to unphosphorylated form, thus inhibiting the binding of the contractile filaments (Webb, 2003). MLCP can be inactivated through phosphorylation by Rho kinase (Webb, 2003; Hilgers & Webb, 2005). Understanding the mechanism of pericyte contraction is important because manipulation of the elements in this process by pathological or pharmacological means can alter pericyte contractility. For example C-type natriuretic peptide causes pericyte-mediated capillary dilation by inhibiting Ca^{2+} release from stores and activating MLCP which inhibits the coupling of actin and myosin, and this could be therapeutically useful in disorders in which excessive pericyte-mediated capillary constriction occurs (Špiranec *et al.*, 2018; Nortley *et al.*, 2019).

Many vasoactive agents that can affect pericyte contractility have been identified, including reactive oxygen species (ROS) (Yemisci *et al.*, 2009), endothelin 1 (Burdyga & Borysova, 2014; Zambach *et al.*, 2020), 20-hydroxyeicosatetraenoic acid

(20-HETE) (Liu *et al.*, 2021) and vasoactive substances in the renin-angiotensin system (RAS) (Hirunpattarasilp, Attwell & Freitas, 2019). These agents, and their effects on cerebral-pericyte contractility, may contribute to CBF dysregulation in many pathological processes such as Alzheimer's disease (AD) (Iturria-Medina *et al.*, 2016; Nortley *et al.*, 2019), hyperoxia (Brugniaux *et al.*, 2018), COVID-19 (Helms *et al.*, 2020) and other peripheral diseases including hypertension, kidney diseases and diabetes (Hirunpattarasilp, Attwell & Freitas, 2019). Because of their importance for the experiments performed in this thesis, the following sections review the properties of these messengers.

1.5 Reactive oxygen species (ROS)

1.5.1 Overview of ROS and oxidative stress

Reactive oxygen species (ROS) are a group of unstable and highly reactive partially reduced derivatives of oxygen, consisting of both radical and non-radical molecules (Ray, Huang & Tsuji, 2012). Free radical ROS, such as superoxide anion (O_2^{*-}) and hydroxyl radicals (OH*), are independent molecules containing at least one unpaired electron in their electron shells (Phaniendra, Jestadi & Periyasamy, 2015). They are prone to accept another election or donate their electron to achieve more stability, making them highly reactive (Phaniendra, Jestadi & Periyasamy, 2015). On the other hand, the non-radical species, such as hydrogen peroxide (H_2O_2), are comparatively more stable but can easily lead to free radical formation inside living organisms (Phaniendra, Jestadi & Periyasamy, 2015; Chen *et al.*, 2018).

Low or moderate controllable amounts of ROS are needed for normal signalling pathways, inducing mitogenic responses, mediating preconditioning mechanisms and modulating immune responses (Carvalho & Moreira, 2018). However, excessive ROS

formation that exceeds what can be controlled by endogenous anti-oxidants, leads to oxidative stress that is connected to biomolecule damage and pathologies such as neurodegenerative diseases, cancer and age-related disorders (Krumova & Cosa, 2016).

1.5.2 Generation of ROS

An oxygen molecule has two unpaired electrons with parallel spins in its outer anti-bonding molecular orbitals, thus it is unable to interact with other molecules which have a pair of electrons but with opposite spins (Krumova & Cosa, 2016). This spin restriction prevents most non-radical organic molecules from being oxidised by oxygen (Krumova & Cosa, 2016). The spin restriction also favours oxygen accepting only one electron at a time during redox reactions with other molecules with unpaired electrons, such as iron in coenzymes and prosthetic groups (a non-protein component that is part of a protein). This results in superoxide (Krumova & Cosa, 2016), which is the primary ROS or the first ROS generated in the process (Fig. 1.4) (Rodiño-Janeiro *et al.*, 2013). Superoxide then undergoes many reactions to produce other ROS (Rodiño-Janeiro *et al.*, 2013).

A single electron transfer to oxygen can be done enzymatically by redox enzymes and non-enzymatically through reduced prosthetic groups or coenzymes such as those in the mitochondrial electron transport chain (ETC) (Turrens, 2003). Enzymatic sources of ROS include the NADPH oxidase (NOX) enzyme family, xanthene oxidase (XO), nitric oxide synthase (NOS), lipooxygenase (LOX) and cyclooxygenase (COX) (Chen *et al.*, 2018). Of these, the NOX family, which is the only enzyme group with a primary function of producing superoxide and hydrogen peroxide, contributes to ROS generation the most (Rodiño-Janeiro *et al.*, 2013; Chen *et al.*, 2018).

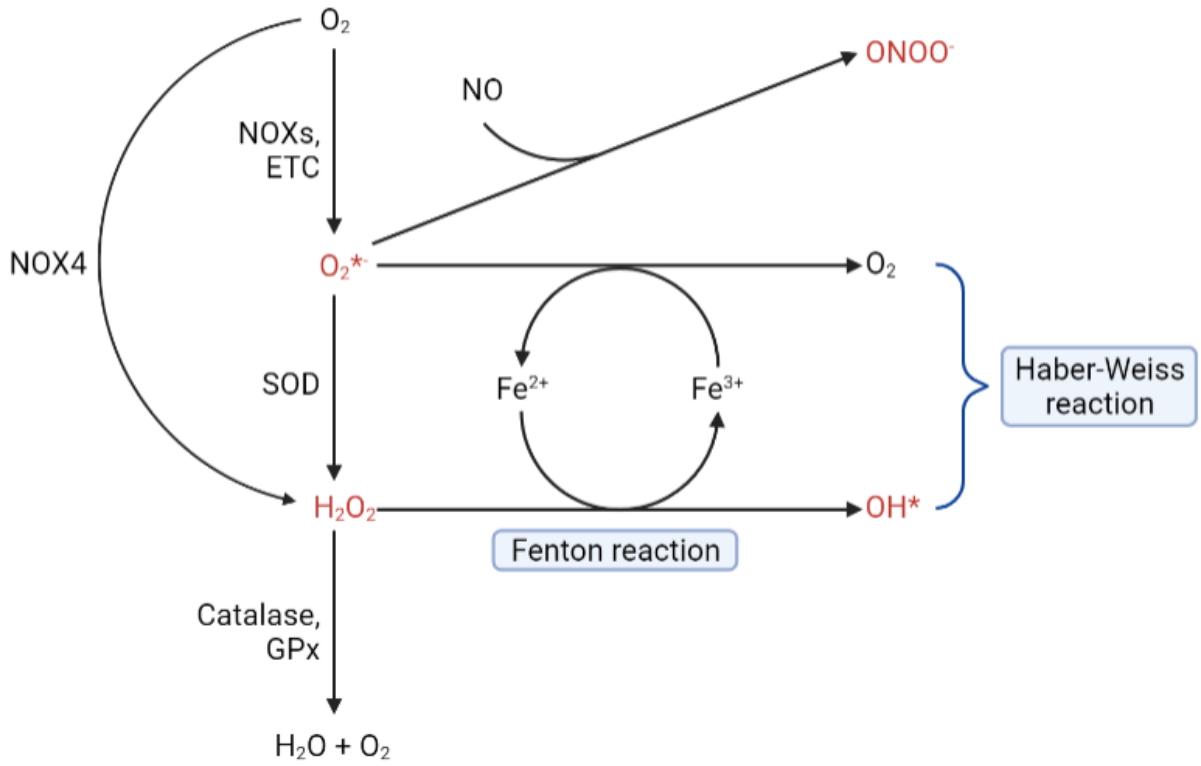

Figure 1.4: Formation of reactive oxygen species (ROS).

The reduction of oxygen (O_2) by one electron by NADPH oxidases (NOXs) or mitochondrial electron transport chain (ETC) yields superoxide (O_2^{*-}), which can react with nitric oxide (NO) to form peroxynitrite ($ONOO^-$) and undergo dismutation by superoxide dismutase (SOD) to form hydrogen peroxide (H_2O_2). H_2O_2 can also be produced from oxygen directly by NOX4 and changed to water (H_2O) and O_2 by catalase or glutathione peroxidase (GPx). Hydroxyl radical (OH*) can be formed by the Fenton reaction, which is the conversion of H_2O_2 and ferrous iron (Fe^{2+}) to OH* and ferric iron (Fe^{3+}), or the Haber-Weiss reaction, which is the combination of Fenton reaction and the reduction of Fe^{3+} to form Fe^{2+} by O_2^{*-}. Thus, the net process in the Haber-Weiss reaction is the conversion of O_2^{*-} and H_2O_2 to O_2, OH* and hydroxide ion (OH^-, not shown). The molecules in red are ROS. (Created with BioRender.com)

1.5.2.1 NADPH oxidase (NOX)

NOXs can be found on biological membranes such as the plasma membrane, nuclear membrane or intracellular vesicles (Bedard & Krause, 2007). These enzymes are comprised of a membrane-bound catalytic subunit which is homologous in all NOXs, and regulatory subunits which are specific to each isoform of NOX and are important in controlling the expression, activation and spatial organisation of the enzyme (Rodiño-Janeiro *et al.*, 2013; Altenhöfer *et al.*, 2015). The common features of the core catalytic subunit of NOX are having six or more trans-membrane helices, a flavin adenine dinucleotide (FAD) and two heme prosthetic redox groups, and an NADPH binding domain at the carboxy terminus in the cytosol (Altenhöfer *et al.*, 2015). The FAD domain and heme groups are involved in transferring an electron from the NADPH to oxygen.

Seven isoforms of NOXs has been identified, including NOXs 1-5 and dual oxidases (DUOXs) 1-2, which have an additional transmembrane protein and an extracellular peroxidase-like domain at the amino terminus (Altenhöfer *et al.*, 2015). Different isoforms use different binding subunits as well as different modes of activation, and can produce different ROS (Rodiño-Janeiro *et al.*, 2013; Altenhöfer *et al.*, 2015). NOX1-3 are regulated by the regulatory proteins, while NOX5 and DUOX 1-2 activity depends on the binding of calcium to the molecule (Rigutto *et al.*, 2009). NOX4 has a constitutive activity, which is regulated by its level of expression and binding proteins (Ha *et al.*, 2010). NOX1-3 and NOX5 produce superoxide as their main products (Rodiño-Janeiro *et al.*, 2013). In contrast, NOX4 and DUOX1-2 release mainly hydrogen peroxide (H_2O_2); however, at least in the case of NOX4, superoxide is initially generated but undergoes dismutation in the extracellular loop of the enzyme (Rigutto *et al.*, 2009; Ha *et al.*, 2010).

In the brain, NOX2 (Serrano *et al.*, 2003) and NOX4 (Cheng *et al.*, 2001; Vallet *et al.*, 2005) are widely expressed, while NOX1 (Infanger, Sharma & Davisson, 2006), NOX3 and NOX5 (Cheng *et al.*, 2001) are detected at a lower level; however, the expression can vary between different brain locations (Infanger, Sharma & Davisson, 2006), developmental stages and cell types (Cheng *et al.*, 2001). NOX1, 2 and 4, which have been detected in neurons at the level of mRNA and protein, are proposed to induce apoptosis and modulate neuronal activity because NOXs underly the Ang II-induced increase in neuronal firing rate (Sun *et al.*, 2005; Bedard & Krause, 2007; Ha *et al.*, 2010; Nayernia, Jaquet & Krause, 2014). In astrocytes, NOX2 (Bedard & Krause, 2007) and NOX4 (Nayernia, Jaquet & Krause, 2014) modulate astrocyte survival, signalling and inflammatory responses (Sorce & Krause, 2009). Information on NOXs in oligodendrocytes is lacking but NOX expression has been reported during maturation (Cavaliere *et al.*, 2012) and on injury of these cells (Johnstone *et al.*, 2013). Microglia contribute to neuroinflammation by producing ROS through phagocytic NOX2 (Green *et al.*, 2001; Choi *et al.*, 2012; Zeng *et al.*, 2018), which generates O_2^{*-} in a compartment being enveloped and phagocytosed in a burst-like style upon stimulation, unlike non-phagocytic NOXs, which produce O_2^{*-} intracellularly at a slow steady rate (Rodiño-Janeiro *et al.*, 2013). In cell lines expressing NOX2, non-activated NOX2 produces superoxide at estimatedly 4 pmol min^{-1} per 50,000 cells, however, after NOX2 is activated with protein kinase C (which is one of the activation mechanisms in phagocytic cells (Raad *et al.*, 2009; Jamali, Valente & Clark, 2010)), the superoxide generation rate is approximately 65 pmol min^{-1} per 50,000 cells (Augsburger *et al.*, 2019). NOXs are the major source of ROS in the vasculature (Guzik *et al.*, 2000). In the cerebral vasculature, endothelial cells express mainly NOX1 and 4, along with NOX2 to a lesser extent (Ago *et al.*, 2005). Cerebral vascular smooth

muscle cells also express NOX1, 2 and 4 (Li & Pagano, 2017), for which the levels of expression are markedly higher than those in the systemic arteries (Miller *et al.*, 2005). In pericytes, transcriptomic data (Zhang *et al.*, 2014; Zeisel *et al.*, 2018) and pharmacological studies (Kuroda *et al.*, 2014) suggest that NOX4 is the main NOX isoform.

1.5.2.2 Mitochondrial production of ROS

The other major source of ROS is mitochondria (Krumova & Cosa, 2016). About 0.2 – 2% of the electrons in the electron transport chain (ETC) leak out and interact with oxygen to form superoxide under physiological conditions (Zhao *et al.*, 2019). Important sites in the ETC that produce ROS include complex I, complex II and complex III (Zhao *et al.*, 2019; Cobley, 2020).The rate of basal superoxide production from isolated mitochondria is less than 0.1 nM min^{-1} mg mitochondrial $protein^{-1}$ (Brand, 2010).

1.5.3 ROS and their effects on the cerebral vasculature

Later in the thesis I will show that in Alzheimer's disease amyloid β evokes capillary constriction by generating ROS. As background, here I explain the known effects of different ROS species on the cerebral vasculature.

1.5.3.1 Superoxide ($O_2^{\bullet-}$)

In cells, the intracellular concentration of superoxide ranges from 10^{-11} to 10^{-12} M (Jaeschke, 2010). It should be noted that basal superoxide production rate in arteries varies from 0.9 pmol min^{-1} mg $(tissue)^{-1}$ in rabbit aorta (Amirmansour, Vallance & Bogle, 1999) to 9 pmol min^{-1} mg $(tissue)^{-1}$ in pig coronary arteries (Brandes *et al.*, 1997) and 978 pmol min^{-1} mg $(tissue)^{-1}$ in human internal mammary arteries (Berry *et al.*, 2000). Most data on cerebral arteries quantify chemiluminescence signal of superoxide, complicating the quantification of absolute values of superoxide

concentration (Didion & Faraci, 2002; Park *et al.*, 2004; Miller *et al.*, 2005; Silva *et al.*, 2011; Merdzo *et al.*, 2017).

Superoxide can act as an oxidant (the electrochemical potential $E^{o'}(O_2^{*-}/ H_2O_2)$ = 0.93 V) or a reductant ($E^{o'}(O_2/ O_2^{*-})$ = - 0.33 V) (Wardman, 1989) but the reactivity of superoxide with biomolecules is low (Phaniendra, Jestadi & Periyasamy, 2015) as reflected by the low observed rate constants of reactions (usually less than 10^2 $M^{-1}s^{-1}$) (Collin, 2019). This is due to the need for a proton or a metal group to stabilise an intermediate, called the peroxide dianion (O_2^{2-}), when superoxide acts as an oxidant (Sheng *et al.*, 2014). However, superoxide can reacts in a kinetically favoured fashion with some specific targets that provide hydrogen atoms for stabilisation such as ascorbate or hydroquinone, or contain metal ions such as cytochrome C or superoxide dismutase (SOD) (Sheng *et al.*, 2014; Collin, 2019). At a low pH, superoxide gets protonated into hydroperoxyl radical (HO_2^*) (pKa = 4.8) (Bielski & Cabelli, 1995), which is present in the cytosol of a normal cell at about 0.3% of the total cytosolic O_2^{*-} (Phaniendra, Jestadi & Periyasamy, 2015). Hydroperoxyl radical is uncharged so it can penetrate phospholipid bilayers (Phaniendra, Jestadi & Periyasamy, 2015) and is a better oxidant for biomolecules such as polyunsaturated fatty acids than superoxide (Collin, 2019).

As the primary ROS, superoxide reacts to produce highly-reactive secondary ROS, causing harm to cells (Phaniendra, Jestadi & Periyasamy, 2015). There are at least four important reactions by which this occurs. Firstly, superoxide undergoes the Haber-Weiss reaction by reacting with hydrogen peroxide using iron as a catalyst to form hydroxyl radical (Fig. 1.3) (Collin, 2019). The Haber-Weiss reaction can be written as:

$$O_2^{*-} + H_2O_2 \rightarrow O_2 + OH^* + OH^-$$

Moreover, hydrogen peroxide can be generated by superoxide and hydroperoxyl radical through two reactions, the disproportionation reaction and the dismutation reaction catalysed by SOD (Fig. 1.4) (Sheng *et al.*, 2014; Phaniendra, Jestadi & Periyasamy, 2015; Collin, 2019). Disproportionation, which can occur under physiological conditions but is not kinetically favoured, is when hydroperoxyl radical reacts with another hydroperoxyl radical or superoxide molecule (Collin, 2019). The dismutation reaction in the presence of SOD can be written as:

$$2O_2^{*-} + 2H^+ \rightarrow H_2O_2 + O_2$$

The disproportionation equation can be written as:

$$HO_2^* + HO_2^* \rightarrow H_2O_2 + O_2$$

$$HO_2^* + O_2^{*-} + H^+ \rightarrow H_2O_2 + O_2$$

Lastly, superoxide can react with nitric oxide, resulting in peroxynitrite (Fig. 1.4), which is highly reactive towards DNA, proteins and lipids (Rodiño-Janeiro *et al.*, 2013; Collin, 2019). The equation is:

$$O_2^{*-} + NO^* \rightarrow ONOO^-$$

Superoxide exerts complex direct and indirect effects on the cerebral vasculature that promote either relaxation or constriction of vascular smooth muscle cells, depending on the concentration and the model (Faraci, 2006). At lower concentrations induced by perfusing 0.1-10 μM NADH (Didion & Faraci, 2002) (superoxide levels were quantified in chemiluminescence units hence the absolute amount of superoxide cannot be determined), superoxide causes dilation of cerebral vessels and arterioles, supposedly acting through potassium channels (Faraci, 2006) such as calcium-activated potassium channels (Wei, Kontos & Beckman, 1996). However, at a higher concentration, generated by perfusing 30-100 μM NADH (Didion & Faraci, 2002), this radical constricts cerebral arteries. This occurs through two

mechanisms - a direct (endothelium-independent) contraction of the muscle and an impairment of endothelium-dependent relaxation (Faraci, 2006). It can also rapidly react with, and deplete, nitric oxide, a potent vasodilator, causing vasoconstriction (Faraci, 2006) and generating peroxynitrite, which has been shown to cause pericyte contraction (Yemisci *et al.*, 2009).

1.5.3.2 Hydrogen peroxide (H_2O_2)

The intracellular H_2O_2 concentration is estimated to have an upper limits of 100 nM to 1 µM H_2O_2 (Rice, 2011) and the basal H_2O_2 production in cerebral arteries is approximately 10 pmol min^{-1} mg (tissue) $^{-1}$ (Miller *et al.*, 2005)

Hydrogen peroxide is the product of a two-electron reduction of oxygen molecules. It can act as a one-electron reductant, a one-electron oxidant or a two-electron oxidant. However, the oxidising power of hydrogen peroxide is low, given that the one-electron transfer is not thermodynamically favoured and only occurs when catalysed by metal ions in the Fenton and Haber-Weiss reactions, and its reactions to most biomolecules are not kinetically favoured (Collin, 2019). The Fenton reaction can be written as:

$$Fe^{2+} + H_2O_2 \rightarrow Fe^{3+} + OH^* + OH^-$$

Hydrogen peroxide reacts with thiols, which provides the basis for the elimination of hydrogen peroxide by glutathione peroxidases and peroxiredoxins (Collin, 2019). While being quite stable, hydrogen peroxide can penetrate biological membranes and act as a second messenger (Phaniendra, Jestadi & Periyasamy, 2015; Chen *et al.*, 2018).

The toxicity of hydrogen peroxide mostly comes from reactions that form stronger ROS such as hydroxyl radical and peroxymonocarbonate (HCO_4^-) (Collin, 2019). Hydrogen peroxide is neutralised by many antioxidant enzymes such as

catalases, glutathione peroxidase and peroxiredoxins to form water and oxygen (Fig. 1.4) (Rodiño-Janeiro *et al.*, 2013; Phaniendra, Jestadi & Periyasamy, 2015).

In the cerebral circulation, exogenous hydrogen peroxide application has yielded conflicting results (Faraci, 2006). Vasodilation of cerebral arteries *in vitro* and of the basilar artery *in vivo* was observed on applying hydrogen peroxide (using 0.44-1000 μM H_2O_2) (Fraile *et al.*, 1994; Yang *et al.*, 1998; Iida, Katusic & Wei, 2000; You, Golding & Bryan, 2005; Faraci, 2006). Relaxation was mediated by potassium channels, including calcium-activated potassium channels (Faraci, 2006) and ATP-sensitive potassium channels (Wei, Kontos & Beckman, 1996). H_2O_2 also has been shown to cause endothelium-dependent contraction in intact arteries (Katusic *et al.*, 1993). One study has shown that a very high concentration (10 mM) of hydrogen peroxide causes vasoconstriction followed by vasodilation in piglet pial arterioles (Leffler *et al.*, 1990). For CNS pericytes, hydrogen peroxide increases intracellular calcium (in culture) and this calcium response is regulated by tyrosine kinases (Kamouchi *et al.*, 2007) or by amiloride-sensitive proteins controlled by thiol-group oxidation (Nakamura *et al.*, 2009). A calcium increase is closely related to pericyte constriction (Khennouf *et al.*, 2018); hence, it can be assumed that hydrogen peroxide may lead to pericyte constriction. Hydrogen peroxide also increases F-actin expression in cultured pericytes (Mohamed, 2013), favouring more contractility.

1.5.3.3 Hydroxyl radical (OH)*

The hydroxyl radical has the most oxidising power among ROS because it can react rapidly with most biological molecules, including DNA, amino acids and fatty acids (Collin, 2019). As a result, its reaction is diffusion controlled occurring over tens of nanometres, and the effect is limited to the site of metal catalysts; however, it may lead to chain reactions, resulting in an extensive range of actions (Kontos, 2001). It is

generated through the Fenton and Haber-Weiss reactions (Collin, 2019; note that some studies state that the Fenton reaction is a part of Haber-Weiss reaction (Gutteridge, 1985b)) (see Sections 1.5.3.1-1.5.3.2, Fig. 1.4). Hydroxyl radicals react in three different ways. (i) They react with aromatic molecules or those containing sulphur groups, causing double bond addition and biomolecule oxidation. For example, addition of OH* causes oxidation of DNA bases (e.g. changing guanine into 8-oxoguanine) and of amino acids (e.g. changing histidine and tryptophan into 2-oxohistidine and N-formylkynurenine/kynurenune respectively), leading to a loss of function of these biomolecules. (ii) Hydroxyl radicals remove an electron from sulphur-containing molecules and inorganic substrates such as transition metals, leading to irreversible biological damage. For example, methionine undergoes electron abstraction to produce sulfuranyl radical cation, leading to permanent damage to protein structures, (iii) OH* causes hydrogen removal from most biological molecules, disrupting their function, such as polyunsaturated fatty acids, 2-deoxyribose and DNA bases, amino acids and hydroxyl or thiol group containing molecules. This leads to a carbon-centred radical, which readily reacts with oxygen to form peroxyl radical, and oxygen or sulphur-centred radicals (Collin, 2019).

Studies of the effects of hydroxyl radicals on the cerebral vasculature are conflicting (Faraci, 2006). On one hand, hydroxyl radicals mediate arteriolar dilation after application of H_2O_2 *in vivo* (Wei & Kontos, 1990) and after ischaemia-reperfusion injury (Nelson *et al.*, 1992). They also promote endothelium-dependent vasodilation of cerebral arterioles by bradykynin (Rosenblum, 1987). On the other hand, hydroxyl radicals prevent vasodilation of cerebral arterioles by deactivating soluble guanylate cyclase (Kontos & Wei, 1993) or by oxidising endothelium-derived relaxing factor (Marshall, Wei & Kontos, 1988). They also mediate cerebral arterial spasm after

subarachnoid haemorrhage in dogs (Asano *et al.*, 1984) and rats (Germanò *et al.*, 1998; Yamamoto *et al.*, 2000), supposedly through lipid peroxidation-induced smooth muscle contraction (Asano *et al.*, 1996). Hydroxyl radicals also act on endothelial cells to increase endothelin (ET)-1 release (Prasad, 1991). Deferoxamine, an iron chelator which blocks production of hydroxyl radicals, inhibits myosin redistribution after application of hydrogen peroxide in retinal pericytes, suggesting a relationship between hydroxyl radical and pericyte contractility (Shojaee *et al.*, 1999).

1.5.3.4 Peroxynitrite ($ONOO^-$)

Peroxynitrite, which is also classified as a reactive nitrogen species (RNS), is generated when superoxide reacts with nitric oxide (Fig. 1.4) (Phaniendra, Jestadi & Periyasamy, 2015). It is a strong oxidant that only slowly reacts with nucleophiles such as transition metals, and sulphur groups such as methionine (Pacher, Beckman & Liaudet, 2007). These low reaction rates occur because of its stable configuration, allowing the negative charge to be distributed over the whole structure and also because of hydrogen bonds which the RNS forms with water molecules (Pacher, Beckman & Liaudet, 2007). As a result, peroxynitrite can cross biological membranes and react with limited targets (Pacher, Beckman & Liaudet, 2007).

Two mechanisms of action of peroxynitrite have been proposed: (i) it oxidises certain molecules through one or two electron transfer processes; and (ii) it can indirectly oxidise biomolecules by forming other highly reactive radicals (Pacher, Beckman & Liaudet, 2007). For example, Peroxynitrite reacts with carbon dioxide to create nitrosoperoxycarbonate ($ONOOCO_2^-$), which spontaneously decomposes into carbonate radical (CO_3^{*-}) and nitrogen dioxide radical (NO_2^*) that can react with tyrosine to form nitrotyrosine (Pavlovic & Santaniello, 2007).

Data on the cerebrovascular roles of peroxynitrite are complex and conflicting. Peroxynitrite produces vasodilation of cerebral arteries *in vitro* in an endothelial-independent fashion, and dilates cerebral arterioles *in vivo*, possibly by activating ATP-sensitive potassium channels and evoking hyperpolarization (Wei, Kontos & Beckman, 1996), while others found that peroxynitrite constricts cerebral arteries *in vitro* by inhibiting calcium-activated potassium channels evoking depolarization (Faraci, 2006). Interestingly, Yemisci *et al.* (2009) found that application of peroxynitrite *in situ* causes a small arteriolar dilation but local constrictions of capillaries, and blocking production of peroxynitrite prevented ischaemic-induced pericyte constriction. This implies that ROS, at least in case of peroxynitrite, can cause constriction of pericytes and that the effects of ROS on pericytes and arterioles may be different.

1.5.4 Pathological conditions associated with ROS

Oxidative stress is related to several pathologies, including Alzheimer's disease (Phaniendra, Jestadi & Periyasamy, 2015), ischaemic stroke (Yemisci *et al.*, 2009) and traumatic brain injury (Ng & Lee, 2019), and might underlie CBF deficits in those diseases. Hyperoxic vasoconstriction is also proposed to be mediated by ROS (Demchenko *et al.*, 2002; Mattos *et al.*, 2019).

1.6 Endothelin (ET)

As explained below (see Section 4.3.3), in Alzheimer's disease amyloid β evokes capillary constriction as a result of the ROS that it generates evoking a release of endothelin. As background, here I explain the known effects of endothelin on the cerebral vasculature.

1.6.1 Overview of ET

Endothelins (ETs) are vasoconstricting peptides that can cause vSMC and pericyte contraction (Chakravarthy *et al.*, 1992; Davenport *et al.*, 2016; Neuhaus *et al.*, 2017). There are three endothelin isoforms, ET-1, ET-2 and ET-3, all of which are composed of 21 amino acids with two disulphide bonds but with different amino acids (Koyama, 2013). ET-1 and ET-2 both stimulate ET_A and ET_B receptors (described in detail below in Section 1.6.3) equally but ET-3 preferentially binds to ET_B receptors. The brain mostly expresses ET-1 and ET-3 (Koyama, 2013). ET-1 is the most common isoform found in the human vasculature and the major source of ET-1 under physiological conditions is vascular endothelial cells (Davenport *et al.*, 2016).

1.6.2 Generation of ET

The processes for making all isoforms of ET are similar (Koyama, 2013). In the case of ET-1, which is continuously synthesised and released by vascular endothelia, the prepro-ET-1 gene is transcribed into prepro-ET-1 mRNA, which in turn is translated into prepro-ET-1 (Davenport *et al.*, 2016). Transcription is the rate-limiting step that can be regulated by cytokines such as transforming growth factor β (TGF β) and tumour necrosis factor α (TNF α) (Koyama, 2013; Davenport *et al.*, 2016). Prepro-ET-1 is processed to form pro-ET-1 that is consequently cleaved by furin-like protease to form Big-ET-1 (Horinouchi *et al.*, 2013). Big-ET-1 is further processed by endothelin-converting enzymes (ECEs) to produce active ET-1 (Rafols & Kreipke, 2011; Koyama, 2013). There are two forms of ECE: (i) ECE-1, which is found in many cells including endothelial cells; and (ii) ECE-2, which is expressed in neurons (Palmer & Love, 2011; Koyama, 2013). ECE-1 activities have been found to increase in the presence of ROS and Aβ (Palmer, Tayler & Love, 2013). Aβ also stimulates ECE-2 in neurons to produce more ET (Palmer & Love, 2011). In hyperoxia, ET-1 release is triggered by

the angiotensin system and Ca^{2+} channels opening on endothelial cells (Higgins *et al.*, 1998).

1.6.3 ET receptors and their effects on the cerebral vasculature

There are two endothelin G-protein coupled receptors, namely ET_A and ET_B (Koyama, 2013). In the cerebral cortex, 90% of the ET receptors are ET_B receptors expressed on neurons and astrocytes. The ET_A receptors are restricted to the cerebral vasculature and leptomeninges (Harland *et al.*, 1995; Rogers *et al.*, 2003), making ET_A receptors important in CBF control (Davenport *et al.*, 2016). In the vasculature, ET_A receptors are generally found on vSMCs and pericytes, and ET_B receptors are expressed on endothelial cells. ET_A receptors are activated more by ET-1 and ET-2 than by ET-3 (Schneider, Boesen & Pollock, 2007). ET_A receptor stimulation on vSMCs acts via $G_{q/11}$ and $G_{12/13}$ proteins to evoke vasoconstriction (Horinouchi *et al.*, 2013). $G_{q/11}$ stimulation leads to activation of phospholipase C, which generates inositol trisphosphate (IP_3) that causes Ca^{2+} release from IP_3-sensitive intracellular Ca^{2+} stores (Horinouchi *et al.*, 2013). Increased intracellular [Ca^{2+}] then activates MLCK through a calmodulin-dependent pathway (see Section 1.4.4), evoking contraction. Activation of $G_{12/13}$ stimulates the ROCK pathway that suppresses the activity of MLCP (Horinouchi *et al.*, 2013) (see Section 1.4.4), again evoking contraction. In pericytes, ET-1 also acts on ET_A receptors to produce contraction through an inositol triphosphate (IP3)-mediated calcium concentration increase (Dehouck *et al.*, 1997; Burdyga & Borysova, 2014; Zambach *et al.*, 2020). The dissociation of ET from ET_A receptors is very slow and the binding is even reported to be irreversible in some studies (Davenport *et al.*, 2016).

All three isoforms of ET bind equally well to ET_B receptors (Schneider, Boesen & Pollock, 2007). Stimulating ET_B receptors has given different effects on vSMC

contractility (Seo *et al.*, 1994; Schneider, Boesen & Pollock, 2007; Dore-Duffy *et al.*, 2011). ET_B receptors on endothelial cells mediate vasodilation through production of nitric oxide and prostacyclins, and through clearance of ET-1 from the circulation (Szok, Hansen-Schwartz & Edvinsson, 2001; Schneider, Boesen & Pollock, 2007; Horinouchi *et al.*, 2013). In contrast, direct activation of ET_B receptors on vSMCs results in vasoconstriction (Clozel *et al.*, 1992; Seo *et al.*, 1994) but the expression of ET_B receptors is low on these cells (Nilsson *et al.*, 2008). On the whole, ET_B receptors act as a counter-regulatory pathway to restrict ET_A-induced vasoconstriction (Davenport *et al.*, 2016).

1.6.4 Pathological conditions associated with ET

ET-1 has been associated with many neurological diseases. The production of ET-1 and ET receptors is increased in brain ischaemia (Matsuo *et al.*, 2001), brain injury (Armstead, 1996) and subarachnoid haemorrhage (Thampatty *et al.*, 2011). Vasoconstriction mediated by ET_A receptors has also been shown in many pathologies such as subarachnoid haemorrhage (Thampatty *et al.*, 2011), Alzheimer's disease (reviewed by Palmer and Love, 2011) and hyperoxia (Dallinger *et al.*, 2000).

1.7 20-hydroxyeicosatetraenoic acid (20-HETE)

Later in this thesis (see Section 5.3.7) I investigate the role of the arachidonic acid derivative 20-HETE in mediating hyperoxia evoked capillary constriction. As background, here I describe the properties of 20-HETE.

1.7.1 Overview and generation of 20-HETE

20-HETE is a potent vasoconstricting agent that has a role during both normal physiologic and pathologic conditions, especially in the kidney and the brain, (Elshenawy *et al.*, 2017). 20-HETE is formed when arachidonic acid (AA), which is a

20-carbon chain fatty acid found in the cell membrane, is metabolised by cytochrome P450 (CYP enzymes), particularly CYP4A and/or CYP4F (Roman, 2002).

CYPs, which catalyse hydroxylation of terminal carbon atoms, are categorised into different subfamilies using their amino acid sequences. Within the same subfamily, different animal species also express different CYPs (Edson & Rettie, 2013). For the CYP4A subfamily, humans express mainly CYP4A11, which produces 20-HETE, but less than CYP4F2 (Gainer *et al.*, 2005; Fan *et al.*, 2016). In contrast, rats and mice express CYP4A1, 2, 3 and 8, and CYP4A10, 12 and 14 respectively (Edson & Rettie, 2013), with CYP4A1 being the most active isoform for 20-HETE synthesis in rats (Gonzalez-Fernandez *et al.*, 2020). CYP4As are expressed in the brain in both cerebral arteries and cerebral microvessels, particularly in vSMCs that produce the majority of the 20-HETE (Harder *et al.*, 1994; Fan *et al.*, 2016), arterial endothelial cells, astrocytes, neurons and pericytes (Davis, Liu & Alkayed, 2017; Gonzalez-Fernandez *et al.*, 2020; Liu *et al.*, 2021)

CYP4As are thought to act as an oxygen sensor (Harder *et al.*, 1996; Frisbee *et al.*, 2001; Roman, 2002). The synthesis of 20-HETE is linearly associated with PaO_2 between 20 and 140 mmHg in rat cremaster arterioles (Harder *et al.*, 1996). CYP4A enzymes in rats have a Michaelis constant (K_m) of ~55 μM at 37^{o}C for oxygen, for the conversion of AA to 20-HETE (Harder *et al.*, 1996; Attwell *et al.*, 2010). This is at the higher end of the range of *in vivo* values of oxygen tension In the brain, which is 20 – 60 μM (Attwell *et al.*, 2010). This means that changes of brain oxygen tension within the *in vivo* range in both directions have a big impact on 20-HETE synthesis from CYP4As.

Other enzymes that participate in 20-HETE production in man are CYP4F2, which has the highest activity, and CYP4F3 (Fan *et al.*, 2016). To my knowledge, there

is no study on how the synthesis of 20-HETE from CYP4F isoforms varies with oxygen level.

1.7.2 The effect of 20-HETE on the cerebral vasculature

20-HETE is produced by vascular mural cells, including pericytes, and acts mainly in an autocrine manner to produce vasoconstriction (Fan *et al.*, 2016; Liu *et al.*, 2021). 20-HETE has been shown to activate protein kinase C (PKC), tyrosine kinase, Rho kinase and mitogen-activated protein kinases (MAPK) to inhibit the large conductance Ca^{2+}-activated K^+ (BK) channels (Harder *et al.*, 1997; Hoopes *et al.*, 2015; Fan *et al.*, 2016). This causes depolarisation that leads to opening of L-type Ca^{2+} channels (Harder *et al.*, 1997; Hoopes *et al.*, 2015; Fan *et al.*, 2016), resulting in a Ca^{2+} influx and contraction. Activation of PKC can also directly activate L-type Ca^{2+} channels and open transient receptor potential canonical 6 (TRPC6) and transient receptor potential vanilloid 1 (TRPV1) channels to allow influx of Ca^{2+} into vascular mural cells (Basora *et al.*, 2003; Wen *et al.*, 2012; Fan *et al.*, 2016). Moreover, activation of Rho kinase can phosphorylate MLCP to deactivate the enzyme, resulting in an increase of contractility of the mural cells (Webb, 2003; Randriamboavonjy, Busse & Fleming, 2003; Hilgers & Webb, 2005) (see Section 1.4.4). 20-HETE can also stimulate NOXs in the vSMCs in arterioles, leading to arteriolar constriction (Hama-Tomioka *et al.*, 2009).

1.7.3 Pathological conditions associated with 20-HETE

20-HETE production has been related to the development of cerebral vasospasm in subarachnoid haemorrhage (Kehl *et al.*, 2002; Poloyac *et al.*, 2005). A reduction of CBF during cortical spreading depression, which is associated with migraine and acute brain injuries, is also proposed to be mediated by 20-HETE (Fordsmann *et al.*, 2013). In addition, the level of 20-HETE is increased in ischaemic

stroke and inhibitors of 20-HETE synthesis can improve neurological outcome and reduce infarct size in strokes (Renic *et al.*, 2009; Ward *et al.*, 2011; Kawasaki *et al.*, 2012). Constriction of arterioles in hyperoxia has also been related to an elevated level of 20-HETE (Harder *et al.*, 1996).

1.8 Renin-angiotensin system (RAS)

In Chapter 6 of this thesis I examine the role of the renin-angiotensin system in the effects of the SARS-CoV-2 virus on the vasculature, while in Chapter 7 I review the role of the RAS system in mediating the effects of peripheral disorders on brain pericytes. Accordingly, here I review briefly the properties of the RAS.

1.8.1 Overview of RAS

Classically, RAS is a renal endocrine pathway that uses renin and angiotensin to regulate water and electrolyte balance, aldosterone synthesis and release, cardiovascular homeostasis and the resistance to blood flow in the body (Tigerstedt & Bergman, 1898; Cosardereliogl*u et al.*, 2020). With the discovery of local RAS systems in non-renal organs, we can now separate the RAS into two systems.

(i) The renal endocrine system, which acts systemically to maintain electrolyte and water balance and cardiovascular homeostasis (Matsusaka *et al.*, 2012; Cosardereliogl*u et al.*, 2020). In this system, renin produced by the juxtaglomerular cells of renal afferent arterioles converts circulating angiotensinogen (from the liver) into angiotensin I (Ang I), which is then converted by angiotensin converting enzyme (ACE) into angiotensin II (Ang II). Angiotensin II is a vasoconstrictor, but also evokes the release of aldosterone from the adrenal cortex to promote retention of Na^+ and water by the body. Angiotensin II is then converted by angiotensin converting enzyme

2 (ACE2) into angiotensin-(1-7), a vasodilator described in more detail below. ACE2 is the receptor for the SARS-CoV-2 virus, which is described further below.

(ii) Local renin-angiotensin systems, which act in an autocrine and paracrine fashion in many organs, such as the adrenal glands, the heart and the brain (Dzau, 1988; Paul, Mehr & Kreutz, 2006).

These two systems affect the brain in a different way. Because most of the components in the systemic RAS cannot pass though the blood-brain barrier (BBB), the effect of this system is limited to brain regions without a tight BBB such as the circumventricular organs, which give projections to other parts of the brain including the paraventricular, supraoptic, and median preoptic nuclei as well as the hypothalamus and the medulla oblongata (Lenkei *et al.*, 1997; Wright & Harding, 2013). Alternatively, the local brain-RAS (b-RAS) can generate all components of the RAS *de novo* (Fuxe *et al.*, 1980). This is supported by the fact that active RAS genes and renin-expressing cells near angiotensinogen-producing cells are found in the brain (Fuxe *et al.*, 1980; Hermann *et al.*, 1987; Shinohara *et al.*, 2017). The b-RAS plays a major role in maintaining physiology and behaviours such as regulation of thirst and water balance, vasopressin production, and blood pressure regulation, and it is also a major modulator of cerebral blood flow (Wright & Harding, 2011).

1.8.2 Components of the brain-RAS

The brain generates angiotensin I from angiotensinogen, which is mainly produced and constitutively secreted from astrocytes (Stornetta *et al.*, 1988; Grobe, Xu & Sigmund, 2008; Wright & Harding, 2013; de Kloet *et al.*, 2015; Xu *et al.*, 2016; Garrido-Gil *et al.*, 2017). Because the expression of renin is low in the brain (Grobe, Xu & Sigmund, 2008; Jackson *et al.*, 2018), the majority of angiotensinogen is cleaved by activated prorenin (a renin precursor), created by the binding of prorenin to the

prorenin receptor (PRR; Fig. 1.5) (Xu *et al.*, 2016). PRR is highly expressed in neurons and microglia and stimulates prorenin without cleavage of the protein (Xu *et al.*, 2016; Garrido-Gil *et al.*, 2017; Zeisel *et al.*, 2018). Further conversion of the decapeptide Ang I to the octapeptide Ang II is catalysed by angiotensin converting enzyme (ACE), cathepsin or chymase (Fig. 1.5) (Mogi, Iwanami & Horiuchi, 2012; Wright & Harding, 2013). Ang II is subsequently converted into angiotensin-(1-7) (Ang(1-7)) by ACE2, which also catalyses the transformation of Ang I to Ang(1-9) (Fig. 1.5) (Cosardereliogl*u et al.*, 2020). Ang(1-7) can also be generated from Ang(1-9) and Ang I through reactions catalysed by ACE, and neutral endopeptidase (neprilysin) or prolyl-endopeptidase respectively (Welches, Bridget Brosnihan & Ferrario, 1993). Ang(1-7) undergoes decarboxylation to form alamandine (Fig. 1.5) (Lautner *et al.*, 2013). Alternatively, Ang II can be converted to Ang III by aminopeptidase A (AP-A) and then to Ang IV by aminopeptidase N (AP-N; Fig. 1.5) (Cosardereliogl*u et al.*, 2020).

The main neuroactive agents in the b-RAS are vasoconstricting Ang II, and vasodilating Ang(1-7) and Ang IV (Cosardereliogl*u et al.*, 2020).

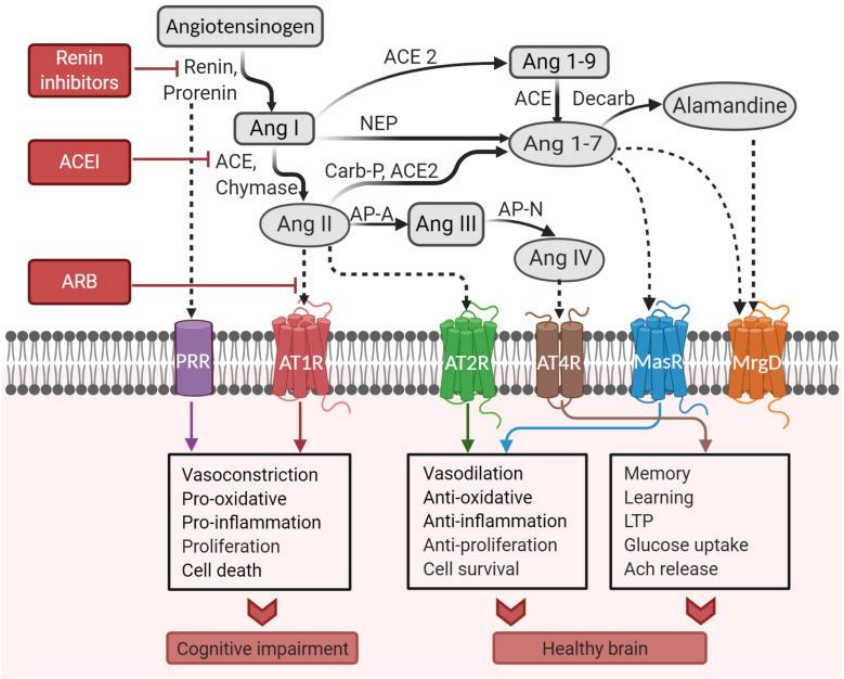

Figure 1.5: Pathways of the brain renin–angiotensin system.

This figure is from Cosardereliogluet *al.* (2020). ACE, angiotensin-converting enzyme; ACEI, angiotensin-converting enzyme inhibitor; Ang, angiotensin; AP-A, aminopeptidase A; AP-N, aminopeptidase N; ARB, angiotensin receptor blocker; AT1R, angiotensin II type I receptor; AT2R, angiotensin II type 2 receptor; AT4R, angiotensin IV receptor; Carb-P, carboxypeptidase-P; decarb, decarboxylase; LTP, long-term potentiation; MasR, Mas receptor; MrgD, Mas-related-G protein-coupled receptor; NEP, neutral endopeptidase; PRR, prorenin receptor (Created with BioRender.com)

1.8.3 Receptors of the brain-RAS and their effects on cerebral vasculature

Receptors of the RAS that are important in regulating blood flow include the AT1 receptors (AT1Rs), AT2 receptors (AT2Rs) and Mas receptors.

AT1Rs are G-protein coupled receptors (Miura, Imaizumi & Saku, 2013) that bind to Ang II better than to Ang III (Chiu *et al.*, 1993). This receptor is present in all cells in the cardiovascular system, including endothelial cells, vSMCs and pericytes (Dasgupta & Zhang, 2011; Kuroda *et al.*, 2014). In the brain, AT1Rs are found in various regions including the cerebral cortex, circumventricular organs, thalamus, basal ganglion, cerebellar cortex and medulla oblongata, and are expressed on neurons, astrocytes, oligodendrocytes and microglia (Johren, Inagami & Saavedra, 1995; Allen, Zhuo & Mendelsohn, 2000; Cosarderelioglu *et al.*, 2020). Rats and mice express two subtypes of AT1Rs, termed AT1a and AT1b, with similar ligand-binding and receptor-effector coupling properties, but their expression levels in the tissues differ; however, only one AT1R gene is found in humans (Dasgupta & Zhang, 2011).

Activation of AT1Rs on vSMCs leads to vasoconstriction. This occurs via:

(i) coupling to the G protein G_q leading to phospholipase C-mediated production of IP_3 which releases internally stored calcium, that binds to calmodulin and activates myosin light chain kinase, and

(ii) coupling to $G_{12/13}$ that activates Rho kinase, which phosphorylates myosin light chain phosphatase, leading to a decrease in its action and increased contractility (Näveri, Strömberg & Saavedra, 1994; Hilgers & Webb, 2005; Faraci *et al.*, 2006) (see Section 1.4.4).

Moreover, AT1Rs increase signalling in various pathways, including via mitogen-activated protein kinase (MAPK), extracellular signal-regulated kinases (ERK) 1/2, receptor tyrosine kinases and non-tyrosine receptor kinases such as c-src (Mehta &

Griendling, 2007). Binding of Ang II to AT1Rs also generates oxidative stress through NOXs in vSMCs, leading to nitric oxide depletion and vasoconstriction (Dasgupta & Zhang, 2011). In retinal pericytes, activation of AT1Rs opens nonspecific cation (NSC) and Ca^{2+}-activated Cl^- channels, resulting in depolarisation and activation of voltage-dependent Ca^{2+} channels (VDCCs) (Kawamura *et al.*, 2004). This leads to Ca^{2+} influx and pericyte constriction (Burdyga & Borysova, 2014) (see Section 1.4.4).

Relevant to the time course of the angiotensin actions I report in Chapter 6, rapid internalisation of AT1Rs can occur after binding of Ang II, particularly via clathrin-coated endocytic vesicles with a typical onset of 2 min or less (Hunyady *et al.*, 2000). About three quarter of the internalised receptors are degraded in lysosomes and the remainder are recycled back to the cell surface (Griendling *et al.*, 1987). The process involves many proteins such as β-arrestin, G protein-mediated phospholipase D_2 and GTPases in the Rab family (Du *et al.*, 2004; Mehta & Griendling, 2007). Phosphorylation of AT1Rs by G protein-coupled receptor kinases (GRKs), which can be triggered by Ang II, may participate in the uncoupling of the receptors from the activated G proteins, leading to desensitisation and internalisation (Kai *et al.*, 1994; Hunyady *et al.*, 2000). Some studies suggest that AT1Rs are also internalised via noncoated-caveolin-mediated endocytosis in vSMCs (Ishizaka *et al.*, 1998); however, this pathway is expected to play a minor role (Hunyady *et al.*, 2000).

AT2Rs are G-protein coupled receptors that have more affinity for Ang III than for Ang II (Chiu *et al.*, 1993; Wright & Harding, 2011). They are found in vSMCs and endothelial cells in arteries (Nora *et al.*, 1998; Matrougui *et al.*, 1999; Toedebusch, Belenchia & Pulakat, 2018). AT2Rs are also detected in pericytes but the level of expression is less than that of AT1Rs (Kuroda *et al.*, 2014). In the brain, AT2Rs are expressed in regions related to learning and memory such as the hippocampus,

cingulate cortex, and lateral septum, as well as other thalamic and subthalamic nuclei, locus coeruleus and inferior olive (Lenkei *et al.*, 1997; Cosardereliogl*u et al.*, 2020). Histologically, AT2Rs are found in neurons and other glia cells (Cosardereliogl*u et al.*, 2020). In most tissue, expression of AT2Rs is reduced after birth but pathological conditions can increase the expression (Dasgupta & Zhang, 2011). One exception is expression in brainstem, which increases with age (Yu *et al.*, 2010).

Activation of AT2Rs on the vasculature leads to vasodilation via multiple mechanisms. AT2Rs can form heterodimers with AT1Rs, causing AT1Rs to lose their function (AbdAlla *et al.*, 2001). Moreover, binding of ligands to endothelial AT2Rs can stimulate bradykinin B2 receptors (B2Rs) by stimulates kininogenases to produce bradykinin (Dasgupta & Zhang, 2011) and by forming heterodimers with B2Rs (Abadir *et al.*, 2006). This process increases NO levels, leading to production of cGMP which promotes vasodilation (Abadir *et al.*, 2006; Dasgupta & Zhang, 2011). In microvascular vSMCs, AT2R activation opens BK channels, resulting in hyperpolarisation and vasodilation (Dimitropoulou *et al.*, 2001; Vincent *et al.*, 2005). Unlike AT1Rs, AT2Rs do not undergo endocytosis when stimulated (Hein *et al.*, 1997).

Mas receptors (MasRs) are also G protein-coupled receptors that are expressed in endothelial cells and vSMCs (Tallant & Clark, 2003; Santos *et al.*, 2018). Pericytes also possess MasRs according to transcriptomic data (Vanlandewijck *et al.*, 2018). Activation of MasRs by Ang(1-7) dilates various vascular beds including the mesenteric, cutaneous, renal and cerebral arteries (Schindler *et al.*, 2007; Santos *et al.*, 2018). The mechanisms underlying MasR-mediated vasodilation involve activation of eNOS and NO production via Akt signalling in endothelial cells (Sampaio *et al.*, 2007; Santos *et al.*, 2018). MasR activation in endothelial cells also decreases Ang II - induced NOX activities and induces release of prostaglandin and bradykinin that act

on vSMCs to decrease ERK 1/2 activity and smooth muscle cell contractility (Schindler *et al.*, 2007; Santos *et al.*, 2018).

Another receptor that might regulate CBF is AT4R (also known as insulin-regulated aminopeptidase (IRAP)), which binds Ang IV. Stimulation of AT4R causes vasodilation in most vascular beds (Chai *et al.*, 2004), for example, perfusing Ang IV in the presence of losartan (an AT1R blocker) and PD123177 (an AT2R blocker) results in a CBF increase, which is inhibited by AT4R blockers (Kramár, Harding & Wright, 1997). The dilatory effect of Ang IV on cerebral arterioles is mediated through endothelial production and release of NO (Kramár *et al.*, 1998).

1.8.4 Pathological conditions associated with the brain-RAS

Many pathologies inside and outside the brain can affect the cerebral RAS. One example is hypertension that causes increased expression of AT1Rs and decreased expression of AT2Rs in the brain, leading to a net vasoconstriction of cerebral circulation (Hirunpattarasilp, Attwell & Freitas, 2019). Another possible condition is COVID-19, in which the viral spike protein may reduce ACE2 expression, leading to an increased Ang II level and a decreased Ang(1-7) level with a likely result of cerebral vasoconstriction (Ni *et al.*, 2020).

1.9 Alzheimer's disease (AD)

1.9.1 Overview of AD

Alzheimer's disease was first described in 1906 by a German psychiatrist named Alois Alzheimer, for a patient with progressive memory disturbance and aggression, along with plaques and neurofibrillary tangles upon histological examination (Alzheimer, 1906). AD is the most common cause of dementia, being responsible for 60 – 80% of the total cases (Anon, 2021). The symptoms vary

according to phases in the development of AD, and include: (i) preclinical AD – a phase when individuals develop brain changes, detected by biomarkers such as abnormal levels of amyloid beta (Aβ) on positron emission tomography (PET) scans or in CSF analysis, without any cognitive symptoms; (ii) mild cognitive impairment (MCI) due to AD – the individuals exhibit biomarker changes with subtle changes in memory and thinking, which can be detected only by close relatives or friends and do not obstruct everyday activities; (iii) dementia due to AD – the last phase where noticeable aberrations in cognitive function causes disruption in daily life activities.

1.9.2 Impact of AD and dementia

Dementia is a very prevalent condition. In 2015, 47 million people with nearly 9.9 million new cases annually suffered from dementia globally, and this number is predicted to reach 75 million by 2030 and 132 million in 2050 (World Health Organization, 2017). In the UK alone, the number of cases was almost 885,000 individuals in 2019 with an estimation of 1.6 million by 2040 (Wittenberg *et al.*, 2019).

Moreover, dementia was the fifth leading cause of mortality with 2.4 million deaths, and caused a loss of 28.8 million disability-adjusted life years (DALYs) in 2016 worldwide (Nichols *et al.*, 2019). For the UK, dementia and AD were a major cause of death in 2019 with 66,424 deaths (Cornish & Owen-Williams, 2020). The mortality comes from complications of dementia, including immobility, swallowing problems and malnutrition, with a very high rate of bronchopneumonia (Brunnström & Englund, 2009; Anon, 2021).

In addition, dementia has a large impact on the economy. The total costs of dementia were £34.7 billion in 2019 and are predicted to reach £94.1 billion in 2040 at constant 2015 prices (Wittenberg *et al.*, 2019). The costs can be separated into social care (45%), unpaid care (40%) and healthcare (14%) (Wittenberg *et al.*, 2019).

1.9.3 Pathophysiology of AD

AD is the result of a complex interplay of various processes involving the proteins Aβ, tau, and ApoE, as well as immune cell activation, infection and sleep disturbance (Long & Holtzman, 2019). Of these, the amyloid cascade hypothesis, along with its new developments, has remained the most credible explanation for the pathogenesis of AD since it was first proposed in 1992 (Hardy & Higgins, 1992; Selkoe & Hardy, 2016; Long & Holtzman, 2019). However, cerebral hypoperfusion has also been suggested to participate in the pathogenesis of AD (de la Torre & Mussivan, 1993; de la Torre, 2018) (see Section 1.9.4) and increasing evidence has shown a close relationship between Aβ and reduced cerebral blood flow, but it is difficult to determine which comes first (see Section 1.9.5). In this thesis, I show that the reduction of cerebral blood flow in AD can be intimately linked to the generation of Aβ.

Aβ is a peptide that can aggregate into amyloid plaques, one of the pathological hallmarks of AD (Alzheimer, 1906; Braak & Braak, 1991). Aβ is produced from the β-amyloid precursor protein (APP), which is a transmembrane protein with an uncertain physiological function that may be related to modulation of cell growth and survival (O'Brien & Wong, 2011). APP, which is encoded by a gene on chromosome 21, is substantially generated in neurons (O'Brien & Wong, 2011). It can undergo nonamyloidogenic processing by the enzyme α-secretase at cell surface or undergo amyloidogenic processing by β-secretase, also known as β-site amyloid precursor protein cleaving enzyme 1 (BACE1), after the APP is internalised into endosomes to form C99 (O'Brien & Wong, 2011). C99 is then cleaved by a protein subunit of the γ-secretase called presenilin at multiple sites, creating Aβ molecules containing 37-43 amino acids, with the majority being $A\beta_{1-40}$ and $A\beta_{1-42}$ (Morishima-Kawashima, 2014;

Qiu *et al.*, 2015). This formation and the release of Aβ from endosomes to extraceullar space is modulated by neuronal activity (Kamenetz *et al.*, 2003).

Aβ monomers can spontaneously aggregate to form soluble oligomers, which can then further combine to form insoluble amyloid fibrils and amyloid plaques (Long & Holtzman, 2019). Of these three forms of "Aβ pool" (monomers, oligomers and amyloid fibrils), soluble Aβ oligomers are the most toxic form that can spread throughout the brain (Selkoe & Hardy, 2016; Chen *et al.*, 2017). They have been shown to initiate multiple pathological processes such as tau pathology, excitotoxicity, axonal transport impairment, oxidative stress and epigenetic changes (Benilova, Karran & De Strooper, 2012; Cline *et al.*, 2018) , leading to a decrease in synapse number, suppression of long-term potentiation and stimulation of long-term synaptic depression and eventually neurocognitive impairment (Selkoe & Hardy, 2016). Soluble oligomeric Aβ also activates microglia and astrocytes, leading to inflammation and oxidative injury to neurons (Selkoe & Hardy, 2016). Moreover, there is a strong correlation between the level of oligomeric Aβ (in CSF and plasma) and cognitive decline in AD patients (Santos *et al.*, 2012; Meng *et al.*, 2019).

Various sizes of Aβ oligomers have been found, ranging from 2-12 Aβ peptides. While some studies show that the low-molecular-weight oligomers, especially the dimers (Zott *et al.*, 2019), trimers and tetramers (Jana *et al.*, 2016; Nortley *et al.*, 2019; Ciudad *et al.*, 2020) are the toxic forms, others have found that high-molecular-weight oligomers (such as Aβ*56, the 56 kDa species) might be responsible for neurotoxicity (Sengupta, Nilson & Kayed, 2016; Cline *et al.*, 2018). These conflicting results are further complicated by differences between $A\beta_{1-40}$ and $A\beta_{1-42}$, which affect the aggregation mechanisms, stability and mechanisms of action (Chen & Glabe, 2006; Palmer & Love, 2011; Qiu *et al.*, 2015).

On the other hand, insoluble Aβ fibrils can deposit to form amyloid plaques. There is no association between the level of plaque deposition and synapse loss (Chen *et al.*, 2017) or cognitive decline in AD patients (Nelson *et al.*, 2012). Nonetheless, Aβ deposition is important in the progression of tau pathology (Long & Holtzman, 2019) and may serve as a reservoir for soluble Aβ oligomers, explaining the finding that more synapse loss occurs near amyloid plaques (Koffie *et al.*, 2009).

There are many pieces of evidence supporting the idea that the amyloid cascade hypothesis is the main pathogenic mechanism of AD, the most important of which are as follows. Aβ deposition is found in brain regions that are affected in all AD patients (Selkoe & Hardy, 2016). Genetic mutations or overexpression of genes related to Aβ are found to cause familial form of AD (Selkoe & Hardy, 2016). For example, mutations within or near the Aβ region of APP gene can result in an aggressive form of familial AD, and Down's syndrome patients (who have a triplication of the APP gene) show increased Aβ production and develop typical AD neuropathologies (Tcw & Goate, 2017). Mutations in presenilin 1 or 2 (De Strooper, 2007) are the main cause of familial AD. Apart from familial AD, sporadic AD can also be explained by the amyloid cascade hypothesis because it may result from failure of Aβ clearance processes (Selkoe & Hardy, 2016). The effects of Aβ oligomers on neurons and glia cells lead to tangle formation in neurons by inducing tau hyperphosphorylation (Long & Holtzman, 2019). Tau is a microtubule-associated protein which is mainly found in axons under normal conditions, but can relocate when hyperphosphorylated to the soma and dendrites, where it alters synaptic function and forms intracellular tangles.

Apart from changes in Aβ homeostasis and tau phosphorylation, AD is also related to vascular pathologies, resulting in the cerebral hypoperfusion commonly

seen in AD patients that may also contribute to the pathogenesis of AD (Zlokovic, 2011). However, the mechanism by which cerebral blood flow is reduced, and the contribution of pericyte dysfunction to this process are not completely understood. As this forms a major part of my thesis work, the following section reviews this aspect of AD pathology in depth.

1.9.4 Changes in the cerebral vasculature and CBF in AD

Anatomical changes of blood vessels and a CBF decrease are found in AD. The most prominent pathological change to the cerebral vasculature in AD is cerebral amyloid angiopathy (CAA) (Esiri & Wilcock, 1986), in which the walls of leptomeningeal arteries and cortical vessels become covered with Aβ (Carrano *et al.*, 2011). Other anatomical vascular changes found in AD include focal constrictions of capillaries and degeneration of vSMCs in irregularly-shaped arterioles (Hashimura, Kimura & Miyakawa, 1991; Kimura, Hashimura & Miyakawa, 1991). Moreover, reduced CBF and increased brain vascular resistance have been found in AD mice (Niwa *et al.*, 2002b; Wiesmann *et al.*, 2017) and in AD patients (Ruitenberg *et al.*, 2005; Yew & Nation, 2017), in which some brain regions show a more than 50% reduction of the CBF (Asllani *et al.*, 2008). The affected regions also exhibit decreased glucose metabolism, suggesting a hypometabolic state (Govindpani *et al.*, 2019).

Several lines of evidence suggest that these anatomical changes and CBF deficits are involved in the pathogenesis of AD rather than being a downstream effect of cerebral atrophy in AD (Pini *et al.*, 2016):

(i) Cardiovascular and cerebrovascular risk factors, including diabetes, hypertension, obesity, physical inactivity and smoking (Carnethon, 2009; Kaptoge *et al.*, 2019), increase the chance to develop AD (Barnes & Yaffe, 2011). Apolipoprotein (apo) E4, which controls lipoprotein metabolism and cholesterol balance, is also a shared risk

factor for AD and cardiovascular diseases (Mahley, 2016). These similarities of the risk factors for AD and for cardiovascular/cerebrovascular diseases suggest a link between impaired vascular function and the occurrence of AD (Kalaria, 2000).

(ii) Risk factors, clinical manifestations and cerebrovascular pathological lesions of AD are similar to those of vascular dementia (de la Torre, 2002), which is a decline of cognition caused by vascular factors (Iadecola *et al.*, 2019). Age, patient education, physical activity, obesity, hypertension, diabetes, inflammation, frailty, concomitant peripheral arterial disease and depression are some of the common risk factors between these two conditions (Iadecola *et al.*, 2019). According to the fifth edition of Diagnostic and Statistical Manual of Mental Disorders (DSM-5), vascular dementia and AD have the same clinical features but differ only in the relationship of the onset of cognitive impairment to the cerebrovascular event and in the clinical course (American Psychiatric Association, 2013). Neuropathological features presented in AD and vascular dementia are also comparable (Snowdon *et al.*, 1997). These similarities between AD and vascular dementia imply that vascular-related factors might cause AD (de la Torre, 2002).

(iii) Multifactorial data-driven analysis on healthy and AD subjects has shown that a CBF deficit is found early in the pathogenesis of AD, followed by changes in biomarkers of Aβ deposition, glucose metabolism and neuronal activities (Iturria-Medina *et al.*, 2016). Brain structural changes and memory decline occur later and eventually $A\beta_{1-42}$, tau and phosphorylated tau can be detected in the CSF (Iturria-Medina *et al.*, 2016). Other studies also found decreased CBF in preclinical AD (Johnson & Albert, 2000; Hays, Zlatar & Wierenga, 2016) and the CBF deficits are related to the progression of AD (Binnewijzend *et al.*, 2016). Interestingly, cerebral hypoperfusion can aggravate neuronal dysfunction, neuropathological changes and

memory impairment, in a manner similar to that found in AD (Zlokovic, 2011). This supports the idea that CBF defects precede the occurrence of AD and may contribute to the pathogenesis of the disease (de la Torre & Mussivan, 1993; de la Torre, 2002; Iturria-Medina *et al.*, 2016; Yew & Nation, 2017; Govindpani *et al.*, 2019).

1.9.5 Reduced CBF and Aβ homeostasis

Reduced CBF can increase the Aβ pool in the brain in several ways. Ischaemia and hypoxia act on caspase-3 (Korte, Nortley & Attwell, 2020) or hypoxia-inducible factor 1α (HIF1α) (Zhang *et al.*, 2007) to upregulate BACE1, which is a key enzyme in amyloidogenic processing of APP, resulting in more Aβ generation (Sun *et al.*, 2006; Zhiyou *et al.*, 2009) (see Section 1.9.3). Moreover, cerebral hypoxia reduces degradation of Aβ through down-regulation of neprilysin, an enzyme that breaks down Aβ (Wang *et al.*, 2011). Brain ischaemia also decreases the level of proteins that facilitate Aβ clearance, such as phosphatidylinositol-binding clathrin assembly protein (PICALM) expressed on endothelial cells (Rudinskiy *et al.*, 2009) and low density lipoprotein receptor-related protein 1 (LRP1) (Yamada *et al.*, 2019; Korte, Nortley & Attwell, 2020). Lastly, decreased CBF also allows re-entry into the brain parenchyma from the blood of Aβ, which is mediated through the receptor for advanced glycation end products (RAGE) to the brain parenchyma (Deane *et al.*, 2003).

Interestingly, Aβ affects cerebral blood vessels. Application of exogenous Aβ causes constriction of cerebral arterioles and arteries in rodent models (Niwa *et al.*, 2001) and of isolated human middle cerebral and basilar arteries (Paris *et al.*, 2003). In addition, cerebrovascular autoregulation and endothelial-dependent vasodilation are attenuated in transgenic mice with *App* mutations (Niwa *et al.*, 2002a). These Aβ-mediated effects on cerebral vessels are thought to be from soluble Aβ, rather than amyloid plaques, because these cerebrovascular effects develop in the absence of

amyloid plaques or cognitive impairment (Iadecola, 2004; Iturria-Medina *et al.*, 2016). Several mechanisms underlying Aβ-dependent vasoconstriction have been studied. These include ROS production, ET generation and direct effect on vascular smooth muscle cells of Aβ (Thomas *et al.*, 1996; Nicolakakis *et al.*, 2008; Palmer & Love, 2011).

1.10 Hyperoxia

Chapter 5 of my thesis is devoted to the effects of hyperoxia on pericytes. In this section I give the background information essential for understanding this work.

1.10.1 Overview of hyperoxia

Hyperoxia is defined as a state which tissue or organs are exposed to a supraphysiological level of oxygen (Mach *et al.*, 2011). The normal brain tissue oxygen tension ($PtiO_2$) is 20-35 mmHg in both humans and animals (Maas *et al.*, 1993; De Georgia, 2015; Ortiz-Prado *et al.*, 2019), or an oxygen concentration of 20-60 μM (Attwell *et al.*, 2010). However, the actual oxygen concentration for brain hyperoxia has not been clearly defined and is rarely studied. Oxygen tension in the blood is more extensively studied and the term hyperoxaemia is used to define a partial pressure of oxygen (PaO_2) of more than 100 mmHg in the blood (Pala Cifci *et al.*, 2020).

Hyperoxia is normally caused by exposure to a high-level of oxygen through human intervention in a normobaric or hyperbaric environment (Ciarlone *et al.*, 2019). Normobaric oxygen supplements are widely used in clinical settings to prevent patients from developing hypoxia and ischaemia (Chu *et al.*, 2018; Brugniaux *et al.*, 2018). On the other hand, hyperbaric oxygenation is not only used in treatments for certain conditions such as refractory wounds, carbon monoxide poisoning and late

radiation tissue injury, but also used in undersea activities for recreational and military operations (Brugniaux *et al.*, 2018; Ciarlone *et al.*, 2019).

1.10.2 Impact of hyperoxia

Hyperoxia can affect many organs including the lungs, the heart and the brain. Systemically, high oxygen exposure leads to increased ROS production and inflammation in animal models of sepsis (Rodríguez-González *et al.*, 2014). It also causes peripheral vasoconstriction, thereby increasing vascular resistance and limiting blood flow to organs (Brugniaux *et al.*, 2018).

In the lungs, excess oxygen administration leads to lung injury from oxidative stress and inflammation (Ciarlone *et al.*, 2019; Nakane, 2020). Oxygen can lead to cell death by altering expresison of genes related to cell death and activating caspases to cause cell apoptosis (Shimada *et al.*, 2016). Moreover, a high oxygen concentration decreases lung compliance through down regulation of surfactant-associated protein (Shimada *et al.*, 2016). Exposure to hyperoxia also impairs lung immunity (Baleeiro *et al.*, 2003) and increases mortality from pulmonary bacterial infections (Tateda *et al.*, 2003; Kikuchi *et al.*, 2009). All of these effects lead to a condition called hyperoxia-induced acute lung injury (HALI), in which inflammation, injury and death of lung alveolar epithelium and capillary endothelium occur (Ciarlone *et al.*, 2019; Nakane, 2020). This results in an impairment of gas exchange and respiratory gas failure (Ciarlone *et al.*, 2019; Nakane, 2020).

In the heart, hyperoxia causes vasoconstriction of the coronary arteries, resulting in decreased coronary blood flow (McNulty *et al.*, 2005). Although more oxygen is carried in the blood, the oxygen delivery to the heart is decreased because of the reduced blood flow under hyperoxic conditions (Brugniaux *et al.*, 2018), leading

to a paradoxical increase of myocardial ischaemia in patients suffering from heart attack who are given excess oxygen (Guensch *et al.*, 2015; Nakane, 2020).

There is no benefit in excess oxygenation in hypoxic brain conditions such as acute stroke (Ding *et al.*, 2018) and hyperoxia may even worsen the neurological outcomes in stroke, subarachnoid haemorrhage and post-cardiac arrest (Janz *et al.*, 2012; Li *et al.*, 2019; Fukuda *et al.*, 2019; López *et al.*, 2019). In preclinical studies, a high oxygen level is associated with worsened neurological outcomes (Pilcher *et al.*, 2012). People can also develop life-threatening CNS oxygen toxicity when exposed to a hyperbaric hyperoxic gas mixture (Ciarlone *et al.*, 2019). The clinical features include hypertension, alteration of heart rate (from bradycardia to tachycardia) and pulmonary abnormalities (paradoxical hyperventilation, dyspnea, coughing and diaphragm and upper airway spasm) before terminating in loss of consciousness and tonic-clonic seizures (Ciarlone *et al.*, 2019).

Importantly, hyperoxia is associated with increased mortality in acutely ill patients such as cardiac arrest, stroke and traumatic brain injury (Stolmeijer *et al.*, 2018; Ni *et al.*, 2019).

Although increased morbidity and mortality are associated with hyperoxia, excessive oxygen supplement is still commonly found in clinical practice and is left untreated (Pannu, 2016). In one study in subarachnoid haemorrhage patients, 90% of the patients had hyperoxia imposed (Yokoyama *et al.*, 2019). Another study in 51 critically ill patients found that mechanically ventilated patients were hyperoxic for more than 60% of their time (Suzuki *et al.*, 2013).

1.10.3 Oxygen and the brain

1.10.3.1 Oxygen supply to the brain

Because cerebral metabolism of glucose and oxygen is very high and the brain uses about one fifth of the total body oxygen consumption (Sokoloff, 1960; Rolfe & Brown, 1997) (see Section 1.2), oxygen delivery via the blood plays a key role in brain function. It can be calculated by multiplying the CBF by the arterio-venous difference in oxygen content (De Georgia, 2015).

CBF can be calculated using an analogy to Ohm's law, by dividing cerebral perfusion pressure (CPP), which is the driving force of the blood going to the brain, by the cerebral flow resistance (Secomb, 2016). CPP is defined as the difference of mean arterial pressure (MAP), which is the pressure that sends blood to all organs, and intracranial pressure (ICP), which is formed because the brain is enclosed in the skull, or central venous pressure (CVP) (whichever is higher) (Mount & Das, 2021).

Arterial oxygen content is the sum of the amount of oxygen dissolved in the plasma and the oxygen that binds to haemoglobin (De Georgia, 2015). Normally, there is 0.0031 ml of O_2 dissolved in 100 ml of plasma for each mmHg of PaO_2 and the maximum capacity of one gram of haemoglobin (Hb) for carrying oxygen is 1.34 ml of O_2 (De Georgia, 2015; Brugniaux *et al.*, 2018). Thus, arterial oxygen content can be calculated using the following equation:

$$Arterial\ oxygen\ content/100\ ml = (1.34 \times Hb \times Arterial\ oxygen\ saturation) + (0.0031 \times PaO_2)$$

where *Hb* is the number of grammes of haemoglobin/100ml of blood.

The balance between arterial oxygen delivery and brain oxygen consumption determines the brain tissue oxygen level, $PtiO_2$, for which a value below 10 – 15 mmHg

signifies brain ischaemia, but the threshold for brain hyperoxia has not yet been studied (De Georgia, 2015).

1.10.3.2 Pathophysiology of brain alterations in hyperoxia

As mentioned above in Section 1.10.2, hyperoxia can cause brain damage and worsen neurological outcomes in studies with animals and humans. The pathophysiology underlying those alterations includes generation of oxidative stress in the brain (Mattos *et al.*, 2019) and a decrease in CBF (Brugniaux *et al.*, 2018).

Oxygen is needed to produce ROS and hyperoxia can increase ROS generation (D'Agostino, Putnam & Dean, 2007; Ciarlone & Dean, 2016; Bin-Jaliah & Haffor, 2018). These ROS cause DNA, lipid and protein damage, and potentially cell death, as well as inducing an inflammatory response (Nakane, 2020).

After exposing patients to hyperoxic conditions, a decrease in CBF of around 10-30% has been detected using various techniques (Watson *et al.*, 2000; Brugniaux *et al.*, 2018; Mattos *et al.*, 2019). There are many mechanisms proposed for this reduction of CBF including ROS production (Zhilyaev *et al.*, 2003; Mattos *et al.*, 2019), increased ET generation (Higgins *et al.*, 1998; Winegrad *et al.*, 1999; Schaffranietz *et al.*, 2001; Kawanabe & Nauli, 2011) (see Section 1.6) and 20-hydroxyeicosatetraenoic acid (20-HETE) production (Zhu, Park & Gidday, 1998; Mishra, Hamid & Newman, 2011) (see Section 1.7.1). Most mechanisms are studied in vSMCs and there is no information on pericytes and their contributions to hyperoxia-induced CBF deficit. This is the subject of my work in Chapter 5 of this thesis.

1.11 Coronavirus disease 2019 (COVID-19)

1.11.1 Overview of COVID-19

Coronavirus disease 2019 (COVID-19) is an infectious disease caused by a novel virus called Severe Acute Respiratory Syndrome CoronaVirus 2 (SARS-CoV-2), which was first detected in Wuhan, China in December 2019 (Zhu *et al.*, 2020). COVID-19 has spread around the world and was declared to be a pandemic disease in March 2020 (Wu & McGoogan, 2020), causing over 3.8 million deaths worldwide, and infecting more than 170 million people (Dong, Du & Gardner, 2020) with its rapid transmission by airborne droplets (Hu *et al.*, 2021; Greenhalgh *et al.*, 2021). COVID-19 patients develop various symptoms, ranging from asymptomatic or mild symptoms to severe life-threatening symptoms (Esakandari *et al.*, 2020). The common symptoms are similar to those of other respiratory tract infection, including cough, shortness of breath and fever. Other symptoms are headache, sore throat, nausea, malaise, muscle pain, loss of smell and/or taste, and diarrhoea (Cascella *et al.*, 2020; Esakandari *et al.*, 2020). In more severe cases, marked respiratory distress, acute respiratory failure, septic shock and multiple organ failure may occur (Cascella *et al.*, 2020).

Neurological symptoms are common in COVID-19 (Helms *et al.*, 2020; Ellul *et al.*, 2020; Wildwing & Holt, 2021). A study of 58 COVID-19 patients hospitalised for acute respiratory distress syndrome (ARDS) showed that neurological symptoms were found in 14% of the patients at the time of admission, but found in 67% of the patients after sedation was withdrawn (Helms *et al.*, 2020). Symptoms included agitation, confusion, diffuse corticospinal tract signs (enhanced tendon reflexes, bilateral extensor plantar responses and ankle clonus) and dysexecutive syndrome (inattention, disorientation or not following commands) (Helms *et al.*, 2020). Other

reported neurological conditions associated with SARS-CoV-2 infection are encephalitis, myelitis, Guillain-Barre syndrome, taste and smell dysfunction, stroke, Parkinsonism and other mental disorders (Ellul *et al.*, 2020; Wildwing & Holt, 2021). These neurological findings can also be found after the patients recover from COVID-19: approximately 34% of COVID-19 patients have neurological or psychiatric manifestations, involving intracranial haemorrhage, ischaemic stroke, nerve disorders, encephalitis or psychotic disorders, in the 6 months following the COVID-19 diagnosis. (Taquet *et al.*, 2021). Moreover, some COVID-19 patients develop persistent brain fog, memory loss, irritability and fatigue ("long-COVID syndrome") after the acute SARS-CoV-2 infection subsided (Theoharides *et al.*, 2021).

1.11.2 Impact of COVID-19

Aside from a high mortality and morbidity rate in COVID-19, this disease has a great socio-economic impact (Nicola *et al.*, 2020; Evans, Lindauer & Farrell, 2020). Because SARS-CoV-2 is very easily transmitted, many countries have enforced social distancing, social isolation, travel restriction and quarantine to prevent further transmission of the disease (Kucharski *et al.*, 2020). This affects the economy at all levels, including the primary sectors which handle raw materials, secondary sectors which manufacture final products, and tertiary sectors which entail service provision (Nicola *et al.*, 2020). Perishable agricultural goods cannot be transported due to lack of staff and a closing down of markets in COVID-19 affected locations, and manufacturing industries face import problems and staff deficiencies (Nicola *et al.*, 2020). Educational institute closure, disruption in supply chains, decline in the stock markets, closure of hospitality venues and lack of tourism are a few examples of the effects of COVID-19 on the economy (Nicola *et al.*, 2020). The rise of domestic abuse is also related to the lockdown (Evans, Lindauer & Farrell, 2020). COVID-19 also put

people at risk of psychological distress, including anxiety, depression and anger, and may lead to rise in suicidal behaviour (Cao *et al.*, 2020; Sher, 2020; Xiong *et al.*, 2020). It also affects interpersonal relationships, leading to harmful processes such as hostility, withdrawal and loss of support (Pietromonaco & Overall, 2020).

1.11.3 Structure of SARS-CoV-2

SARS-CoV-2 is classified as being in the betacoronavirus genus, which is closely related to bat-derived severe acute respiratory syndrome (bat SARS-like coronavirus) and more distantly related to SARS-CoV (Severe Acute Respiratory Syndrome CoronaVirus) and MERS-CoV (Middle East Respiratory Syndome-related CoronaVirus) (Lu *et al.*, 2020). The positive single-stranded RNA genome of coronavirus is contained within a capsid formed by nucleocapsid protein (N) and further covered by an envelope containing envelope (E) protein, membrane (M) protein and spike (S) protein (Brian & Baric, 2005). S protein is important in mediating virus entry into host cells and can potentially be a target for antiviral drug treatments (Wang *et al.*, 2020). The spike proteins form homotrimers on the viral surface to perform their function (Wang *et al.*, 2020). The S protein is composed of 2 functional subunits, S1 and S2 subunits.

The S1 subunit contains a N-terminal domain and a receptor binding domain (RBD), which participates in binding of the virus to angiotensin converting enzyme 2 (ACE2) receptors on the host cell (Hoffmann *et al.*, 2020; Wang *et al.*, 2020). The coupling of ACE2 receptors to the RBD of SARS-CoV-2 is similar to that of the RBD from SARS-CoV but the affinity of the former is higher due to more interactions of amino acids from both sides (Lan *et al.*, 2020). For example, SARS-CoV-2 F486 engages with ACE2 Q24, L79, M82 and Y83 but the homologous SARS-CoV L472 only engages with ACE2 L79 and M82 (Lan *et al.*, 2020). Other important sites of the

RBD from SARS-CoV-2 include Y489 and Y495, in which mutations can greatly affect free energy changes of the binding and determine the infectivity of the virus (Chen *et al.*, 2020). Variations in the ACE2 region also determine the strength of RBD-ACE2 coupling and this is the reason for the differences in infectivity among different mammalian species (Conceicao *et al.*, 2020). The amino acid differences between hamsters and rats at the RBD-binding site of ACE2 receptors, such as Q24K, T27S, D30N, L79I, Y83F and especially K353H, make hamsters more susceptible to COVID-19 and better models for studying this infection (Conceicao *et al.*, 2020). The RBD has two states, a “lying-down” state which helps in immune evasion, and a “standing-up” state, which allows binding of the RBD to the ACE2 receptor (Shang *et al.*, 2020).

The S2 subunit participates in membrane fusion of the virus and the host cell (Hoffmann *et al.*, 2020; Murgolo *et al.*, 2021). Activation of spike protein for membrane fusion via irreversible conformational changes is achieved by cleavage of S2 protein at the so-called S2’ cleavage site by host proteases such as TMPRSS2 and other serine proteases (Yuki, Fujiogi & Koutsogiannaki, 2020; Murgolo *et al.*, 2021).

At the border between the S1 and S2 subunits, there is a cleavage site called the S1/S2 protease cleavage site that is a target for furin (a ubiquitous proprotein convertase) or other cellular protease such as TMPRSS2 (Murgolo *et al.*, 2021). The cleavage primes the virus entry by changing the state of RBD to standing-up to allow coupling of RBD and ACE2 receptor to occur (Shang *et al.*, 2020; Örd, Faustova & Loog, 2020) and facilitate cleavage of the S2’ site on S2 (Murgolo *et al.*, 2021). This cleavage site is not found in SARS-CoV, in which the RBDs are normally in the standing-up state (Shang *et al.*, 2020; Wang *et al.*, 2020).

1.11.4 Cell entry mechanisms of SARS-CoV-2

There are two pathways for the viral genome to enter host cells.

(i) The cell surface pathway: In this process, the viral RNA is delivered directly across the host plasma membrane without involvement of endocytosis (Murgolo *et al.*, 2021). It begins with the priming of the S protein by furin-mediated cleavage of the S1/S2 site, that allows binding of the RBD to ACE2 receptors on host cells (Shang *et al.*, 2020; Örd, Faustova & Loog, 2020). This coupling with the host cell receptors triggers activation of the S-protein via a second cleavage process at the S2' cleavage site by TMPRSS2 and leads to membrane fusion, followed by the entry of viral RNA into host cells (Shang *et al.*, 2020; Murgolo *et al.*, 2021).

(ii) The endocytic pathway: After S protein priming by cleavage of the S1/S2 site, the protein binds to its ACE2 receptor, leading to endocytosis of both the ACE2 receptor and the viral particle (Abassi *et al.*, 2020b; Murgolo *et al.*, 2021). The endosome is then fused with a lysosome and lysosomal cathepsin L (CTSL) cleaves the S protein at the CTSL cleavage site to allow membrane fusion between the viral capsid membrane and the lysosome membrane to occur (Murgolo *et al.*, 2021).

The main pathway that the virus uses depends greatly on the presence of surface serine proteases, especially TMPRSS2, on the host cell (Murgolo *et al.*, 2021). The cell surface pathway is favoured in cells that express TMPRSS2 such as the lung and intestinal epithelium, while the endocytic pathway is used when host cells do not possess the enzyme (Hoffmann *et al.*, 2020; Murgolo *et al.*, 2021). However the brain shows significantly lower expression of *Tmprss2* gene when compared to that in the lung tissue (Ma *et al.*, 2020) and transcriptomic data in mouse brain showed that brain endothelial cells, vSMCs and pericytes do not express *Tmprss2* gene (Zeisel *et al.*, 2018). Hence, it may be assumed that brain vasculature cells prefer the endocytic

pathway but there is no study addressing this hypothesis yet. Nevertheless, brain pericytes do get infected (Bocci *et al.*, 2021) and in mouse brain the SARS-CoV-2 receptor ACE2 is mainly expressed on pericytes with a lesser amount on endothelial cells (He *et al.*, 2020).

Regardless of the internalisation pathway employed, the ACE2 activity of the host cell may be decreased either through internalisation of ACE2 with the virus (Rothlin *et al.*, 2021) or through obstruction of the catalytic site (Castiglione *et al.*, 2021)

1.11.5 Access of SARS-CoV-2 to the brain

SARS-CoV-2 RNA or proteins could be detected in the brain of 21 out of 40 investigated patients who died from COVID-19, regardless of the presence of neurological symptoms (Matschke *et al.*, 2020), meaning that SARS-CoV-2 can access the brain.

After primary infection in the respiratory tract or the gastrointestinal (GI) tract, SARS-CoV-2 may invade the blood stream through the infection of type II alveolar epithelial cells in the lung, or of epithelial cells of the GI tract, both of which highly express ACE2 receptors and have been shown to be affected in COVID-19 (Lima *et al.*, 2020). After the virus enters the blood stream (viremia), it can pass through the BBB either directly by transcytosis or indirectly via peripheral immune cell transmigration (Lima *et al.*, 2020; Zhang *et al.*, 2021). SARS-CoV-2 can bind to ACE2 receptors on the endothelium at the BBB and disrupt the barrier (Baig *et al.*, 2020). Release of inflammatory mediators from the infection at other sites can also disrupt the BBB especially at its tight junctions, thereby allowing virus invasion of the CNS to occur more easily (Kumar *et al.*, 2020). Moreover, the virus may access the brain

parenchyma through the choroid plexus and the circumventricular cerebral organs, which are not covered by the BBB (Lima *et al.*, 2020).

Another pathway that SARS-CoV-2 may use to invade the CNS is through neuronal connections (Lima *et al.*, 2020). This hypothesis is based on the fact that SARS-CoV can invade the brain through the olfactory epithelium (Netland *et al.*, 2008). SARS-CoV-2 has been shown to cause anosmia and infect olfactory epithelial sustentacular cells and olfactory bulb pericytes in mice, so the olfactory epithelium may analogously provide an invasion route to the olfactory bulb and the brain for SARS-CoV-2 (Brann *et al.*, 2020; Meinhardt *et al.*, 2021). Accessing the CNS through the trigeminal nerve from the conjunctiva and the vagus nerve from the GI tract have also been hypothesised (Lamers *et al.*, 2020; Lima *et al.*, 2020).

In addition to the virus particles travelling into the brain, the S1 portion of the spike protein, which contains RBD, can move by transcytosis across the BBB to reach the brain (Rhea *et al.*, 2021).

1.11.6 Reduced CBF in COVID-19

CBF deficits have been noted in COVID-19 patients (Helms *et al.*, 2020). Bilateral frontotemporal hypoperfusion was found in all 11 patients admitted because of ARDS from COVID-19 who underwent MRI perfusion imaging (Helms *et al.*, 2020). Another case report showed a marked decrease in CBF in bilateral fronto-parietal regions from arterial spin labelling (ASL) in a patient with ARDS from COVID-19 (Soldatelli *et al.*, 2020). Moreover, following up 51 COVID-19 patients, who did not develop any neurological symptoms at 3 months after discharge, revealed that there was a significant reduction of CBF in MRI scans of 32 patients with severe symptoms when compared to 19 patients with mild symptoms or 31 healthy controls (Qin *et al.*, 2021).

One proposed mechanism that may underlie the CBF deficits in COVID-19 patients is a reduction of ACE2 activity either through endocytosis or obstruction of its catalytic site by the virus (Abassi *et al.*, 2020a; Castiglione *et al.*, 2021; Rothlin *et al.*, 2021). This will decrease the level of Ang(1-7) (see section 1.8.3) which acts on MasRs to cause vasodilation, and will increase the level of Ang II which causes vasoconstriction via activation of AT1R (Abassi *et al.*, 2020a) (see Section 1.8.3). The role of pericytes in mediating reduction of CBF in SARS-CoV-2 infection has not been studied even though pericytes are the cells that express the majority of ACE2 in the brain (Bocci *et al.*, 2021). In Chapter 6 of this thesis I investigate how SARS-CoV-2 may reduce brain blood flow by binding to pericytes.

1.12 Aim of the thesis

The main aim of this thesis is to provide more understanding of pericyte contractility and its role in CBF regulation in both physiological and pathological conditions.

In Chapter 3, I studied the general properties of pericytes, by focusing on:

(i) pericyte identification methods - I investigated the accuracy of pericyte detection under live bright-field imaging, which is one of the main techniques employed in this thesis, and studied the properties of Neurotrace 500/525, a novel putative pericyte-specific dye (Damisah *et al.*, 2017) for labelling pericytes;

(ii) pericyte contractility - I studied the site of capillary constriction in relation to pericyte somata, investigated contractility of proximal pericytes in the presence of commonly used vasoactive agents such as noradrenaline and adenosine, and provided a model for future investigations of the contractility of mid-capillary pericytes.

In Chapter 4, I studied the role of pericyte contractility in the pathogenesis of Alzheimer's disease with my colleagues Dr. Ross Nortley and Dr. Nils Korte. The emphasis was on:

(i) the effect of Aβ on capillary diameter - I investigated the effects of Aβ on pericyte contractility *in vitro* by applying exogenous Aβ onto rat brain slices, and *in vivo* by measuring capillary diameters in AD mice in the cerebral cortex with endogenous Aβ plaque deposition compared to those in the plaque-sparing cerebellum;

(ii) the mechanisms underlying Aβ-induced pericyte contraction - I examined the involvement of ROS and ET in the pathogenesis of Aβ-evoked capillary constriction;

(iii) reversal of Aβ-evoked pericyte contraction - I studied the possibility of using blockers of ROS and ET, and a vasodilator (C type natriuretic peptide, or CNP) as therapeutic approaches to reducing Aβ-induced vasoconstriction.

In Chapter 5, I investigated the role of pericytes in mediating hyperoxia-induced CBF deficits, with a focus on:

(i) the effect of a high concentration of oxygen on pericytes - I studied capillary diameters in brain slices from adult rats and human in the presence of hyperoxia and also studied calcium signalling in pericytes in mouse brain slices when exposed to a high oxygen level;

(ii) the mechanisms underlying hyperoxic capillary constriction - I investigated the role of ROS, ET and 20-HETE in this process.

In Chapter 6, I investigated the contribution of pericyte contractility to CBF deficits found in COVID-19 patients with my colleagues, Dr. Greg James and Dr. Felipe Freitas, with a particular interest in:

(i) the expression of ACE2 receptors on pericytes - I used immunohistochemistry to detect and quantify ACE2 receptor expression on cerebral pericytes from hamster brain slices;

(ii) the effect of the RBD of SARS-CoV-2 on the RAS system and on pericyte contractility and death - I first investigated the effect of components in the RAS on cerebral capillaries and studied how the RBD modulates this process in brain slices from hamsters and human, and I also explored the effect of the RAS and the RBD on pericyte death using propidium iodide staining.

Together these studies have led to significant advances in our understanding of the role of capillary pericytes in controling cerebral blood flow in health and disease.

Chapter 2: Methods

In this chapter, I will outline the principle methodology of the experiments performed for this thesis. Detailed techniques specific to certain experiments can be found in the Methods section of the relevant chapter.

2.1 Solutions and drugs

All solutions were prepared using double reverse-osmosis purified water (Millipore Corporation, Milli-Q). Drugs and dyes listed in Table 2.1 were dissolved in either water or dimethyl sulfoxide (DMSO) if needed, before being diluted to the final concentration in bicarbonate-buffered artificial cerebrospinal fluid (aCSF) unless specified otherwise.

2.1.1 Bicarbonate-buffered aCSF

Bicarbonate-buffered aCSF was used in experiments with live brain slices from both rodents and humans. This solution contained (in mM) 124 NaCl, 2.5 KCl, 1 $MgCl_2$, 2 $CaCl_2$, 1 NaH_2PO_4, 26 $NaHCO_3$, 10 D-glucose, and 0.1 Na-ascorbate. It was heated to 33-36^oC and oxygenated with 20% O_2, 5% CO_2 and 75% N_2 for most experiments since 20% O_2 has been shown to produce an approximately physiological [O_2] in the slice (10-40 µM or 1-4%) at the depths where I normally image (Hall & Attwell, 2008), or with 95% O_2, and 5% CO_2 for hyperoxia experiments in Chapter 5 since this produces an unphysiologically high [O_2] in the slice of 150-400 µM or ~15-40% (Hall *et al.*, 2012). The solution was normally made up fresh before experiments, but could be kept for up to 2 days at 4^oC. This solution was chosen as the main extracellular solution because bicarbonate is the main buffer in both cerebrospinal and intracellular fluids (Jones, Faas & Mody, 2014).

Table 2.1: Sources, catalogue number and concentration of drugs and dyes used in this thesis.

Drug	Supplier	Catalog No.	Concentration used
(-)-Noradrenaline (NA)	Sigma-Aldrich	A7257	2 μM
A-779	Sigma-Aldrich	SML1370	10 μM
Adenosine (Ado)	Sigma-Aldrich	PHR1138	100 μM
Amyloid β-Protein (1-40) (HFIP-treated)	Bachem	4090147	72 nM
Amyloid β-Protein (1-42) (HFIP-treated)	Bachem	4090148	72 nM
Angiotensin II	Cayman Chemical	17150	50 nM, 150 nM, 2 μM
BQ-123	Alfa Aesar	J66169	1 μM
C-type natriuretic peptide (CNP)	Generon	350143	100 nM
Deferoxamine (DFO)	Sigma-Aldrich	D9533	100 μM
Diphenyleneiodonium (DPI)	Sigma-Aldrich	D2926	10 μM
Ebselen	Cayman Chemical	70530	2 μM
GKT135831	Cayman Chemical	17764	450 nM
HET0016	Cayman Chemical	75780	100 nM
Hydrogen peroxide	Sigma-Aldrich	386790	1 mM

Hydrozyfasudil hydrochloride	Santa Cruz	sc-202176	10 µM
Jasplakinolide	Santa Cruz	sc-202191	5 µM
L-glutamic acid monosodium salt (glutamate)	Sigma-Aldrich	G1626	500 µM
L-NNA	Cayman Chemical	80220	100 µM
Losartan potassium (Losartan)	Sigma-Aldrich	PHR1602	20 µM
Mitoquinone (MitoQ)	MedChem Express	HY-100116A	500 nM
PD123319	abcam	ab144564	5 µM
U-46619	Cayman Chemical	16450	200 nM
Dye	Supplier	Catalog No.	Concentration used
DAPI	-	-	100 ng/ml
Dihydroethidium (DHE)	Cayman Chemical	12013	8 µM
Isolectin B4, Alexa Fluor 568	Invitrogen	I21412	5 µg/ml
Isolectin B4, Alexa Fluor 647	Invitrogen	I32450	2.5 - 3.3 µg/ml
MitoSOX	Invitrogen	M36008	5 µM
Neurotrace 500/525	Invitrogen	N21480	1:100 - 1:1000
Propidium iodide (PI)	Sigma-Aldrich	81845	7.5 µM
Texus Red dextran	Invitrogen	D1864	12.5 mg/ml

2.1.2 HEPES-buffered aCSF

Unlike bicarbonate-buffered aCSF, which requires CO_2 to adjust the pH to its physiological value (Shipman, 1969), HEPES-buffered aCSF does not need a continuous supply of CO_2. For this reason, it was used in *in vivo* surgery, where continuous CO_2 bubbling could be challenging. The solution consisted of (in mM) 140 NaCl, 2.5 KCl, 1 $MgCl_2$, 2 $CaCl_2$, 1 NaH_2PO_4, 10 HEPES, 10 D-glucose, and NaOH to adjust the pH to 7.4, bubbled with 100% O_2 before use.

2.1.3 Amyloid beta (Aβ) preparation

Aβ was applied to investigate how it affected capillary diameter (Chapter 4). The method used to prepare Aβ was adapted from that described by Nortley et al. (2019). Synthetic HFIP-treated $Aβ_{1-42}$ (Bachem, 4090148) and $Aβ_{1-40}$ (Bachem, 4090147) were dissolved in DMSO at 5 mM, bath-sonicated for 10 min and vortexed for 30 sec. To oligomerise the protein, the solution was diluted in ice cold phosphate-buffered saline (PBS) to a final concentration of 100 μM, vortexed for 15 – 30 sec and then incubated for 24 h at 4°C. The solution was then centrifuged at 14,000 g at 4°C for 10 min to remove any Aβ fibrils presented. Monomeric and oligomeric Aβ in the supernatant were quantified using a Pierce BCA protein assay kit (Thermo Scientific, 23227) by calibrating against known concentrations of bovine serum albumin. The purplish reaction products from BCA protein assay were quantified using a spectrophotometer and the results were multiplied by a factor of 1.51 to correct for the different chromophoric development of albumin and Aβ (Jan, Hartley & Lashuel, 2010). Finally, the supernatant was then diluted with bicarbonate-buffered aCSF to the final concentration.

Confirmation of Aβ oligomeric preparation was performed in collaboration with my colleague, Dr. Pablo Izquierdo (UCL, NPP), via SDS-PAGE using an XCell

SureLock Mini-Call Electrophoresis System (Invitrogen, EI0001) with self-made 12% tris-glycine resolving gels and 5% tris-glycine stacking gels. Samples containing 3.74 μg of dissolved Aβ were loaded onto gels along with Novex sharp pre-stained protein standard (Invitrogen, LC5800) and separated electrophoretically at 150 V. SilverXpress Silver Staining kit (Invitrogen, LC6100) was used according to the manufacturer's protocol to visualise the protein.

2.2 Transgenic mice expressing fluorescent constructs

Transgenic mice were employed to visualise pericytes and endothelial cells, and to sense their intracellular calcium concentration.

2.2.1 NG2-DsRedBAC transgenic mice

NG2-DsRedBAC transgenic mice (JAX stock # 008241) express the genetically encoded red fluorescent protein, DsRed, under the NG2 promoter, enabling the identification of NG2-expressing cells including pericytes and oligodendrocyte progenitor cells (OPCs). The bacterial artificial chromosome (BAC) modification technique was used to generate this mouse line (Fig. 2.1 illustrates the generation of the transgene (Zhu, Bergles & Nishiyama, 2008)). Both homozygous and heterozygous transgenic mice were used for experiments in Chapter 3, since both express DsRed in the cells. Pericytes and OPCs can be distinguished from the position of the pericytes on blood vessels, and also by their morphology.

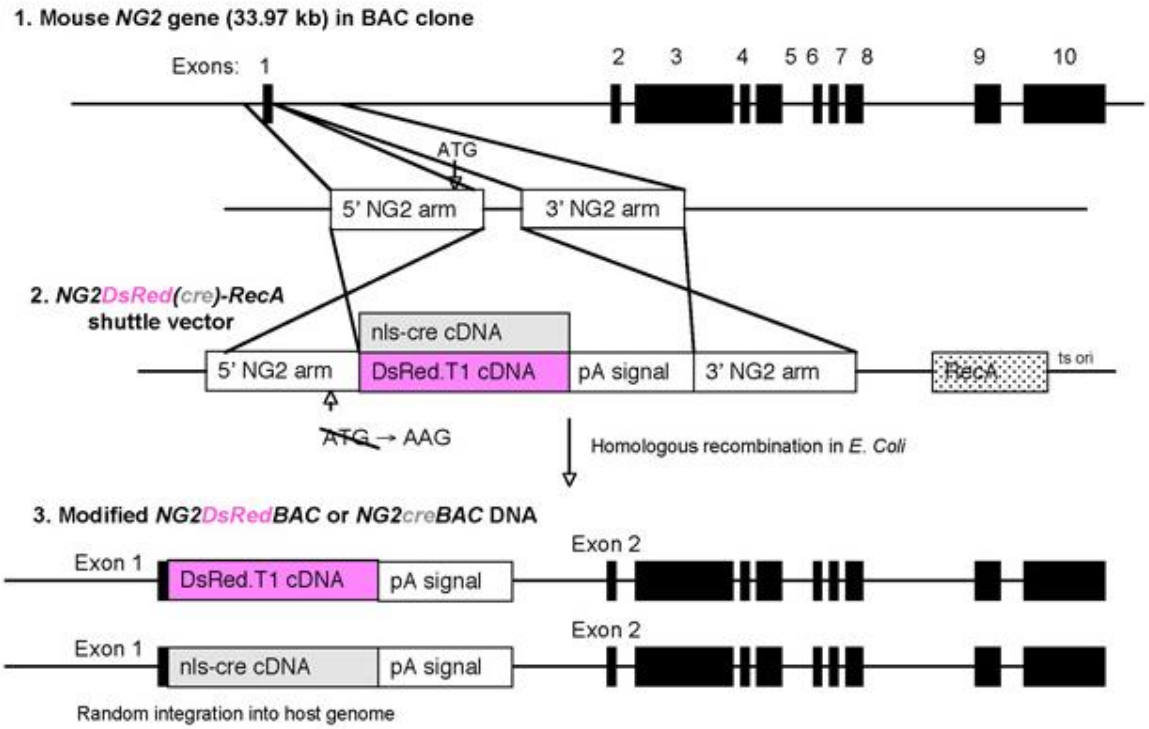

Figure 2.1: Generation of NG2-DsRed BAC transgenes.

The figure and legend are from Zhu *et al.* (2008). Diagram 1 shows the structure of the mouse NG2 gene (not to scale). Exons are indicated as black blocks. The regions used for 5' and 3' homology arms are indicated (the 5' and 3' homology arms are parts of the target genome sequence that have identical genome sequences to the homology arms used in the construct of shuttle vectors, allowing homologous recombination-mediated targeted integration of the vectors into the target genome : Ishii *et al.*, 2014). Diagram 2 shows the structure of the NG2-DsRedBAC-RecA shuttle vector that was used to modify the BAC DNA in order to insert the DsRed cDNA and polyadenylation sequence into the BAC clone that contained the NG2 gene in the center. Diagram 3 shows the structure of the modified BAC DNA that was used for microinjection into fertilized oocytes. pA signal, polyadenylation signal; ATG, translation initiation codon of the NG2 gene; ts ori, temperature-sensitive origin of replication.

2.2.2 Pdgfb-iCreER x PC::G5-tdT mice

Pdgfb-iCreER x PC::G5-tdT mice (i.e. a Cre-dependent GCaMP5G line, where PC stands for “Polr2a, CAG, GCaMP5G, tdTomato”) were kindly provided by my lab colleague Dr. Lila Khennouf. These transgenic mice innately express a green fluorescent protein, eGFP, in endothelial cells under the *Pdgfb* promoter. When the mice are injected with tamoxifen, they express the red dye tdTomato and a calcium indicator, GCaMP5G in PDGFB expressing cells. This provides a means to label endothelial cells with eGFP or tdTomato and to measure calcium concentration in these cells.

These mice were based on an in-house cross of Pdgfb-iCreER mice and PC::G5-tdT mice (JAX stock # 024477). Pdgfb-iCreER mice were generated using the phage artificial chromosome (PAC) technique to insert the coding sequence of eGFP and a tamoxifen-inducible Cre recombinase (iCreERT2) into the *Pdgfrb* gene locus (Fig. 2.2 shows the design of the transgene (Claxton *et al.*, 2008)), which is widely expressed in vascular endothelial cells. PC::G5-tdT mice were created to have a GCaMP5G-IRES-tdTomato knock-in in the *Polr2a* locus (Fig. 2.3 shows the construct of the allele (Gee *et al.*, 2014)) to encode a Cre-dependent GCaMP5G. Mice that were heterozygous or homozygous for Pdgfb-iCreER as well as homozygous for PC::G5-tdT were used to label endothelial cells in *in vivo* experiments in Chapter 3 without tamoxifen induction.

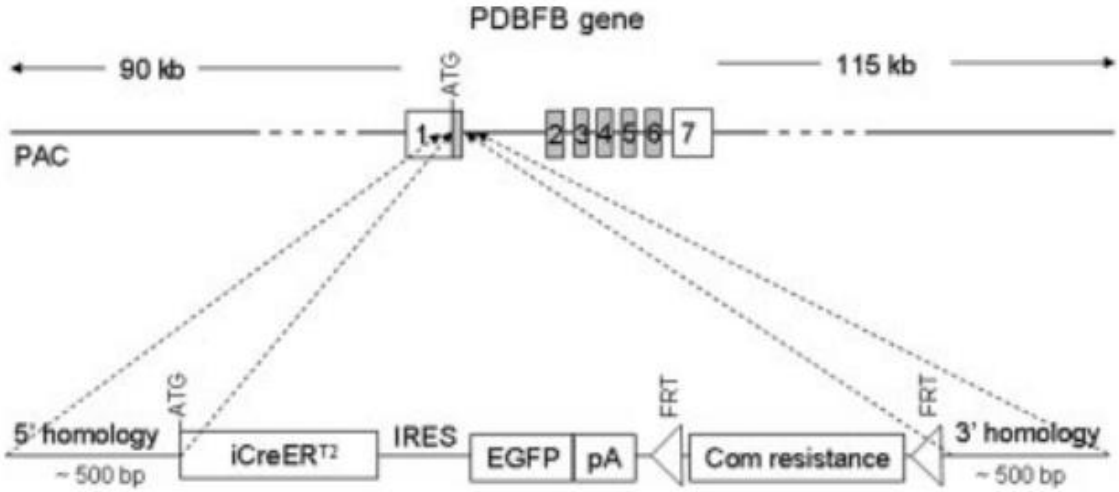

Figure 2.2: Schematic diagram of Pdgfb-iCreER transgene.

The figure and legend are from Claxton *et al.* (2008). A sequence-containing iCreER^{T2}, an IRES element, eGFP, and an FRT-flanked chloramphenicol resistance cassette was recombined into the open reading frame of the *Pdgfb* gene in a PAC. After subsequent removal of the chloramphenicol selection cassette, the PAC was then used for transgenesis by pronuclear injection.

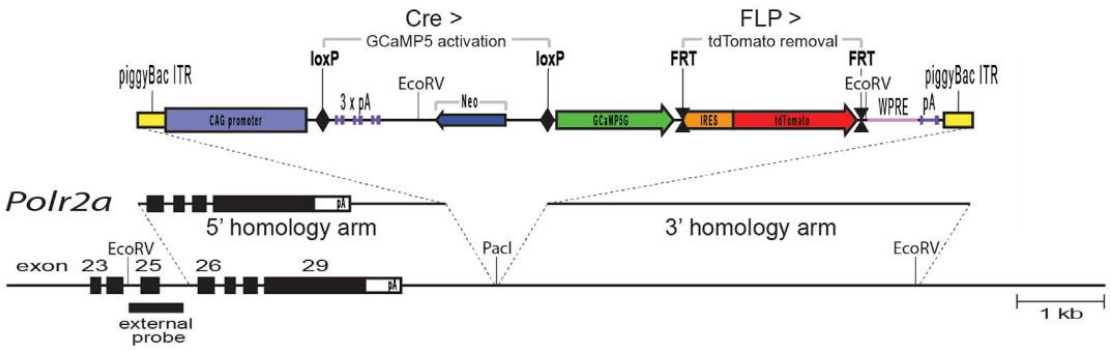

Figure 2.3: Schematic diagram of the PC::G5-tdT allele.

The figure and legend are from Gee *et al.* (2014). Both 5' and 3' homologies of the targeting vector are shown in relation to the endogenous *Polr2a* gene encoding the largest subunit of RNA polymerase II (the 5' and 3' homology arms of vectors, which have the same genomic sequence as the 5' and 3' homology arms of the target sequence, facilitate homologous recombination-mediated targeted integration of the vector into the target genome: Ishii *et al.*, 2014) The reporter component of the targeting vector is shown on top. The CAG promoter drives GCaMP5G and IRES-tdTomato expression following Cre-mediated excision of the STOP (3 x pA) cassette. The IRES-tdTomato reporter can be independently removed with recombinase. ITR, inverted terminal repeats; pA, polyadenylation signal; WPRE, woodchuck hepatitis posttranscriptional regulatory element.

2.2.3 NG2-DsRedBAC x APP$^{NL\text{-}G\text{-}F/NL\text{-}G\text{-}F}$ mice

NG2-DsRedBAC x APP$^{NL\text{-}G\text{-}F/NL\text{-}G\text{-}F}$ mice were kindly provided by my lab colleague, Dr. Nils Korte (UCL, NPP). These mice produce a genetically encoded red fluorescent protein, DsRed, in NG2-expressing cells such as pericytes and OPCs and develop amyloid beta (Aβ) amyloidosis with humanised Aβ to imitate Alzheimer's disease (AD) pathology.

The mice were based on an in-house cross of NG2-DsRedBAC mice (see Section 2.2.1) and APP$^{NL\text{-}G\text{-}F/NL\text{-}G\text{-}F}$ mice. APP$^{NL\text{-}G\text{-}F/NL\text{-}G\text{-}F}$ mice were generated by humanising the mouse Aβ sequence and knocking-in 3 AD-related mutations of the *APP* gene, including the Swedish mutation, the Beyreuther/Iberian mutation and the Arctic mutation (Fig. 2.4) (Saito *et al.*, 2014). These mice generate a normal amount of amyloid precursor protein (APP) but the animals show increased total amounts of $A\beta_{40}$ and $A\beta_{42}$, an increased ratio of $A\beta_{42}$ to $A\beta_{40}$ and aggressive Aβ amyloidosis, which begins at 2 months of age in homozygous animals (Saito *et al.*, 2014). Because the mutant APP in knocked in, this should avoid artefacts caused by overexpression of APP.

Homozygous or heterozygous NG2-DsRedBAC and homozygous APP$^{NL\text{-}G\text{-}F/NL\text{-}G\text{-}F}$ mice were used for *in vivo* experiments in Chapter 4, which were performed by Dr. Nils Korte, to study the role of pericytes in AD.

2.2.4 NG2-CreERT2 x PC::G5-tdT mice

NG2-CreERT2 x PC::G5-tdT mice were kindly supplied by my lab colleague Dr. Thomas Pfeiffer. These mice express a red fluorescent protein, tdTomato, and when induced with tamoxifen, produce the genetically encoded calcium indicator GCaMP5G in pericytes, smooth muscle cells and OPCs. The mice were obtained by crossing NG2-CreERT2 mice, which have CreERT2 knocked-in at the NG2 locus (Fig 2.5

shows the schematic gene construct (Huang *et al.*, 2014)), with PC::G5-tdT mice (as described in Section 2.2.2).

NG2-CreERT2 x PC::G5-tdT mice were induced by oral gavage of tamoxifen (1 mg per 10 g body weight) for four consecutive days (starting from post-natal day 21 (P21)) to monitor calcium concentration changes in pericytes in *in vitro* experiments in Chapter 5. The mice used for experiments were heterozygous NG2-creERT2 and heterozygous or homozygous PC::G5-tdT.

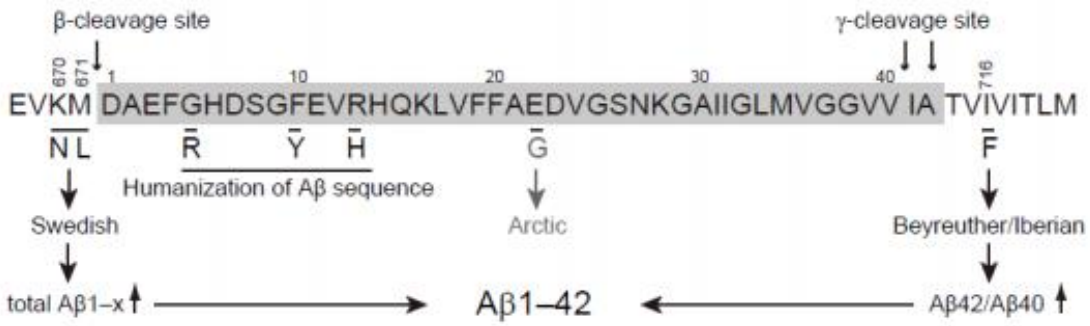

Figure 2.4: Design of the APP$^{NL\text{-}G\text{-}F/NL\text{-}G\text{-}F}$ mouse model.

The figure and the legend are from Saito *et al.* (2014). They humanized the mouse Aβ sequence and introduced Swedish and Beyreuther/Iberian mutations by knockin technology. They also generated mutant mice that in addition carried the Arctic mutation.

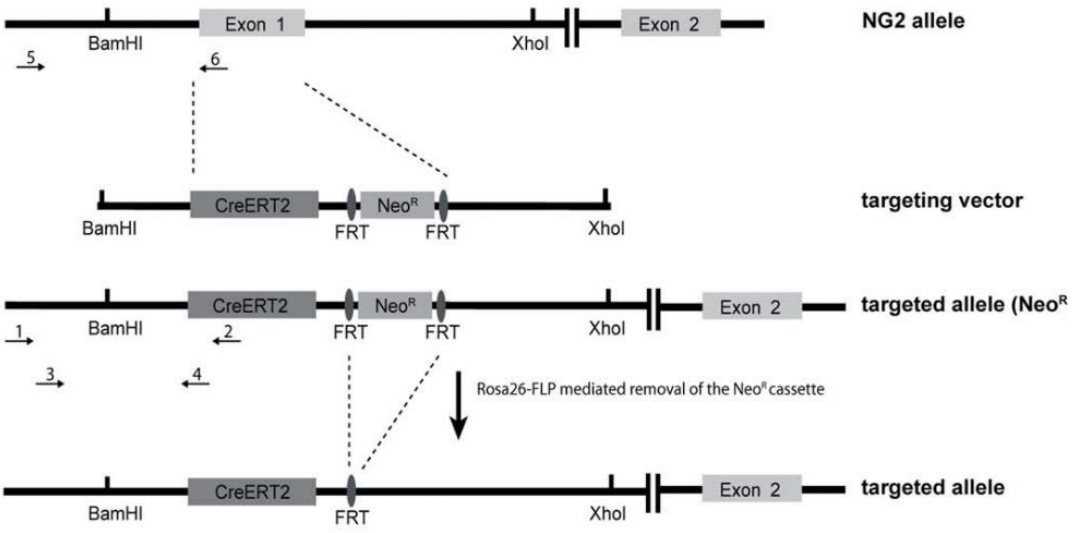

Figure 2.5: Scheme of gene targeting strategy for NG2-CreERT2 mouse.

The figure and legend are from Huang *et al.* (2014). Exon 1 of the NG2 locus was replaced by the open reading frame of CreERT2 followed by a FRT flanked Neo resistance cassette (Neo^R). Primers 1-4 were used for nested PCR to identify the homologous recombined ES cell clones. Neo^R was removed in vivo by crossbreeding NG2-CreERT2-NeoR mice to Rosa26-FLP mice. Then the NG2-CreERT2 knock-in mice were finally generated.

2.3 Bright-field imaging

Bright-field imaging of brain slices was employed for many of the experiments in this thesis, as follows.

2.3.1 Brain slice preparation

2.3.1.1 Live rodent brain slices

All animal procedures were performed in accordance with EU and UK regulations (the UK Animals (Scientific Procedures) Act 1986). The experiments used P19 – P22 Sprague-Dawley rats, adult transgenic mice and adult Syrian golden hamsters. Animals were sacrificed humanely by cervical dislocation followed by decapitation. For hamsters, the animals were anesthetized with isoflurane (Zoetis, IsoFlo^{R}) before schedule 1 killing was performed.

The process for brain extraction and slicing was slightly modified from that previously described (Mishra *et al.*, 2014). After decapitation, the animal's head was immediately immersed in ice-cold recovery solution containing (in mM) 92 NaCl, 2.5 KCl, 1 $MgCl_2$, 2 $CaCl_2$, 1.2 NaH_2PO_4, 30 $NaHCO_3$, 20 HEPES, 25 D-glucose, 5 Na-ascorbate, 3 Na-pyruvate, 1 kynurenic acid, and NaOH to bring the pH to 7.35, oxygenated with 95% O_2 / 5% CO_2. The head was immersed in this solution every 5-10 s to cool it down during the brain extraction. A midline incision on the scalp from the base of the neck to the nose was made using scissors. Skin flaps were retracted laterally to reveal the underlying skull. The skull was cut using fine scissors on the midline along the sagittal suture from posterior to anterior, and additional lateral incisions were made from the back of the neck anteriorly to both sides of the nose to create skull flaps. The skull flaps were deflected laterally using fine forceps to expose the brain. A small spatula was inserted on the lateral side of the brain to gently retract it away from the skull base and the brain was placed, ventral side facing up, on a

customised Petri dish lined with Sylgard (Dow Corning, cat no. 184) containing the recovery solution. The brain was cut coronally to remove the cerebellum and a part of the brain stem using a razor blade and the brain was then flipped over to rest on the cut surface. A second cut with a razor blade was performed to remove the ventral third of the brain. The specimen was mounted onto the slicing block of a Vibratome (Leica, VT 1200S) using cyanoacrylate glue, with the posterior part of the brain facing downwards and the ventral side supported by a cuboid block of 3-5% agarose. The tissue was placed in ice-cold slicing solution containing (in mM) 93 NMDG, 2.5 KCl, 10 $MgCl_2$, 0.5 $CaCl_2$, 1.2 NaH_2PO_4, 30 $NaHCO_3$, 20 HEPES, 25 D-glucose, 5 Na-ascorbate, 3 Na-pyruvate, 1 kynurenic acid, and HCl to bring the pH to 7.35, bubbled with 95% O_2 / 5%CO_2. The brain was sliced into 300 µm thick coronal sections, which were incubated in the same solution at 35^{o}C. After 20 minutes, the brain slices were transferred to the recovery solution at room temperature, for at least 10 minutes before usage.

2.3.1.2 Live human brain slices

Human brain slices were employed to extend to humans the most important results obtained from rodents. Ethical approval from the National Health Service (REC number 12/NW/0568) and informed consent from all patients were received for working with live human brain tissue obtained from neurosurgical operations. This part of the work was in collaboration with Miss Huma Sethi, a Consultant Neurosurgeon in the Division of Neurosurgery, in the National Hospital for Neurology and Neurosurgery at Queen Square. Only anonymised details of age, sex and surgical indication of the patients were passed on from the surgeon. All other patient data were kept confidential. All procedures involving human tissue were in accordance with the Human Tissue Act (2014).

Apparently normal cortical brain tissue, which is removed for access in neurosurgical operations for brain tumours, and which would otherwise be discarded, was placed in the ice-cold slicing solution pre-oxygenated with 95% O_2 / 5% CO_2. The tissue was transported to the laboratory in less than 15 min. A thin layer of cyanoacrylate glue was used to mount the tissue onto the slicing block supported by a cuboid block of 3-5% agarose. The tissue was placed in the ice-cold slicing solution and sliced with a Vibratome (Leica, VT 1000S) into 300 µm thick brain slices. The brain slices were incubated for 20 minutes in the same solution at 35^{o}C before being transferred to the recovery solution at room temperature for at least 10 minute before being used.

2.3.2 Imaging of capillaries and arterioles

In some experiments, brain slices were pre-incubated for at least 30 min to label capillaries or pericytes with dyes such as isolectin B4 conjugated to Alexa Fluor 568 (Invitrogen, I21412, 5 µg/ml) which labels the basement membrane around capillaries and pericytes, or Neurotrace 500/525 (Invitrogen, N21480,1:100 – 1:1,000 dilution, Chapter 3) which has been described to specifically label pericytes *in vivo* (Damisah *et al.*, 2017). Other experiments in Chapter 6 required brain slices to be incubated in bicarbonate-buffered aCSF with drugs prior to imaging. All incubations were done in customised 48-well or 12-well plates, which had oxygenating gas (20% O_2, 5% CO_2 and 75% N_2) blown over them, and were put in a water bath to keep the temperature at 35^{o}C.

Brain slices, with or without pre-incubation, were transferred to a bright-field microscope and perfused with bicarbonate-buffered aCSF while suitable vessels for experiments were identified (except for experiments in Chapter 6, in which the slices were perfused with aCSF with drugs because the slices were pre-incubated in aCSF

with drugs before the transfer), oxygenated with 20% O_2, 5% CO_2, and 75% N_2 at 33-36^oC with a flow rate of 2.5 – 4 ml/min. This low partial pressure of O_2 was selected so that the O_2 level in slices is similar to that occurring in vivo (Hall & Attwell, 2008; Hall *et al.*, 2014). Healthy capillaries (<10 μm diameter without rings of arteriolar smooth muscle around them) or healthy arterioles (≥10 μm diameter with visible rings of smooth muscle) were identified at 20 – 50 μm depths from the slice surface in the grey matter of the cortex under a 40x water immersion objective (Olympus, LUMPLFLN40XW). For capillaries, regions which had a candidate pericyte (identified by a bump-on-a-log morphology), and had at least 30 μm length along the vessels in focus, were chosen. Images were captured typically every 30 s except for experiments with angiotensin II (Ang II) in Chapter 6, in which the images were taken every 5 s because of a fast vascular response to Ang II. A Coolsnap HQ2 CCD camera and ImagePro Plus 7.0 acquisition software were used to take the images, with a pixel size of 200 nm.

2.3.3 Vessel diameter analysis

Images were aligned with the MultiStackReg plugin function of the ImageJ Fiji program and made into a time lapse video. The movie was opened in Metamorph software (Molecular Devices) to allow measurement of vessel internal diameters by manually placing a measurement line perpendicular to the vessel at the pericyte location. The ends of the line were placed at the locations with the largest intensity gradient across the vessel wall. Experiments with a shift in focus were discarded. Diameter measurements were logged into Microsoft Excel and five diameter measurements of each vessel at the time of interest, typically at the end of the experiment or at the peak of constriction, were averaged and used for statistical analysis.

2.3.4 Calculation of effect of vascular diameter changes on blood flow

This calculation is based on the method previously described (Nortley *et al.*, 2019). The resistance to flow (R) was calculated from Poiseuille's law (which assumes laminar flow of a pure liquid and thus ignores the presence of cells in the blood), in which

$$R = \frac{kL}{{r_1}^4}$$

where k is a constant, L is the length of the vessel from a pericyte soma to midway between two pericytes and r_1 is the vessel radius which is initially assumed to be the same everywhere. When pericytes constrict or dilate capillaries and the capillary radius decreases or increases from a value of r_1 at the midpoint between pericytes to a value of r_2 at the pericyte soma then, assuming that the radius changes linearly with the distance, the resistance can be calculated as (Nortley et al., 2019):

$$R = \frac{kL({r_1}^2 + r_1 r_2 + {r_2}^2)}{3{r_1}^3 {r_2}^3}$$

Relative to the resistance (R_1) for when the vessel radius is assumed to be constant at r_1, the factor by which the resistance is changed is

$$\frac{R}{R_1} = \frac{\left[1 + \frac{r_1}{r_2} + \left(\frac{r_1}{r_2}\right)^2\right] \times \frac{r_1}{r_2}}{3} \quad \text{…eqn. 1}$$

For example, normally, when a pericyte is relaxed, the capillary radius at the pericyte soma is ~1.1 times that between pericytes r_1 (both in brain slices, Fig. 3.7C, and *in vivo*, Fig. 4.2), for which eqn. (1) predicts that the resistance of the capillary segment will be $R_{relaxed}/R_1$ = 83% of the value it would have if the diameter were not 10% dilated at the soma. If a vasoconstrictor is applied which produces a constriction of X% at the pericyte soma, then the ratio of the new radius at the soma (r_2) to r_1 will be (eqn 2)

$$\frac{r_2}{r_1} = \left(\frac{100 - X}{100}\right) \times 1.1 \quad \text{…eqn. 2}$$

By inserting the result from eqn. 2 into eqn. 1, it is possible to calculate the factor by which the resistance is changed ($R_{contracted}/R_1$) relative to the whole capillary having diameter r_1. Then, by taking the ratio of this new constricted resistance to the value (relative to the whole capillary having diameter r_1) in the absence of the constrictor (0.83: see above), the effect of the constrictor on the resistance of the capillary segment can be calculated.

Because capillaries confer most resistance in the cortical blood supply, accounting for 57% of the total vascular resistance within the brain parenchyma (Gould *et al.*, 2017) and flow is inversely correlated with vascular resistance, the new flow will be changed by a factor of

$$\frac{New\ flow}{Original\ flow} = \frac{(43\% + 57\%)}{[43\% + (Rcontracted/Rrelaxed) \times 57\%]} \quad \text{…eqn. 3}$$

where we only take into account changes in the resistance of capillaries without any changes being assumed to occur in arterioles and venules.

2.4 Immunohistochemistry

Immunohistochemistry was employed for a range of experiments examining capillary properties.

2.4.1 Live rodent and human brain slice preparation

Rodent and human brain slices with a thickness of 200 – 300 μm (depending on the experiment) were prepared using the method described in Section 2.3.1.

2.4.2 Live labelling of vessels, ROS and death cells

For experiments in Chapter 3, brain slices were incubated for at least 30 min in 5 μg/ml isolectin B4 conjugated to Alexa Fluor 568 (Invitrogen, I21412), or neurotrace

500/525 at 1:100 dilution, to label blood vessels and pericytes at 35^{o}C and oxygenated with 20% O_2, 5% CO_2 and 75% N_2.

Experiments using dihydroethidium (DHE; Cayman Chemical, 12013) in Chapter 5 to measure superoxide, were performed by incubating slices with DHE 8 µM in bicarbonate-buffered aCSF at 35^{o}C bubbled with either 95% O_2 / 5% CO_2 (hyperoxic condition) or 20% O_2, 5% CO_2 and 75% N_2 (control) for 1 h.

Experiments with mitoSOX (Invitrogen, M36008) to label mitochondrial superoxide in Chapter 5 were done by placing brain slices in bicarbonate-buffered aCSF with or without hyperoxia for 1 h at 35^{o}C and then loading the slices with mitoSox 5 µM for 15 min.

For cell death analysis in Chapter 6, brain slices were put in extracellular solution containing 7.5 µM propidium iodide (PI; Sigma-Aldrich, 81845) and isolectin B4 conjugated to Alexa Fluor 647 (Invitrogen, I32450, 3.3 µg/ml) at 35^{o}C and bubbled with 20% O_2, 5% CO_2 and 75% N_2 for 3 h.

2.4.3 Antibody labelling

Rodent and human brain slices were fixed in 4% paraformaldehyde (PFA), shaking at room temperature, for 20 min – 1 h (depending on the experiment) and then washed three times in phosphate-buffered saline (PBS) for 10 min.

For some antibodies to work, antigen retrieval was performed to allow more binding of the antibody and antigen. Brain slices were incubated in 95-100^{o}C sodium citrate buffer, consisting of 10 mM sodium citrate, 0.05% Tween 20 and HCl to adjust the pH to 6.0, for 20 min. The slices were then removed from the water bath and placed at room temperature for 20 min in the same solution before being rinsed with PBS for 5 min 2 times.

Brain slices, with or without undergoing antigen retrieval, were incubated in blocking solution containing 10% horse serum, 0.3% Triton X-100 or 0.2% Saponin (Sigma-Aldrich, S7900) depending on the experiment, 200 mM glycine and 150 µM bovine serum albumin in PBS, at 4^{o}C shaking overnight. The slices were transferred to blocking solution with primary antibodies and incubated at 4^{o}C with agitation overnight or for three days for experiments with ACE2 antibody (R and D systems, AF933), then rinsed with PBS 4 times (10 min each time). Secondary antibodies and/or isolectin B4 were applied to the brain slices at 4^{o}C overnight. The slices were washed with PBS every 10 min for 4 cycles. For nucleus counter staining, the brain slices were incubated in PBS containing DAPI nuclear stain (100 ng/ml) for 1 h at room temperature and washed in PBS for 5 min. The primary and secondary antibodies used in this thesis are listed in Table 2.2.

The slices were mounted on microscope slides with DAKO fluorescent mounting medium (DAKO, S3023), covered with a glass cover slip and sealed with CoverGlip^{TM} coverslip Sealant (Biotium, 23005).

Table 2.2: Sources, catalogue number and concentration of antibodies used in this thesis.

Primary antibody	Supplier	Catalog No.	Dilution
Goat anti-ACE-2	R and D systems	AF933	1:200
Goat anti-αSMA	Abcam	ab21027	1:200
Mouse anti-NG2	Abcam	ab50009	1:200
Rabbit anti-adenosine A1 receptor	Abcam	ab82477	1:200
Rabbit anti-adenosine A2a receptor	Abcam	ab3461	1:200
Rabbit anti-adenosine A2b receptor	Cohesion Biosciences	CPA3755	1:200
Rabbit anti-adenosine A3 receptor	Sigma-Aldrich	AB1590P	1:200
Rabbit anti-myosin light chain	Abcam	ab2480	1:200
Rabbit anti-Pdgfrβ	Santa Cruz	sc-432	1:200

Secondary antibody	Supplier	Catalog No.	Dilution
Donkey anti-goat 488	Invitrogen	A11055	1:500
Donkey anti-goat 633	Invitrogen	A21082	1:500
Donkey anti-mouse 555	Invitrogen	A31570	1:500
Donkey anti-rabbit 488	Invitrogen	A21206	1:500
Donkey anti-rabbit 647	Invitrogen	A31573	1:500

2.4.4 Confocal imaging

Imaging of fixed slices was performed on a laser scanning confocal microscope (Carl Zeiss Microscopy, LSM 700 microscope) with a 20x objective (Carl Zeiss Microscopy, Plan-Apochromat 20x/0.8 M27) or a 63x oil immersion objective (Carl Zeiss Microscopy, Plan-Apochromat 63x/1.4 Oil DIC M27). There were 4 laser wavelengths: (i) 405 nm for DAPI, (ii) 488 nm for Alexa fluor 488 and neurotrace 500/525, (iii) 555 nm for DsRed, propidium iodide, DHE, MitoSox, and Alexa fluor 555, and (iv) 639 nm for Alexa fluor 647. Images were captured as a single frame or a Z-stack depending on the experiment. Laser power and gain settings were adjusted to optimise the signals. Importantly, when images were taken for intensity quantification or comparison between different conditions, the settings were kept constant to eliminate potential bias arising from different settings. In the process of analysis, the experimental conditions for the images were blinded by a customised imageJ plugin (courtesy of Dr. Lorena Arancibia-Carcamo, UCL, UK Dementia Research Institute).

2.5 *In vivo* surgery

Experiments on *in vivo* animals were performed to study how the passage of RBCs affected the vessel wall *in vivo* and to study pericyte contraction in AD *in vivo*. All procedures on animals were done in accordance with EU and UK regulations (the UK Animals (Scientific Procedures) Act 1986).

2.5.1 The study of dilation of capillaries as red blood cells pass

2.5.1.1 Surgical procedure

Pdgfb-iCreER x PC::G5-tdT mice were used for the *in vivo* experiments in Chapter 3 at P245 – P247 without tamoxifen injection.

Induction of anaesthesia was achieved with a bolus injection of xylazine (Bayer plc, Rompun^{R} 2% w/v, 10 mg/kg intraperitoneally (i.p.)) following by an injection of ketamine (Zoetis, Ketavet^{R} 100 mg/ml, 60 mg/kg i.p.) after 10 minutes.

The depth of anaesthesia was monitored using the paw withdrawal reflex every 20 minutes and supplemental ketamine injections of 30 mg/kg i.p. were given to maintain anaesthesia depth throughout the surgical procedures. The mouse was placed on a heating pad, and core body temperature was measured through a rectal temperature probe and kept at 37^{o}C and eyes were kept from drying by using polyacrylic acid eye drops (Dr. Winzer Pharma).

Tracheal cannulation was performed to give mechanical ventilation (Harvard apparatus, MiniVent model 845). The right femoral vein was cannulated for intravenous (i.v.) administration of drugs.

The mouse was fixed to a customised stereotaxic frame and lidocaine/prilocaine gel (AstraZeneca, EMLA^{TM} Cream 5%) was topically applied before exposing the skull. A customised headplate was then glued to the skull to make a sealed well. A craniotomy with a diameter of 3 mm was performed using a surgical drill over the right somatosensory barrel cortex region, with a center approximately 3 mm to the right of, and 0.5 mm behind, bregma. The dura mater was then gently removed. The cortex was kept moist with HEPES-buffered aCSF and covered with 0.5% agarose gel. A glass cover slip was placed on top of the craniotomy for vessel imaging.

The mice were injected with Texas red labelled dextran (TxRed; MW 70 kDa; Invitrogen, D1830, 1.25% w/v, 100 µl i.v.) to visualise plasma and the anaesthesia was changed to α-chloralose (Sigma-Aldrich, C8849, 50 mg/kg/h i.v. Then the mouse was placed under a two photon microscope (Carl Zeiss Microscopy, LSM 710) and secured

on a custom-built stage to image brain capillaries and red blood cells (RBCs, see below). After the experiments were finished, the mouse was humanely sacrificed by cervical dislocation followed by decapitation.

2.5.1.2 Imaging of capillaries and red blood cells

Capillaries were detected using a water immersion 20x objective (Carl Zeiss Microscopy, W Plan-Apochromat 20x/ 1.0 DIC M27 75 mm) based on (i) the eGFP signal in endothelial cells; and (ii) the intraluminal size of a single RBC passage (as detected by lack of a TxRed signal inside the lumen). Two-photon excitation was performed using a LSM 710 microscope (Carl Zeiss Microscopy) with a Newport-Spectrophysics Ti:sapphire MaiTai laser pulsing at 80 MHz. A horizontal segment across a vertical vessel was illuminated with the 940 nm excitation wavelength laser and eGFP (labelling endothelial cells) and TxRed (labelling plasma) signals were collected at the same time. The images were taken in a time series of 1,000 frames with a frequency of 100 Hz, a frame size of 120 pixels for the x-axis and 4 pixels for the y-axis, a pixel size of 0.09 µm and a pixel dwell time of 13.50 µs.

2.5.1.3 Vessel diameter analysis for high speed imaging

Images were processed with ImageJ Fiji and analysed with Matlab. Inner diameters were calculated after fitting Gaussian curves to the fluorescence labelling of both vessel walls in Origin 2018 (see Section 3.2.6) and analysis was performed using these values.

2.5.2 The study of pericyte contractility in AD mice *in vivo*

2.5.2.1 Surgical procedure

In vivo surgery for AD and WT mice to visualise pericytes and measure capillary diameters was done by my colleague, Dr. Nils Korte.

Mice used in this experiment were NG2-DsRedBAC x $APP^{NL\text{-}G\text{-}F/NL\text{-}G\text{-}F}$ mice (see Section 2.2.3) in which APP with a humanised Aβ region with AD-related mutations is knocked in and pericytes express a red fluorescent protein, dsRed. The age of P119 – P143 (i.e. roughly 4 months) was chosen because at this age these homozygous AD mice have developed a significant density of Aβ plaques. The mice were anaesthetised by injecting two doses of urethane 15 min apart, with a total dosage of 1.55 g/kg. The general conditions of the mice were maintained as described in Section 2.5.1.1; however, the mice did not undergo tracheal cannulation or femoral vein catheterisation.

A 3 mm diameter craniotomy was performed as outlined in Section 2.5.1.1 over the primary somatosensory cortex, which is caudal to the coronal suture and approximately 2 to 6 mm lateral to the midline. To image cerebellar vessels, the craniotomy was done over the right cerebellar hemisphere. The dura was left intact. The animal and the headplate were secured on a custom-built stage under the objective during imaging.

The animal was injected retro-orbitally with 1 mg of albumin-fluorescein isothiocyanate conjugate (FITC-albumin; Sigma, A9771) in 100 µl of saline.

2.5.2.2 Imaging of pericytes and capillaries

A wavelength of 820 nm and 900 nm from a Newport-Spectrophysics Ti:sapphire MaiTai laser pulsing at 80 MHz was used to illuminate FITC-albumin and DsRed with a 20x water-immersion objective (Carl Zeiss Microscopy, W Plan-Apochromat 20x/1.0 DIC M27 75 mm). The mean laser power was kept under 35 mW below the objective. Penetrating arterioles were recognised by their diameter (> 10 µm) and the surrounding vascular smooth muscle cells expressing DsRed. Image stacks were taken across cortical layers I to IV, with a maximum depth of 400 µm from

the cortical surface, in 2 µm steps with a frame size of 512 pixels by 512 pixels for the x- and y-axes and a pixel size of 0.38 µm.

2.5.2.3 Vessel diameter analysis

The analyses were performed blind by Dr. Nils Korte and me. To measure vessel diameters, a line perpendicular to the vessel axis was drawn using ImageJ across the whole width of the FITC-albumin dye fluorescence. The diameter was measured either manually or automatically by using a customised code to fit a Gausian function to calculate the full width at quarter maximum of the peak fluorescence intensity.

2.6 Calcium imaging

Calcium imaging was employed to probe mechanisms underlying changes of pericyte contractile tone.

2.6.1 Live rodent brain slice preparation

For calcium imaging experiments in Chapter 5, sagittal brain slices from NG2-CreERT2 x PC::G5-tdT mice were prepared by my colleague Dr. Thomas Pfeiffer. The schedule 1 method and the surgical method to expose the brain were performed as described in Section 2.3.1.1. The brain was then extracted from the base of the skull using a small spatula and the specimen was placed with the ventral side facing downwards on a filter paper to dry the excess fluid. A razor blade was used to cut off the lateral quarter of each hemisphere and to make a midline incision to separate both hemispheres. The brain hemispheres were flipped to rest on the lateral sides and another cut was made to discard the ventral one third of each hemisphere. Then the brain pieces were mounted onto the slicing block of a Vibratome (Leica, VT 1200S) using a thin layer of cyanoacrylate glue before being submerged in ice-cold slicing

solution oxygenated with 95% O_2 and 5% CO_2. Sagittal cortical slices with 300 µm thickness were cut and transferred to slicing solution at 35^{o}C for 20 min and then to recovery solution at room temperature for at least 10 min until used.

2.6.2 Imaging of pericytes

Brain slices were transferred to a two-photon microscope (Carl Zeiss Microscopy, LSM 710 microscope) and perfused with bicarbonate-buffered aCSF gassed with 20% O_2, 5% CO_2 and 75% N_2 at 33-36^{o}C with a flow rate of 3 – 4 ml/min. Pericytes were identified by their tdTomato signal and morphology resembling a bump-on-a-log using a water immersion 20x objective (Carl Zeiss Microscopy, W Plan-Apochromat 20x/ 1.0 DIC M27 75 mm). By using the Zen program (Carl Zeiss Microscopy), I identified a region of interest, which was at least 20 µm in depth and had at least 3 pericytes in the image stack. Acquisition parameters of (i) pixel dwell time > 2 µs, (ii) step size = 2 µm, (iii) scan time of the overall stack ≤ 30 s and (iv) pixel size ~ 0.3 µm were maintained by varying the frame size, speed of image acquisition, digital zoom and stack size. Laser power and digital gain were adjusted to get a suitable intensity. Pericytes were excited with a 940 nm excitation wavelength laser (Newport-Spectraphysics Ti:sapphire MaiTai laser pulsing at 80 MHz) and signals from tdTomato (labelling pericyte outline) and GCaMP5G (measuring calcium signaling in pericytes) were collected simultaneously. The image focus was readjusted after every five image stacks were taken (~ 2.5 min).

2.6.3 Calcium signaling analysis

An image sequence of maximum intensity Z-projections of the image stacks taken was created using the ImageJ Fiji program and individual pericytes were aligned to correct for slice movement using the Template Matching and Slice Alignment plugin. By using the Polygon selections tools, the pericyte soma was delineated and its

calcium intensity profile across time was measured and plotted. The data were exported to Microsoft Excel and the averages of five intensity measurements around the times of interest, normally at the peak of any Ca transient or at the end of the experiment, were used for further statistical analysis.

2.7 Statistical analysis

All statistical analyses were performed using Prism 7.00 (GraphPad). Data are presented as mean ± s.e.m. Normality of data was examined by the Shapiro-Wilk normality test. Equality of variance between two normally distributed data sets was examined using the F test. Two-tailed Student's t-tests and t-tests with Welch's correction were used when the variance was equal or unequal respectively. Comparison of data that failed the normality test was made using a Mann-Whitney test. When comparing normalised capillary diameters after application of drugs to a normalised baseline (which is equal to one in all vessels due to the normalisation process and not by chance), a Wilcoxon signed-rank test was performed. To correct for multiple comparisons within a figure panel, a procedure similar to the Holm-Bonferroni method was used (i.e. for N comparisons, the smallest P-value is multiplied by N, the second smallest P-value by N-1, etc.). Corrected p-values of less than 0.05 were considered significant. When determining whether the slope of linear regression is different from zero, the t statistic for the slope was used.

Chapter 3: Contractile properties of pericytes

3.1 Introduction

Capillaries contribute the most vascular resistance to the intracerebral circulation, potentially making them a major determinant of cerebral blood flow (Boas *et al.*, 2008; Hall *et al.*, 2014; Gould *et al.*, 2017; Peyrounette *et al.*, 2018; Rungta *et al.*, 2018). The blood flow resistance in capillaries is proposed to be regulated by pericytes (Hall *et al.*, 2014; Attwell *et al.*, 2016), which are mural cells with a bump-on-a-log morphology for their somata and which have processes running along and around the vessels (Attwell *et al.*, 2016; Cheng *et al.*, 2018). The circumferential processes are expected to be able to adjust the diameter of the underlying capillary when they contract or relax. However, studies in the pericyte field have shown inconsistent results regarding pericyte contractility (Hill *et al.*, 2015; Attwell *et al.*, 2016), which might occur for several reasons.

The first reason is that pericytes have a continuum of phenotypes, rather than being a homogenous group of cells (Armulik *et al.*, 2011), causing variations in the definition and detection of pericytes (Attwell *et al.*, 2016). Originally, pericytes were described by Eberth (Eberth, 1871) and Rouget (Rouget, 1873) and were then named by Zimmerman (Zimmermann & Zimmermann, 1923) as cells located on the abluminal surface of capillaries with bump-on-a-log morphology, which is a major characteristic shared by pericytes (although pericytes at vessel branch points do not show this feature). However, pericytes can be further classified into three subtypes (Uemura *et al.*, 2020), as follows: (i) proximal capillary pericytes, located on the 1st to 4th order capillaries which express contractile proteins (Grant *et al.*, 2019), and regulate blood flow (Hall *et al.*, 2014; Attwell *et al.*, 2016; Rungta *et al.*, 2018); (ii) mid-capillary pericytes, which are further along the vascular tree (>4th branch order) and are

important in blood-brain barrier regulation (Armulik *et al.*, 2010; Attwell *et al.*, 2016); and (iii) post-capillary pericytes, which are near the venule end of the capillary bed, and modulate transmigration of white blood cells into the brain parenchyma (Attwell *et al.*, 2016; Török *et al.*, 2021). With this classification, conflicting results are prone to arise when studying “pericytes” of different subtypes. Correct identification of the pericyte subtype of interest is important to get consistent results and to interpret data from other studies. Recently, a fluoro-Nissl dye Neurotrace 500/525 has been proposed to specifically label non-contractile pericytes (Damisah *et al.*, 2017). Damisah et al. (2017) found that the cells stained by this dye expressed the pericyte markers Pdgfrβ and NG2 (Cheng *et al.*, 2018), but not αSMA (Damisah *et al.*, 2017). They were also not contractile during either spontaneous or evoked vasomotion *in vivo* (Damisah *et al.*, 2017). However, it must be noted that this group defined pericytes as cells with processes that do not fully wrap around vessels, do not express αSMA and are not contractile (Hill *et al.*, 2015; Damisah *et al.*, 2017), contrary to the original definition of pericytes which is widely used (Eberth, 1871; Rouget, 1873; Zimmermann & Zimmermann, 1923; Attwell *et al.*, 2016) which includes the pericytes throughout the capillary bed. Hence, it is unclear to which subtype the “pericytes” in the Neurotrace 500/525 study belong (Damisah *et al.*, 2017) and whether the dye is suitable for studies of pericyte contractility. This makes it hard to interpret results from subsequent studies using Neurotrace 500/525 to identify pericytes (Nelson *et al.*, 2020; Kovacs-Oller *et al.*, 2020). More information on the labelling properties of Neurotrace 500/525 are thus needed before it can be used in further studies. This is one of the aims of this chapter.

Another factor contributing to the inconsistent results across pericyte studies is that vascular responses from pericytes might not be homogenous across the whole

capillary tree. It has been suggested that capillary contractile responses occur close to pericyte somata (Mishra *et al.*, 2014; Cai *et al.*, 2018; Kureli *et al.*, 2020), however, no actual data have been quantified for contraction near versus away from the soma. Clarification of the relationship of the pericyte soma to capillary constriction is important because diameter measurement away from the soma might underestimate the vascular resistance changes if the maximum contraction is seen near pericyte somata.

In studying pericyte contractility, proximal capillary pericytes have been the main target of investigation (Cai *et al.*, 2018; Khennouf *et al.*, 2018; Rungta *et al.*, 2018), however, mid-capillary pericytes have also been suggested to contain αSMA (Bandopadhyay *et al.*, 2001; Alarcon-Martinez *et al.*, 2018), a protein needed for contraction in smooth muscle cells (Wang, Zohar & McCulloch, 2006). These mural cells also exhibit calcium responses during neuronal stimulation (Rungta *et al.*, 2018). Mid-capillary pericytes were also shown to constrict capillaries when they were depolarised (Hartmann *et al.*, 2021). However, mid-capillary pericytes mostly extend their processes along the vessels rather than around the vessels, suggesting that the main force exerted by these cells might not be a constricting force and that these cells might affect cerebral blood flow via other mechanisms.

One possible mechniam is that these pericytes change capillary elasticity, which is a factor that could govern microcirculation blood flow. Cultured pericytes on silicon substrata caused deformation and increased mechanical stiffness of the substrata, and this process was inhibited by application of blockers of actomyosin contraction (Lee *et al.*, 2010). Furthermore, ablation of mid-capillary pericyte resulted in dilated capillary segments in the first week (Berthiaume *et al.*, 2018), implying that

the elasticity or tone of the capillary walls is governed by these pericytes (Dessalles, Babataheri & Barakat, 2021).

Elasticity of microvessels can affect microcirculation blood flow by allowing passive dilation of the vessels. This passive dilation will decrease the flow resistance. For example, according to Poiseuille's law for laminar flow of a pure liquid, resistance is inversely proportional to the 4th power of the vessel diameter so if upstream dilation of arterioles or low branch order capillaries results in a local increase of blood pressure then the mid-capillary bed vessels could dilate in response to the pressure and reduce their hydraulic resistance (Rungta *et al.*, 2018). Furthermore, the flow in vessels with small diameters is strongly affected by the cells suspended in the blood, meaning that it is not possible to treat blood as a homogeneous fluid and use continuum mechanics (Secomb, 2016), indeed the elasticity of the vessel wall affects the thickness of cell-free layer near the vessel wall. The layer is formed because flowing RBCs have a tendency to move away from the capillary wall (Kim *et al.*, 2009). This layer acts as a lubricant to prevent static frictional force between the RBC and the vessel wall (Lighthill, 1968; Caro *et al.*, 2011; Secomb, 2016). Moreover, an increase in the thickness of this layer reduces the apparent haematocrit and viscous resistance to the flow, leading to an increase in blood flow (Toksvang & Berg, 2013). The thickness of the cell-free layer is determined by the summation of the compliances of the RBCs and the vessels (Lighthill, 1968). An *in vivo* experiment in rabbit mesenteric microvessels showed that the cell-free layer was thicker when RBCs flowed through elastic microvessels when compared to that when RBCs flowed through hardened microvessels (that were fixed with 4% paraformaldehyde: Maeda *et al.*, 1996). The flow resistance was also lower in elastic microvessels than in hardened microvessels (Maeda *et al.*, 1996). Finally, it should be recognised that the smallest capillaries are

smaller than the size of a RBC or leukocyte, so the cells need to deform to pass through them, and a more elastic wall will facilitate this. Thus, for all these reasons, increasing the tone of pericyte processes that run longitudinally along a mid-capillary bed capillary is expected to increase the resistance of the vessel.

The objectives of the experiments in this chapter were to investigate pericyte identification techniques, and how pericytes regulate capillary blood flow. Identification techniques studied included morphological identification of pericytes using bright-field imaging and the use of Neurotrace 500/525 as a pericyte label. The contractility of capillary pericytes at the arteriole end of the capillary bed was tested using noradrenaline and adenosine. The relationship between the distance from the pericyte soma and the diameter response to contractile agonists was also explored, to address potential sources of conflict in the literature. Finally, the last aim was to show that capillary walls in the brain are elastic, implying a possible role even for mid-capillary bed pericytes in regulating cerebral blood flow *in vivo*.

3.2 Methods

3.2.1 Solutions and drugs

Bicarbonate-buffered and HEPES-buffered aCSF were prepared as previously described in Section 2.1. Drugs were either directly dissolved in the superfusion solution (e.g. U46619 and Neurotrace 500/525) or dissolved to make a stock solution in double purified water (e.g. isolectin B4) or DMSO (e.g. jasplakinolide) or saline (e.g. TxRed dye) before being diluted to the final concentrations in the superfusion solution.

3.2.2 Transgenic mice expressing fluorescent constructs

NG2-DsRedBAC transgenic mice (see Section 2.2.1), which label pericytes with the genetically encoded red dye DsRed, were used to identify pericytes in immunohistochemistry experiments (see Section 3.3.3).

Pdgfb-iCreER x PC::G5-tdT mice (see Section 2.2.2) without tamoxifen injection were used for *in vivo* experiments to fluorescently label endothelial cells which express eGFP constitutively (see Section 3.3.7).

3.2.3 Bright-field imaging

All bright-field imaging experiments used 300-µm-thick cerebral cortical brain slices from P19-P22 Sprague-Dawley rats. The rodent slices were prepared as previously described (see Section 2.3.1). In some experiments, isolectin B4 conjugated to Alexa Fluor 568 (5 µg/ml, Section 3.3.1) or Neurotrace 500/525 (1:100, section 3.3.3) were applied in a 30-min incubation of the brain slices, to fluorescently label pericytes before the slices were imaged as previously described (see Section 2.3.2). Slices were perfused with bicarbonate-buffered aCSF oxygenated with 20% O_2, 5% CO_2, and 75% N_2 at 33-36^{o}C for 5 minutes as a baseline, before the application of drugs. Images were taken at pericyte locations unless stated otherwise and analysed with Metamorph software (see Section 2.3.3).

3.2.4 Immunohistochemistry

Brain slices from P19-P22 Sprague-Dawley rats (300 µm thick, Section 3.3.2 and 3.3.4) or from NG2-DsRedBAC transgenic mice (200 µm thick, Section 3.3.3) were prepared as outlined in Section 2.4.1. Pre-incubation in 35 ^{o}C oxygenated aCSF with Neurotrace 500/525 (see Section 3.3.2 – 3.3.4) or jasplakinolide (see Section 3.3.4) was performed before fixation with 4% PFA while shaking at room temperature for 1 h. Fixed brain slices were incubated in blocking solution, primary antibodies and

secondary antibodies at 4 ºC overnight for each step (see Section 2.4.3). DAPI nuclear stain was applied for 1 h and the slices were mounted, before imaging with a confocal microscope as described in detail in Section 2.4.4.

3.2.5 *In vivo* surgery

In vivo surgery was performed as previously described (see Section 2.5.1.1). In short, Pdgfb-iCreER x PC::G5-tdT mice without tamoxifen injection were anesthetised with xylazine and ketamine and underwent tracheostomy, right femoral vein cannulation and craniotomy over the right somatosensory barrel cortex. The mice were injected with TxRed dye iv to label plasma and transferred to be imaged under a two photon microscope. Segments of capillaries that ran vertically across the image (i.e. perpendicular to the line scan direction were identified and signals of eGFP from endothelial cells and TxRed from plasma were simultaneously collected at an image frequency of 100 Hz.

3.2.6 Vessel diameter analysis for high speed imaging

To assess whether the passage of RBCs led to a distension of capillary walls, such that pericyte tone might affect the speed of RBC passage, we employed high speed imaging of *in vivo* animals. Image sequences were first processed in ImageJ Fiji with Enhance Contrast and Subtract Background plugins.

3.2.6.1 Creating intensity profiles of the endothelial eGFP signal

Frames with RBCs were identified by a lack of TxRed signal inside the lumen (as seen in Fig. 3.1A, unlike Fig. 3.1B which has TxRed in the vessel). A 2-pixel-thick line was drawn across the vessel to measure the pixel intensities of the eGFP signal along the line in each frame (Fig. 3.1C) and the intensity profiles of all frames were exported to Matlab.

3.2.6.2 Determination of "RBC" and "no RBC" frames

The same line was also used in the TxRed channel as a landmark to create a kymograph, where the TxRed intensity profile along the line in each frame was extracted and stacked along the y-axis of the kymograph for all frames, thus creating an intensity-time plot, with the Kymograph Builder plugin (Fig. 3.1D left). When RBCs flow through microvessels, a layer of cell-free plasma is formed next to the vessel wall (Fig. 3.1D left) and the thickness of this layer is different in each capillary segment (Maeda *et al.*, 1996). Because the algorithm developed to determine whether there is a RBC in the frame measures the proportion of the total pixels without TxRed, the varying thickness of the cell-free layer in different capillaries interferes with this process. Thus this plasma layer needs to be cropped out to allow the automated algorithm to work. The edges of the cell-free layers were manually marked by observing the edge of RBCs and the kymograph was cropped to those lines (Fig. 3.1D left). The cropped plot was then binarised using the getHistogram built-in macro function to separate the intensity into 2 bins – 0 and 1 (Fig. 3.1D right). The frame was defined to be "RBC" when the number of black pixels (0 intensity) across the cropped kymograph was more than 75% of the total and "no RBC" when the black pixels failed to reach 75% of the total (Fig. 3.1D right). The "RBC" status of each frame was then collected and exported to Microsoft Excel.

3.2.6.3 Outer wall diameter quantification

In Matlab, the eGFP intensities were plotted and smoothed for each frame and the two peaks of intensity representing the 2 vessel walls were identified (green dots in Fig. 3.1E). For each vessel wall, the peak height was calculated by subtracting the trough intensity outside the wall (red dots in Fig. 3.1E) from the peak intensity. The half peak heights (horizontal blue lines, and blue dots inside red circles in Fig. 3.1E)

on the outside walls were defined as being the outer wall locations. The outer wall diameter was calculated by subtracting these two values. The inner wall vessel diameter could not be accurately measured on a frame-by-frame basis from the eGFP signal using Matlab because of the noise in the signal inside the vessel.

The outer wall diameter of each frame was exported to Microsoft Excel to be plotted against frame number and a straight line was fitted to represent the mean change of diameter as a function of time (Fig. 3.1F). The vessel was excluded from analysis if the slope of the line was significantly different from zero, implying that the vessel was not stable in diameter, and the small effects of RBCs passing on the vessel walls might be masked by these factors.

Each frame was then allotted using its “RBC” status to the RBC or no-RBC categories. The outer diameters measured in Matlab were classified by their “RBC” status and the means and s.e.m. of external capillary diameters of the “RBC” frames and of the “no RBC” frames were calculated.

3.2.6.4 Inner diameter quantification

The eGFP signals inside the vessels were noisy because of interference from the eGFP signals from above and below the captured frames, making it difficult to measure internal capillary diameters using Matlab. To measure the inner diameters of the “RBC” frames, the intensity profiles of the “RBC” frames were combined and averaged to get a representative intensity profile. The same procedure was also applied to the “no RBC” frames. A Gaussian distribution was fitted to each vessel wall for each representative distribution (using Origin 2018) and the centre (X) and full width at half maximum ($FWHM$) of each vessel wall were measured (Fig. 3.1G). The inner diameter of the vessel lumen was then calculated using the following equation:

$$Inner\ diameter = (X_2 - \frac{FWHM_2}{2}) - (X_1 + \frac{FWHM_1}{2}) \quad \text{…eqn. 4}$$

The outer and inner diameters of “RBC” and “no RBC” frames for each vessel were used for statistical analysis.

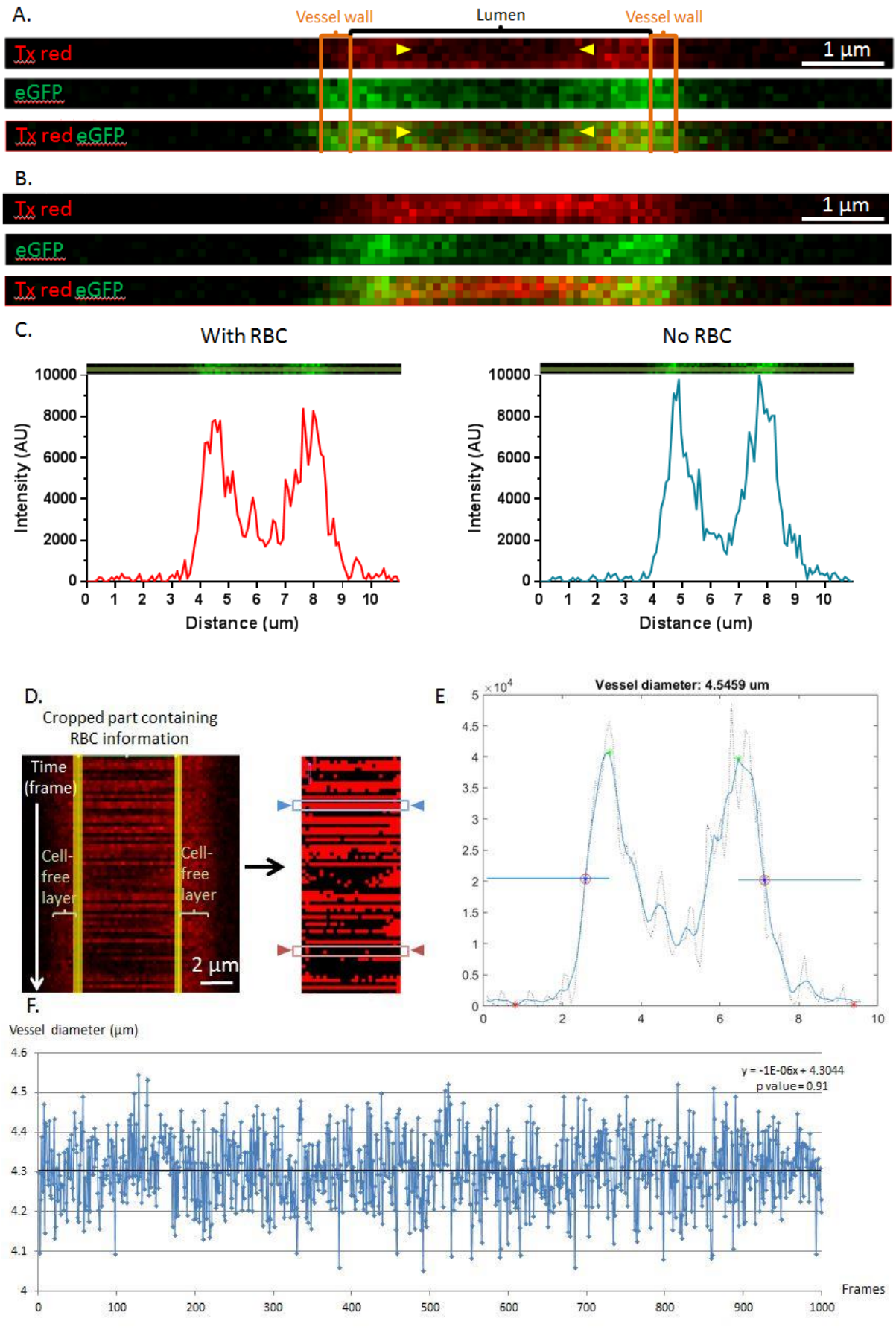
A.
Vessel wall
Lumen
Vessel wall
Tx red
1 µm
eGFP
Tx red eGFP
B.
Tx red
1 µm
eGFP
Tx red eGFP
C.
With RBC
No RBC
Intensity (AU)
Distance (um)
D.
Cropped part containing RBC information
Time (frame)
Cell-free layer
Cell-free layer
2 µm
E
Vessel diameter: 4.5459 um
F.
Vessel diameter (µm)
y = -1E-06x + 4.3044
p value = 0.91
Frames

G.

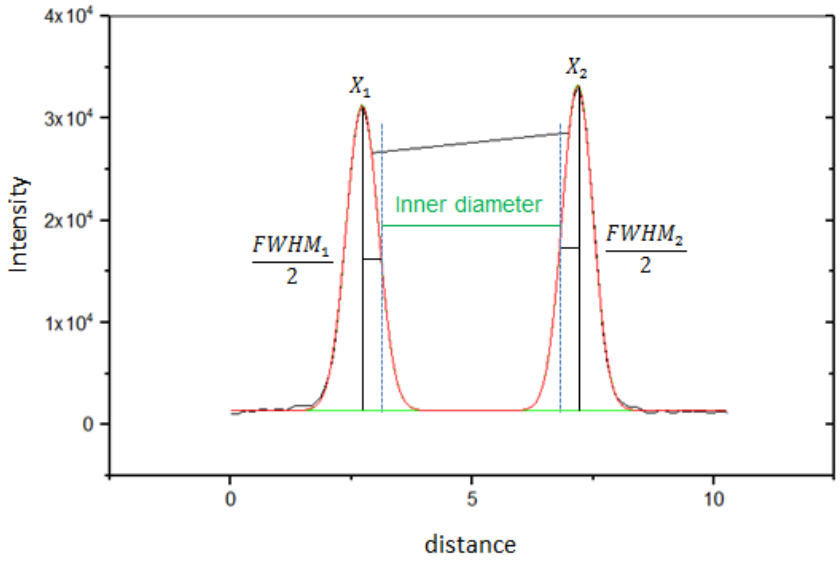

Figure 3.1: Method for vessel diameter analysis of *in vivo* experiments on Pdgfb-iCreER x PC::G5-tdT mice, injected with TxRed dye.

A. Representative images of a "RBC" frame in (top) the TxRed channel – showing TxRed dye in plasma, (middle) the eGFP channel – showing eGFP signals in endothelial cells and (bottom) the merged image. Yellow arrowheads depict the edges of a RBC, defined by the lack of TxRed signal inside the lumen.

B. Representative images of a "no RBC" frame in (top) the TxRed channel, (middle) the eGFP channel and (bottom) the merged image. TxRed dye can be observed across the lumen of the vessel.

C. The eGFP channels from representative images in (left) A and (right) B are depicted. The eGFP intensity profiles, plotting intensities against the distance, are shown below the vessel images.

D. (Left) A kymograph, where the TxRed intensity for each frame was stacked to create an intensity-time plot, was created. The edge of the RBC was identified by observing the the edge of the black pixels (shown as the transparent yellow line). A field of interest was cropped along the edges of RBC and binarised (right) to determine the "RBC" status of the frame. Red arrowheads show the "RBC" frame, where the black

pixels across the cropped kymograph are more than 75%, and blue arrowheads show the “no RBC” frame, where the black pixels failed to reach 75%.

E. Matlab analysis of outer diameter of the representative image in A. The intensity profile in A. was smoothed and the peak intensities (green dots) of both walls and trough intensities of both walls (red dots) were identified. The intersection of half peak height (blue horizontal line) and intensity profile create an intersection point (blue dots inside red circles in Fig. 3.1E) with each vessel wall. Vessel diameter shown above the graph was calculated from the difference of the X-axis values of the intersection points.

F. A representative graph of a stable vessel plotting vessel diameters calculated from E against frames. Linear regression was performed and the equation and p-value assessing whether the slope is significantly different from zero are shown in the right upper part.

G. A representative graph of a vessel fitted with Gaussian distribution on both vessel walls using the Origin program. Inner diameter was calculated as:

$$Inner\ diameter = (X_2 - \frac{FWHM_2}{2}) - (X_1 + \frac{FWHM_1}{2}) \quad \text{…eqn. 4}$$

3.2.7 Statistical analysis

Statistical analysis of the data was performed as previously described (see Section 2.7).

3.3 Results

3.3.1 Identification of pericytes using bright-field imaging is accurate

The bump-on-a-log morphology (for pericytes on straight parts of capillaries) and their anatomical location on the outer surface of the capillary are defining characteristics of pericytes (Eberth, 1871; Rouget, 1873; Zimmermann & Zimmermann, 1923; Attwell *et al.*, 2016). Although mouse pericytes can be identified using transgenic mice expressing dsRed under control of the NG2 promoter, for bright-field imaging experiments in this thesis on rat and human tissue, being able to morphologically identify pericytes is important to allow detection of capillary responses near pericyte somata (Mishra *et al.*, 2014).

To test the accuracy of identifying pericytes morphologically, I incubated rat brain slices for 30 min with isolectin B4 conjugated to Alexa Fluor 568, to visualise the basement membrane which surrounds pericytes and the outer surface of endothelial cells. Initially, candidate pericytes were identified while illuminated by only white light, using their bump-on-a-log appearance and small somata (<10 μm). Then, to test whether they had been correctly identified as pericytes, I turned on the fluorescence illuminator to inspect the isolectin B4 signal (Fig. 3.2). The pericyte candidates were considered to be pericytes if they were surrounded by isolectin B4 signal. Previous unpublished work in the Attwell lab has confirmed that over 93% of transgenically labelled NG2-dsRed expressing pericytes are surrounded by isolectin B4 signal, validating the use of isolectin B4 to define pericytes.

The accuracy of purely morphological identification of pericyte was 96.3% (correct in 26 out of 27 trials) for all pericytes both near and away from arterioles. Thus, it is possible to identify pericytes using morphology only in bright-field imaging.

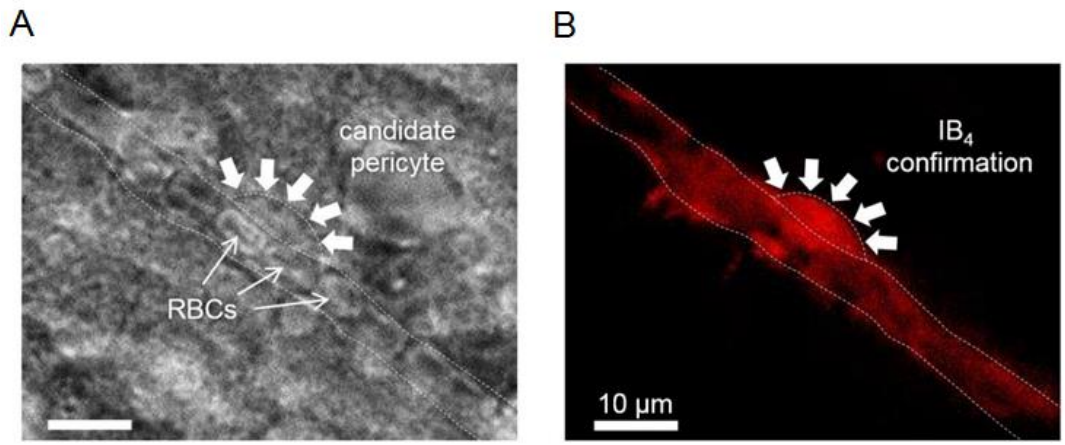

Figure 3.2: Identification of pericytes by morphology.

(A) Bright-field image of a candidate pericyte with a bump-on-a-log-shaped soma (white arrows) on a capillary from a P21 rat brain slice. Faint dotted lines represent the outline of the vessel. (B) The same field as in (A) but illuminated with 568 nm light to visualise isolectin B4 conjugated to Alexa Fluor 568, which stains the basement membrane. The pericyte candidate was confirmed to be a pericyte because it was surrounded by basement membrane.

3.3.2 Neurotrace 500/525 preferentially labels higher branch order pericytes

Neurotrace 500/525 was shown to specifically label pericytes *in vivo* with 99% colocalisation with fusiform looking cells expressing a PDGFRβ-driven signal (Damisah *et al.*, 2017). However, the definition of pericytes used by these authors excluded contractile cells. In order to clarify the subtypes of pericytes labelled by this dye, I incubated live rat brain slices in Neurotrace 500/525 (1:1000) for 30 min before fixing the slices and performing immunohistochemistry.

Neurotrace 500/525 colocalised well with PDGFRβ antibody labelling in the higher order capillaries while the colocalisation with arterioles and proximal capillaries was less obvious (Fig. 3.3A). Quantification of Neurotrace 500/525 labelled cells revealed that 10.8% of Neurotrace 500/525 positive cells were not pericytes (because they did not label for PDGFRβ) and were not located on capillaries. Of the Neurotrace-labelled pericytes that were on vessels, the majority (~60%) were on the venule end of the capillary bed (>7th capillary branch order) (Fig. 3.3B), while the remainder were on lower branch order capillaries, with the number labelled increasing with capillary branch order (Fig. 3.3B). This implies that there is a very high possibility that a pericyte randomly selected from a pool of Neurotrace 500/525 positive cells is not on the proximal capillary pericytes that are typically used for contractility studies.

Analysis of the percentage of all the PDGFRβ-expressing pericytes on each branch order that were also labelled by Neurotrace 500/525 showed that the percentage was greater for higher branch order capillaries, ranging from 16% for the first capillary branch order to 73.5% for the seventh branch order (Fig. 3.3C). This suggests that the majority of proximal capillary pericytes on the 1st – 4th capillary branch orders are not labelled by this dye.

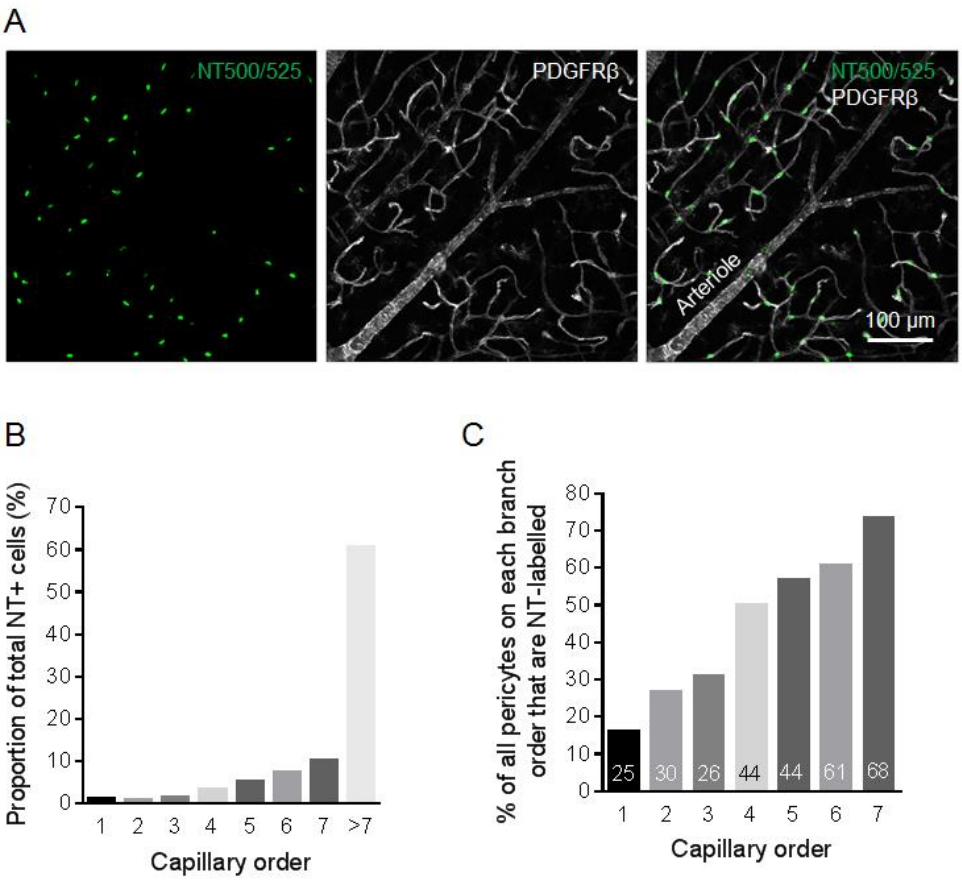

Figure 3.3: Neurotrace 500/525 preferentially labels high branch order pericytes. (A) Labelling rat cortical microvessels with Neurotrace 500/525 and (after fixation) with antibody to PDGFRβ (for arteriolar smooth muscle and pericytes) showed that Neurotrace 500/525 preferentially labelled pericytes away from the arteriole end of the capillary bed and the proximal capillaries. (B) Percentage of Neurotrace 500/525 (NT) labelled pericytes present on different capillary branch orders (sum is 100% of NT-labelled pericytes). Non-vascular cells labelled with Neurotrace 500/525, accounted for 10.8% of Neurotrace 500/525 labelled cells, and were omitted from the graph. (C) Proportion of PDGFRβ-labelled pericytes on each capillary order that were positive for Neurotrace 500/525, showing that pericytes on higher branch order capillaries were more likely to be labelled by this dye. The number on each bar represents the number of pericytes on that capillary branch order.

3.3.3 A subgroup of Neurotrace 500/525 positive cells is contractile

Neurotrace 500/525 labelled pericytes were originally reported to not express αSMA or constrict blood vessels (Damisah *et al.*, 2017) but experiments in Section 3.3.2 showed that some pericytes on proximal capillaries, which are known to be contractile, were labelled by this dye.

To definitively assess whether Neurotrace 500/525 positive pericytes have contractile filaments, I used immunohistochemistry to detect αSMA and phosphorylated myosin light chain in 200 µm thick brain slices from NG2-DsRed BAC transgenic mice that were pre-incubated with Neurotrace 500/525 (1:100) for 1 h. The majority of Neurotrace 500/525 positive cells did not detectably express αSMA or phosphorylated myosin light chain (because of the limited number of channels that can be visualised with a confocal microscope, it was not possible to assess αSMA and phosphorylated myosin light chain expression in the same cells); however, some, especially those near arterioles, expressed these contractile elements (Fig. 3.4).

Bright-field imaging of rat brain slices pre-incubated with Neurotrace 500/525 (1:100) for 30 min before experimenting was performed in collaboration with an undergraduate project student, Heidy Chen, who I was supervising, to investigate the contractility of Neurotrace 500/525 positive pericytes. In three animals, 42% of pericytes identified near the arteriole end of the capillary bed with Neurotrace 500/525 labelling contracted in response to a vasoconstrictor, the thromboxane A_2 analogue U46619 (200 nM, table 3.1), and the constriction occurred near the soma of the Neurotrace 500/525 positive pericytes (Fig. 3.5, see also Fig. 3.7A). Thus, contrary to the previous report (Damisah *et al.*, 2017), a portion of Neurotrace 500/525 positive pericytes are contractile.

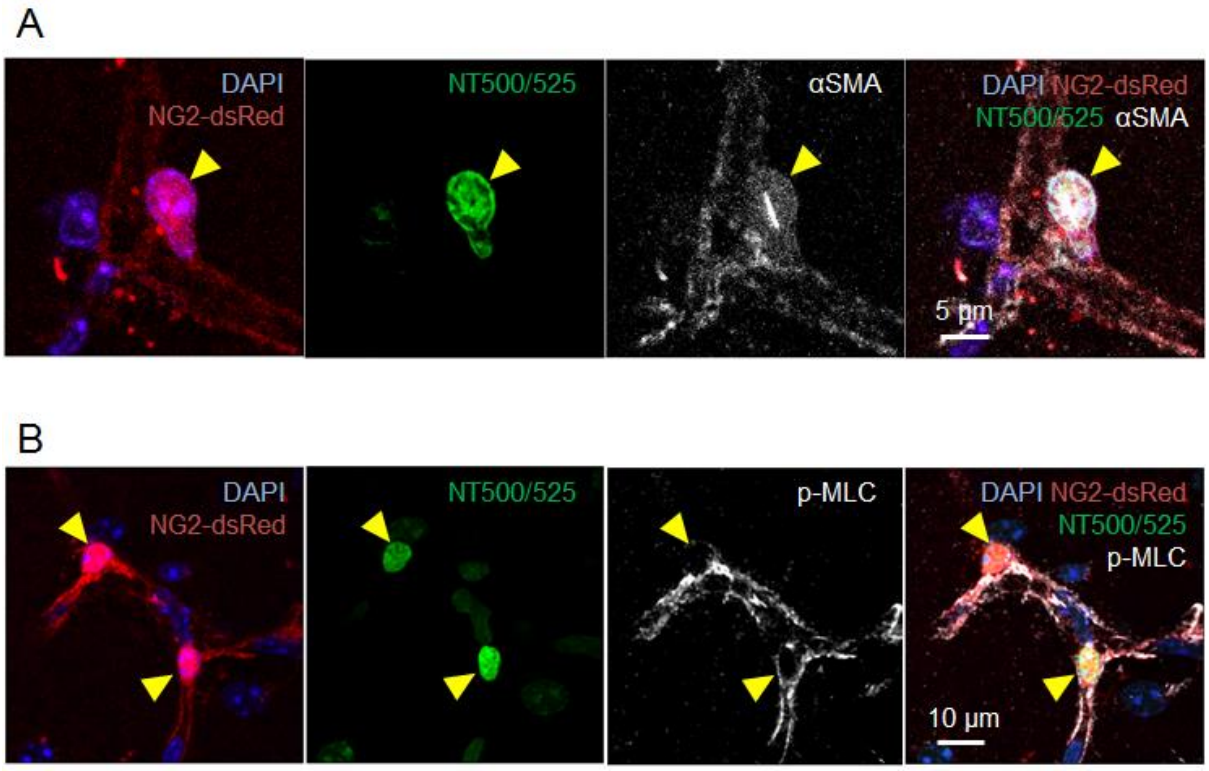

Figure 3.4: Some Neurotrace 500/525 positive pericytes express contractile filaments.

(A and B) Cortical pericytes (yellow arrows) from NG2-DsRed BAC transgenic mice labelling for DAPI (for nuclei), Neurotrace 500/525 and αSMA (A) or phosphorylated-myosin light chain (p-MLC) (B) showed co-localisation of Neurotrace 500/525 and contractile elements in pericytes.

	Total Neurotrace 500/525 labelled pericytes tested	Contracted pericytes (capillaries constricted)	% contractile pericytes
1st animal	5	2	40
2nd animal	2	0	0
3rd animal	5	3	60
Total	12	5	41.67

Table 3.1: Approximately 42% of Neurotrace 500/525 positive pericytes are contractile from bright-field imaging. This experiment was performed in collaboration with an undergraduate project student, Heidy Chen, who I was supervising. The table gives the total number of Neurotrace 500/525 labelled pericytes that were studied on capillaries of low branch order (near arterioles), the number of those cells that constricted capillaries upon application of the thromboxane A_2 analogue U46619 (200 nM), and the percentage of contractile pericytes in three animals. The data suggest that ~42% of pericytes labelled by this dye are contractile.

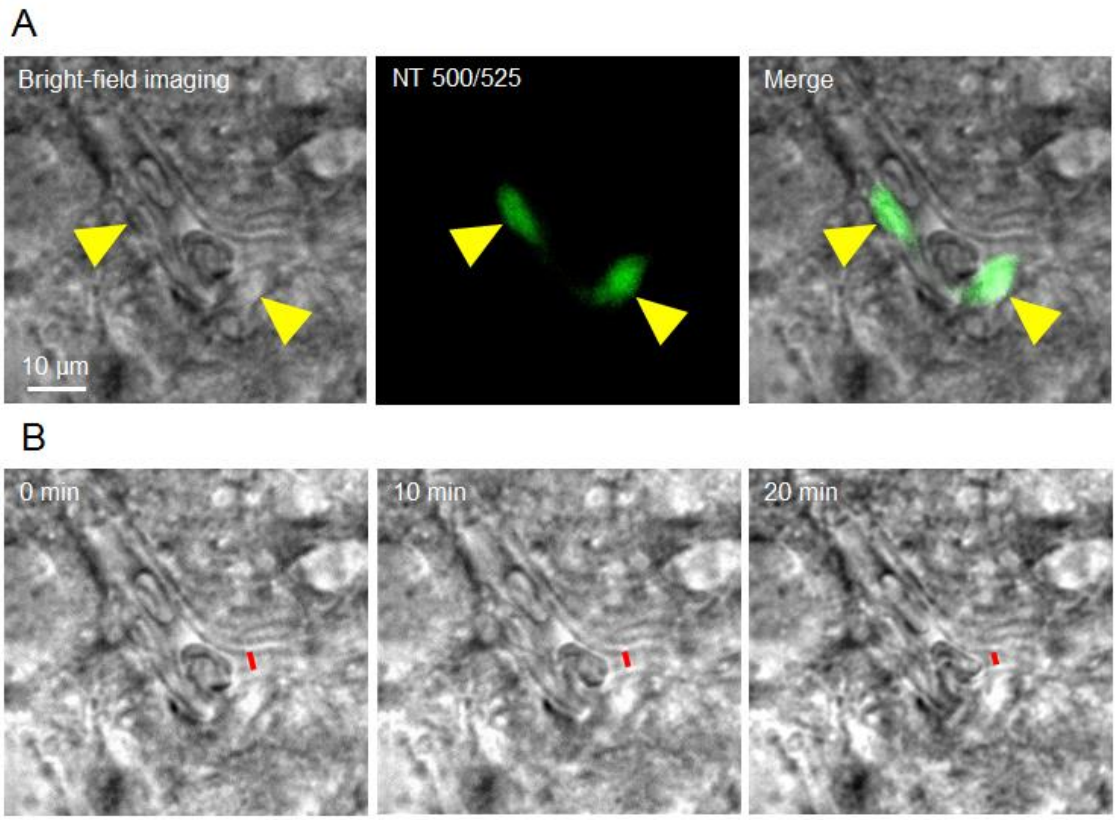

Figure 3.5: Representative images of contractile pericytes labelled by Neurotrace 500/525. (A) A representative image of a rat cortical capillary under bright-field microscopy or illumination with 500 nm light to detect Neurotrace 500/525 before superfusion of the thromboxane A_2 analogue U46619 (200 nM). Yellow arrows indicate pericytes. (B) The field in (A) at time 0, 10 and 20 min after application of U46619 (200 nM), showing that Neurotrace 500/525 labelled pericytes are contractile. Red line depicts diameter near the pericyte soma.

3.3.4 Neurotrace 500/525 is taken up by pericytes via a non-endocytic pathway

There is limited information on how Neurotrace 500/525 is taken up into pericytes. To explore whether Neurotrace 500/525 gets transported into fixed cells because that will allow post-fixation labelling of pericytes by Neurotrace 500/525, Heidy Chen and I incubated live and fixed rat cortical brain slices in Neurotrace 500/525 (1:100) for 30 min and stained for PDGFRβ and isolectin B4 to identify pericytes. Pericytes were stained by Neurotrace 500/525 only when they were incubated live (Fig. 3.6A, B), suggesting that fixed pericytes did not take up Neurotrace 500/525.

The uptake process for the dye was not endocytosis, because pre-incubation of the live slices with the actin stabiliser jasplakinolide (1μM) for 30 min before application of Neurotrace 500/525 did not inhibit the labelling when compared to a DMSO vehicle control ($p=0.95$, Fig. 3.6C, D), implying that endocytosis, which depends on actin assembly (Smythe & Ayscough, 2006), was not involved in the dye transport into the cells.

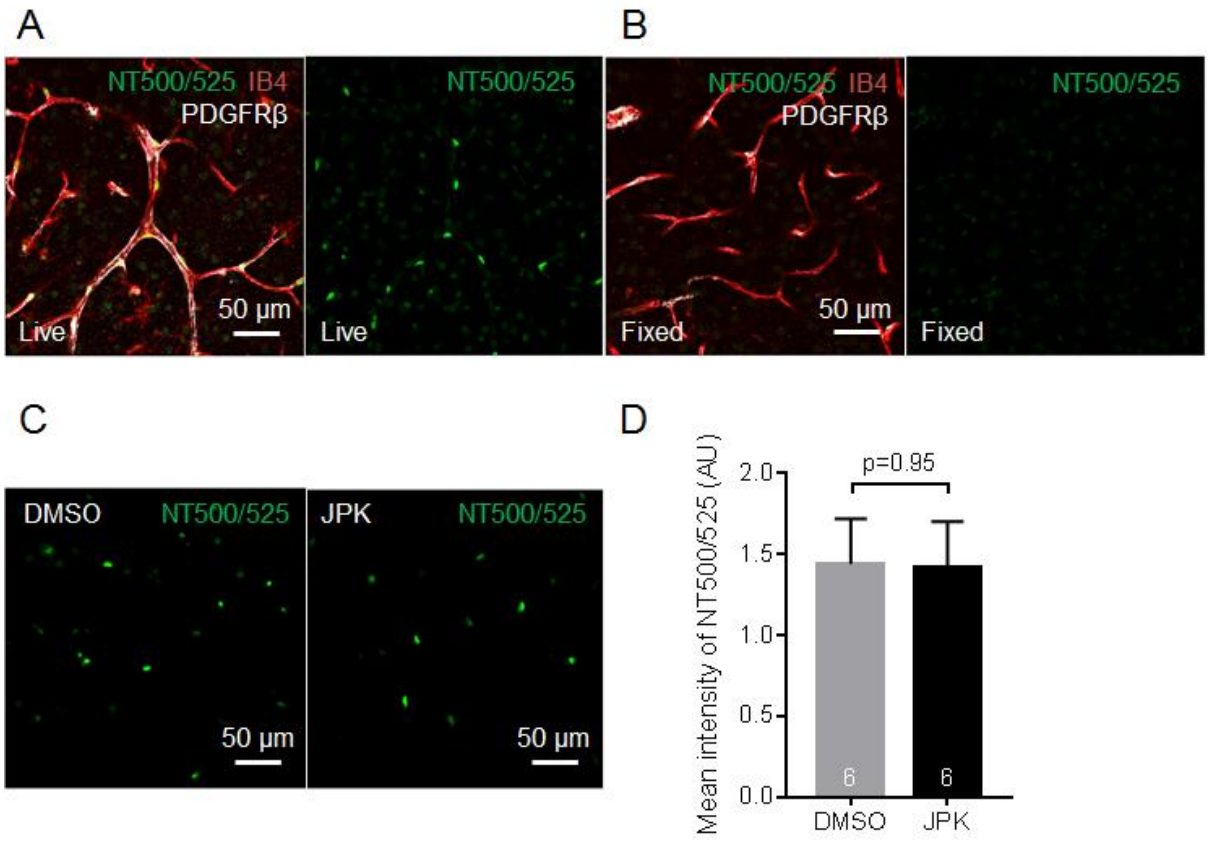

Figure 3.6: Neurotrace 500/525 was taken up into live pericyte via a non-endocytotic pathway. (A and B) Live (A) and fixed (B) rat cortical brain slices were incubated in Neurotrace 500/525 and labelled for basement membrane with isolectin B4 and for microvessels with PDGFRβ. This shows that Neurotrace 500/525 was taken up only in live but not fixed pericytes. (C) Neurotrace 500/525 signal in the absence and presence of the actin stabiliser jasplakinolide (1µM), applied 30 min before application of Neurotrace 500/525. (D) Mean intensity in (C), showing that preventing endocytosis did not stop the uptake of the dye. The numbers on the bars represent the number of stacks.

3.3.5 Capillary constriction occurs mainly near pericyte locations

To test whether the capillary constriction responses are homogenous across the capillary tree, or only occur focally near pericyte somata, where most circumferential processes appear to be located (Nortley *et al.*, 2019), I perfused a vasoconstrictor, the thromboxane A_2 analogue U46619 (200 nM), for 20 min while bright-field imaging, and measured capillary diameters at different distances from the pericyte somata. Because the pericyte soma density in the cortex of P21 rats was 2.2 ± 0.2 per 100 µm of capillary (Hall *et al.*, 2014), suggesting that one pericyte covers a capillary length of approximately 45.5 µm, or ~23 µm each side of the soma, I measured the diameter at distances up to 15 µm away from somata to be certain that the vascular responses were minimally influenced by other adjacent pericytes.

On application of U46619 to 9 capillaries with a pericyte on them, locations near the pericyte somata showed the greatest constriction (36.3 ± 7.5%), followed by at 5 µm (22.9 ± 7.2%, p=0.012 compared to at the soma), at 10 µm (16.1 ± 5.9%, p=0.0078 compared to at the soma) and at 15 µm (11.60 ± 6.06%, p=0.0078 compared to at the soma) distance from the soma (Fig. 3.7 A, B). Thus, capillary constriction is greatest near the pericyte soma, consistent with most of the circumferential processes of the pericyte being located near the soma (Nortley et al., 2019).

When vessel diameters were plotted against distance from the pericyte soma in the absence of U46619, there was a non-significant trend for the diameter to be larger near the soma (p=0.081 comparing the slope to zero). However, in the presence of U46619, there was a significantly smaller mean diameter near the soma (p=0.046, Fig. 3.7C).

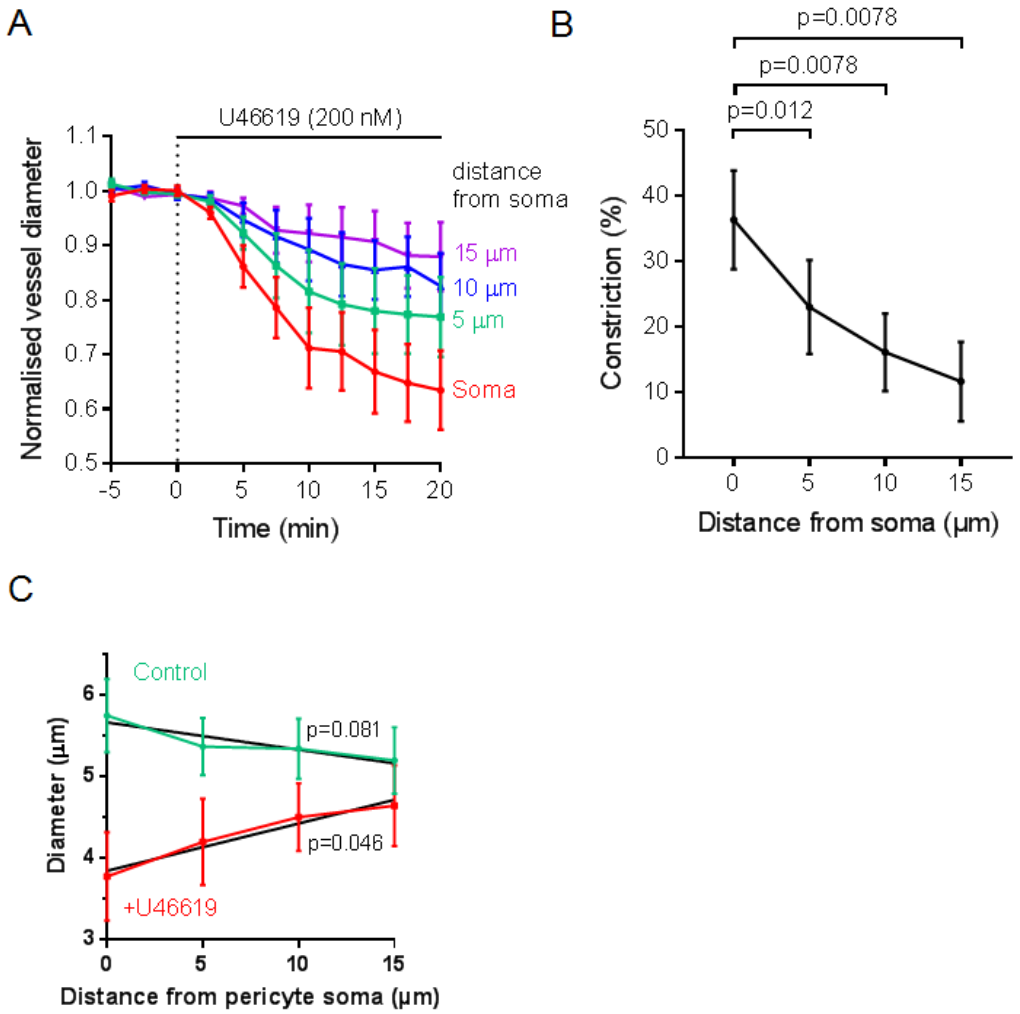

Figure 3.7: Pericyte contraction causes maximal capillary constriction at the pericyte soma.

(A) Time course of capillary diameter in the presence of the thromboxane A_2 analogue U46619 (200 nM) at the soma and 5-15 µm away from the soma (mean data from 9 rat pericytes), showing that the maximum constriction occurs near the soma. (B) Constriction in (A) averaged from t=18-20 min at different distances from soma, showing significantly more constriction at the pericyte soma when compared to other distances. (C) Mean capillary diameter plotted against distance from the pericyte soma before (control) and after 20 min application of U46619 (+U46619). Linear regression lines are superimposed and p-values comparing the slopes to a slope of zero are shown.

3.3.6 Low branch order capillary pericytes constrict in the presence of noradrenaline and dilate in the presence of adenosine

To test the contractility of proximal pericytes and check whether the preparation could be used to quantify changes in capillary diameter, I used live imaging of brain slices to identify pericytes on 1st-4th branch order capillaries, by tracing the vessels back to the penetrating arterioles. I then measured capillary diameter responses when applying vasoactive agents, including noradrenaline and adenosine. I either perfused aCSF with added noradrenaline (2 μM) for 10 min before applying adenosine (100 μM) in the presence of noradrenaline for 20 min, or only perfused aCSF with added noradrenaline for 30 min.

Noradrenaline (2 μM) caused a similar constriction of ~13.6% in both groups (in the group to which adenosine was subsequently applied: 13.7 ± 2.1%, n=9 and in no-adenosine group: 13.6 ± 1.9%, n=9, Fig. 3.8A), which were both significantly different from the normalised baseline (p=0.0039 for both groups). To compare the effect of adenosine, renormalisation to the mean capillary diameter after perfusing noradrenaline for 10 min was performed to enable further analysis. Application of adenosine (100 μM) on top of noradrenaline caused a vasodilation of 5.2 ± 4.0% (n=9) but in the absence of adenosine, noradrenaline alone caused a further vasoconstriction of 11.2 ± 4% (n=9, p=0.011, Fig. 3.8B, C). Thus, proximal capillary pericytes are contractile and constrict and dilate in response to noradrenaline and adenosine respectively.

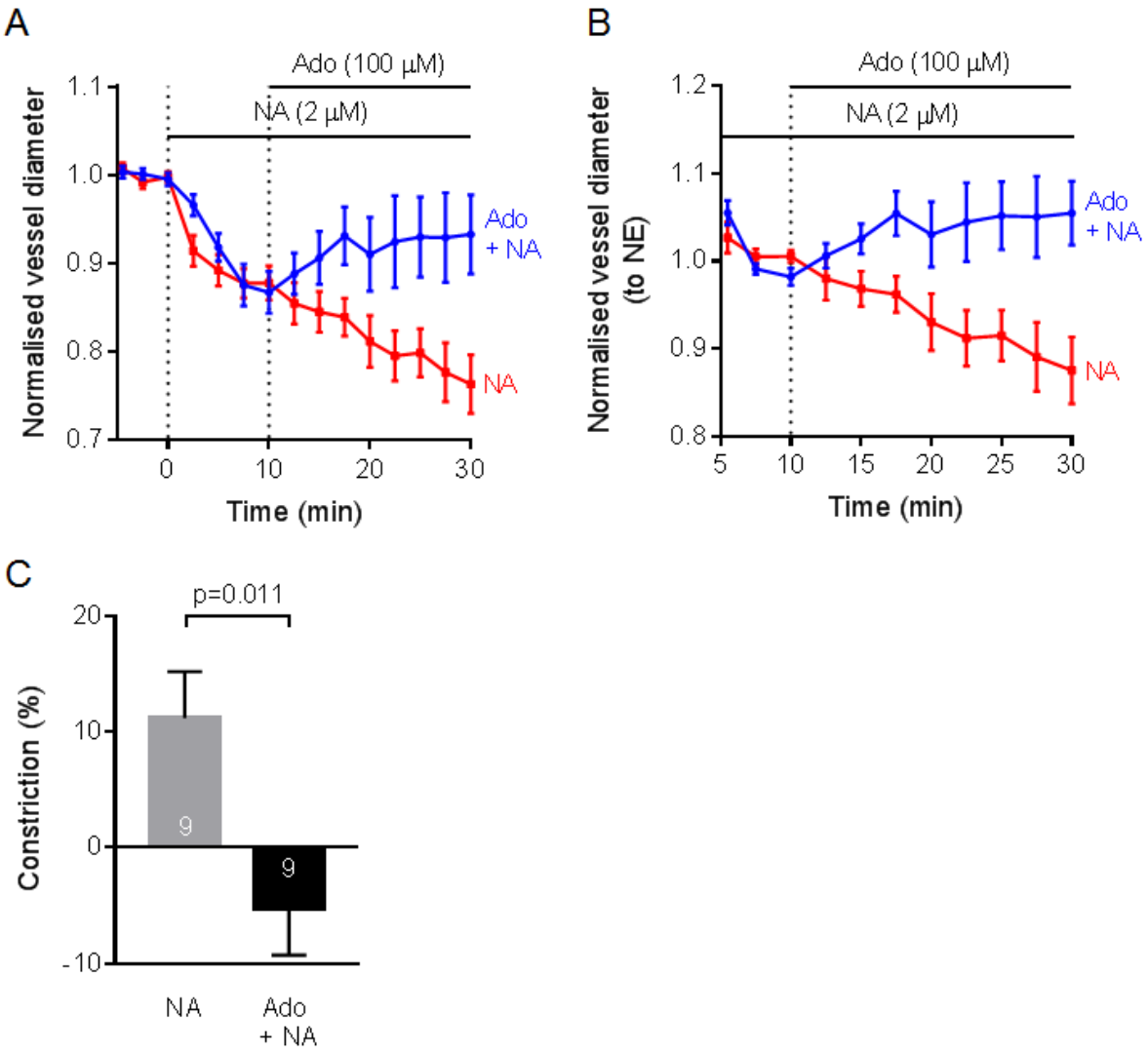

Figure 3.8: Proximal capillary pericytes respond to noradrenaline and adenosine.

(A) Time course of capillary diameter near proximal capillary pericytes (from 1st-4th capillary branch orders) after applying noradrenaline (NA, 2 µM) for 10 min and superimposing adenosine (Ado, 100 µM) for 20 min (blue trace), showing that vasoconstriction occurs in the presence of NA and vasodilation follows after application of Ado. The graph was normalised to the aCSF baseline. (B) Time course of capillary diameter normalised to the vascular diameter at t=8-10 min of NA to quantify the effect of Ado. (C) Constriction in (B) at t=18-20 min of adenosine, indicating that Ado causes significant dilation of capillaries.

3.3.7 Capillaries become passively dilated in the presence of RBCs

To investigate the elasticity of the capillary wall *in vivo*, which may be governed by mid-capillary pericytes (Rungta *et al.*, 2018), the first step was to assess whether the capillary wall deforms when RBCs pass through the vessel. If this were the case, then alterations of pericyte tone could alter blood flow by making it easier or more difficult for RBCs (or neutrophils) to pass.

As described in Sections 2.5.1 and 3.2.5, I employed high speed 2-photon imaging of capillaries *in vivo*, with Texas Red in the plasma, and with the endothelial cells labelled with eGFP in Pdgfb-iCreER x PC::G5-tdT mice. A time series of images in both the eGFP and TxRed channels was taken simultaneously at a frequency of 100 Hz for 1,000 frames (see Section 2.5.1.2). The eGFP channel was used to measure the external diameter of the capillary in each frame using Matlab and the TxRed channel was used to determine whether the frame was “RBC” (when there was a RBC in that frame, detected by a lack of TxRed signal in the lumen) or “no RBC” (lacking an RBC in the lumen: see Section 2.5.1.3). By measuring the diameter of the capillary as a function of time and correlating this with the moments when RBCs passed the measurement location (defined by a lack of TxRed signal in the plasma, i.e. for an “RBC” frame), I observed movement of the capillary wall as RBCs passed.

A total of 77 capillaries from 3 animals were imaged. After the images were processed by ImageJ Fiji and Matlab (see Section 2.5.1.3), the outer diameter of the capillary in each frame was measured from the eGFP images. The external diameters were then plotted in Microsoft Excel to exclude unstable vessels (see Section 2.5.1.3), leaving a total of 33 capillaries for further analyses. After classifying the frames into “RBC” and “no RBC”, I found that on average there were 393 “RBC” frames per 1000 frames taken of each vessel.

The external capillary diameters measured by Matlab were 4.890 ± 0.150 μm (n=33) for “RBC” frames and 4.878 ± 0.150 μm for “no RBC” frames (significantly different with $p<0.0001$, paired t-test, Fig. 3.9A). After normalisation to the diameters of the “no RBC” frames, the mean normalised external capillary diameter of the “RBC” frames (1.002 ± 0.0003) was significantly larger than that of the “no RBC” frames ($p<0.0001$, Wilcoxon signed rank test, Fig. 3.9B).

Mean eGFP intensity profiles for the “RBC” frames and the “no RBC” frames were created by combining and averaging all intensity profiles in each group. Each wall of the intensity profile for each group was fitted with a Gaussian distribution using Origin 2018 to calculate the centre and full width at half maximum of each wall. Then the internal capillary diameters of the representative intensity profiles of the “RBC” frames and “no RBC” frames could be calculated (see Section 2.5.1.3)

The internal capillary diameter of image frames when an RBC was present (“RBC” frames) was 3.256 ± 0.152 μm (n=33) which was significantly larger than that of frames lacking RBCs (“no RBC” frames) which was 3.238 ± 0.150 μm, ($p=0.011$, paired t-test, Fig. 3.9C). When the inner diameters of the “RBC” frames were normalised to those of “no RBC frames”, the mean normalised diameter of the “RBC” frames (1.005 ± 0.002) was significantly bigger than that of the “no RBC” frames ($p=0.048$, Wilcoxon signed rank test, n=33, Fig. 3.9D).

This suggests that passive capillary dilation occurs during RBC flow and proves that capillaries are elastic *in vivo*.

It might be argued that the difference in diameter observed with an RBC present or absent (~12-18 nm) is much less that the limit of resolution for optical microscopy. This is possible because I am not directly imaging two points that are just 12-18 nm apart. Instead, a function is being used to give a smoothed estimate of the position of

the edge of the lumen, and the position obtained in this way is defined with arbitrary accuracy (it is limited only by noise in the signal detected by the detector).

The smallest internal capillary diameter estimated was 1.9 µm. which is quite small compared to the normal RBC diameter of 4-7 µm in mice (O'Connell *et al.*, 2015), although there are a few examples showing that a capillary luminal diameter of about 2 µm can be found in mice *in vivo* (Shaw *et al.*, 2021) and in rats (Ivanov, Kalinina & Levkovich, 1981). Typically, the mean capillary luminal diameter of mouse cerebral microvessels is around 3.5-5 µm (Steinman *et al.*, 2017; Shaw *et al.*, 2021). These small calculated internal capillary diameters could be an underestimation of the true values. Quantification of very thin vessel walls is greatly affected by the noise in the signal, resulting in an overestimation of the thickness of the walls. Hence the capillary luminal diameters, estimated by subtracting vessel wall thicknesses from the external capillary diameters, might be an underestimation. However, this should equally affect the values from the RBC and non-RBC frames, and thus should not affect the comparison made between these two values.

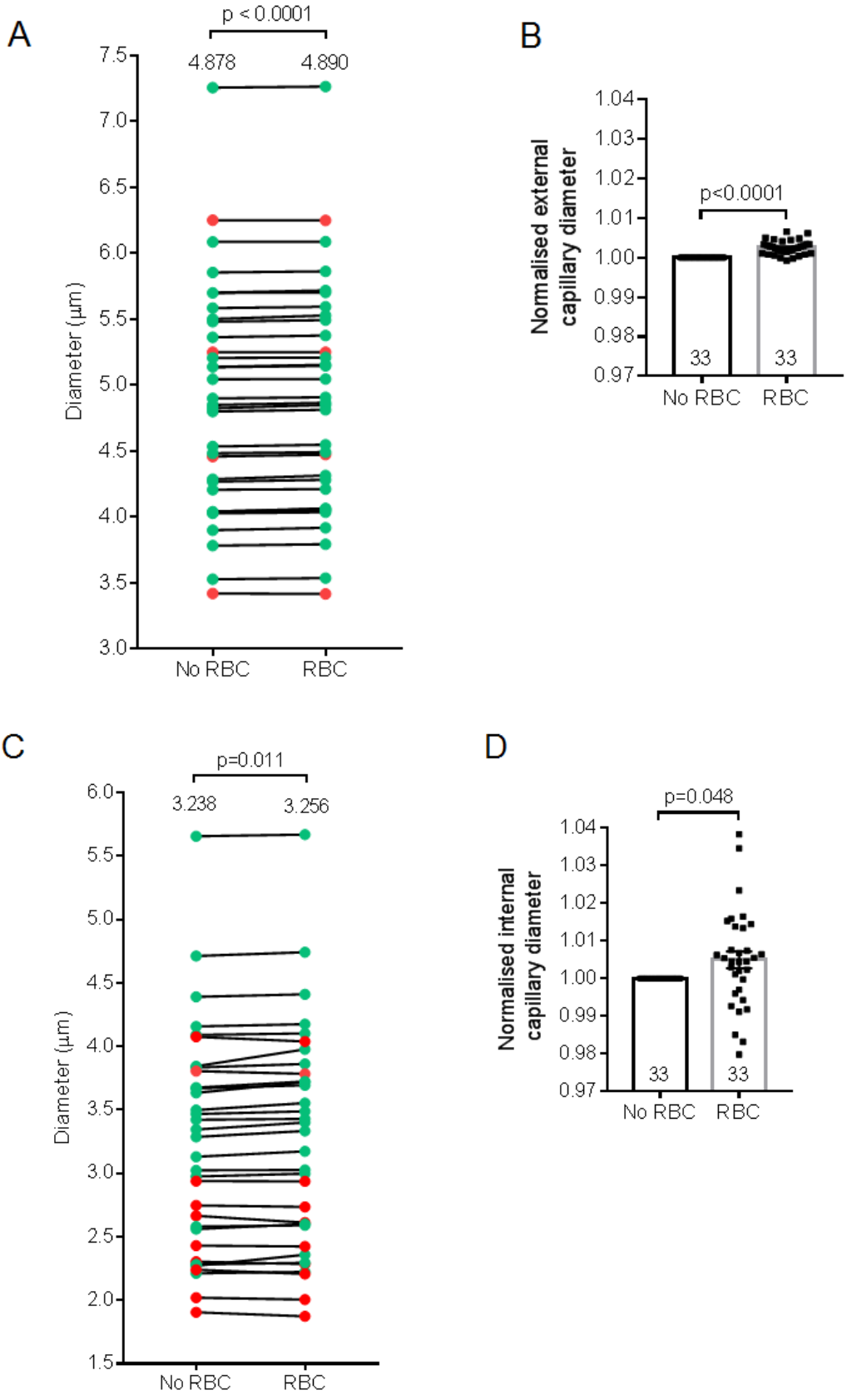
A
p < 0.0001
4.878
4.890
Diameter (µm)
No RBC
RBC
B
Normalised external capillary diameter
p<0.0001
33
33
No RBC
RBC
C
p=0.011
3.238
3.256
Diameter (µm)
No RBC
RBC
D
Normalised internal capillary diameter
p=0.048
33
33
No RBC
RBC

Figure 3.9: RBC presence causes dilation of capillaries.

(A) The outer diameter of each capillary (dot) in the “no RBC” frames and “RBC” frames is presented. The mean outer diameters of both “no RBC” and “RBC” frames are shown above the dots. The dots are coloured green when the “RBC” frame of that vessel has a larger diameter and are coloured red when the “RBC” frame has a smaller diameter than the “no RBC” frame.

(B) The outer diameter of “RBC” frames is plotted normalised to the outer diameter of the “no RBC” frames for each capillary, showing a significantly larger outer diameter in the “RBC” frames.

(C) The inner diameter of each capillary (dot) in the presence and absence of RBCs is illustrated, showing a significantly larger mean inner diameter in the “RBC” frame when compared to that in the “no RBC” frame. The mean values for both frames are shown above the dots. Green dots are used when the inner capillary diameter is larger in the “RBC” frame and the red dots are used when the inner diameter is larger in the “no RBC” frame.

(D) The inner diameter of “RBC” frames is plotted normalised to the mean inner diameter of the “no RBC” frames.

3.4 Discussion

The experiments in this chapter demonstrate five important points for studying pericyte contractility.

(i) Pericyte identification could be achieved accurately using solely morphology and anatomical position in bright-field imaging.

(ii) Pericyte recognition using Neurotrace 500/525 labelling does not identify all pericytes, especially the proximal capillary pericytes, implying that we need to be careful when interpreting experiments using Neurotrace 500/525 to study pericyte contractility.

(iii) Contrary to an earlier report, some pericytes labelled with Neurotrace 500/525 are contractile.

(iv) Capillary diameter changes should be measured near pericyte somata to detect the maximum effect of pericyte contractility, because pericytes contract capillaries the most near their somata.

(v) Capillaries are elastic and passively dilate in response to RBCs (and presumably neutrophils) flowing by, so modulation of capillary compliance by changes in the contractile tone of pericyte processes might provide a means to regulate cerebral blood flow, and this could occur even in mid-capillary bed pericytes that exhibit few circumferential processes.

Conflicting results from studies of pericyte contractility have occurred in part as a result of a drift in pericyte definition and studying different subtypes of pericytes (Attwell *et al.*, 2016), so validated detection methods for identifying the different subtypes are needed to address this problem. I have tested two methods for detecting pericytes.

(i) Using morphological identification of pericytes under a bright-field microscope. This method follows the original definition of pericytes as cells with a bump-on-a-log morphology located on the capillaries (Eberth, 1871; Rouget, 1873; Zimmermann & Zimmermann, 1923), which would cover all branch orders of pericyte. This definition is widely used by many other studies (Hall *et al.*, 2014; Khennouf *et al.*, 2018; Rungta *et al.*, 2018; Grant *et al.*, 2019). Under white light illumination, I demonstrated that it is possible to identify pericytes with high accuracy in brain slices so morphological identification appears to be a valid way to detect pericytes, but it does require great familiarity with the appearance of pericytes.

(ii) Using the fluoro-Nissl dye Neurotrace 500/525. Damisah *et al.* (2017) claimed that this dye is specific to pericytes which are not contractile and do not express αSMA, and they defined all αSMA positive cells to be smooth muscle cells. This definition does not follow the widely used definition (Attwell *et al.*, 2016), by which a subgroup of pericytes, especially on proximal capillaries, expresses αSMA (Alarcon-Martinez *et al.*, 2018; Grant *et al.*, 2019). Hence the properties of this dye need to be explored using the widely accepted definition of pericytes. By using immunohistochemistry, I have shown that some of pericytes labelled by Neurotrace 500/525 expressed contractile filaments such as αSMA and phosphorylated myosin light chain. Some Neurotrace 500/525 labelled pericytes also caused capillary constriction when a vasoconstrictor was applied *in vitro*. However, most of the Neurotrace 500/525 positive pericytes were located on higher branch order capillaries, which have previously been reported to express less αSMA and thus to be less contractile (Uemura *et al.*, 2020). These data suggest that Neurotrace 500/525 preferentially labels pericytes in the middle and at the venule end of the capillary bed. Because Neurotrace 500/525 does not label all pericytes and is not taken up by the majority of proximal capillary pericytes,

the use of Neurotrace 500/525 in studying pericyte contractility might be limited, and results from studies using this dye (Nelson *et al.*, 2020; Kovacs-Oller *et al.*, 2020) might underestimate pericyte-mediated changes of capillary diameter. Another important point in using Neurotrace 500/525, especially for immunohistochemistry, is that this dye is only taken up by live cells via a non-endocytic pathway and so it cannot be applied after fixation to stain pericytes. In addition I found that about 10% of Neurotrace positive cells were not pericytes, in contrast to only 1% from an *in vivo* study (Damisah *et al.*, 2017). This difference might arise from the *in vitro* application of Neurotrace 500/525, causing some unspecific binding to other cells when compared to the *in vivo* setting.

Another source of inconsistency in previous studies of pericyte contractility might be non-homogenous vascular responses produced by pericyte contraction. Pericytes caused the greatest capillary constriction near their somata. This is in accordance with observations from other studies (Mishra *et al.*, 2014; Cai *et al.*, 2018; Kureli *et al.*, 2020) and is supported by the fact that most of the circumferential pericyte processes, which cause luminal constriction (Dessalles, Babataheri & Barakat, 2021), are found near the pericyte somata (Nortley *et al.*, 2019). Thus, in order to get consistent results from studying pericyte contractility, it would be best to measure capillary responses near pericyte somata. The substantial and significant decrease of capillary constriction with distance away from the pericyte somata also strongly supports the idea that pericytes are the main regulator of capillary lumen diameter. In human tissue and in *in vivo* mice, a larger capillary diameter was found near pericyte somata in the absence of a vasoconstrictor (Nortley *et al.*, 2019), although my findings did not show a significant result for this, probably due to the lower number of pericytes studied.

Noradrenaline evoked capillary constriction near pericytes on low branch order capillaries, as seen in other studies (Peppiatt *et al.*, 2006; Hall *et al.*, 2014). Adenosine evoked capillary dilation of a magnitude similar to that previously reported for cardiac pericytes (O'Farrell *et al.*, 2017) and retinal pericytes (Li & Puro, 2001).

In the 1960s it was believed that capillaries were indistensible, because internal pressure increases appeared to produce no diameter increase. Subsequent work established that capillaries can be distended, but that the distension is small, and the resistance to distension might be provided by the capillary basement membrane and by pericytes (Smaje, Fraser & Clough, 1980; Lee *et al.*, 2010). Mid-capillary bed pericytes, which have few circumferential processes and little αSMA expression, have been generally assumed to not significantly regulate blood flow. Recently, however, optogenetic experiments by the Shih group (Hartmann *et al.*, 2021) have shown that depolarisation of these pericytes can decrease cerebral blood flow. My data on deformation of the capillary wall by the passage of RBCs suggest a mechanism that could underlie this effect. Even if pericytes only have processes that run along the capillary wall, when the tone in these processes is increased it will stiffen the capillary, making it less deformable, and thus less easy to pass RBCs (and white blood cells). By using this *in vivo* model, it is possible to use the difference in capillary diameters of "RBC" and "no RBC" frames as a proxy to assess the elasticity/stiffness of capillary walls. This method might be useful for studying the effect of mid-capillary pericyte contraction on vessel wall elasticity. For instance, with increased contractile tone of mid-capillary pericytes (evoked e.g. by optogenetic stimulation of a single pericyte or localised application of a vasoconstrictor), I predict that there will be a smaller diameter difference between "RBC" and "no RBC" frames, meaning that the vessel walls are less distensible. Indeed, the elasticity of capillaries that I have characterised could

affect the overall resistance of the vasculature by (i) increasing the capillary diameter to accommodate RBC flow as well as plasma flow by increasing the luminal diameter, and hence decreasing the resistance (Rungta *et al.*, 2018; Cheng *et al.*, 2018); and by (ii) increasing the cell-free layer thickness that keeps the RBCs and capillary wall apart (Lighthill, 1968; Maeda *et al.*, 1996). It could even be speculated that, when mid-capillary pericytes contract, the resulting decrease of capillary compliance, resulting in less passive dilation and a thinner lubricating film, may eventually cause RBC flow to "seize up" and stop the flow (Lighthill, 1968; Caro *et al.*, 2011). More experiments are needed to examine this point, but such stalling has been seen when neutrophils occlude capillaries (Reeson, Choi & Brown, 2018; Hernández *et al.*, 2019).

3.5 Suggestion for future work

In this chapter, I labelled cerebral pericytes with Neurotrace 500/525 (Damisah *et al.*, 2017) *ex vivo* to study the pericyte-labelling properties of this dye. Applying Neurotrace 500/525 *in vivo*, possibly in NG2-DsRedBAC transgenic mice that genetically express a red fluorescent protein in pericytes, and quantifying the number of pericytes in each capillary branch that are labelled might be performed to further characterise the dye for future usage in pericyte identification. Using an *in vivo* model will provide more accurate results because there is no tissue damage from the slicing procedure, which might interfere with the labelling, and vascular trees are intact, allowing continuous tracing of the vasculature and its branching pattern. Moreover, it would be possible to systematically quantify the contractility of Neurotrace 500/525-labelled pericytes and to assess the usefulness of this dye in *in vivo* settings, in which pericyte identification can be difficult without the use of transgenic mice. I have tried performing this experiment and found that topical application in an acute *in vivo* setting

(less than 3 h) did not yield satisfactory labelling, which might be caused in part by brain swelling after surgery. Thus, it might be preferable to image the animal one day after the surgery to introduce the dye, since it remains present for at least 48 h (Damisah *et al.*, 2017).

Further studies on the uptake mechanism of Neurotrace 500/525 might explain why only a subset of pericytes is labelled. The experiment could be done by investigating whether there is a maximum capacity for dye uptake, suggesting an involvement of integral membrane proteins (Berne, Levy & Koeppen, 2008), and exploring the effect of temperature on the labelling. The dependence on temperature of the uptake would suggest an involvement of protein conformational changes found in active transport (Berne, Levy & Koeppen, 2008).

I established a model in which capillary elasticity can be observed using changes in capillary diameters in the presence and absence of RBCs within the capillary lumen (see Section 3.3.7). This model might be useful for investigating the effect of mid-capillary pericytes on cerebral blood flow (CBF). My hypothesis is that the contraction of these cells decreases capillary elasticity, resulting in an increased resistance to flow (Maeda *et al.*, 1996; Lee *et al.*, 2010). Further optimisation of the imaging settings is required to allow a faster scanning speed and allow measurement of the RBC velocity and size of the cell-free layer. An interesting alternative approach for achieving a faster scanning speed is to do line scans. The key experiment needed to test my hypothesis is activating mid-capillary pericytes, ideally through optogenetics that allows the targeting of only one pericyte of interest, and observing changes in capillary elasticity, thickness of cell-free layer and RBC velocity.

3.6 Conclusion

As pericytes emerge as a potential therapeutic target in many diseases, correct methodology for studying pericyte contractility is needed to get consistent results across studies. My data provide a rough framework for studying pericyte contractility, emphasising the use of appropriate methods for pericyte identification and measurement of capillary diameter responses. In addition, my data also show that capillaries are distensible, implying that control of capillary elasticity by mid-capillary pericytes might modify cerebral blood flow.

Chapter 4: Alzheimer's disease and pericyte contractility

4.1 Introduction

Alzheimer's disease (AD) is a neurological disease characterised by progressive memory and cognitive function loss, with pathological hallmarks of extracellular amyloid plaques and neurofibrillary tangles (Alzheimer, 1906; Braak & Braak, 1991). Aside from amyloid deposition and hyperphosphorylated tau protein aggregation, another striking feature in AD patients is cerebral vascular dysfunction and reduced cerebral blood flow, as reported in many studies (Ruitenberg *et al.*, 2005; Asllani *et al.*, 2008; Schuff *et al.*, 2009; Iturria-Medina *et al.*, 2016; Yew & Nation, 2017). This vascular impairment occurs in the early stage of AD (Ruitenberg *et al.*, 2005; Iturria-Medina *et al.*, 2016) and may contribute to dementia rather than being just a consequence of neuronal dysfunction and brain atrophy (de la Torre & Mussivan, 1993; de la Torre, 2002; Iturria-Medina *et al.*, 2016; Yew & Nation, 2017; Govindpani *et al.*, 2019). Focal constrictions of capillaries (without involvement of large arteries), which resemble pericyte-induced constrictions have been found in the brain of AD patients (Hashimura, Kimura & Miyakawa, 1991; Kimura, Hashimura & Miyakawa, 1991). This suggests an involvement of pericytes, the contractile cells on capillaries (Attwell *et al.*, 2016). Pericyte involvement could theoretically have a large effect on cerebral blood flow, because capillaries provide more resistance than penetrating arterioles or venules to the intracerebral circulation (Boas *et al.*, 2008; Hall *et al.*, 2014; Gould *et al.*, 2017; Peyrounette *et al.*, 2018; Rungta *et al.*, 2018).

Several mechanisms for how Aβ affects blood vessels in AD have been proposed and one promising mechanism is through vascular oxidative stress (Thomas *et al.*, 1996; Nicolakakis *et al.*, 2008). Many studies support the idea that vascular oxidative stress, which causes contraction of smooth muscle cells (Touyz *et al.*, 2018;

Zeisel *et al.*, 2018), is increased in AD. A high level of amyloid deposition has been found together with overexpression of oxidative stress markers and mitochondrial damage in the walls of microvessels from both AD mice and patients (Aliev *et al.*, 2002; Aliyev *et al.*, 2005). Applying Aβ peptides to blood vessels leads to superoxide production, vasoconstriction and endothelial damage (Thomas *et al.*, 1996; Niwa *et al.*, 2001; Park *et al.*, 2017). The level of aconitase, an enzyme sensitive to oxidative stress, is decreased in the blood vessels of AD mice (Carvalho *et al.*, 2013), and antioxidants such as luteolin (Liu *et al.*, 2009) or a combination of N-acetyl cysteine, tempol and pioglitazone (Nicolakakis *et al.*, 2008) or overexpression of superoxide dismutase (SOD) (Massaad *et al.*, 2010) can rescue cerebrovascular function in AD mice. However, the effects of Aβ and oxidative stress on pericytes are largely unexplored.

The origin of reactive oxygen species (ROS) generated in AD, which might be a valuable therapeutic target, is still under debate. NADPH oxidase (NOX) is involved in the pathogenesis of AD (Infanger, Sharma & Davisson, 2006; Sorce & Krause, 2009; Hernandes & Britto, 2012; Carvalho & Moreira, 2018), especially the subtypes NOX2 and NOX4, which are found at high levels in AD-susceptible areas in the brain such as the hippocampus (Austin *et al.*, 2015). NOX2 is activated in AD human brains (Shimohama *et al.*, 2000) at the earliest stages of dementia (Bruce-Keller *et al.*, 2010) and $A\beta_{1\text{-}42}$ can stimulate NOX2 in microglia (Bianca *et al.*, 1999; Carrano *et al.*, 2011) and perivascular macrophages, probably via binding of Aβ to scavenger receptor CD36 (Park *et al.*, 2011), leading to cerebrovascular oxidative stress (Park *et al.*, 2017). On the other hand, NOX4, normally expressed at a high level in vascular smooth muscle cells, endothelial cells and pericytes (Chen *et al.*, 2012), is also increased in level in an age-dependent fashion in a manner that correlates linearly

with cognitive impairment in AD mice (Bruce-Keller *et al.*, 2011). ROS are also produced by mitochondria in AD (Zhu *et al.*, 2004; Massaad *et al.*, 2010). Aβ-induced neurovascular dysfunction may be associated with oxidative damage of DNA in endothelial cells, leading to activation of poly (ADP)-ribose polymerase (a DNA repair enzyme), which increases the level of ADP ribose (Park *et al.*, 2014). As a consequence, transient receptor potential melastatin-2 (TRPM2) channels open to increase endothelial intracellular calcium concentration, leading to endothelial dysfunction (Park *et al.*, 2014). Finally, reactive nitrogen species (RNS), which can constrict pericytes (Yemisci *et al.*, 2009), are also increased in concentration in AD, and can be detected as several nitration products including 3-nitrotyrosine (Smith *et al.*, 1997; Butterfield *et al.*, 2007) and 5-nitro-γ-tocopherol (Williamson *et al.*, 2002) in AD patients.

Another pathway of Aβ-induced vasoconstriction is through endothelin (ET) production (Palmer & Love, 2011). The ET-1 level is increased in AD patients when compared to healthy controls (Minami *et al.*, 1995; Palmer *et al.*, 2012; Palmer, Tayler & Love, 2013), probably via upregulation of ECE-1 in endothelial cells (Palmer, Tayler & Love, 2013) and of ECE-2 in neurons (Miners, Palmer & Love, 2016) (see Section 1.6.2). Interaction between Aβ and RAGE has also been shown to increase mRNA for prepro-ET-1 in mouse brain endothelium (Deane *et al.*, 2003). Moreover, ROS induced by Aβ such as hydroxyl radicals can also enhance ET-1 release from endothelial cells, thus promoting endothelin-induced vasoconstriction in AD (Prasad, 1991). The role of ROS-induced ET production is also supported by the fact that SOD, an enzyme breaking down superoxide, can stop Aβ-induced ET-1 release from cultured human brain endothelial cells (Palmer, Tayler & Love, 2013).

Other mechanisms underlying Aβ-induced CBF deficits include reduced degradation of Aβ-containing fibrin clots, which leads to blood vessel occlusion and inflammation (Strickland, 2018). A direct action of $A\beta_{1-40}$ on vascular smooth muscle cells to cause vasoconstriction has also been proposed (Palmer & Love, 2011). In addition, a loss in AD of the cholinergic innervation that normally causes vasodilation may also contribute to the CBF deficit (Farkas & Luiten, 2001). Overexpression of contractile proteins and arterial hypercontractility in AD, resulting from upregulation of transcription factors related to vascular smooth muscle cell differentiation, serum response factor (SRF) and myocardin (MYOCD), can also lead to reduced CBF (Chow *et al.*, 2007; Kisler *et al.*, 2017a).

Most previous studies have focussed on vSMCs on arteries and arterioles but the effect of Aβ on pericytes has not yet been studied despite the fact that pericytes may be major regulators of intracerebral blood flow (Gould *et al.*, 2017).

The objective of this chapter was to investigate the effect of Aβ, especially $A\beta_{1-42}$ oligomers, on the contractility of pericytes and the pathophysiology underlying this process, focusing mainly on oxidative stress and its consequences.

4.2 Methods

4.2.1 Solutions and drugs

Bicarbonate-buffered aCSF was prepared as described in Section 2.1.1, with or without drugs, for superfusing rodent cortical slices in live imaging experiments.

Aβ was prepared and quantified by using a BCA protein assay as described in Section 2.1.3. Peptide concentrations measured were corrected by a factor of 1.51 (see Section 2.1.3) and the Aβ concentrations stated in the following sections have

been corrected in this way. Aβ oligomers were quantified with SDS-PAGE (see Section 2.1.3) to estimate the degree of aggregation of the Aβ isoforms.

4.2.2 Transgenic mice expressing fluorescent constructs

NG2-DsRedBAC x $APP^{NL\text{-}G\text{-}F/NL\text{-}G\text{-}F}$ mice (see Section 2.2.3), in which APP with a humanised Aβ region with AD-related mutations is knocked in and the pericytes are fluorescently labelled by a red fluorescent protein DsRed, were used for *in vivo* surgery to study pericyte contraction in AD. These mice show Aβ deposition starting at 2 months of age.

4.2.3 Bright-field imaging

All experiments in this chapter used cortical tissue from P19 – P22 Sprague-Dawley rats of both sexes. The constriction evoked by Aβ showed an overlapping ranges of value for 5 male vessels and 2 female vessels (data from a larger number of vessels are presented in Nortley *et al.* (2019)). Brain extraction and preparation of 300-µm-thick live slices were performed as described in Section 2.3.1.1. As described in Section 2.3.2, live rat cortical slices (when used without pre-incubation of drugs) were perfused with 33-36ºC bicarbonate-buffered aCSF oxygenated with 20% O_2, 5% CO_2, and 75% N_2 and imaged under a bright-field microscope. Brain slices were perfused with only aCSF for 5 minutes to establish the baseline capillary diameter before application of drugs. For experiments with pharmacologic inhibitors for investigation of signalling pathways of Aβ, the blockers were perfused for 15 minutes before applying Aβ to allow the effect of inhibitors to stabilise. Each drug was also tested on its own without Aβ for the same duration to establish the effect of the drug alone on the capillary diameter. Vessels less than 10 µm in diameter without rings of smooth muscle were selected as capillaries, and one region per vessel with a candidate pericyte was imaged. Images were taken every 30 s by a CCD camera and

the vessel diameters were analysed with Metamorph software (see Section 2.3.3). The effect of changes in capillary diameter on cerebral blood flow was calculated as previously described (see Section 2.3.4).

4.2.4 *In vivo* AD mouse experiments

Surgery for AD and WT mice to quantify capillary diameters *in vivo* was performed by my colleague, Nils Korte, and the analyses were performed blinded by Nils Korte and me. The overall contribution for these *in vivo* experiments was 75% and 25% for Dr. Nils Korte and me, respectively.

The surgical procedure was described in detail in Section 2.5.2.1. In brief, NG2-DsRedBAC x $APP^{NL\text{-}G\text{-}F/NL\text{-}G\text{-}F}$ mice at P119 – P143 (i.e. roughly 4 months) were anaesthetised with urethane and underwent a craniotomy over the primary somatosensory cortex or right cerebellar hemisphere, before being transferred to a two-photon microscope to be imaged. The animal was injected with albumin-fluorescein isothiocyanate conjugate (FITC-albumin) retro-orbitally to label the plasma. Signals of FITC-albumin from the capillary lumen and DsRed from vascular smooth muscle cells and pericytes were collected by taking image stacks in 2 µm steps across cortical layers I to IV (see Section 2.5.2.2).

The image stacks were analysed with ImageJ Fiji by drawing a line across the whole width of the FITC-albumin dye fluorescence (perpendicular to the vessel axis). Measurement of vessel diameter was performed manually or automatically by fitting a Gaussian function to determine the full width at a quarter maximum of the peak fluorescence intensity (see Section 2.5.2.3).

4.2.5 Statistical analysis

Statistical analysis was performed as described in Section 2.7. For pharmacological inhibition experiments, normalisation to the last 10 images of the

condition with inhibitors alone was performed to quantify the effect of the second drug applied or of Aβ.

4.3 Results

4.3.1 Oligomeric Aβ evokes pericyte contraction in rat cortical capillaries

It was shown previously by my colleague, Dr. Ross Nortley, that $A\beta_{1-42}$ and $A\beta_{1-40}$, evoke a slow capillary constriction of ~25% after 40 min of application in human cortical brain slices and of ~16% in rat brain slices after 1 h (Nortley *et al.*, 2019). As the first experiment in this chapter, I tried to reproduce these results to verify that my Aβ preparation method worked, as well as to see whether I could get a similar constriction, which would be important for later pharmacological experiments that I wished to carry out to study reactive oxygen species pathways involved in Aβ-induced vasoconstriction.

Oligomerised Aβ was prepared (see Section 2.1.3) and the degree of Aβ isoform aggregation was confirmed by silver staining of an SDS-PAGE gel. This confirmation of Aβ oligomeric preparation was performed with my colleague, Dr. Pablo Izquierdo. When $A\beta_{1-42}$ was dissolved and incubated at 4°C for 24 h, the main oligomers formed had a molecular weight between 15 – 18 kDa while monomers have a molecular weight of ~5 kDa (Fig. 4.1A), suggesting that the oligomers formed according to this protocol were mostly Aβ trimers and tetramers. Using densitometry, I estimated from Fig. 4.1A that the percentages of monomers (molecular weight (MW) 2.5 to 6.5 kDa), dimers (MW 6.5 – 11.5 kDa), trimers (MW 11.5 – 15.5 kDa) and tetramers (MW 15.5 – 20.5 kDa) were 13.4%, 14.7%, 20.4% and 51.5% respectively.

In rat cerebral cortical slices, both $A\beta_{1-42}$ (monomers and oligomers, 72 nM when calculated using the monomer molecular weight) and $A\beta_{1-40}$ (72 nM) caused

significant vasoconstriction near potential pericyte locations of 18.9 ± 2.2% (n=7, $p=4.7x10^{-5}$ compared to aCSF) and 13.2 ± 5.6% (n=5, p=0.024 compared to aCSF) respectively after 1 h (Fig. 4.1B, C). The difference of response between $A\beta_{1-42}$ and $A\beta_{1-40}$ was not significant (p=0.32). Note that, after 1 h, the aCSF control caused an insignificant diameter increase of 6.2 ± 2.2% (n=5, p=0.063 compared to baseline).

By using a Poiseuille's law analysis described in Chapter 2 (see Section 2.3.4), I estimated that the ratio of the capillary radius at the pericyte soma (r_2) to the radius at capillary positions between pericytes (r_1 where no change of diameter is assumed to occur) to be (r_2/r_1) ~ 0.892, 0.955 and 1.17 with application of $A\beta_{1-42}$, $A\beta_{1-40}$ and aCSF for 1 h (see eqn.2 in Section 2.3.4) and the ratio of the resistance from the constriction ($R_{contracted}$) to the resistance for a uniform radius of r_1 (R_1) will be ($R_{contracted}/R_1$) ~ 1.262, 1.098 and 0.739 accordingly (see eqn.1 Section 2.3.4). Comparing experiments with $A\beta_{1-42}$ to aCSF control, the ratio of resistance in the experimental group compared to that in the control group ($Rcontracted/(Rrelaxed)$) will be 1.71 and the decrease of blood flow evoked by $A\beta_{1-42}$ due to capillary constriction will be 28.8% (see eqn. 3 in Section 2.3.4) (assuming that only pericytes and not arterioles or venules are affected). For $A\beta_{1-40}$, the ($Rcontracted/(Rrelaxed)$) will be 1.49 and the decrease of blood flow will be 21.7% when taking into account only pericyte contraction.

Overall, this preliminary experiment showed that my Aβ preparation leads to oligomerisation of Aβ peptide mostly into trimers and tetramers. Furthermore, both $A\beta_{1-42}$ and $A\beta_{1-40}$ cause capillary constriction at pericyte somata with a magnitude comparable to what has been previously shown by others.

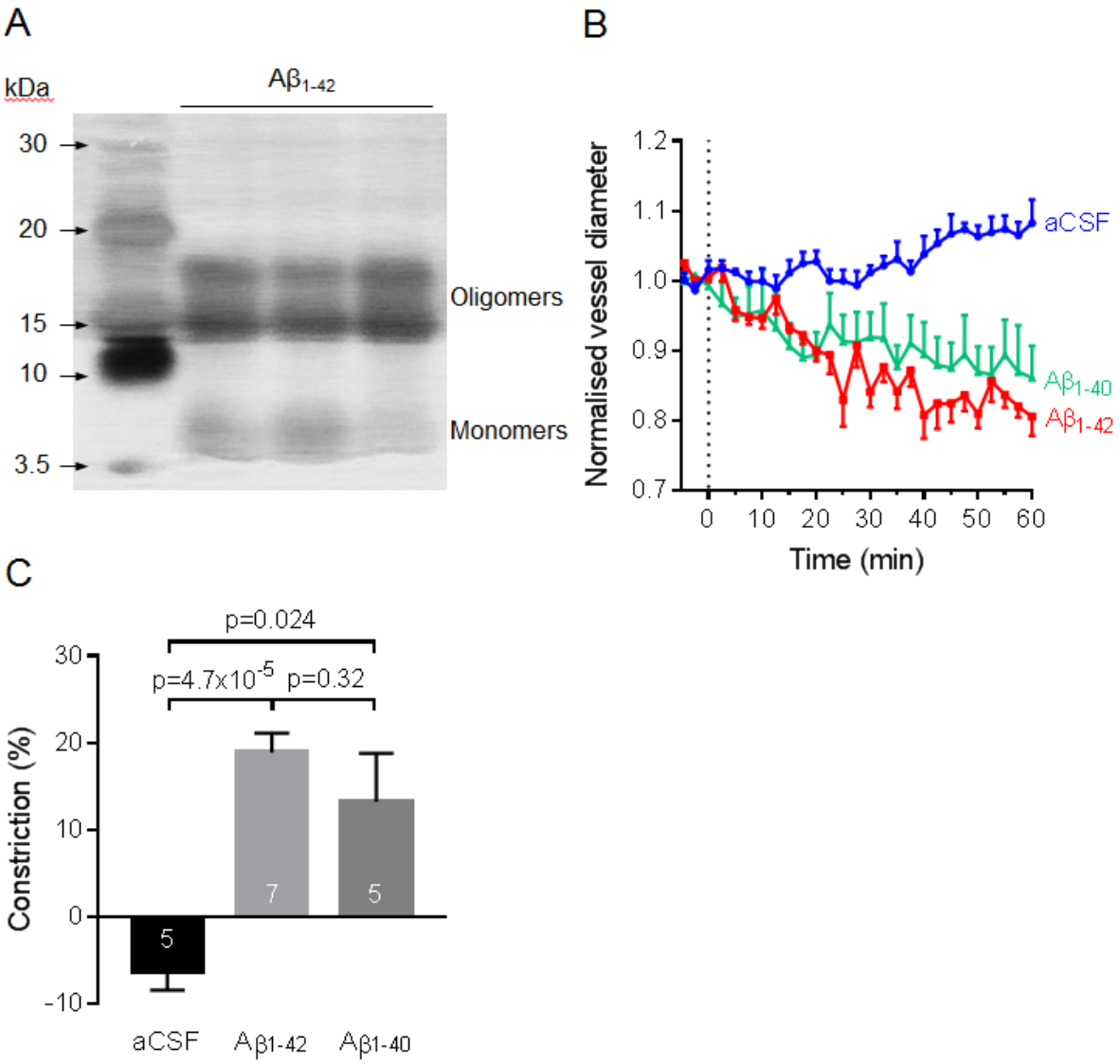

Figure 4.1: Oligomerisation of Aβ and Aβ-evoked capillary constriction.

(A) SDS-PAGE gel with silver staining for solutions with $A\beta_{1-42}$, showing monomers and low molecular weight oligomers weighing between 15 – 18 kDa.

(B) Capillary constriction at pericyte locations in response to 1 h of oligomeric $A\beta_{1-42}$ (72 nM, n=7) and oligomeric $A\beta_{1-40}$ (72 nM, n=5) compared to 1 h of aCSF alone. Dotted line indicates the time when application of Aβ started.

(C) Constriction in (B) at t=58-60 min, showing significant capillary constriction in the presence for 1 h of $A\beta_{1-42}$ (72 nM, n=7) and $A\beta_{1-40}$ (72 nM, n=5).

4.3.2 Pericyte contraction in *in vivo* AD mice

To confirm whether the pericyte contraction evoked by Aβ in rat brain slices occurs *in vivo* in a mouse model of Alzheimer's disease, craniotomies on AD and wild-type mice were performed to visualise brain capillaries. The regions of interest were (i) the cerebral cortex, where Aβ level rises and Aβ plaques can be found; and (ii) the cerebellar cortex, which is normally spared from Aβ plaques, implying a lower level of Aβ. Vessel diameters as a function of distance along the capillary from pericyte somata were quantified by Dr. Nils Korte and me. Because pericytes maximally constrict vessels at pericyte somata, where most of their circumferential processes are located (see Figure 3.6), we would expect the vessel diameters at the somata to be the smallest and those away from the somata to be larger, if pericytes contract.

In cerebral cortex, there was a significant constriction at pericyte somata in the AD mice (n=4 animals) relative to the vessel diameter away from the soma ($p=3.2\times10^{-10}$) while a dilation was seen near the soma in wild-type animals (n=3 animals, $p=9.9\times10^{-8}$, Fig. 4.2). The absolute capillary diameter at pericyte somata was also smaller in the AD mice compared to those in wild-type mice. On the other hand, in the cerebellar cortex of both wild-type and AD mice (n=3 animals each) capillaries had a significantly larger vessel diameter near pericyte somata compared with that midway between somata (p=0.002, Fig. 4.2).

Thus, pericyte-mediated capillary constriction also occurs in the cerebral cortex of *in vivo* AD mice, but not in the cerebellar cortex, presumably because this capillary constriction is evoked by Aβ, the concentration of which is higher in the neocortex than in the cerebellum. For the spatial profiles shown for cortex in Fig. 4.2, the APP mice had a capillary radius at capillary positions between pericytes, r_1, of 4.44 μm and a radius at the pericyte soma, r_2, of 3.79 μm, while WT mice had r_1 ~ 4.56 μm and r_2~

5.03 µm. Inserting these values into the eqns. 1 in Section 2.3.4 gives the values of the factor by which the resistance is changed of $R_{contracted}/ R_1$ = 1.39 in APP mice and of $R_{relaxed}/ R_1 = 0.82$ in WT mice. Hence, the cerebral blood flow difference between APP mice and WT mice is 27.9% (from $R_{contracted}/R_{relaxed}$ using eqn. 3 of Section 2.3.4).

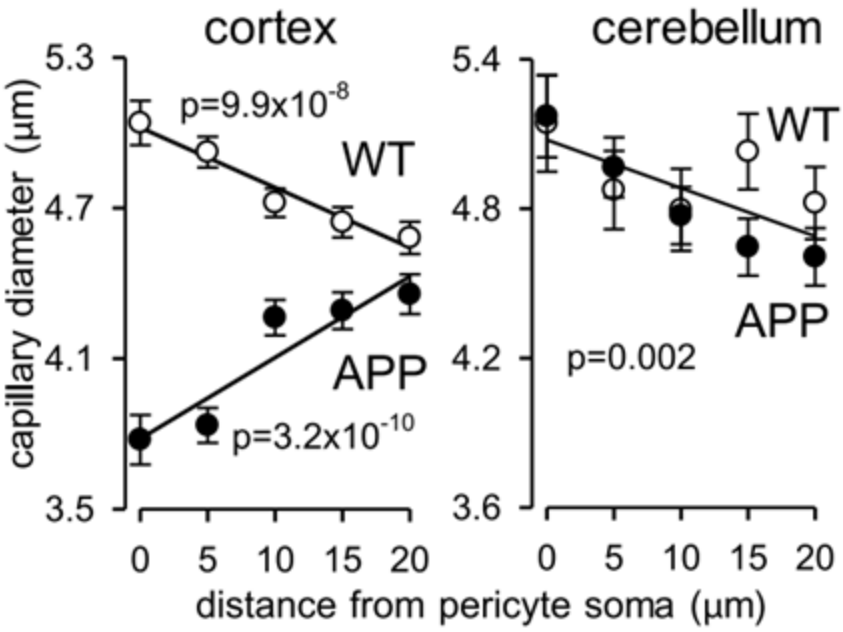

Figure 4.2: Pericytes contract in the cerebral cortex, which has amyloid plaques, but not in the cerebellum, which lacks Aβ plaques in AD mice. This experiment was performed in collaboration with my colleague, Dr. Nils Korte. Graphs plotting capillary diameter against distance from pericyte somata show (left) a smaller vessel diameter at the pericyte soma in the cerebral cortex of AD mice (n=4) and a larger diameter at the soma in the cerebral cortex of WT mice (n=3), whereas (right) no constriction at pericyte somata was detected in the cerebellar cortex of both AD (n=3) and WT mice (n=3). Linear regression lines are drawn for all data sets and p-values comparing the slopes to a zero slope are shown. Compare with Fig. 3.7C showing the U46619-evoked constriction in capillaries in brain slices.

4.3.3 $A\beta_{1-42}$ causes capillary vasoconstriction via ROS and endothelin signalling to pericytes

In this sub-section, preliminary results obtained by my colleague, Dr. Ross Nortley, are described here because they provided the basis for my work on the effects of how ROS and endothelin-1 generate the Aβ-evoked vasoconstriction.

The $A\beta_{1-42}$ (57 nM) induced pericyte constriction was completely blocked by perfusing superoxide dismutase 1 (SOD1, 150 units/ml, n=19, $p=3.7x10^{-6}$, Fig. 4.3A), which is a superoxide scavenging enzyme and also prevents formation of hydroxyl radicals through the Fenton reaction (Gutteridge, 1985a; Gutteridge, Maidt & Poyer, 1990; Wang *et al.*, 2018). SOD1 can also indirectly inhibit formation of hydroxyl radical via prevention of lipid peroxidation, which is normally caused by hydroperoxyl radical and hydroxyl radical (McCord, 2008; Ayala, Muñoz & Argüelles, 2014). The $A\beta_{1-42}$-evoked constriction was also prevented by application of the endothelin-1 type A receptor (ET_A) inhibitor BQ-123 (1 μM, n=14, p=0.008, Fig. 4.3A). No vascular changes were observed after applying only BQ-123 (1 μM, -0.7 ± 5.2%, n=13, p=0.9) or SOD1 (150 units/ml, 3.4 ± 5.8%, n=9, p=0.57) alone. This suggests that $A\beta_{1-42}$ evokes vasoconstriction through ROS, in particular through superoxide or hydroxyl radicals or a downstream derivative, and endothelin-1.

Supporting this, endothelin-1 (5 nM, n=12) alone evoked a strong vasoconstriction after 15 min that was not inhibited by application of SOD1 (150 units/ml, n=8, $p=1.3x10^{-8}$, Fig. 4.3B), suggesting that endothelin acts downstream of ROS. On the other hand, applying H_2O_2 (1 mM) to generate ROS evoked a significant capillary constriction after 20 min (n=9, $p=1.1x10^{-5}$), which was partially inhibited in the presence of BQ-123 (1 μM, n=11, p=0.009, Fig. 4.3C), implying that H_2O_2 acts to constrict capillaries partially via ET_A activation. Because H_2O_2 evoked constriction

while SOD1 (which generates H_2O_2) blocked the Aβ-evoked constriction, SOD1 may mainly be acting downstream of H_2O_2, for example, by blocking hydroxyl radical formation, to prevent the Aβ-evoked constriction. These experiments suggest that $Aβ_{1-42}$ constricts capillaries via generation of ROS, which cause pericyte contraction, in part, by elevating the endothelin-1 level to activate ET_A receptors.

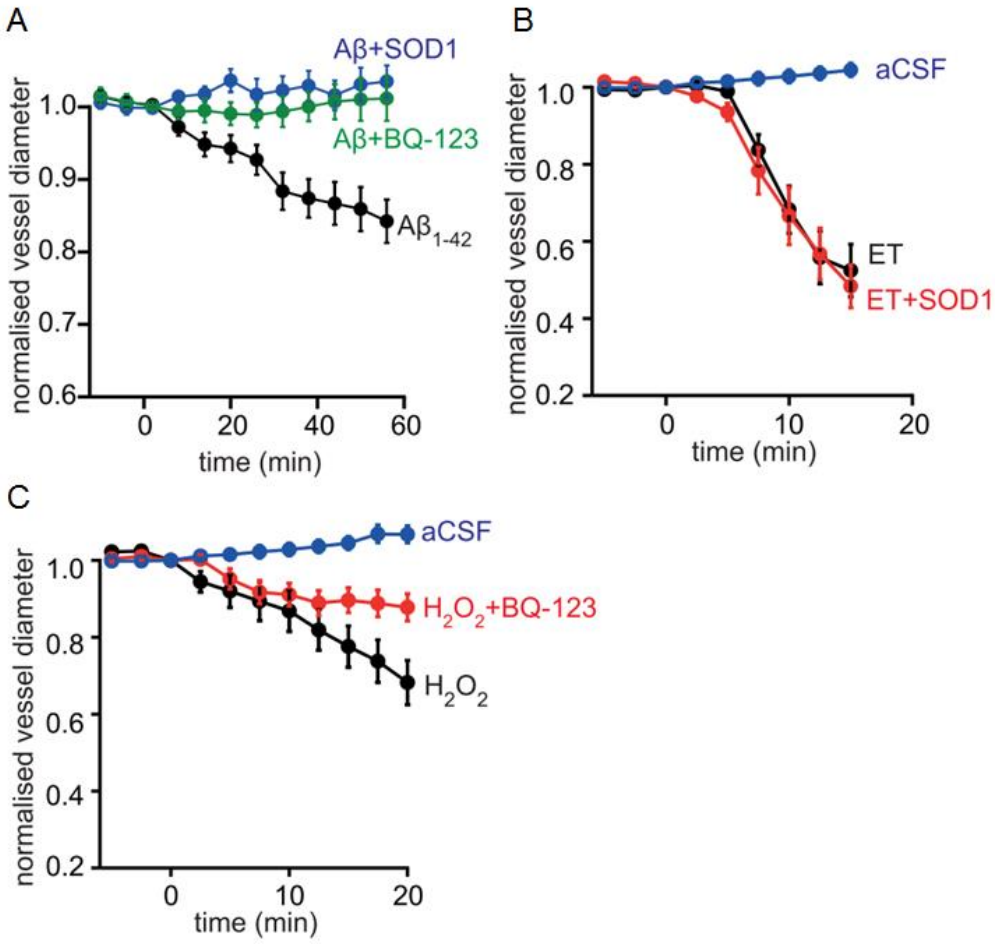

Figure 4.3: $A\beta_{1-42}$ oligomers evoke capillary constriction through reactive oxygen species (ROS) and the endothelin type A receptors, with ROS acting upstream of endothelin signalling. Experiments in this figure were done by Dr. Ross Nortley, and are included as a basis for understanding my subsequent work on this topic. (A) The time course of vessel diameter after application of $A\beta_{1-42}$ alone (57 nM, n=19) or in the presence of SOD1 (150 units/ml, n=19) or the ET_A inhibitor BQ-123 (1 μM, n=14). (B) The time course of vessel diameter after application of aCSF alone, endothelin-1 (ET) alone (5 nM, n=12) or ET with SOD (150 units/ml, n=8). (C) The time course of vessel diameter after application of aCSF alone, the ROS generator H_2O_2 alone (1mM, n=9) or H_2O_2 with the ET_A inhibitor BQ-123 (1 μM, n=11). Inhibitors alone were given 5 to 15 min before superfusing $A\beta_{1-42}$.

4.3.4 ROS mediating Aβ-evoked pericyte contraction are mainly generated by NOX4

To test for the involvement of NADPH oxidase (NOX) in generating the ROS that mediate $A\beta_{1-42}$-evoked capillary constriction, I bath applied the nonspecific NOX blocker, diphenyleneiodonium (DPI) to cerebral cortical slices. Pericyte contraction evoked by $A\beta_{1-42}$ was significantly inhibited by 75% in the presence of DPI (10 μM), resulting in a constriction of only 4.7 ± 3.5% (n=4, p=0.011 compared to no DPI, Fig. 4.4A, B). DPI alone did not significantly evoke a vascular response after 1 h (evoking a non-significant constriction of 6.9 ± 3.5%, n=5, p=0.13).

Applying the NOX4 blocker, GKT137831 (0.45 μM), completely prevented the capillary constriction evoked by 1 h of $A\beta_{1-42}$ application, resulting in a diameter change of only 1.0 ± 3.3% (n=7, significantly reduced, p=0.0024, Fig. 4.4A, B). In contrast, superfusing the NOX2 blocker, ebselen (2 μM), reduced the constriction by only 45% (leaving a diameter reduction of 10.5 ± 2.5% following 1 h of $A\beta_{1-42}$, n=8, significantly reduced, p=0.027, Fig. 4.4A, B). Applying these inhibitors alone for 1 h did not affect vessel diameter (GKT137831, -5.6 ± 5.2%, n=6, p=0.31; ebselen, -0.9 ± 4.4%, n=8, p=0.84). These experiments suggest that NOX4, mainly found in endothelial cells or pericytes (Zhang *et al.*, 2014; Zeisel *et al.*, 2018), rather than NOX2 , which is found in immune cells such as microglia (Zhang *et al.*, 2014; Zeisel *et al.*, 2018), is the main NOX generating the ROS that cause Aβ-evoked capillary vasoconstriction in AD. It must be stressed, however, that these experiments only assess ROS generation by short-term application of Aβ, and during the development of human AD over years it is possible that the main ROS generators are microglia or other immune cells.

I have used the drugs mentioned above to block their standard targets, but it should be noted that drugs can also act on other targets, which might complicate the

interpretation of these experiments. DPI can also inhibit other enzymes such as nitric oxide synthase, NADH:ubiquinone oxidoreductase and xanthine oxidase (Riganti *et al.*, 2004). Ebselen can also block NOX1, NOX5 (but this is not present in rats and mice (Nayernia, Jaquet & Krause, 2014)), lipoxygenase, cyclooxygenase, protein kinase C, cytochrome P-450, the cysteine protease, glutathione-s-transferase, prostaglandin H ynthetase, b5 reductases and H^+/K^+-ATPase (Sarma & Mugesh, 2008; Altenhöfer *et al.*, 2015). The concentration that I used is not able to inhibit nitric oxide synthase (IC_{50} 8.5 μM) nor function as a glutathione peroxidase mimetic (Altenhöfer *et al.*, 2015). GKT137831 also inhibits NOX1 (Altenhöfer *et al.*, 2015). NOX1 could potentially contribute to the constriction but because the concentrations of ebselen and GKT137831 used should similarly inhibit NOX1 (yet produce a 2-fold difference in inhibition of the Aβ-evoked vasoconstriction), the constriction could not be due to NOX1 activity. Moreover, according to transcriptomic data, NOX1 is not expressed in either pericytes nor vascular endothelial cells on capillaries, arguing against a major role for NOX1 in capillary constriction (Zeisel *et al.*, 2018).

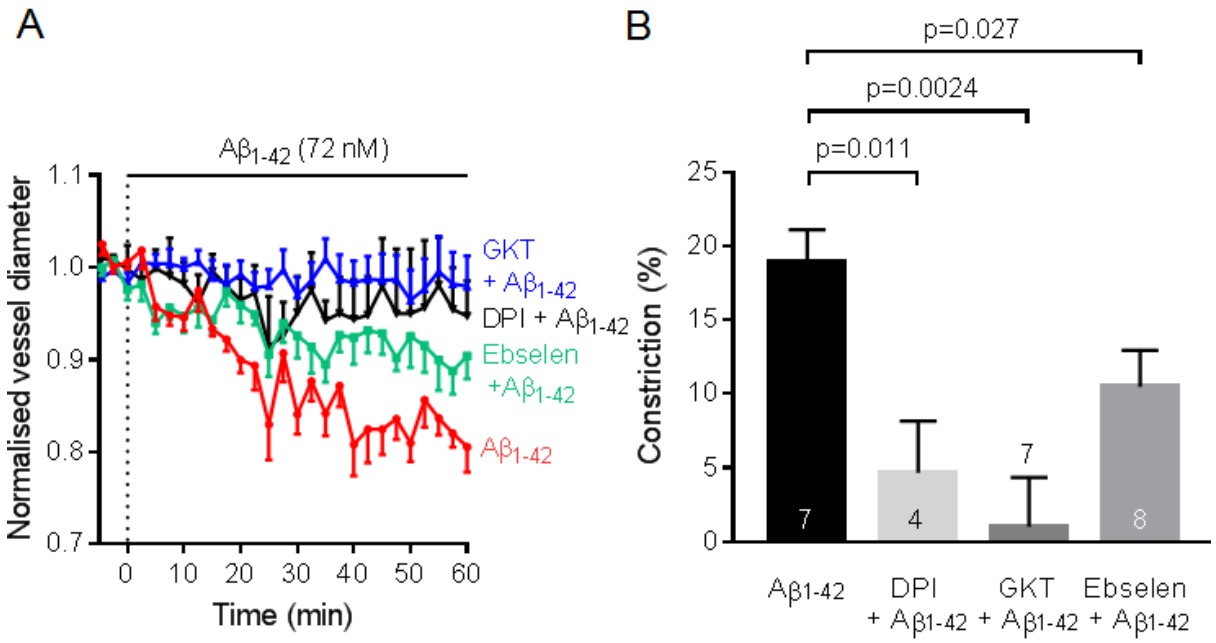

Figure 4.4: Aβ1-42 oligomers evoke capillary constriction through reactive oxygen species (ROS) generated mainly through NADPH oxidase 4.

(A) Oligomeric Aβ1-42 (72 nM, n=7, red trace) evoked a constriction of capillaries after 1 h that was largely inhibited in the presence of the unspecific NOX blocker DPI (10 µM, n=5, black trace) or the specific NOX4 inhibitor GKT137831 (GKT, 0.45 µM, n=7, blue trace), but the constriction was only partly inhibited by the specific NOX2 inhibitor ebselen (2 µM, n=8, green trace). Blockers were perfused 15 min before the application of Aβ1-42 (dotted line). Diameter is normalised to the pre-Aβ baseline.

(B) Constriction in (A) at t=58-60 min, showing that the Aβ1-42 evoked capillary constriction was significantly inhibited by DPI, GKT137831 and ebselen.

4.3.5 Hydroxyl radicals are the main ROS causing $A\beta_{1-42}$ evoked constriction

Figure 1.3 shows the ROS products generated by NADPH oxidases. As noted above, SOD1 inhibits the Aβ-evoked constriction, but this does not prove that the agent evoking ET release and constriction is superoxide itself, because SOD1 also inhibits hydroxyl radical production through inhibition of the Haber-Weiss reaction and conversion of ferric iron to ferrous iron as well as prevention of lipid peroxidation (Gutteridge, 1985b; Gutteridge, Maidt & Poyer, 1990; McCord, 2008; Ayala, Muñoz & Argüelles, 2014; Wang *et al.*, 2018) (Fig. 1.4). To test whether hydroxyl radicals, the ROS end product with the most oxidising properties (Collin, 2019), contribute to $A\beta_{1-42}$ induced pericyte contraction, I used deferoxamine (DFO), an iron chelator, to inhibit the iron-catalysed Fenton reaction that produces hydroxyl radicals.

Vasoconstriction evoked by $A\beta_{1-42}$ was largely inhibited by superfusing DFO (100 µM), which significantly reduced the constriction to 4.7 ± 4.7% after 1 h of $A\beta_{1-42}$ (n=7, p=0.019, Fig. 4.5A, B), suggesting that hydroxyl radical is the main ROS species underlying the constriction. DFO alone did not evoke a significant diameter change after 1 h (-0.2 ± 3.9%, n=6, p>0.99). It should be noted that this *ex vivo* experiment might be affected by trace metals found in the solutions or perfusion system and an *in vivo* experiment might be needed to further support this finding.

To test the vasoconstricting effect of hydroxyl radical, I first established a ROS induced capillary constriction by applying H_2O_2 (1mM), resulting in a constriction of 16.3 ± 3.3% after 25 min (n=6, Fig. 4.5C). Application of DFO abolished this effect, evoking a vascular response of only 2.6 ± 2.6% (100 µM, n=7, significantly reduced, p=0.0041, Fig. 4.5C), implying that the hydroxyl radical induces capillary constriction in the presence of oxidative stress.

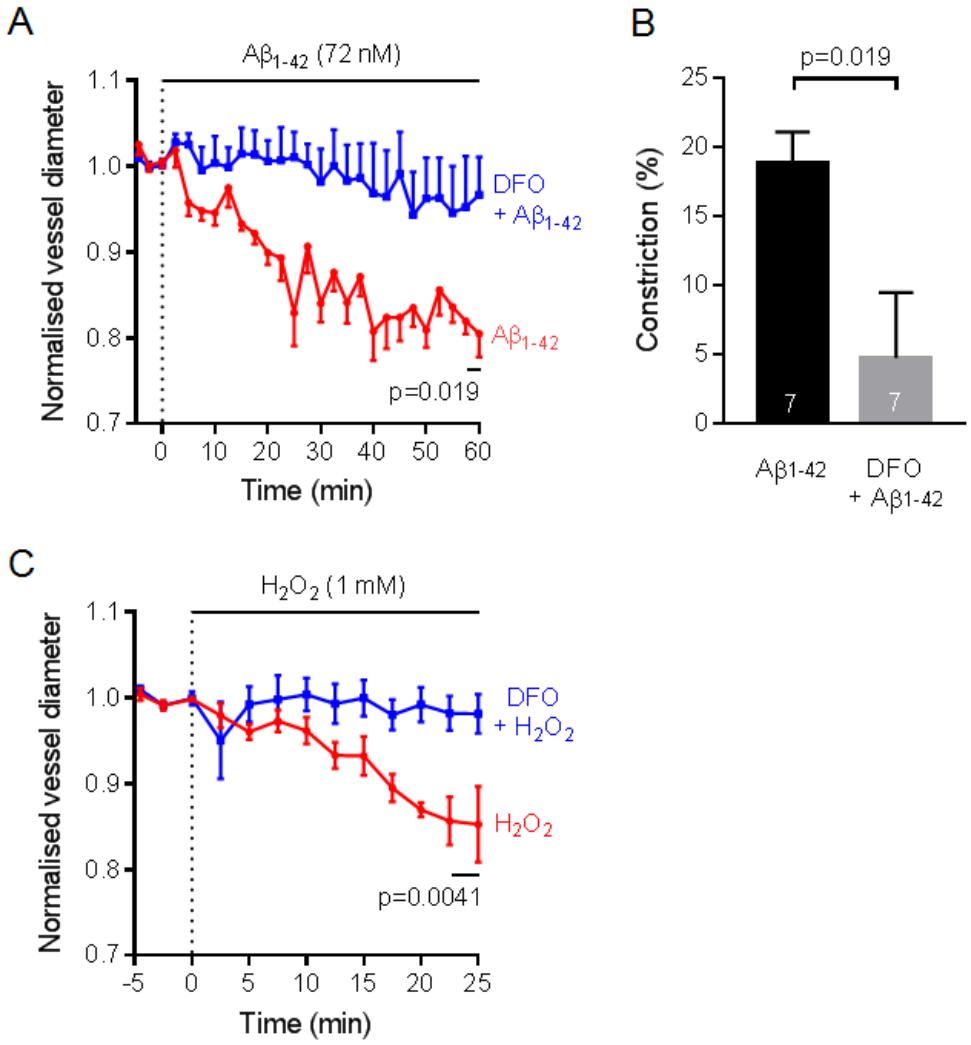

Figure 4.5: The ROS responsible for capillary constriction evoked by oligomeric Aβ or H_2O_2 is likely to be the hydroxyl radical.

(A) Constriction of capillaries in response to 1 h of application of oligomeric $Aβ_{1-42}$ (72 nM, n=7) alone or in the presence of the iron chelating agent deferoxamine (DFO, 100 μM, n=7).

(B) Constriction in (A) at t=58-60 min.

(C) Time course of diameter after applying H_2O_2 alone (1 mM, n=6) or in the presence of DFO (100 μM, n=7).

DFO was applied 15 min before superfusing $Aβ_{1-42}$ or H_2O_2. Dotted line indicates the time when application of Aβ or H_2O_2 started.

4.3.6 Reactive nitrogen species are not involved in $A\beta_{1-42}$ evoked constriction

NADPH oxidases usually produce superoxide (although NOX4 produces mainly H_2O_2 and only a small amount of superoxide: Nisimoto *et al.*, 2014; but see Kuroda *et al.*, 2014). Application of SOD1, which converts superoxide to H_2O_2, inhibited the $A\beta_{1-42}$ induced pericyte contraction (see Section 4.3.1), suggesting that superoxide might be involved in the contraction process. Superoxide can be closely connected to reactive nitrogen species (RNS) because it reacts rapidly with nitric oxide to create peroxynitrite (Phaniendra, Jestadi & Periyasamy, 2015), which has been shown to cause pericyte contraction in the brain (Yemisci *et al.*, 2009). The resulting depletion of nitric oxide, a potent vasodilator, by formation of peroxynitrite could potentially lead to vasoconstriction.

In order to test for an involvement of RNS, I applied N_ω-nitro-L-arginine (L-NNA), a nitric oxide synthase inhibitor, which depletes nitric oxide from brain slices. A constriction of 17.6 ± 1.6% was seen after 1 hour of $A\beta_{1-42}$ in the presence of L-NNA (100 µM, n=6), which is not significantly different to the constriction of 18.9 ± 2.2% seen in the absence of L-NNA (p=0.82, Fig 4.6A, B), implying that the $A\beta_{1-42}$ evoked capillary vasoconstriction does not involve RNS or depletion of NO. L-NNA alone had no significant effect on vessel diameter after 1 h, evoking a diameter increase of 0.52 ± 8.0% (n=6, p=0.44).

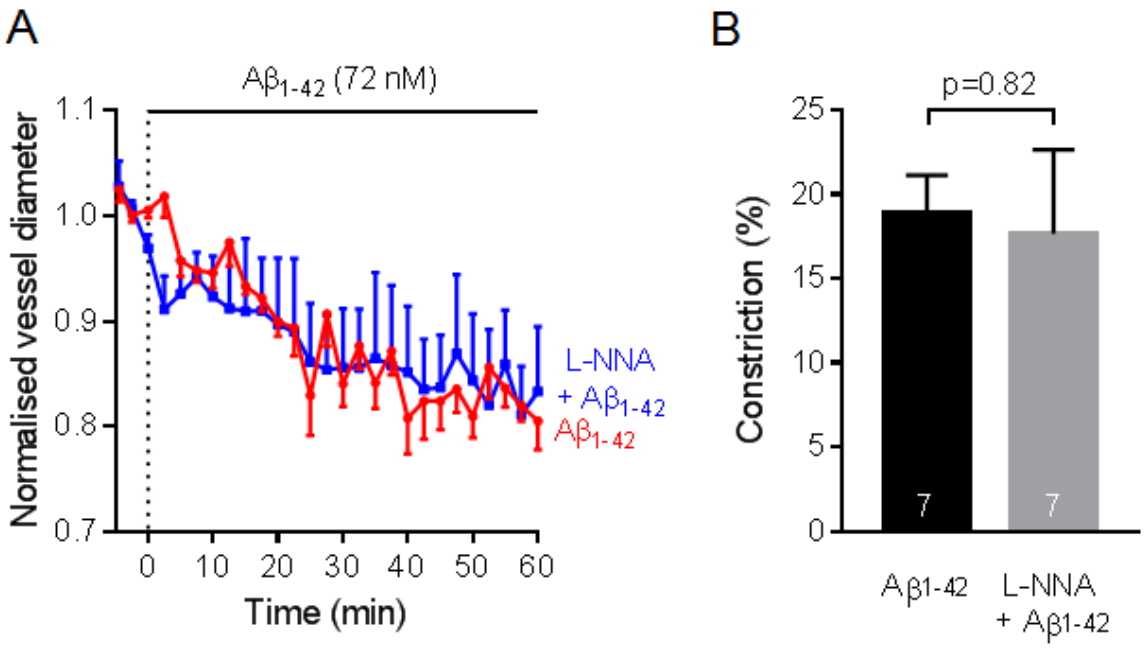

Figure 4.6: Reactive nitrogen species are not involved in the Aβ-evoked capillary constriction.

(A) The $A\beta_{1-42}$ (72 nM, n=7) evoked capillary constriction after 1 h was not inhibited by application of the nitric oxide synthase inhibitor L-NNA (100 μM, n=6). L-NNA was applied 15 min before application of $A\beta_{1-42}$. The dotted line represents the time when application of Aβ started. Diameter was normalised to the mean diameter averaged over the 5 minute period before Aβ was applied.

(B) Constriction in (A) at t=58-60 min, suggesting that the $A\beta_{1-42}$ mediated pericyte contraction was not significantly inhibited by the nitric oxide synthase inhibitor L-NNA.

4.3.7 Reversal of $A\beta_{1-42}$ evoked pericyte contraction

Preventing further Aβ-evoked capillary constriction during the development of AD, or reversing the existing capillary constriction resulting from $A\beta_{1-42}$ evoking ROS generation and ET release, might provide a basis for future AD therapy. The first method that I employed to try to do this was to attempt to inhibit the $A\beta_{1-42}$ evoked capillary constriction by blocking the downstream effector, endothelin-1, with the ET_A receptor blocker BQ-123. Superfusing BQ-123 (1 μM) for 40 min in the continued presence of $A\beta_{1-42}$, after 40 min of perfusion of $A\beta_{1-42}$ alone, could not stop the progression of the $A\beta_{1-42}$ evoked vasoconstriction (unlike when BQ-123 was pre-applied in Fig. 4.3A). A further constriction of 5.7 ± 6.1% (n=3) was observed, compared to a constriction of 12.9 ± 3.3% from another 40 min of $A\beta_{1-42}$ alone (n=7, Fig.4.7A), and the final diameter reached was not significantly affected by the BQ123 (p=0.29). This suggests that blocking ET_A receptors alone might not be enough to halt the progression of $A\beta_{1-42}$ evoked pericyte contraction. Consistent with this, previous work has shown that established ET_A receptor mediated responses are only slowly reversed by antagonists to this receptor (Warner, Allcock & Vane, 1994).

The following experiments were performed in collaboration with my colleague, Dr. Nils Korte, who contributed to 25% of the experiments. The strategy of applying a NOX4 blocker (GKT137831, 0.45 μM) together with an ET_A blocker (BQ-123, 1 μM) for 1 h (n=5) could stop further development of the $A\beta_{1-42}$ induced capillary constriction (p=0.027) but could not rapidly reverse the effect (Fig. 4.7B). However, C-type natriuretic peptide (CNP, 100 nM, n=6), which was chosen because it is able to reverse endothelin effects by raising the cyclic GMP concentration (Špiranec *et al.*, 2018) as described below, could rapidly reverse the $A\beta_{1-42}$ evoked constriction (p=0.029, Fig. 4.7B).

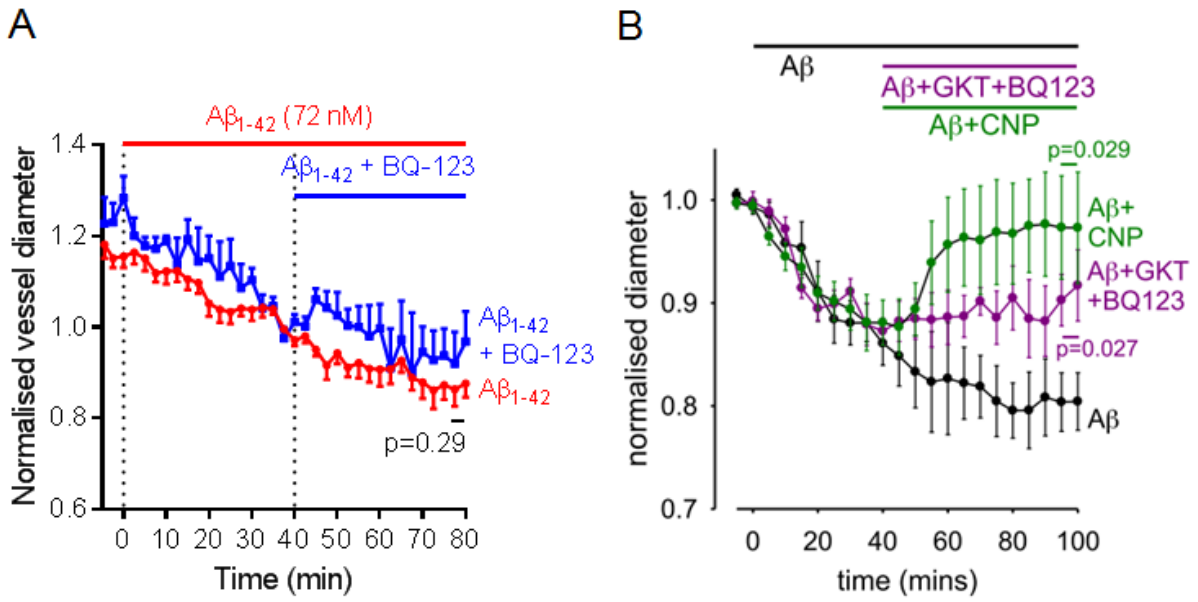

Figure 4.7: Reversal of Aβ-evoked capillary constriction by C-type natriuretic peptide or combining the ET_A blocker BQ123 with the NOX4 blocker GKT137831.

(A) Time course of capillary diameter on applying $Aβ_{1-42}$ alone for 80 min (72 nM, n=7), or $Aβ_{1-42}$ alone for 40 min then superfusing also the ET_A receptor blocker BQ123 for 40 min (1 μM, n=3). There was no significant difference between the two conditions. Diameters were normalised to the average value over the period from t=35-40 mins before the blockers were applied.

(B) Time course of capillary diameter when applying $Aβ_{1-42}$ (72 nM) alone for 100 min, or $Aβ_{1-42}$ alone for 40 min then $Aβ_{1-42}$ with C-type natriuretic peptide (CNP, 100 nM, n=6), or with the combination of the ET_A blocker BQ-123 (1 μM) and the NOX4 blocker GKT137831 (0.45 μM), for 1 h (n=5). CNP could reverse the constriction rapidly but although the combination of BQ-123 and GKT137831 stopped the progression of the $Aβ_{1-42}$ evoked capillary constriction it did not produce a rapid recovery of the diameter.

4.3.8 $A\beta_{1-40}$ also constricts capillaries via endothelin signalling to pericytes

$A\beta_{1-40}$ (72 nM, n=5), like $A\beta_{1-42}$, could evoke a significant capillary vasoconstriction (see Section 4.3.1). This was completely inhibited by pre-applying BQ-123, the presence of which with $A\beta_{1-40}$ resulted in a net dilation of -6.2 ± 1.6% (1 µM, n=5, p=0.010 compared to no BQ-123, Fig. 4.8A, B). This contradicts the statement that $A\beta_{1-40}$ does not act through endothelin receptor activation (Palmer & Love, 2011).

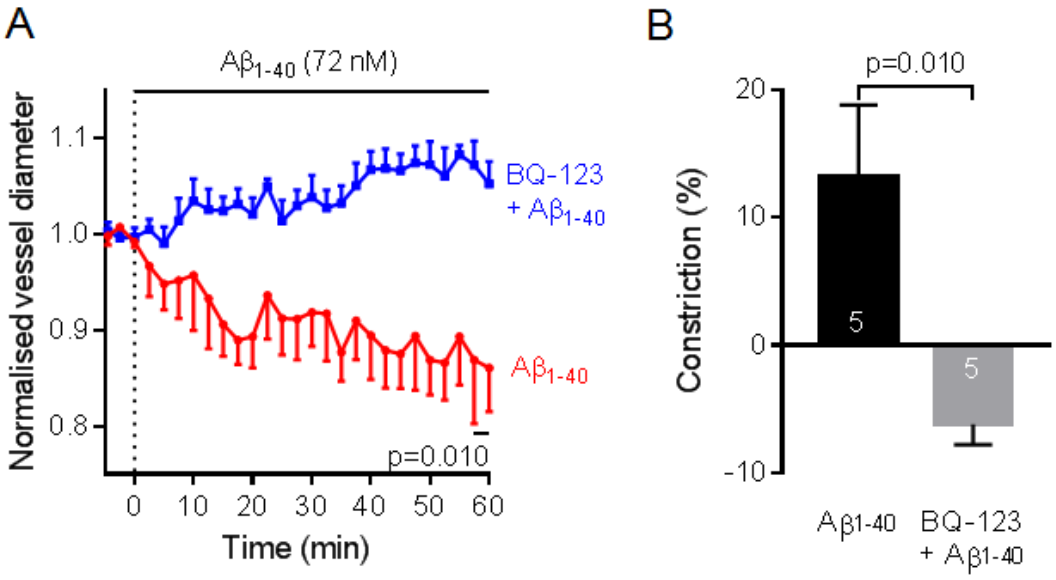

Figure 4.8: $A\beta_{1-40}$ oligomers constrict capillaries via endothelin A receptors.

(A) Capillary diameter changes at pericyte locations in response to 1 h of oligomeric $A\beta_{1-40}$ alone (72 nM, n=5) or in the presence of endothelin A receptor blocker BQ-123 (1 µM, n=5). Dotted line indicates the beginning of $A\beta_{1-40}$ application. BQ-123 was perfused 15 min before applying $A\beta_{1-40}$.

(B) Constriction in (A) at t=58-60 min, showing that $A\beta_{1-40}$ evoked pericyte contraction was completely inhibited by BQ-123.

4.4 Discussion

My data provide three key results for understanding the effects of Aβ on capillaries and pericytes and the role of this in AD:

(i) Aβ oligomers at low nanomolar concentrations constrict capillaries through pericyte contraction;

(ii) Hydroxyl radicals, generated largely through NOX4, and downstream endothelin release, play important roles in this constriction; and

(iii) Reversal of this process could restore cerebral blood flow in principle.

Firstly, to validate the Aβ oligomerisation method used, I employed SDS-PAGE and found that $A\beta_{1-42}$ formed oligomers with a molecular weight of three to four times that of monomeric Aβ, indicating that trimers and tetramers were formed by the preparation, similar to what has been shown by other groups (Chen & Glabe, 2006; Ying *et al.*, 2009). $A\beta_{1-42}$ trimers (Jana *et al.*, 2016) and tetramers (Jana *et al.*, 2016; Ciudad *et al.*, 2020) have also been suggested to be the toxic oligomers (although some research suggests that dimers can be toxic: Zott *et al.*, 2019). This proves that the oligomerisation method works well and that the oligomeric solutions could be used to investigate the effects of $A\beta_{1-42}$ on pericytes.

Soluble $A\beta_{1-42}$ evoked rodent capillary constriction *in vitro*. *In vivo* in AD mice, pericyte-mediated contraction was also found along the capillaries in cerebral cortex, where there were Aβ plaques, but not in the cerebellum which lacked Aβ deposition. Because plaques are thought to be less harmful than oligomers (Glabe, 2006) and do not correlate well with AD progression (Nelson *et al.*, 2012), one possibility for why capillary constriction was only found in plaque-laden cerebral cortex is that the plaques serve as a reservoir for soluble oligomeric Aβ (Koffie *et al.*, 2009), which constricts the

capillaries. Another possibility is that the plaques might represent areas with a high level of soluble Aβ.

From the capillary constriction data in Fig. 4.2A, the resulting cerebral blood flow reduction (calculated as in Section 2.3.4) was predicted to be around 28%, but this value might well be an underestimation of the cerebral blood flow reduction found in AD patients. Indeed, in human biopsies a larger pericyte-mediated constriction was observed which predicted an ~50% reduction of blood flow (Nortley *et al.*, 2019) and actual MRI measurements of cerebral blood flow demonstrate an approximately 45% reduction of blood flow in AD patients (Asllani *et al.*, 2008). Furthermore, it should be noted that:

(i) only vasoconstriction of capillaries was taken into account in the calculation, disregarding a potential constriction of arteries and arterioles (Niwa *et al.*, 2000), although no constriction of these vessels was seen in our APP^{NL-G-F} mice (Nortley et al., 2019);

(ii) the mouse measurements of capillary diameter were obtained at an age of 4 months, i.e. relatively early in the progression of Aβ plaque deposition (which begins at 2 months of age and saturates at 7 months in these mice (Saito *et al.*, 2014)), whereas human data typically come from patients who are more advanced in the disease.

Thus, it is likely that Aβ-evoked pericyte-mediated capillary constriction plays an important role in AD. The reduced cerebral blood flow that it produces is known to upregulate the β-secretase which produces Aβ, thus generating a positive feedback loop that ultimately results in an amplification of Aβ production and tau hyperphosphorylation, with accompanying synapse loss and neuron death (Nortley *et al.*, 2019).

Pharmacological blocking experiments on the Aβ-evoked capillary constriction revealed that $A\beta_{1-42}$ acts to produce oxidative stress, which affects pericytes via endothelin signalling (Fig. 4.9). The ROS involved are produced mainly through NOX4, as shown by the fact that NOX4 block could completely inhibit Aβ-evoked capillary constriction. This is not unexpected since NADPH oxidases are a major source of vascular ROS (Paravicini & Touyz, 2008), especially NOX4 which is widely expressed in smooth muscle cells (Chen *et al.*, 2012), endothelial cells (Chen *et al.*, 2012) and pericytes (Kuroda *et al.*, 2014). Transcriptomic studies also suggest that expression of NOX4, rather than NOX2, occurs in capillary endothelial cells and pericytes (Zeisel *et al.*, 2018). Interestingly, NOX4 activity has been shown to be linearly correlated with the cognitive deficit occurring in AD (Bruce-Keller *et al.*, 2011). However, because inhibition of NOX2 by ebselen also inhibited Aβ-evoked capillary constriction by 50%, a role for NOX2, mostly expressed by microglia (Bianca *et al.*, 1999; Carrano *et al.*, 2011) and perivascular macrophages (Park *et al.*, 2017), in Aβ-evoked vasoconstriction cannot be dismissed.

I provided evidence that hydroxyl radicals are likely to be the main form of ROS generating Aβ-induced pericyte contraction (Fig. 4.9). Deferoxamine is an iron chelator that can inhibit the iron-catalysed OH*-producing Fenton reaction, in which hydrogen peroxide is converted to OH*, and the Haber-Weiss reaction, in which superoxide reacts with hydrogen peroxide in the presence of iron to form OH*. Deferoxamine inhibited Aβ-evoked vasoconstriction, implying that hydroxyl radicals play a key role in this process. Indeed, intramuscular deferoxamine has been shown to slow AD progression in patients (Crapper McLachlan *et al.*, 1991). Inhibition of Aβ-evoked capillary constriction by SOD (Fig. 4.3A) is also consistent with this idea. Although SOD mainly catalyses the conversion of superoxide anion (O_2^{*-}) to H_2O_2 (Collin, 2019),

it can also inhibit formation of hydroxyl radicals in two ways, by (i) inhibiting reduction of ferric ion (Fe^{3+}) from iron-sulphur clusters (a component of some enzymes in the Krebs cycle and aconitase) by O_2^{*-} to release ferrous iron that can interact in the Fenton reaction (Gutteridge, Maidt & Poyer, 1990; Wang *et al.*, 2018), and (ii) inhibiting the Haber-Weiss reaction (Gutteridge, 1985b). The O_2^{*-} scavenging property of SOD might not be a plausible explanation for inhibition of vasoconstriction because (i) the main product of NOX4 is thought to be H_2O_2 (Nisimoto *et al.*, 2014; Altenhöfer *et al.*, 2015; but see Kuroda *et al.*, 2014); and (ii) SOD converts O_2^{*-} to H_2O_2 (Collin, 2019), which causes vasoconstriction (Fig. 4.3C) so adding SOD would promote rather than inhibit constriction by this mechanism (Fig. 1.4). Because NOX4 creates mainly H_2O_2, the level of O_2^{*-} should not be high, meaning that the low level of H_2O_2 created by perfusing SOD1 should minimally contribute to OH* production, allowing inhibition of the Fenton reaction by SOD1 to dominate the effect of SOD1 on Aβ-evoked constriction. Hence, the inhibition of Aβ-induced pericyte contraction might be better explained by SOD1 reducing hydroxyl radical formation.

Hydroxyl radicals might act to promote constriction via endothelin-dependent and endothelin-independent pathways. An endothelin-dependent pathway is indicated by the fact that hydroxyl radicals have been shown to enhance endothelin release from endothelial cells (Prasad, 1991). Furthermore, SOD can prevent enhanced endothelin coverting enzyme 1 (ECE-1) activity and Aβ-mediated endothelin release (Palmer, Tayler & Love, 2013) from endothelial cells. As evidence for an endothelin-independent pathway, in cultured isolated pericytes, hydrogen peroxide evokes Ca^{2+} release from internal stores (Kamouchi *et al.*, 2007), which will increase pericyte contractility (Hamilton, Attwell & Hall, 2010). Post-translational oxidative modification by hydroxyl radicals of proteins involved in vasoconstriction, such as calcium

channels, the sarcoendoplasmic reticulum calcium transport ATPase (SERCA), Rho kinase, actins and myosins, might also increase contractility in pericytes as occurs in smooth muscle cells (Touyz *et al.*, 2018) and contribute to an endothelin-independent effect of hydroxyl radical on pericytes. Arguing against a significant contribution of an endothelin-independent pathway to the generation of the Aβ-evoked constriction, however, is the fact that blocking ET_A receptors with pre-applied BQ123 completely blocked the constriction evoked by $A\beta_{1-42}$ and $A\beta_{1-40}$ (Fig. 4.3A and Fig. 4.8A).

Interestingly, my results suggest that RNS are less likely to contribute to the Aβ-evoked constriction. One of the possible reasons is that the generation of RNS requires nitric oxide and superoxide (Wang *et al.*, 2018); but NOX4 mainly produces H_2O_2 (Nisimoto *et al.*, 2014; Altenhöfer *et al.*, 2015; but see Kuroda *et al.*, 2014), so there might not be much superoxide present to interact with nitric oxide. Also, the diameter of cortical capillaries, unlike arterioles, does not depend on nitric oxide release (Mishra *et al.*, 2016), so a loss of nitric oxide resulting from the generation of RNS should not contribute to the Aβ-evoked vasoconstriction.

Finally, and with relevance to preventing the fall of cerebral blood flow that occurs in AD, it is possible to stop the progression of the Aβ-evoked capillary constriction. Inhibiting endothelin signalling alone (by blocking ET_A receptors) was not enough to inhibit the on-going process (Fig. 4.7A). One of the reasons might be that the dissociation rate of endothelin from its receptor is very low (Waggoner, Genova & Rash, 1992) and so BQ-123 can only slowly reverse the effect (Warner, Allcock & Vane, 1994). The combination of a NOX4 blocker and an ET_A blocker inhibited the progression of the constriction but could not reverse it (Fig. 4.7B). Potentially importantly for future therapies, application of CNP, a powerful vasodilator (Fig. 4.10) that raises the intracellular level of cyclic GMP and thus can reverse the effect of

endothelin by inhibiting Ca^{2+} release from internal stores and by activating myosin light chain phosphatase (Sangaralingham & Burnett, 2018; Špiranec *et al.*, 2018), was able to restore the capillary diameter. Thus, activation of this pathway might offer a potential therapeutic pathway for reversing the fall of cerebral blood flow that occurs early in AD (Iturria-Medina *et al.*, 2016).

4.5 Suggestions for future work

The experiments that I carried out suggest that Aβ activates NOX4. Further experiments could be performed to clarify how NOX4 stimulation occurs. Many candidate receptors for Aβ, such as the receptor for advanced glycation end products (RAGE), LRP1, TREM2, PrP and TLR4 (Donahue *et al.*, 2006; Guo *et al.*, 2020), could be involved in this process so pharmacological blocking of these receptors to observe changes in Aβ-induced vasoconstriction or Aβ-activated ROS production could potentially be helpful.

Because the Fenton reaction inhibitor deferoxamine inhibits Aβ-evoked capillary constriction (see Section 4.3.5), slows the progression of AD in patients (Crapper McLachlan *et al.*, 1991) and is already approved for usage for other medical indications, it is an interesting potential therapeutic approach for treating CBF deficits in AD. Other potential treatments are: (i) a combination of a NADPH oxidase (NOX) 4 blocker together with an endothelin A receptor blocker; and (ii) C-type natriuretic peptide (CNP), both of which were shown to prevent the progression of Aβ-induced pericyte contraction (and in the case of CNP to reverse it; see Section 4.3.7). Future work might include washing glassware with acid before testing the inhibition of Aβ-evoked capillary constriction with deferoxamine, to remove any trace metals on the glassware. The next step would be testing the inhibitory effect of all potential

treatments on Aβ-mediated pericyte contraction in human brain slices and *in vivo* AD mice. There are a few limitations of using AD mice including the dependence on the familial AD mutations (Drummond & Wisniewski, 2017). In contrast, most of the AD patients are sporadic AD (Bertram & Tanzi, 2004). Also, the AD mice are not able to replicate all features of AD (Drummond & Wisniewski, 2017). However, these mice allow us to experiment in a more controlled manner. The next step would be to examine of the benefit of these potential treatments on cognitive function in AD mice before testing them in clinical studies on AD patients.

4.6 Conclusion

My data suggest that Aβ-evoked capillary constriction is an important process which leads to a sizable reduction of cerebral blood flow in preclinical AD patients, and that this process is mediated via NOX4, hydroxyl radicals and endothelin, all of which could be potential therapeutic targets. The experiments also show that it is possible to stop or reverse the progression of the capillary constriction using drugs targeting pathogenic factors such as NOX4 and the endothelin A receptor or using a strong vasodilator such as C-type natriuretic peptide. It would be interesting to test therapeutic approaches targeting these pathogenic factors and pericytes in clinical trials, in order to develop medication to prevent the fall of cerebral blood flow that may cause and/or speed the onset of AD.

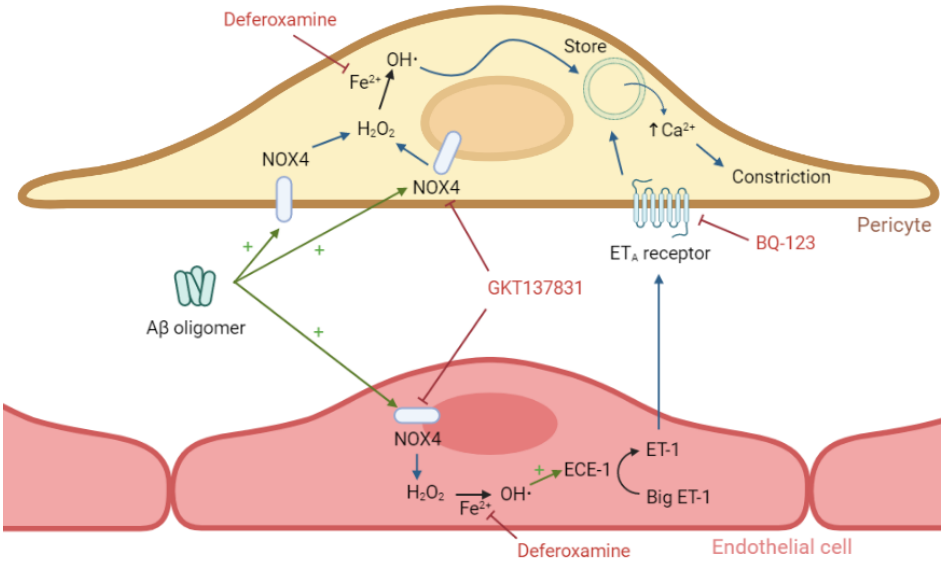

Figure 4.9: Schematic diagram of possible mechanisms underlying Aβ-mediated capillary constriction. Aβ oligomers stimulate NADPH oxidase (NOX) 4, which is expressed in the intracellular membranes of pericytes and endothelial cells, and supposedly at focal adhesion points of pericytes as shown in smooth muscle cells (Hilenski *et al.*, 2004), to produce some superoxide but mainly H_2O_2. This process can be inhibited by the specific NOX4 blocker GKT37831. H_2O_2 generates hydroxyl radicals (OH*) via the iron-catalysed Fenton reaction, which can be inhibited using the iron chelator deferoxamine. In endothelial cells, hydroxyl radicals enhance the activity of endothelin coverting enzyme 1 (ECE-1), resulting in increased conversion of big endothelin 1 (ET-1) to ET-1, which is then secreted. ET-1 interacts with endothelin A (ET_A) receptors on pericytes. In addition there is a possible direct effect of intracellular hydroxyl radicals (via an endothelin-independent pathway) within pericytes that increases calcium release from stores (although the fact that the ET_A receptor blocker BQ-123 completely blocks Aβ-evoked constriction argues against a major role for this pathway). The resulting rise in $[Ca^{2+}]_i$ (either via hydroxyl-evoked release from stores or endothelin-evoked release) will lead to pericyte contraction and capillary constriction.

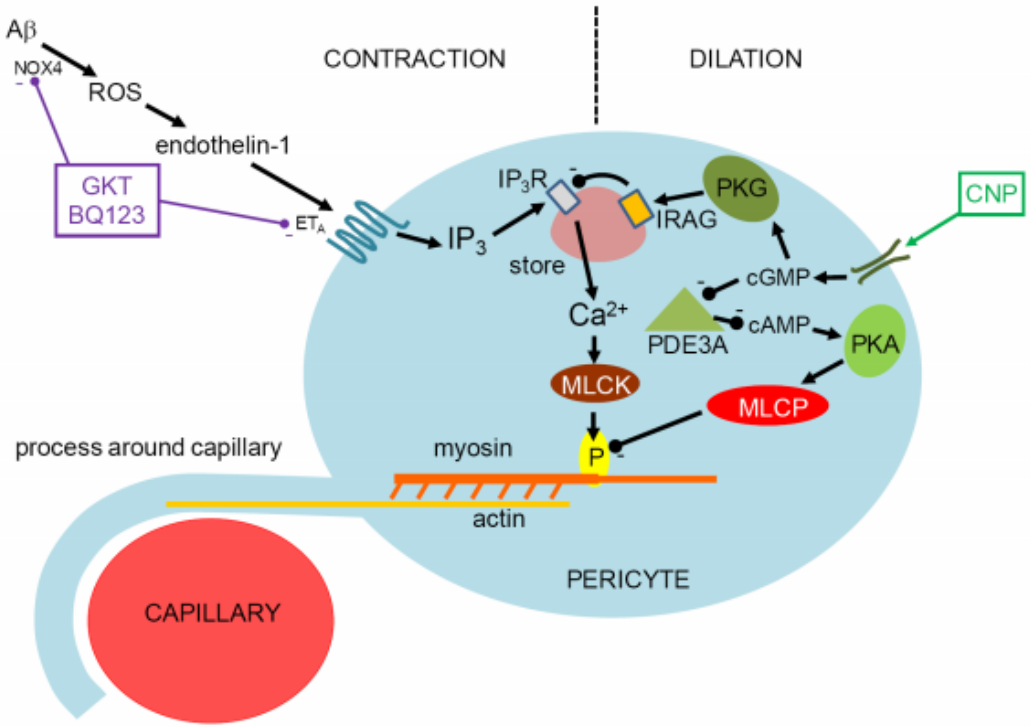

Figure 4.10: Pathways regulating pericyte contraction.

This figure and legend are from Nortley *et al.* (2019), to which paper I contributed the data in this Chapter. Schematic diagram of a pericyte with a contractile process around a capillary. Aβ generates ROS (via NOX4) which evoke release of endoethelin-1 (ET), which can activate contraction by binding to ET_A receptors. These generate IP_3 to release Ca^{2+} from internal stores, which evokes contraction by activating myosin light chain kinase (MLCK). This pathway can be inhibited by blocking NOX4 with GKT137831 (GKT) and blocking ET_A receptors with BQ-123. Alternatively, C-type natriuretic peptide (CNP) can block the ET-evoked contraction by acting on guanylate cyclase receptors that generate cCGMP. This inhibits Ca^{2+} release from stores by activating protein kinase G to phosphorylate the IP_3R interacting protein IRAG. cGMP also inhibits cAMP phosphodiesterase 3A (PDE3A) leading to a rise of [cAMP] which activates protein kinase A (PKA), which in turn activates myosin light chain phosphatase (MLCP) to inhibit contraction.

Chapter 5: Hyperoxia and pericyte contractility

5.1 Introduction

Hyperoxia is a condition where excess oxygen is supplied to tissue or organs (Mach *et al.*, 2011), either at normal atmospheric pressure or under hyperbaric conditions. A similar but better defined term is hyperoxaemia, which is a partial pressure of oxygen higher than 100 mmHg in the blood (Pala Cifci *et al.*, 2020). Hyperoxia and hyperoxaemia mostly occur iatrogenically when treating and preventing tissue hypoxia. Because treatment guidelines rarely state the upper limit of partial pressure of oxygen or oxygen saturation for patients (O'Driscoll, Howard & Davison, 2011; Connolly *et al.*, 2012; American College of Surgeons Committee on Trauma., 2018), hyperoxaemia is not actively monitored and is frequently left uncorrected (Pannu, 2016), despite the fact that monitoring and correcting hyperoxaemia is easy to do. As a result, hyperoxaemia is very prevalent. In one study of 196 subarachnoid haemorrhage patients, arterial hyperoxia was observed in ~90% of the patients (Yokoyama *et al.*, 2019) and a total of 263,841 litres of excess O_2 was given to 51 critically ill patients in another study (Suzuki *et al.*, 2013). Aside from being very commonly found, hyperoxia is associated with worsened neurological outcomes in preclinical studies (Pilcher *et al.*, 2012) and with higher mortality rates in critically ill patients (Ni *et al.*, 2019).

Breathing in hyperoxic gas reduces blood flow in several organs, such as the heart, skeletal muscles and brain (Brugniaux *et al.*, 2018). A decrease in cerebral blood flow of 10-30% in hyperoxic patients was found using various techniques such as angiography and MRI (Watson *et al.*, 2000; Brugniaux *et al.*, 2018; Mattos *et al.*, 2019) and vasoconstrictions of the internal carotid arteries and vertebral arteries were

detected (Mattos *et al.*, 2019). Cerebral arteriolar constriction during hyperoxia was also observed in rats (Gordon *et al.*, 2008).

As a result, inhalation of hyperoxic gas may affect oxygen delivery, which is the product of arterial oxygen content and organ blood flow, in two opposing ways. On the one hand, it increases oxygen content by raising the concentration of oxygen dissolved in the plasma, while either (i) having no effect on the amount of oxygen bound to haemoglobin because haemoglobin becomes saturated with oxygen at a PaO_2 of 100 mmHg (Hafen & Sharma, 2021) or else (ii) increasing the amount of O_2 bound to haemoglobin if this is abnormally low in a disease state (Brugniaux *et al.*, 2018). On the other hand, hyperoxia reduces the amount of blood flow. As a result, some studies have found that tissue oxygenation increases with hyperoxia (Ganz *et al.*, 1972; Hlatky *et al.*, 2008), while others have shown that breathing hyperoxic gases does not increase oxygen delivery to organs (Smit *et al.*, 2018a, 2018b) and can even compromise oxygen delivery (Rossi *et al.*, 2007; Brugniaux *et al.*, 2018). If haemoglobin is already saturated with O_2, it is important to note that each mmHg of PaO_2 above 100 mmHg increases arterial oxygen content by only 0.0031 ml of O_2 per 100 ml of plasma (see Section 1.10.3.1), implying a rise of total O_2 level in the blood of only 1.5% of its normal value for a 100 mmHg rise of PaO_2. Hence, depending on the initial degree of saturation of haemoglobin, the reduction of blood flow evoked could easily outweigh the increase in oxygen content in hyperoxia, leading to a decrease in oxygen delivery.

No study has investigated the relationship between hyperoxia and the contractile tone of cerebral pericytes, which control the diameters of the cerebral capillaries that confer most of the intracerebral blood flow resistance (Gould *et al.*,

2017). Many mechanisms of hyperoxia-induced constriction in arteries and arterioles have been proposed, including the following.

(i) Increased production of reactive oxygen species (ROS), as more ROS were detected in pulmonary capillary endothelial cells (Brueckl *et al.*, 2006) and in mouse brains in hyperoxic conditions (Demchenko *et al.*, 2002). Also, hyperoxia increases ROS generation in the cytosol of cells in the caudal solitary complex in rats (Ciarlone & Dean, 2016) and in the mitochondria in rat brain cortex (Bin-Jaliah & Haffor, 2018) and rat hippocampus (D'Agostino, Putnam & Dean, 2007). Application of superoxide dismutase in rats (Zhilyaev *et al.*, 2003) or of ascorbic acid in human patients (Mattos *et al.*, 2019), both of which have anti-oxidant properties, was able to inhibit the hyperoxia-induced decrease of cerebral blood flow. This supports the role of ROS in generating the hyperoxic vasoconstriction. ROS mediating hyperoxia-evoked vasoconstriction might originate from either an NADPH oxidase (NOX), especially NOX2 and NOX4, or mitochondria, because their ROS-generating activities are increased at a high oxygen level (Turrens *et al.*, 1982; Turrens, 2003; Pendyala *et al.*, 2009; Nisimoto *et al.*, 2014). The vasoconstricting effect of hyperoxia-induced ROS was suggested to be generated by the ROS (a) scavenging the vasodilator nitric oxide (NO) (Demchenko *et al.*, 2002; Zhilyaev *et al.*, 2003), (b) increasing the level of the vasoconstrictor endothelin (ET) (Prasad, 1991) as described below or (c) releasing calcium from intracellular stores (Kamouchi *et al.*, 2007);

(ii) Secondly, constriction could reflect production of ET either through ROS-mediated pathways (as in (i, b) above) or other pathways (as may also explain the amyloid β-evoked constriction of capillaries described in Chapter 4). Hyperoxia induces secretion of ET from cultured bovine endothelial cells from the retina and adrenal glands (Higgins *et al.*, 1998), and also from isolated rat endothelial cells (Winegrad *et al.*,

1999). Increased cerebral release of big-ET, a precursor of ET (Kawanabe & Nauli, 2011), was observed after experimental hyperoxia in neurosurgical patients (Schaffranietz *et al.*, 2001). In addition, blocking ET receptors partly reduced the effect of hyperoxia on retinal blood flow in newborn piglets (Zhu, Park & Gidday, 1998).

(iii) Finally hyperoxia may lead to the generation of the vasoconstrictor 20-hydroxyeicosatetraenoic acid (20-HETE). In vascular smooth muscle cells, the conversion of arachidonic acid to 20-HETE, which is catalysed by cytochrome P450 (CYP) 4A, has a Michaelis constant (K_m) of ~55 μM at 37°C for oxygen (Harder *et al.*, 1996; Attwell *et al.*, 2010). Consequently, the rate will not be maximal at the oxygen tension in most tissues (*in vivo* values of oxygen tension in the brain are 20-60 μM (Attwell *et al.*, 2010)), thus allowing cells to use 20-HETE production as an oxygen sensing mechanism (Roman, 2002). CYP4A is also found in pericytes and is implicated in pericyte contraction (Gonzalez-Fernandez *et al.*, 2020). Indeed, hyperoxia has been shown to increase 20-HETE generation in the peripheral circulation (Ngo *et al.*, 2013) and in the retina (Zhu, Park & Gidday, 1998; Mishra, Hamid & Newman, 2011);

The objective of this chapter is to assess the effect of a high oxygen level on pericyte contractility, in order to test whether hyperoxia-induced capillary constriction contributes to the decrease of cerebral blood flow occurring during hyperoxia. In this chapter, I used aCSF oxygenated with 95% O_2 and 5% CO_2 to create a hyperoxic condition within brain cortical slices (giving tissue O_2 concentrations of ~100-150 μM: Attwell *et al.*, 2010) and aCSF oxygenated with 20% O_2, 5% CO_2, and 75% N_2 to create normoxic conditions (giving O_2 concentrations of ~40 μM within the slice: Hall and Attwell, 2008; Attwell *et al.*, 2010). A better understanding of hyperoxic

vasoconstriction might be useful in explaining poorer neurological outcomes in patients with hyperoxia.

5.2 Methods

5.2.1 Solutions and drugs

Bicarbonate-buffered aCSF for live imaging experiments, immunohistochemistry and calcium imaging was prepared as stated in section 2.1.1. Drugs were diluted to their final concentration in this solution before use.

5.2.2 Transgenic mice expressing fluorescent constructs

NG2-CreERT2 x PC::G5-tdT mice (see Section 2.2.4) were injected with tamoxifen to induce expression of the calcium indicator GCaMP5G as well as the red fluorescent protein tdTomato in NG2 positive cells, including pericytes. These mice were used to visualise calcium signals inside pericytes in Section 5.3.2.

5.2.3 Bright-field imaging

Cortical brain slices from P19-P23 Sprague-Dawley rats of both sexes or from excised normal brain tissue from patients undergoing surgical tumour removal, were used for bright-field imaging. The brain extraction and slicing procedure were outlined in section 2.3.1. There was no difference between the hyperoxia-evoked vasoconstriction of 14 male vessels and that of 6 female vessels ($p=0.57$).

Live slices (300 μm thick) were transferred to the tissue bath of a bright-field microscope perfused with bicarbonate-buffered aCSF at 33-36 ^{o}C and oxygenated with 20% O_2 (and 5% CO_2, 75% N_2). A capillary segment with a candidate pericyte was identified and imaged in bicarbonate-buffered aCSF for 5 min to establish the baseline diameter and then in aCSF with drugs or aCSF oxygenated with 95% O_2 (and 5% CO_2). Images were captured by a CCD camera every 30 s and were analysed with

Metamorph software to measure capillary diameters at candidate pericyte locations. The effect of capillary diameter changes on blood flow was estimated by the method described in Section 2.3.4.

5.2.4 Calcium imaging

Sagittal brain slice of 300 μm thickness were prepared from NG2-CreERT2 x PC::G5-tdT mice as described in section 2.6.1. The slices were perfused with bicarbonate-buffered aCSF at 33-36 ^{o}C and oxygenated with 20% O_2 (and 5% CO_2, 75% N_2) under a two-photon microscope. Pericytes were identified with a water immersion 20x objective by tracing penetrating arterioles to find cells with a bump-on-a-log morphology expressing a Cre-induced tdTomato signal. An excitation laser of 940 nm wavelength was used to stimulate pericytes, and signals from both tdTomato and the calcium indicator GCaMP5G were simultaneously collected. Image focus was readjusted after taking five image stacks. The image sequences were aligned using the ImageJ programme and pericyte somata were manually encircled and the intensity of GCaMP5G of every image stack was quantified as described in Section 2.6.

5.2.5 Immunohistochemistry

For experiments to measure cytosolic superoxide with dihydroethidium (DHE), I incubated coronal cortical slices from P19 - P23 Sprague-Dawley rats of both sexes in bicarbonate-buffered aCSF with DHE 8 μM at 35^{o}C and oxygenated with either 95% O_2 (and 5% CO_2 - the hyperoxic condition) or 20% O_2 (and 5% CO_2, 75% N_2 - the normoxic condition) for 1 h as described in Section 2.4.2. There was no significant difference in the intensity of DHE signals from 12 image stacks from male rats and 6 image stacks from female rats in hyperoxia ($p=0.66$) or in normoxia ($p=0.30$). The slices were immediately mounted on glass slides, kept hydrated with PBS, covered with glass cover slips and transferred to be imaged under a confocal microscope.

Image stacks were taken randomly in the cortex with a 20x objective and the mean fluorescence of the plane with maximum intensity was measured using ImageJ.

To measure mitochondrial superoxide in the hyperoxic condition, I incubated P19 – P23 Sprague-Dawley rat cortical slices with aCSF at 35^{o}C and bubbled with either 95% O_2 (and 5% CO_2 - the hyperoxic condition) or with 20% O_2 (and 5% CO_2, 75% N_2 - the normoxic condition) for 1 h and then loaded the cells with MitoSOX 5 μM for 15 min (see Section 2.4.2). In hyperoxia, MitoSOX signals from 6 image stacks from female rats were significantly higher (by 93.8%) than those from 12 image stacks from male rats ($p=0.0076$) but in normoxia, the MitoSOX signals from female were significantly lower (by 50.6%) than those from male rats ($p=0.033$). However, slices from the same animals were used for both oxygenation conditions so the comparison between conditions was not affected by the sex difference. The slices were then fixed with 4% PFA at room temperature for 1 h and washed three times in PBS for 10 min. The slices were then mounted onto glass slides with DAKO fluorescent mounting medium, covered with glass cover slips and imaged under a confocal microscope on the next day. Image stacks were taken at random. For each image stack, the mean fluorescence of the image plane with the maximum intensity was measured with ImageJ and used for further analysis. The intensity quantification was performed soon after the fixation because MitoSOX signals might decay afterwards.

Some of the brain slices from the hyperoxic condition were then unmounted and blocked in Triton X-100 based blocking solution (as previously described in Section 2.4.3) at 4^{o}C overnight. To visualise pericytes and blood vessels, the slices were incubated with mouse anti-NG2 antibody (1:200; for pericytes) overnight before being incubated with donkey anti-mouse 488 (1:500) as the secondary antibody overnight. The slices were then mounted and imaged with a confocal microscope to

visualise whether the previously imaged fluorescence of MitoSOX correlated with the NG2 signals. This procedure was followed so that the quantification of MitoSOX intensity was performed before the slices underwent rigorous washing and incubating in solutions to label NG2, which might affect the intensity of the MitoSOX signal in the slices.

5.2.6 Statistical analysis

Statistical analyses were performed as outlined in Section 2.7. For experiments with pharmacological inhibition of hyperoxic vascular changes, vessel diameters were normalised to the values in the last 10 images of the vessels when the inhibitors alone were applied before application of hyperoxia.

5.3 Results

5.3.1 Hyperoxia induces capillary constriction in rat and human cortical slices

Hyperoxia decreases cerebral blood flow and this can paradoxically decrease oxygen delivery to the human brain (Brugniaux *et al.*, 2018). It is unclear whether the fall of blood flow seen is mediated through pericyte-evoked constriction of capillaries, which are the most resistant vascular segment in the intracerebral circulation (Gould *et al.*, 2017).

To investigate the role of pericytes in hyperoxia-evoked blood flow reduction, I perfused bicarbonate-buffered aCSF oxygenated with 95% O_2 and 5% CO_2 onto rat cortical brain slices for 30 min, after a 5 min baseline of aCSF with 20% O_2, 5% CO_2 and 75% N_2. The aCSF oxygenated with 95% O_2 caused vasoconstriction of 23.0 ± 2.9% (n=20) while continuing oxygenation with 20% O_2 caused a vascular constriction of -1.2 ± 0.5% (n=5, significantly different, p=0.0005, Fig. 5.1A-C).

Hyperoxic capillary constriction was also found in human brain tissue obtained from neurosurgical operations. In human cortical slices, a capillary constriction of 20.8 ± 5.9% (n=5) was found after the slices were perfused with hyperoxic solution for 1 h compared to a vasoconstriction of 0.4 ± 0.9% (n=5, p=0.0091, Fig. 5.2A-C) found in normoxia (20% O_2). I used the Poiseuille's law analysis given in Chapter 2 (see Section 2.3.4) to estimate the likely flow change that this constriction would produce. As explained in Section 2.3.4, when pericytes are relaxed the capillary radius at capillary positions between pericytes (r_1) is less than that at the pericyte soma (r_2) with (r_2/r_1)~1.1 in rodent capillaries. This ratio will be reduced by hyperoxia by a multiplicative factor of 0.792 (from the 20.8% constriction given above). Inserting these two values of (r_2/r_1) into eqn. (1) of Section 2.3.4 predicts that the decrease of blood flow occurring in hyperoxia (assuming that only pericytes, and not arterioles or venules, are affected by the hyperoxia) will be ~25%.

These experiments suggest that hyperoxia can cause capillary constriction and a cerebral blood flow deficit in both rats and humans.

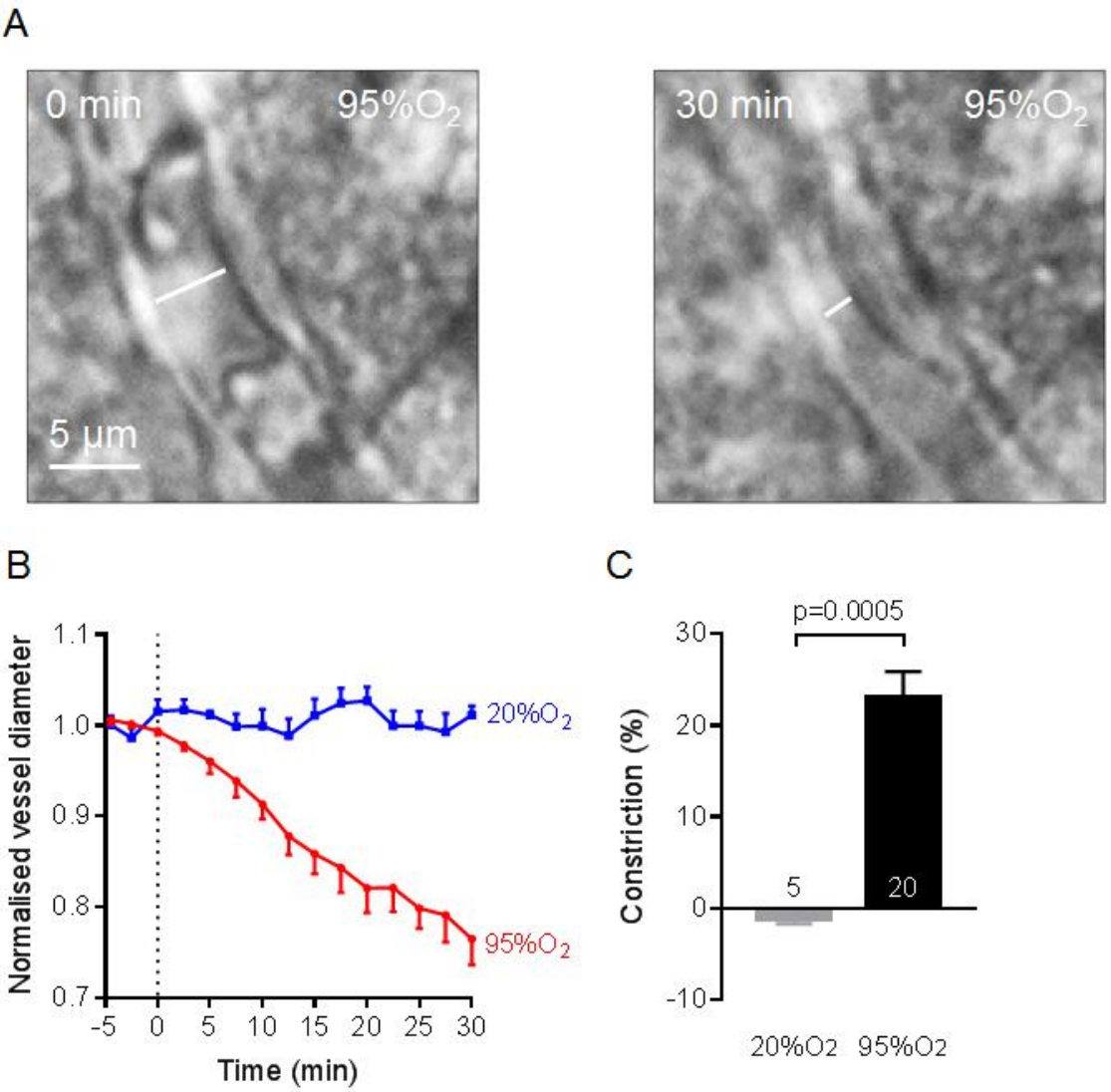

Figure 5.1: Hyperoxia-evoked capillary constriction in rat cerebral cortex.

(A) Representative bright-field images of a rat cortical capillary at 0 (left) and 30 (right) min after application of hyperoxic aCSF oxygenated with 95% O_2, showing capillary constriction evoked by hyperoxia. The white lines in both images display the vessel diameters. (B) Time course of capillary diameter on applying aCSF oxygenated with 95% O_2 (n=20) or aCSF oxygenated with 20% O_2 (also present in the baseline period, n=5) for 30 min. Dotted line indicates the time when application of hyperoxic solution started. (C) Constriction in (B) at t=28-30 min, showing a significant capillary constriction in the presence of hyperoxia in rat cortex.

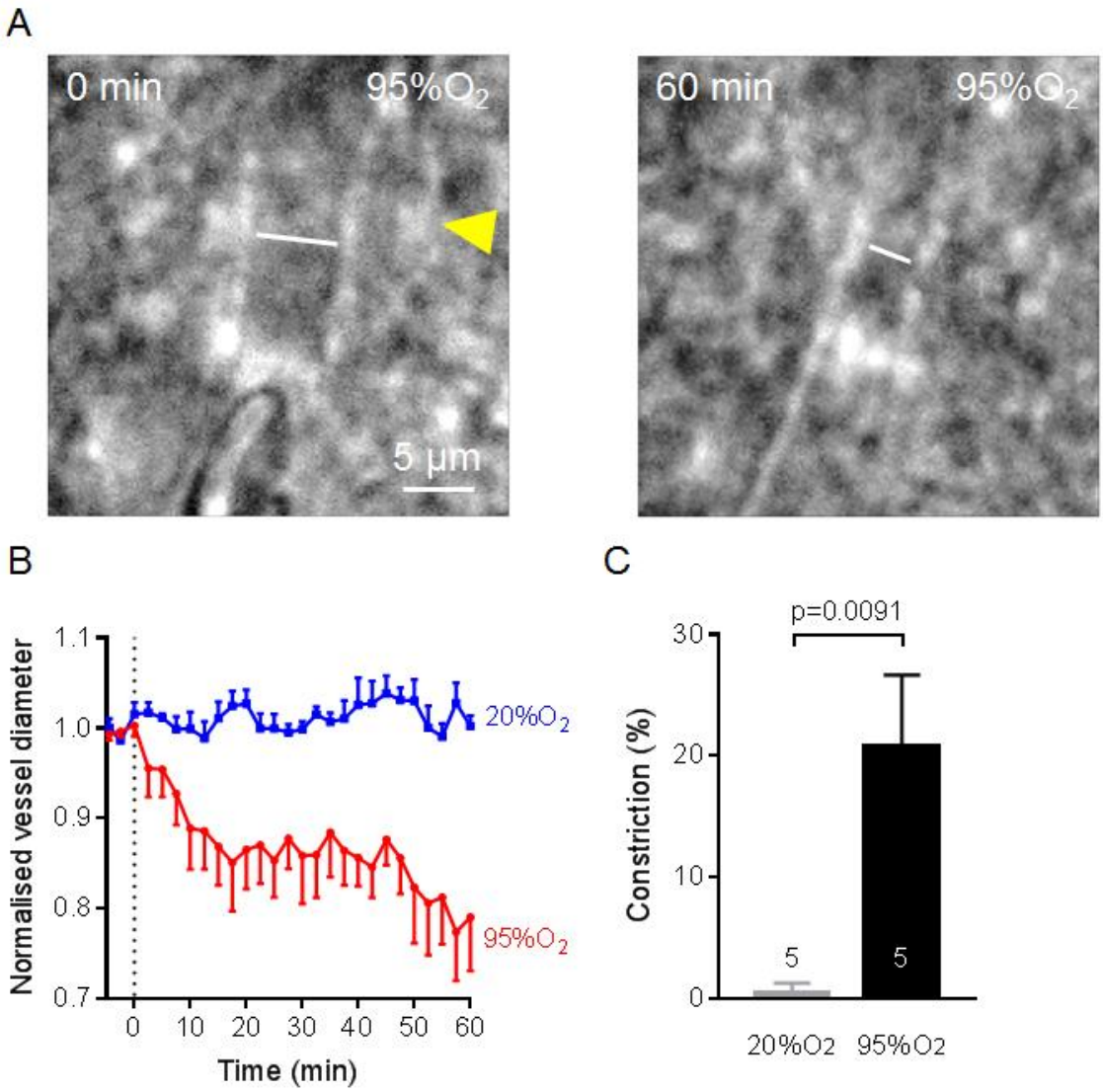

Figure 5.2: Hyperoxia-induced pericyte contraction in human cortical tissue.

(A) Bright-field images of a human cortical capillary with a candidate pericyte (the yellow arrow) at time 0 (left) and 60 (right) min after application of hyperoxic aCSF oxygenated with 95% O_2, showing a capillary constriction. The white lines represent vessel diameters. (B) Capillary constriction at pericyte locations in human cortical tissue was found after application of hyperoxic aCSF (95% O_2, n=5) but not with normoxic aCSF (20% O_2, also present in the baseline period, n=5). Dotted line indicates the time when application of hyperoxia started. (C) Constriction in (B) at t=58-60 min, showing that hyperoxia evoked a significant capillary constriction in human cerebral cortex.

5.3.2 Hyperoxia increases pericyte $[Ca^{2+}]_i$ in NG2-CreERT2 x PC::G5-tdT mice

Pericyte contractility is positively correlated with intracellular calcium concentration (Khennouf *et al.*, 2018; Rungta *et al.*, 2018) and calcium is needed for calmodulin-induced activation of myosin light chain kinase, resulting in phosphorylation of the myosin light chain that interacts with αSMA to cause contraction (Hamilton, Attwell & Hall, 2010).

Brain slices from NG2-CreERT2 x PC::G5-tdT mice were used to quantify calcium signals in pericytes. Hyperoxia evoked an increase in GCaMP fluorescence in pericytes (Fig. 5.3A, B) with the largest percentage increase ($\Delta F/F$), after 4-6 min, of 11.5 ± 3.3% (averaged over 5 frames, n=8, p=0.0007 compared to $\Delta F/F$ of 0.0 ± 1.3%, n=16 from capillaries perfused with normoxic solution, Fig. 5.3C, D). This implies that hyperoxia can raise the intracellular calcium concentration in pericytes, which presumably generates the capillary constriction shown above. Note that the Fig. 5.3C shows the exact value at each time point but statistical analysis was performed using the average intensity from 5 frames.

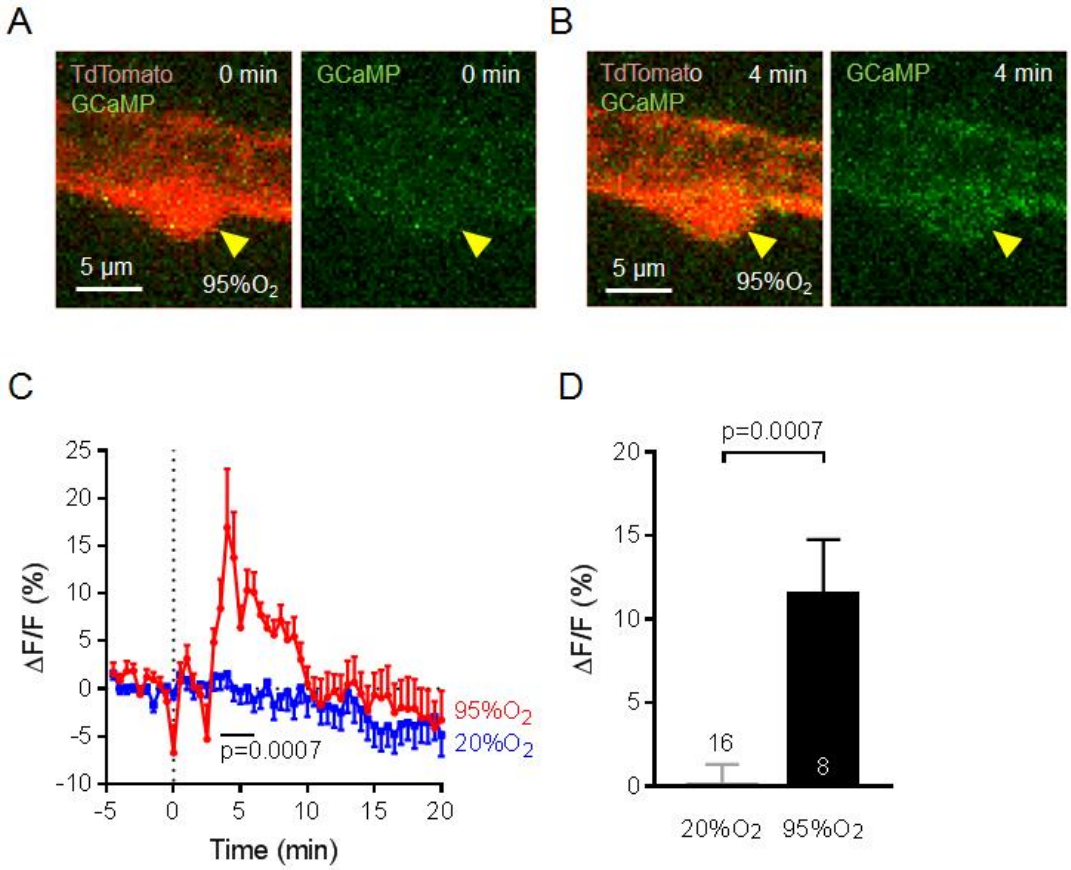

Figure 5.3: Hyperoxia-evoked $[Ca^{2+}]_i$ rise in mouse cerebral cortex pericytes.

(A and B) Fluorescent images of a cortical pericyte (yellow arrows) from NG2-CreERT2 x PC::G5-tdT mice, which express TdTomato (red) and the calcium indicator GCaMP5G (green) in pericytes, at time 0 (A) and 4 min (B) after application of hyperoxic solution. There was a rise in GCaMP5G fluorescence after superfusing hyperoxic aCSF, indicating that $[Ca^{2+}]_i$ is increased. (C) Time course of the increase of GCaMP5G fluorescence (ΔF/F) on application of aCSF oxygenated with 95% O_2 (n=8) or aCSF oxygenated with 20% O_2 (also used for the baseline period, n=16) for 20 min, showing a peak increase of $[Ca^{2+}]_i$ at time 4-6 min. The calcium signal then decays even though the contraction continues to increase (Figs. 5.1 and 5.2), possibly reflecting an increase of Ca^{2+}-sensitivity of the myofilaments e.g. due to rho kinase activity. (D) ΔF/F in (C) at t=4-6 min, showing a significant increase in GCaMP5G fluorescence after application of aCSF oxygenated with 95% O_2.

5.3.3 Hyperoxia-evoked capillary constriction in rat slices was partially reversed by returning to normoxia

To investigate whether hyperoxia-induced pericyte contraction can be reversed after switching back to normoxia, I first perfused rat cortical slices with aCSF gassed with 95% O_2 for 30 min before changing the solution back to aCSF gassed with 20% O_2 for another 30 min.

Returning the slices to superfusion of 20% O_2 could only partly but significantly reverse the hyperxia-evoked capillary constriction by 33.4%, reducing the constriction from 31.7 ± 4.9% after 30 min of hyperoxic solution (not significantly different from the constriction seen in section 5.3.1, p=0.18) to 21.1 ± 3.9% after 30 min of reintroduction of normoxic aCSF (n=7, p=0.017, Fig. 5.4A, B). This implies that the higher oxygen tension causes a prolonged constriction that needs a long time to recover.

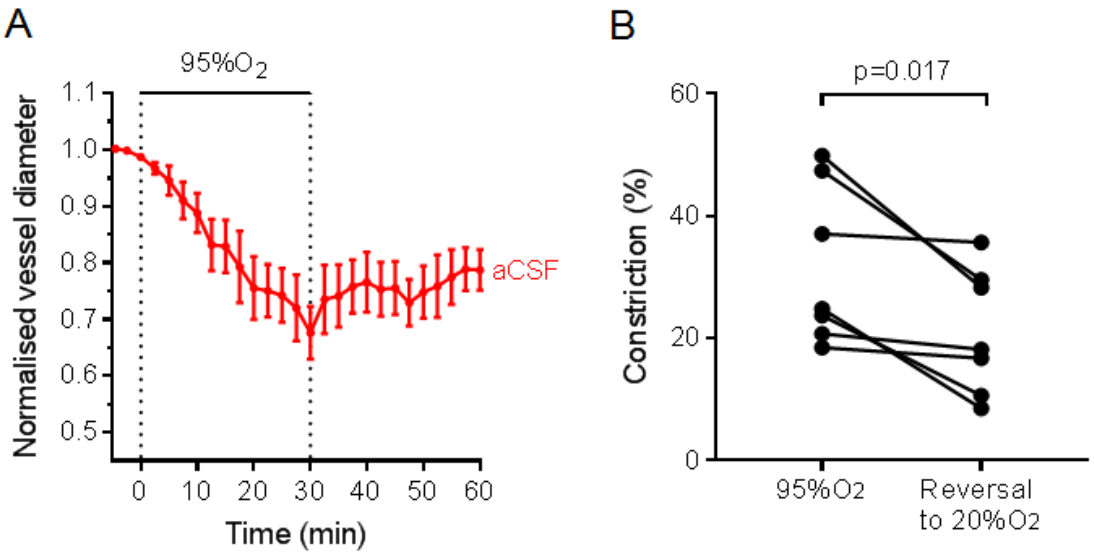

Figure 5.4: Vasoconstriction evoked by hyperoxia is partly reversed by returning to normoxia.

(A) Capillary diameter changes at pericyte locations in response to 30 min of aCSF oxygenated with 95% O_2 then 30 min of aCSF oxygenated with 20% O_2 (n=7), showing that hyperoxia-evoked constriction was partially reversed when the gas was changed back to 20% O_2.

(B) Comparison of the constriction at the end of application of hyperoxic solution (t=28-30 min) and of normoxic solution (t=58-60 min).

5.3.4 Reactive oxygen species are generated in hyperoxic conditions

Because hyperoxia has been shown to increase cellular ROS production (Pendyala *et al.*, 2009), I performed live cell staining with DHE to visualise cytosolic superoxide production and with MitoSOX to visualise mitochondrial superoxide production, in order to identify the source of ROS that are generated in hyperoxic conditions. MitoSOX is a mitochondrially-targeted superoxide indicator that accumulates in the mitochondrial matrix (Robinson *et al.*, 2006).

When compared to application of aCSF oxygenated with 20% O_2, application of aCSF oxygenated with 95% O_2 significantly increased the mean fluorescence of DHE (n=18 in each condition, p=0.0068, Fig. 5.5A, B) and of MitoSOX (n=18 in each condition, p=0.030, Fig. 5.5C, D), suggesting that both cytosolic and mitochondrial ROS production in the brain cortex are increased in hyperoxia. Note that biological membranes at neutral pH are relatively impermeable to superoxide (Mumbengegwi *et al.*, 2008). DHE labelling was typically cytosolic in appearance, whereas MitoSOX labelled small bodies that were presumably mitochondria, but with the magnification used it would be difficult to differentiate for certain between cytosolic and mitochondrial staining.

By using immunohistochemistry to label for the pericyte marker PDGFRβ in brain slices that were incubated with 95% O_2 and MitoSOX, I showed that pericytes were also stained by MitoSOX (Fig. 5.5E). However, other cells in the brain slices were also stained with this dye, suggesting that there was mitochondrial ROS production in both pericytes and other cells in the brain during tissue hyperoxia. Quantification of MitoSOX signals after the intense washing steps and incubation performed to label NG2 might not reflect the real intensity before this processing since the dye might diffuse out of the mitochondria during the processing. Thus, it is not possible to reliably

quantify the MitoSOX signals in pericytes using this approach. Employing Isolectin B4 labelling might circumvent this problem in future work.

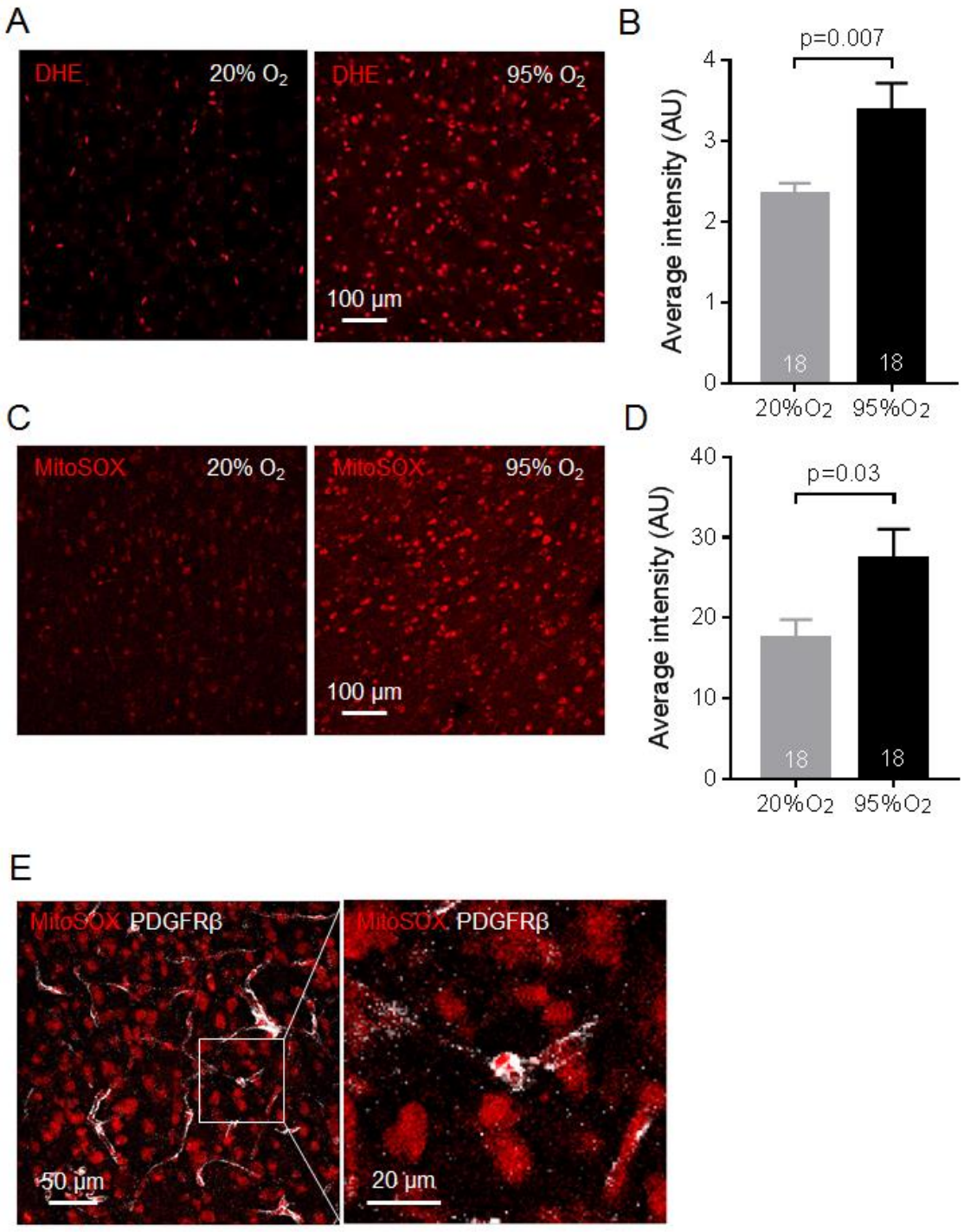

Figure 5.5: Hyperoxia induces cytosolic and mitochondrial ROS production.

(A) Dihydroethidium (DHE) staining of rat cortical slices incubated in aCSF with 20% O_2 (left) and with 95% O_2 (right) to visualise cytosolic superoxide production. Cytosolic

reactive oxygen species (ROS) production was increased when the slices were hyperoxic.

(B) Average intensities of DHE staining of rat cortical slices incubated in aCSF oxygenated with 20% O_2 and with 95% O_2, showing a significantly higher level of fluorescence in hyperoxic slices.

(C) MitoSOX staining for mitochondrial ROS production in rat brain slices in normoxic and hyperoxic conditions, showing an increase in mitochondrial ROS production when the slices were in hyperoxic solution.

(D) Average intensities of MitoSOX staining of normoxic (incubated in aCSF oxygenated with 20% O_2) and hyperoxic (incubated in aCSF oxygenated with 95% O_2) rat cortical slices, showing that mitochondrial ROS production was enhanced in hyperoxia.

(E) Pericytes (labelled by PDGFRβ, white) generated mitochondrial ROS (labelled by MitoSOX staining, red) in hyperoxic conditions. Other cells in the brain were also stained by MitoSOX.

5.3.5 Blocking cytosolic ROS production by NOX or blocking mitochondrial ROS production does not prevent hyperoxia-evoked constriction

Hyperoxia was previously shown to increase ROS production (Demchenko *et al.*, 2002; Mattos *et al.*, 2019). One potential source of this ROS generation is NOX, which is the only enzyme that has a primary function of creating ROS (Rodiño-Janeiro *et al.*, 2013). NOX4 is the main NOX in the vasculature, and is present in pericytes and endothelial cells while NOX2 is present in perivascular macrophages, parenchymal microglia and to a lesser extent in endothelial cells and pericytes (Chen *et al.*, 2012; Zeisel *et al.*, 2018). These enzymes can produce more ROS when the concentration of oxygen is higher (Nisimoto *et al.*, 2014). Another potential origin of hyperoxia-induced ROS is from mitochondria, because mitochondrial superoxide production increased linearly with oxygen concentration (Turrens *et al.*, 1982; Turrens, 2003).

To examine the contribution of NOXs, especially NOX4, in hyperoxia-evoked capillary constriction, I applied the specific NOX4 inhibitor GKT137831 (which I showed in Chapter 4 completely blocked the capillary constriction evoked by $A\beta_{1-42}$) or the nonspecific NOX blocker diphenyleneiodonium (DPI) for 15 min before application of hyperoxia and observed diameter changes in rat cortical slices (in chapter 4, section 4.3.4, I showed that these drugs alone had no effect on capillary diameter). GKT137831 (0.45 μM) failed to stop hyperoxia-induced vasoconstriction, and in its presence 30 min of hyperoxia evoked a capillary constriction of 28.3 ± 12.1% (n=5, p>0.99 compared to hyperoxic capillary constriction without any blocker, Fig. 5.6A, B). In addition, DPI (10 μM) could not prevent hyperoxic vasoconstriction, with hyperoxia evoking a constriction of 22.9 ± 5.8% (n=5, p=0.99 compared to no DPI, Fig. 5.6A, B).

Investigation of the involvement of the mitochondrial ROS in hyperoxic vasoconstriction in rat brain slices was performed by perfusing a mitochondrially-targeted antioxidant, MitoQ (500 nM) for 15 min before superimposing 95% O_2. A constriction of 17.2 ± 3.8% (n=11, p=0.71 compared to in the absence of the blocker, Fig. 5.6A, B) was seen in the presence of MitoQ.

These experiments suggest that NOXs and mitochondria are not involved in the production of ROS that mediate hyperoxic capillary constriction. Although the total cytosolic and mitochondrial ROS production have been shown to be increased in hyperoxia (see Section 5.3.4), it is difficult to determine the amount of ROS production within pericytes because of the limitations described in Section 5.3.4.

Applying GKT137831 (0.45 μM), DPI (10 μM) or MitoQ (500 nM) alone (in normoxia) for 15 min did not evoke significant capillary diameter changes (GKT137831: -2.5 ± 0.9%, n=5, p=0.13; DPI: 5.0 ± 1.5%, n=5, p=0.063; MitoQ: 0.0 ± 1.1%, n=11, p=0.97).

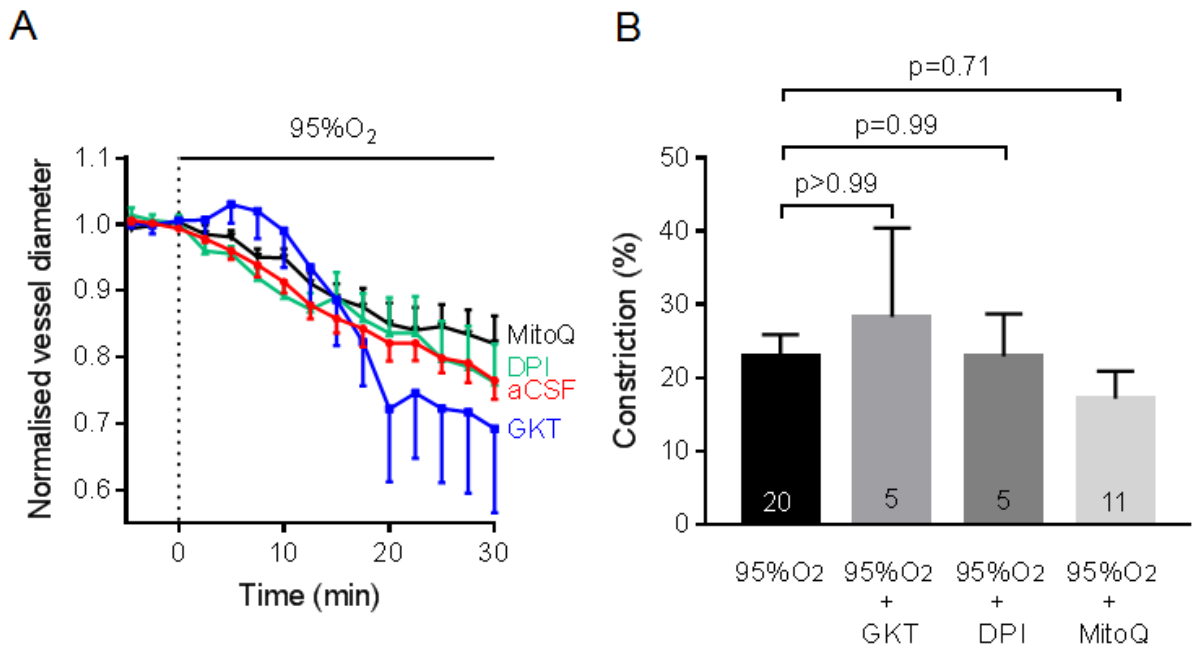

Figure 5.6: Hyperoxia-evoked capillary constriction is not inhibited by a NADPH oxidase blocker or mitochondrial ROS blocker alone.

(A) Hyperoxic aCSF (n=20, red trace) induced capillary constriction after 30 min that was not inhibited by the presence of the NOX4 inhibitor GKT137831 (GKT, 0.45 μM, n=5, blue trace), the nonspecific NOX blocker DPI (10 μM, n=5, green trace) or the mitochondrially-targeted antioxidant MitoQ (500 nM, n=11, black trace). Inhibitors were applied for 15 min before application of 95% O_2 (dotted line) and diameters were normalised to the pre-hyperoxia baseline.

(B) Constriction in (A) at t=28-30 min, showing that hyperoxic vasoconstriction was not inhibited by GKT137831, DPI or MitoQ.

5.3.6 Hyperoxia does not evoke capillary constriction through endothelin (ET) signalling or depletion of nitric oxide

Hyperoxia has been shown to reduce retinal blood flow through endothelin release (Dallinger *et al.*, 2000; Song *et al.*, 2016). Others have shown that hyperoxia constricted cerebral arteries through the nitric oxide (NO)-scavenging effect of superoxide (Zhilyaev *et al.*, 2003).

To investigate whether ET is involved in hyperoxic vasoconstriction, I perfused an inhibitor of vasoconstricting endothelin-1 type A (ET_A) receptors (BQ-123, 1 µM) for 15 min onto rat cortical slices before increasing the oxygen level to 95% O_2. Hyperoxia in the presence of BQ-123 evoked a vasoconstriction of 17.8 ± 4.2% (n=9, not significantly different (p=0.66) compared to the constriction from hyperoxia without any blocker, Fig. 5.7A, B), indicating that ET does not contribute to hyperoxia evoked capillary vasoconstriction.

The nitric oxide synthase inhibitor N_ω-nitro-L-arginine (L-NNA) also could not prevent hyperoxia-evoked capillary constriction in rat brain slices. In its presence, a capillary constriction of 20.3 ± 3.7% (100 µM, n=9, p=0.59, Fig. 5.7A, B) was found after application of 95% O2 for 30 min. This implies that depletion of NO is not the cause of this vasoconstriction.

Finally, I showed that the combination of the ET_A inhibitor BQ-123 (1 µM) and the nitric oxide synthase inhibitor L-NNA (100 µM) failed to prevent hyperoxia-induced vasoconstriction. The capillary constriction after imposing 30 min of 95% O_2 was 29.9 ± 4.4% (100 µM, n=10, p=0.58 compared to without the blockers, Fig. 5.7A, B), confirming that ET and NO signalling are not involved in the hyperoxic vasoconstriction.

As control experiments, application of BQ-123 (1 μM), L-NNA (100 μM) or BQ-123 with L-NNA in normoxia did not evoke significant diameter changes after 15 min (BQ-123: -0.3 ± 3.2%, n=9, p=0.43; L-NNA: 0.9 ± 3.5%, n=9, p=0.73; BQ-123 with L-NNA: 1.1 ± 1.3%, n=10, p=0.77).

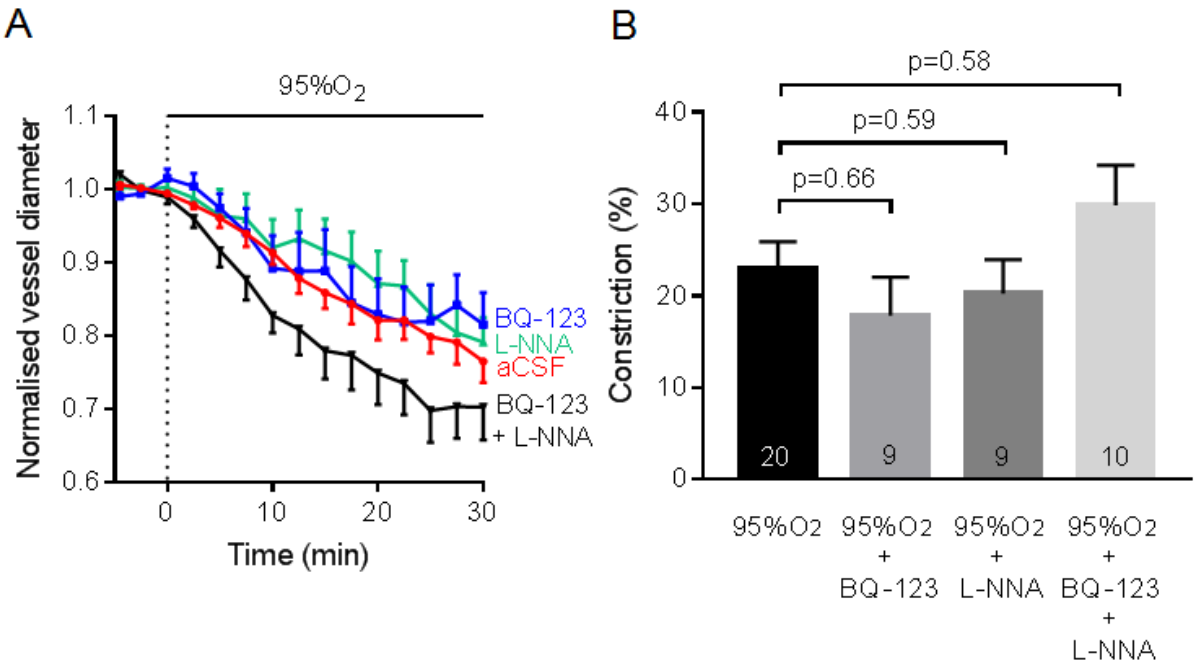

Figure 5.7: Hyperoxia-evoked pericyte contraction is not mediated through endothelin signalling or depletion of nitric oxide.

(A) Time course of capillary diameter on applying aCSF oxygenated with 95% O_2 (n=20, red trace) alone, or in the presence of the endothelin-1 type A receptor (ET_A) inhibitor BQ-123 (1 μM, n=9, blue trace); the nitric oxide synthase inhibitor N_ω-nitro-L-arginine (L-NNA, 100 μM, n=9, green trace); or the combination of BQ-123 and L-NNA (n=10, black trace). Diameters were normalised to the pre-hyperoxic phase (before the dotted line). (B) Constriction in (A) at t=28-30 min, showing that the hyperoxia-evoked capillary constriction was not significantly blocked by BQ-123, L-NNA or the combination of BQ-123 and L-NNA.

5.3.7 20-hydroxyeicosatetraenoic acid (20-HETE) is involved in hyperoxic capillary constriction in rat but not in human brain slices

Increased production of the vasoconstricting arachidonic acid derivative 20-hydroxyeicosatetraenoic acid (20-HETE) has been shown to be one of the mechanisms underlying hyperoxic vasoconstriction in the peripheral circulation (Ngo *et al.*, 2013) and in the retina (Mishra, Hamid & Newman, 2011). However, the involvement of 20-HETE generation in hyperoxia-evoked pericyte-mediated cerebral capillary contraction has not been studied.

In rat brain slices, I showed that the 20-HETE synthesis inhibitor, HET0016 (100 nM) could inhibit by 58% the hyperoxic vasoconstriction evoked by 30 min of 95% O_2, reducing the constriction to 9.5 ± 2.6% (n=8) from a constriction of 23.0 ± 2.9% (n=20, p=0.011, Fig. 5.8A, B) without the blocker. This implies that hyperoxia evokes pericyte contraction partly via 20-HETE production in rats, which is consistent with the measured EC_{50} for O_2 of 55 μM for the enzyme that makes 20-HETE (Harder *et al.*, 1996), so that more 20-HETE is made when the superfused [O_2] is increased from 20% to 95% and the [O_2] level in the brain slice rises from around 40 μM to around 125 μM (reviewed by Attwell *et al.*, 2010).

Surprisingly, such inhibition of hyperoxic capillary constriction by HET0016 was not found in human tissue. Application of 95% O_2 for 1 h in the presence of HET0016 (100 nM) evoked a constriction of 31.7 ± 17.3% (n=5) compared to a constriction of 20.8 ± 5.9% (n=5, p=0.57, Fig. 5.8C, D) in the absence of the inhibitor. This suggests that the production of 20-HETE might not contribute to hyperoxic pericyte contraction in the human brain, since HET0016 is known to block the production of 20-HETE in human tissue (Miyata *et al.*, 2001).

Application of HET0016 (100 nM) alone for 15 min did not evoke significant vascular responses either in rat (1.1 ± 1.3%, n=8, p=0.31) or in human (5.3 ± 2.2%, n=5, p=0.13) brain slices.

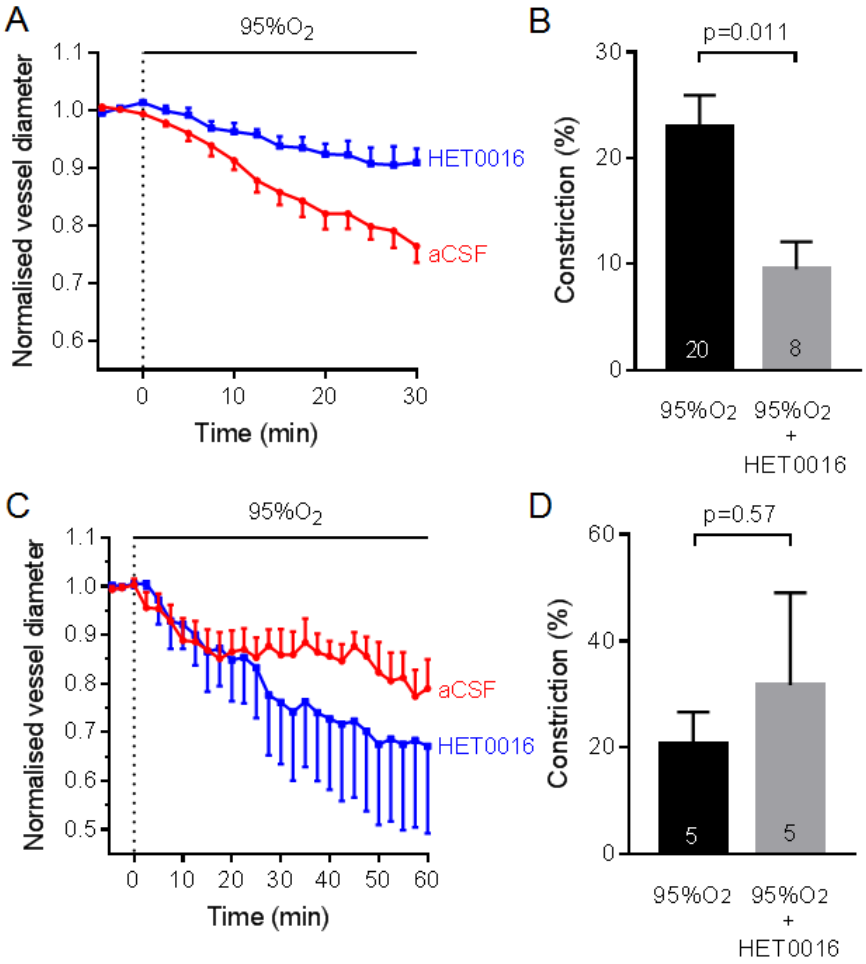

Figure 5.8: Hyperoxia-induced vasoconstriction is partly mediated by 20-HETE production in rat but not in human brain slices.

(A) Hyperoxic vasoconstriction after 30 min in rat cortical slices was partly inhibited by application of the inhibitor of the synthesis of 20-hydroxyeicosatetraenoic acid (20-HETE) HET0016 (100 nM, n=8). Diameters were normalised to the pre-hyperoxic phase (before the dotted line). (B) Constriction in (A) at t=28-30 min, showing that application of HET0016 partially blocked hyperoxia-evoked capillary constriction in rat cortical slices. (C) Hyperoxia-induced constriction after 60 min in human cortical slices was not prevented by superfusing HET0016 (100 nM, n=5). Diameters were normalised to the pre-hyperoxic phase (before the dotted line). (D) Constriction in (C) at t=58-60 min.

5.4 Discussion

The data from experiments in this chapter suggest two key results for understanding cerebral capillary diameter responses to hyperoxia: (i) a high level of oxygen causes pericyte contraction, resulting in smaller capillary diameters and thus reduced cerebral blood flow; and (ii) hyperoxia-evoked capillary constriction is mediated partly via 20-HETE at least in rats.

In these experiments, I used solution bubbled with 95% O_2 and 5% CO_2 to mimic hyperoxic conditions. This produces an unphysiologically high [O_2] in the slice of 285-345 μM (Hall *et al.*, 2012), i.e. a PO_2 of 220-265 mmHg, which is similar to the value for hyperbaric hyperoxic patients (brain tissue oxygen tension of 220 mmHg on average) (Hlatky *et al.*, 2008; Rockswold *et al.*, 2010). 20% O_2 has been shown to produce an approximately physiological [O_2] in the slice (10-40 μM) at the depths where I normally image (Hall & Attwell, 2008) and was used to mimic normoxic conditions. This is similar to the brain tissue oxygen tension of less than 50 mmHg in normoxic patients (Maas *et al.*, 1993; Attwell *et al.*, 2010; Mach *et al.*, 2011; De Georgia, 2015; Ortiz-Prado *et al.*, 2019).

Perfusing hyperoxic solution caused pericyte contraction and capillary constriction in both rat and human brain slices, with a predicted *in vivo* blood flow reduction of ~25% from human tissue experiments. This prediction is comparable to the results of studies in patients that showed a cerebral blood flow deficit of 10 - 30% after inhalation of hyperoxic air (Watson *et al.*, 2000; Brugniaux *et al.*, 2018; Mattos *et al.*, 2019). Capillaries from rats were found to react faster and more strongly to hyperoxia than capillaries from human tissue, which might be explained by the difference in species. However, it must be noted that the conditions of human tissue slices were worse than those of rats, because the time from tissue excision to tissue

slicing was longer due to the transportation time from the operating theatre, thus complicating the comparison between responses in rat and human tissue.

Supporting a role for pericytes in hyperoxic vasoconstriction, I found a rapid rise in pericyte intracellular calcium concentration in response to hyperoxic solution. Because calcium is needed for the activation of myosin light chain kinase that promotes binding of actin and myosin (Hamilton, Attwell & Hall, 2010), pericyte calcium concentration controls pericyte contraction (Khennouf *et al.*, 2018; Rungta *et al.*, 2018). However, vasoactive stimuli can also affect pericyte contraction via pathways such as Rho kinase (Hamilton, Attwell & Hall, 2010) which alter the sensitivity of the contractile apparatus to calcium (Khalil, 2010). This may explain the observed difference in the time courses of the calcium concentration rise and the capillary constriction.

Upon returning to normoxia after hyperoxia, constricted capillaries slowly relaxed but a complete reversal was not achieved in 30 min. In contrast, a study in healthy volunteers found that cerebral blood flow returned to normal after a period of six min of breathing air after breathing 100% O_2 for 30 min (Watson *et al.*, 2000). This difference might arise from differences in the experimental conditions, such that in *ex vivo* experiments replenishment of vasodilating agents was slower than *in vivo*.

I tested several underlying mechanisms of hyperoxic vasoconstriction proposed in studies of cerebral arteries, to see whether they are relevant in hyperoxia-induced pericyte contraction, as follows.

(i) Production of ROS.

I found that the production of both cytosolic and mitochondrial ROS in brain cortex was increased in hyperoxia (Fig. 5.5). This is consistent with other studies showing that hyperoxia increases ROS generation in the cytosol of cells in the caudal

solitary complex in rats (Ciarlone & Dean, 2016), in isolated lung mitochondria (Turrens *et al.*, 1982; Turrens, 2003) and in mitochondria of rat brain cortex (Bin-Jaliah & Haffor, 2018). From immunohistochemistry, pericytes, as well as other cells in the brain, were shown to produce mitochondrial superoxide in hyperoxia but it was difficult to deduce rigorously what percentage of the total ROS production was due to pericytes. Further experiments labelling pericytes in live tissue might be useful to quantify ROS in pericytes.

Surprisingly, blocking NOXs (including NOX4, which has been shown to increase activity in high oxygen (Nisimoto *et al.*, 2014)), or reducing mitochondrial ROS production with MitoQ, was not sufficient to suppress hyperoxic vasoconstriction. Conceivably, therefore, hyperoxia-evoked capillary constriction might not be mediated through ROS.

Further evidence that ROS might not mediate hyperoxic vasoconstriction is that blocking potential pathways involved in ROS-evoked contraction of smooth muscle cells did not inhibit the vasoconstriction caused by hyperoxia. The proposed mechanisms by which ROS cause vasoconstriction include depletion of NO by superoxide (Demchenko *et al.*, 2002; Zhilyaev *et al.*, 2003), induction of endothelin-1 release (Prasad, 1991) and a direct ROS effect on mural cells to release intracellular calcium from internal stores (Kamouchi *et al.*, 2007). Although several studies on cerebral arteries have shown that hyperoxia promotes the production of superoxide, which binds to NO to create peroxynitrite (Rodiño-Janeiro *et al.*, 2013; Collin, 2019) and thus attenuates NO-dependent vasodilation (Demchenko *et al.*, 2002; Zhilyaev *et al.*, 2003), I found that blocking NO production with L-NNA could not prevent hyperoxic capillary constriction. However, this could also be because, unlike in arterioles, NO is not involved in capillary dilation (Mishra *et al.*, 2016). Blocking ET_A receptors did not

affect hyperoxia-induced capillary constriction in this study, arguing against a role of endothelin in this process. The possibility of hyperoxia-induced ROS acting directly to release calcium from pericyte internal stores (Kamouchi *et al.*, 2007) thus increasing the intracellular calcium concentration and evoking capillary constriction cannot be assessed by the experiments performed.

Hence, from these experiments, it can be concluded that there is an increased overall ROS production in both the cytosol and mitochondria in hyperoxia but ROS might not contribute to generating hyperoxia-induced vasoconstriction. Further studies to quantify ROS production in pericytes and to link ROS to pericyte contraction in hyperoxia are needed.

(ii) Release of ET

As discussed in the paragraph above, although several studies have shown that endothelin was produced in hyperoxic conditions (Higgins *et al.*, 1998; Winegrad *et al.*, 1999), blocking endothelin signalling with BQ-123 did not prevent hyperoxic capillary vasoconstriction. Thus ET signalling does not contribute to this pericyte-mediated vasoconstriction.

(iii) Production of 20-HETE

Increased 20-HETE production via the reaction catalysed by CYP4A was shown in hyperoxia (Zhu, Park & Gidday, 1998; Mishra, Hamid & Newman, 2011; Ngo *et al.*, 2013). This can be explained by the fact that this reaction in rats has a Michaelis constant (K_m) of ~55 μM at 37^{o}C so increasing the oxygen level from 20% O_2 (giving [O_2] in the tissue of ~40 μM) to 95% O_2 ([O_2] in the tissue of ~125 μM) would accelerate this reaction (Harder *et al.*, 1996; Attwell *et al.*, 2010). 20-HETE causes vasoconstriction in the cerebral circulation (Harder *et al.*, 1994; Lange *et al.*, 1997) by inducing contraction of vascular smooth muscle cells (Hama-Tomioka *et al.*, 2009;

Elshenawy *et al.*, 2017) and pericytes (Gonzalez-Fernandez *et al.*, 2020). This occurs by activation of L-type Ca^{2+} channels via inhibition of large conductance Ca^{2+}-activated K^+ channels and PKC signalling (Harder *et al.*, 1997; Hoopes *et al.*, 2015), activation of Rho kinase (Randriamboavonjy, Busse & Fleming, 2003) and stimulation of NOX to increase superoxide production in vascular smooth muscle (Hama-Tomioka *et al.*, 2009). Thus, production of 20-HETE is well poised to be an underlying mechanism in hyperoxic vasoconstriction.

Indeed, in rats, I found that HET0016, the 20-HETE synthesis blocker, could partially suppress hyperoxia-induced capillary constriction. However, interestingly, this inhibition was not found in human tissue. One possibility is that the CYPs expressed in human are CYP4A11 and CYP4F2, which produces the highest amount of 20-HETE in human (Fan *et al.*, 2016), while those expressed in rats are CYP4A1, 2, 3, and 8 (Edson & Rettie, 2013), hence the sensitivity to oxygen of the enzymes in human and rats might be different. To my knowledge, there is no study exploring the oxygen sensitivity of CYP enzymes in human tissue and more experiments are needed to explore the reason underlying this difference in responses in rats and in human.

Oxygen-induced 20-HETE generation might also contribute to the increased ROS production found in hyperoxia, because 20-HETE has been shown to increase ROS production from NADPH oxidases (Hama-Tomioka *et al.*, 2009) and from mitochondria (Lakhkar *et al.*, 2016). Another pathway that might be involved is the release of adenosine, which is expected to decrease in hyperoxia.

In conclusion, in rat brain slices, hyperoxia evokes capillary constriction as a result of the higher $[O_2]$ promoting 20-HETE production, which evokes a $[Ca^{2+}]_i$ increase in pericytes, leading to pericyte contraction.

5.5 Suggestions for future work

Following on from the work in this chapter that demonstrates hyperoxic capillary constriction *ex vivo*, extending these findings to *in vivo* experiments to quantify both baseline CBF and stimulation-evoked CBF changes during hyperoxia would be valuable. Moreover, *in vivo* experiments would also allow investigation of the contribution of 20-HETE to this vasoconstriction by intravenously injecting HET0016, which significantly inhibits brain 20-HETE formation (Mu *et al.*, 2008).

Because it is possible that the increased ROS seen in hyperoxia are generated in cells other than pericytes, marking pericytes with isolection B4 would allow quantification of the signal inside pericytes. Another possible mechanism underlying hyperoxic vasoconstriction is the reduction of adenosine release expected in hyperoxia. Inhibiting adenosine receptors in brain slices perfused with solutions oxygenated with 20% O_2 and 95% O_2 could be done to determine whether adenosine evokes vasodilation in normoxic conditions. If there is a constriction with adenosine blockers in experiments with normoxia but not with hyperoxia, adenosine might contribute to the hyperoxic vasoconstriction.

While 20-HETE was found to contribute to hyperoxic pericyte contraction in rats, it was not involved in hyperoxic vasoconstriction in humans (see Section 5.3.7). The discrepancy, which might occur because of different subtypes of CYP4A and CYP4F in different species (Edson & Rettie, 2013), could be addressed by quantification of the level of 20-HETE production in brain slices from rats and human in hyperoxic condition, possibly via ELISA. This would define whether 20-HETE production is increased in hyperoxia in each species or not.

Because the experiments in this chapter showed that 20-HETE did not underlie the hyperoxia-induced capillary constriction in humans, pharmacological attempts to

block the hyperoxic vasoconstriction in human brain slices with other drugs such as ROS scavengers including ascorbic acid, ET_A blockers, nitric oxide synthase inhibitors or inhibitors of voltage gated calcium channels, might provide more insight into the underlying mechanism of hyperoxia-induced pericyte contraction in humans.

5.6 Conclusion

My experiments showed that hyperoxia evokes pericyte contraction and capillary vasoconstriction and that these processes were mediated via 20-HETE (at least in rats). Hyperoxia-evoked capillary constriction can result in a significant reduction of cerebral blood flow, thus there might be less energy substrate available for the brain and slower removal of metabolic waste products. Both of these might lead to poorer brain function, especially in critically ill patients at risk of receiving excess oxygen.

Chapter 6: COVID-19 and pericyte contractility

6.1 Introduction

Coronavirus disease 2019 (COVID-19) is a pandemic disease (Ghebreyesus, 2020), which is caused by a novel virus called Severe Acute Respiratory Syndrome CoronaVirus 2 (SARS-CoV-2). The virus primarily infects the respiratory system (Esakandari *et al.*, 2020) and COVID-19 patients can present with varying severity ranging from having mild symptoms, including fever and sore throat, to having severe symptoms, such as respiratory failure and septic shock (Wu & McGoogan, 2020).

Other organ systems, such as the central nervous system, can also be affected by SARS-CoV-2, probably via either viral spreading through the blood (Lescure *et al.*, 2020) or from the effects of inflammatory mediators (Østergaard, 2021). Upon further investigation, cerebral hypoperfusion is found in COVID-19 patients even without any focal signs suggestive of stroke (Helms *et al.*, 2020; Soldatelli *et al.*, 2020) or neurological complications (Qin *et al.*, 2021). These findings suggest that SARS-CoV-2 not only affects the macro-vasculature, resulting in apparent stroke and intracranial haemorrhage, but also affects the microvasculature and causes dysfunction as seen in the brains of the patients (Østergaard, 2021; Lee *et al.*, 2021).

Angiotensin converting enzyme 2 (ACE2) plays an important role in COVID-19 infection because it is a major receptor for SARS-CoV-2 (Ou *et al.*, 2020). ACE2 is expressed in lung epithelial cells, hence explaining why SARS-CoV-2 primarily causes respiratory symptoms. In the brain and the heart, the main cells that express ACE2 are pericytes and venous vascular smooth muscle cells (He *et al.*, 2020; Chen *et al.*, 2020b), and ACE2-expressing brain pericytes have been shown to become infected in COVID-19 (Bocci *et al.*, 2021). Aside from being the receptor for SARS-CoV-2, ACE2 also plays an important role in the renin-angiotensin-aldosterone system (RAS)

by converting vasoconstricting angiotensin II (Ang II) to vasodilating angiotensin-(1-7) (Ang(1-7): Santos *et al.*, 2018), both of which can affect the contractility of vascular smooth muscle cells and pericytes, as follows.

Ang II mediates its action through two different receptors, the AT1 receptors (AT1Rs) and AT2 receptors (AT2Rs) (Kaschina & Unger, 2003). In vascular smooth muscle cells and retinal pericytes, activating AT1Rs evokes vasoconstriction (Kawamura *et al.*, 2004; Vincent *et al.*, 2005; De Silva & Faraci, 2013), while stimulation of AT2Rs results in hyperpolarisation and vasodilation (Dimitropoulou *et al.*, 2001; Vincent *et al.*, 2005). Both AT1Rs and AT2Rs are found in human brain pericytes but the expression of AT1Rs is larger than that of AT2Rs (Kuroda *et al.*, 2014), so the net effect of Ang II on pericytes may be expected to be contraction. The ACE2-derived Ang(1-7) mediates its effect through Mas receptors (MasRs) which relax vascular smooth muscle cells (Gironacci *et al.*, 2000; Schindler *et al.*, 2007). Transcriptomic data show that pericytes also express MasRs (Vanlandewijck *et al.*, 2018), suggesting that a similar mechanism of dilation might also happen in pericytes. Hence, the net effect of ACE2 is to decrease the concentration of vasoconstricting Ang II and increase that of vasodilating Ang(1-7).

In SARS-CoV-2 infection, the function of ACE2 is proposed to be disrupted in two ways.

(i) First there can be internalisation of ACE2 along with the virus (Wang *et al.*, 2008; Ou *et al.*, 2020). Binding to ACE2 of the spike protein of the virus, or even of just its receptor binding domain (RBD; the portion of the spike protein that interacts with ACE2 (Lan *et al.*, 2020)), as shown for the closely-related SARS virus (Wang *et al.*, 2008), can trigger internalisation of the virus and ACE2 (Rothlin *et al.*, 2021). This reduces the availability of this enzyme, inhibiting conversion of Ang II to Ang(1-7).

(ii) Secondly, binding of SARS-CoV-2 to ACE2 might block the catalytic site on ACE2 (Castiglione *et al.*, 2021) and again hinder the conversion of Ang II to Ang(1-7). Thus, SARS-CoV-2 or its RBD is hypothesised to reduce ACE2 activity, and this could change the local concentrations of Ang II and Ang(1-7), leading to a cerebral blood flow deficit as seen in COVID-19 patients (Helms *et al.*, 2020; Soldatelli *et al.*, 2020; Qin *et al.*, 2021).

Because pericytes express the majority of ACE2 in the brain (He *et al.*, 2020), possess receptors for both Ang II and Ang(1-7) (He *et al.*, 2018), and are also located on the capillaries which offer the main resistance to intracerebral blood flow (Gould *et al.*, 2017), they are likely to be affected in COVID-19 may thus decrease cerebral blood flow.

The aim of this chapter is to test the hypothesis that SARS-CoV-2 affects pericyte contractility through reduced ACE2 activity, thus causing a cerebral blood flow deficit.

6.2 Methods

6.2.1 Solutions and drugs

Bicarbonate-buffered aCSF was prepared for live imaging experiments and for live incubation for death analysis as outlined in Section 2.1.1. Drugs were diluted in this solution to the final concentrations to be used in the experiments.

Synthesis of RBD and mutated RBD-Y489R (used below) was performed by Professor Ray Owens' group (Oxford University). In short, the vector pOPINTTGneo (Nettleship *et al.*, 2015) was inserted with codon optimised Genblocks (IDT Technology) for the RBD (amino acids 330-532) of SARS-CoV-2 (Genbank MN908947), and human ACE2 (amino acids 19-615). This also included a C-terminal

BirA-His6 tag and pOPINTTGneo-3C-Fc to create C-terminal fusions to Human IgG Fc. The RBD-Y489R mutant was created by first creating two fragments from amplifying the RBD-WT gene using oligos (i) TTGneo_RBD_F and RBD-Y489R_R; and (ii) TTGneo_RBD_R and RBD-Y489R_F. The two resulted fragments were then joined with TTGneo_RBD_F and TTGneo_RBD_R.

TTGneo_RBD_F	5'-gcgtagctgaaaccggcccgaatatcacaaatctttgt-3'
TTGneo_RBD_R	5'-GTGATGGTGATGTTTATTTGTACTTTTTTTCGGTCCGCACAC-3'
RBD-Y489R_F	5'-GGCGTCGAGGGTTTTAACTGTCGCTTCCCACTTCAGTCATACGG-3'
RBD-Y489R_R	5'-CCGTATGACTGAAGTGGGAAGCGACAGTTAAAACCCTCGACGCC-3'

Infusion® cloning was used to insert the gene carrying the Y489R mutation into the vector pOPINTTGneo incorporating a C-terminal His6 tag. The resulted plasmid was sequenced to confirm the successful introduction of the mutation. Recombinant protein was briefly expressed in Expi293™ (ThermoFisher Scientific, UK). Immobilised metal affinity chromatography, using an automated protocol implemented on an ÄKTAxpress (GE Healthcare, UK) and a Superdex 200 10/300GL column using phosphate-buffered saline (PBS) pH 7.4 buffer, was used to purify recombinant proteins from supernatants of cell culture. Recombinant RBD-WT and ACE2-Fc were generated as previously described (Huo *et al.*, 2020). The sequence of the RBD was:

*ETG*P**N**ITNLCPFGEVF**N**ATRFASVYAWNRKRISNCVADYSVLYNSASFSTFKCYGV
SPTKLNDLCFTNVYADSFVIRGDEVRQIAPGQTGKIADYNYKLPDDFTGCVIAWNSN
NLDSKVGGNYNYLYRLFRKSNLKPFERDISTEIYQAGSTPCNGVEGFNCYFPLQSY
GFQPTNGVGYQPYRVVVLSFELLHAPATVCGPKKSTN*KHHHHHH*

(where residues in italics are from the expression vector). The bold residues indicate the glycosylated residues and the underlined residue shows the position of the amino acid that is mutated from tyrosine to arginine in the RBD-Y489R mutant used below.

6.2.2 Bright-field imaging

Syrian golden hamsters were chosen for the experiments because there is more similarity between the human ACE2 spike sequence and that in hamsters, than between the ACE2 spike sequence in humans and that in rats or mice (Chan *et al.*, 2020). In particular, amino acid 353, which is a lysine (K) in human and hamsters but a histidine (H) in mouse, is a key determinant of the infectivity of SARS-CoV (Frieman *et al.*, 2012). Syrian golden hamsters (age 5-24 weeks) of both sexes were humanely culled by cervical dislocation under isoflurane anesthesia in accordance with UK and EU animal law and the brains were extracted. Cortical slices (300 μm thick) were prepared using a vibratome from the extracted brains as outlined in Section 2.3.1.1.

For live imaging experiments on human tissue, healthy brain tissue overlying the tumour, which would normally be discarded during the tumour removal surgery, was given by Miss Human Sethi, consultant neurosurgeon, Division of Neurosurgery, National Hospital for Neurology and Neurosurgery under ethical approval from the National Health Service (REC number 12/NW/0568). The tissue used in the experiments in this chapter was from female subjects aged 40-74. Cortical brain slices (300 μm thick) were prepared from the tissue.

Live pre-incubation in agents for some experiments (see Section 6.3.4-6.3.7, 6.3.9) was performed by placing brain slices from either hamsters or human tissue in aCSF with or without drugs (at 35^{o}C and oxygenated with 20% O_2, 5% CO_2 and 75% N_2).

Brain slices from hamsters and human tissue, with or without pre-incubation, were put under a bright-field microscope and perfused with bicarbonate-buffered aCSF, bubbled with 20% O_2, 5% CO_2, and 75% N_2 at 33-36^{o}C. Healthy capillaries were identified by vascular diameters of less than 10 μm and by the absence of smooth

muscle. Regions with a candidate pericyte were imaged every 30 s except for experiments with Ang II, which evoked fast capillary diameter changes and which therefore used imaging evey 5 s. The images were analysed with Metamorph Software to measure the capillary diameters.

6.2.3 Immunohistochemistry

For immunohistochemistry for ACE2 in Section 6.3.1, hamster cortical slices (200 µm thick) were fixed (while shaking) in 4% paraformaldehyde (PFA) at room temperature for 20 min and rinsed thrice with PBS. Antigen retrieval with sodium citrate buffer at 95-100^{o}C was performed as described in Section 2.4.3. The brain slices were blocked in a blocking solution containing 10% horse serum, 0.2% saponin, 200 mM glycine and 150 µM bovine serum albumin in PBS overnight at 4^{o}C. Then, the slices were incubated with the blocking solution containing primary antibodies for 72 h at the same temperature, washed four times with PBS and put in the blocking solution with secondary antibodies at 4^{o}C overnight. After the brain slices were washed in PBS four times, staining of nuclei by DAPI (100 ng/ml) was performed at room temperature for 1 h. The slices were mounted onto the glass slides and imaged under a confocal microscope.

For pericyte death experiments (see Section 6.3.8), 300 µm thick hamster brain slices were incubated in bicarbonate buffered aCSF containing 7.5 µM propidium iodide (PI) and isolectin B4 conjugated to Alexa Fluor 647 (3.3 µg/ml) with or without Ang II (50 nM) and/or RBD (0.7 mg/l) at 35^{o}C, oxygenated with 20% O_2, 5% CO_2, and 75% N_2. The slices were fixed for 1 h in 4% PFA and rinsed thrice with PBS. Then the slices were incubated in PBS containing DAPI (100 ng/ml) for 1 h and mounted on glass slides. Image stacks of the brain cortex were taken with a confocal microscope. The first 20 µm of images from the slice surface were not analysed because the cells

were affected by the slicing procedure. The analysis of pericyte death was performed by my colleague, Dr. Felipe Freitas. The number of total pericytes (identified as bump-on-a-log cells enveloped by isolectin B4-stained basement membrane) and the number of dead pericytes (i.e. that were positive for PI), were counted and analysed.

6.2.4 Surface plasmon resonance

These experiments were performed by Professor Ray Owens using a Biacore T200 system (GE Healthcare). A sensor Chip Protein A (GE Healthcare) with a running buffer of PBS pH 7.4 with 0.005% vol/vol surfactant P20 (GE Healthcare) at 25^{o}C was used in all assays. ACE2-Fc was coated onto the sample flow cell of this sensor chip while the reference flow cell was not coated. 0.1 μM of RBD-WT or RBD-Y489R was injected at a flow rate of 30 μl/min with an association time of 1 min over the two flow cells.

6.2.5 Statistical analysis

Statistical analyses were performed as previously described in Section 2.7. For the live imaging experiments with pharmacological inhibition of Ang II-evoked vasoconstriction, the vessel diameters were normalised to the last 10 measurements of the vessel diameters during the application of the blockers alone.

6.3 Results

6.3.1 ACE2 is expressed mainly in capillary pericytes in the brain

ACE2 is important in COVID-19 infection because it is the main binding site for the SARS-CoV-2 virus (Hoffmann *et al.*, 2020; Ou *et al.*, 2020) and also has the function of converting Ang II to Ang(1-7) (Santos *et al.*, 2018). To detect the expression of ACE2 in the brain, I performed immunohistochemistry on hamster cortical slices and found that ACE2 was mostly detected on capillary pericytes (Fig. 6.1A, B). The

expression of ACE2 co-localised with the expression of PDGFRβ, which is a marker for vascular smooth muscle cells and pericytes, with ~75% overlap (Fig. 6.1C, D). Further categorisation of PDGFRβ positive cells into (i) smooth muscle cells on penetrating arterioles, and (ii) pericytes on capillaries, revealed that ~75% of ACE2 expression in PDGFRβ cells belonged to capillary pericytes (Fig. 6.1C, E). This implies that pericytes are the main locus of ACE2 in the brain and this explains why they are prone to SARS-CoV-2 infection, as has been reported in COVID-19 patients (Bocci *et al.*, 2021).

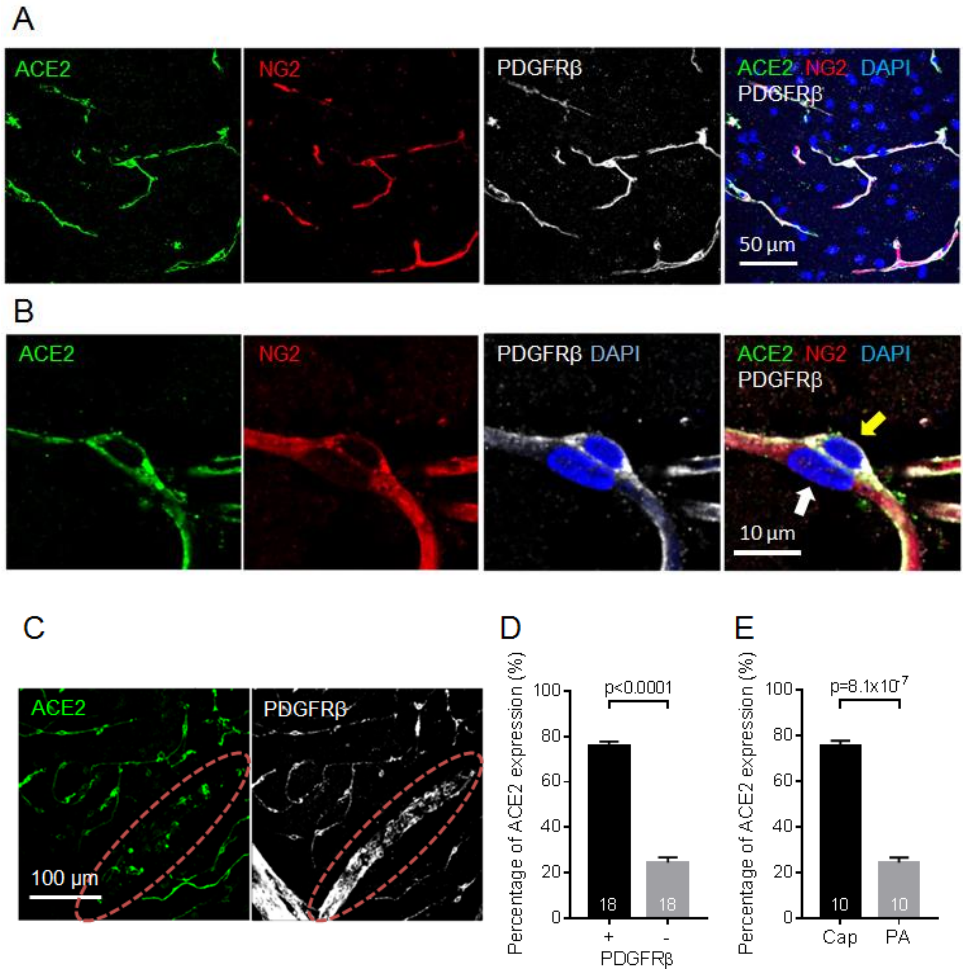

Figure 6.1: ACE2 is mostly expressed in cerebral pericytes.

(A and B) Fluorescent images at low (A) and high (B) magnification showing that ACE2 (green) co-localised with markers for pericytes and microvessels: NG2 (red) and PDGFRβ (white). Nuclei of cells were stained with DAPI (blue). ACE2 was expressed in pericytes (yellow arrow in B) but not endothelial cells (white arrow in B). (C) Lower magnification maximum intensity projection of ACE2 (green) and PDGFRβ (white) labelling showing that the expression of ACE2 co-localised with the expression of PDGFRβ and that the majority of ACE2 expression in PDGFRβ-positive areas was on capillaries. Red circle indicates a penetrating arteriole.

(D) ACE2 labelling integrated over stacks overlapping with a binarised mask of PDGFRβ and with the inverse of this mask. Number of image stacks is given on bar.

(E) Integrated ACE2 labelling in stacks over capillaries and penetrating arterioles.

6.3.2 Hamster pericytes are reactive to vasoactive drugs

Because there is no previous study using the hamster brain for studying pericyte contractility, the contractility of pericytes in the hamster brain slice preparation needed to be confirmed before utilising the brain slices for further bright-field imaging experiments. This experiment was performed in collaboration with my colleague, Dr. Greg James.

Application of the thromboxane A_2 analogue U46619 (200 nM) to hamster brain slices for 15 min evoked a capillary constriction of 31.3 ± 5.9% (n=9, p=0.0014 compared to the aCSF baseline, Fig. 6.2) at potential pericyte locations. Superimposing glutamate (500 μM) onto the U46619-contricted capillaries for 10 min dilated the previously constricted capillaries by ~55%, leaving a constriction of 14.2 ± 7.0% (n=9, p=0.006 compared to the capillary diameter at the end of U46619, Fig. 6.2). This suggests that pericytes from the hamster brain can react to vasoactive agents, similar to pericytes from the rat brain that exhibit U46619-evoked contraction (Mishra *et al.*, 2016) and glutamate-induced relaxation (Hall *et al.*, 2014). The hamster brain slice preparation was thus deemed suitable for further live imaging experiments.

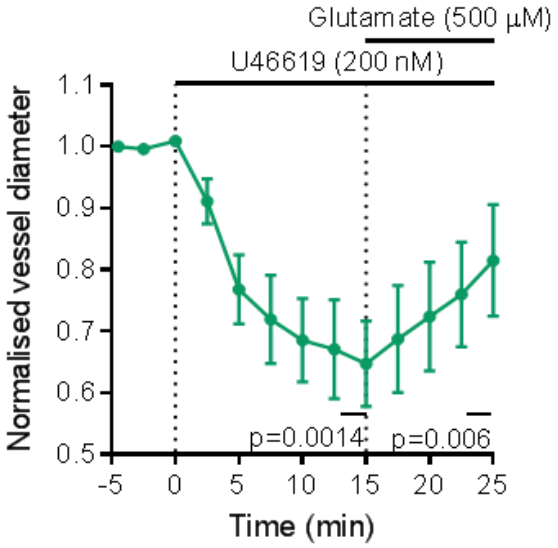

Figure 6.2: Pericytes in hamster brain slices are responsive to vasoactive agents.

Time course of capillary diameter in hamster brain slices after application of U46619 (200 nM) for 15 min and then superimposing glutamate (500 µM) for 10 min. The p value at the end of 15 min of U46619 compares the diameters at t=13-15 min to those at the aCSF baseline before application of U46619. The p value at the end of 10 min of superimposed glutamate compares the diameters at t=23-25 min and those at t=13-15 min.

6.3.3 Ang II evokes capillary constriction via AT1Rs, and dilation directly via AT2Rs and indirectly via MasRs

As discussed above, SARS-CoV-2 infection is proposed to reduce ACE2 function, leading to an increased level of Ang II and a decreased amount of Ang(1-7). To understand how SARS-CoV-2 affects pericyte contractility, data on Ang II-induced capillary pericyte responses need to be acquired, but this has not previously been done for brain pericytes.

The experiments in this section were performed with my colleague, Dr. Greg James. By using live imaging, I showed that Ang II (150 nM) evoked a transient peak capillary constriction of 7.5 ± 1.6% (n=9) after around 2.5 min. In the presence of the AT1R blocker losartan (20 μM), the peak capillary constriction evoked by Ang II was reduced to 2.5 ± 2.3% (n=10, significantly reduced, p=0.027, Fig. 6.3A, C), implying that Ang II evoked the vasoconstriction through AT1Rs. Losartan alone did not evoke a significant diameter change after 15 min (-0.9 ± 1.7%, n=10, p=0.43 compared to the aCSF baseline).

Inhibiting AT2Rs with PD123319 (1 μM) insignificantly increased the peak constriction to 15.1 ± 7.1% (n=9, p=0.79 compared to the constriction without PD123319, Fig. 6.3B, C), suggesting that AT2Rs might contribute only a slight vasodilation. However, application of PD123319 alone for 15 min induced a constriction of 7.5 ± 3.8% (n=9, p=0.0078 compared to the aCSF baseline).

After Ang II has been converted by ACE2 to Ang(1-7), this acts on MasRs to dilate vessels, at least in other organs (Schindler *et al.*, 2007). To examine the role of Ang(1-7) in Ang II-evoked capillary diameter changes, I applied the MasR blocker A779 (10 μM) for 15 min before superimposing Ang II (150 nM). A779 significantly enhanced the peak of Ang II-induced vasoconstriction to 36.0 ± 4.8% (n=5, p<0.0001,

Fig. 6.3B, C), implying that activation of MasR (by Ang(1-7) derived by ACE2 from the applied Ang II) opposes the pericyte constriction evoked by Ang II acting on AT1Rs. Superfusing A779 alone for 15 min evoked a statistically insignificant constriction of 0.8 ± 2.5% (n=5, $p>0.99$ compared to the aCSF baseline).

From all of these experiments, I conclude that Ang II activates AT1Rs and AT2Rs to cause pericyte contraction and perhaps a slight relaxation respectively. In addition, Ang II is converted to Ang(1-7) that acts on MasRs to oppose the capillary constriction produced by AT1R activation.

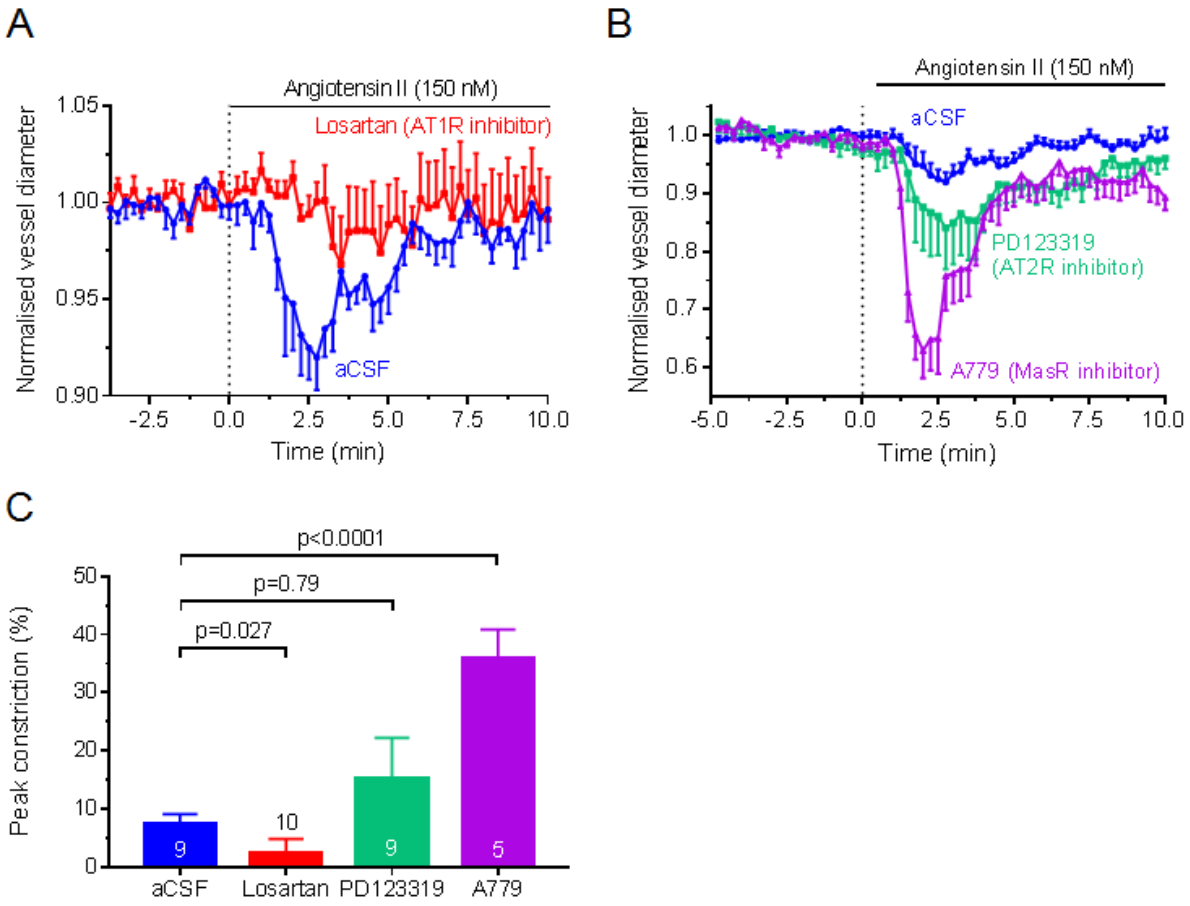

Figure 6.3: Ang II induces pericyte contraction via AT1Rs but contraction is opposed by activation of MasRs (and possibly AT2Rs).

(A) Time course of capillary diameter (mean ± s.e.m.) on applying Ang II (150 nM, n=9) alone or in the presence of the AT1R blocker losartan (20 μM, n=10).

(B) Time course of capillary diameter when perfusing Ang II (150 nM, n=9, blue trace) alone or in the presence of the AT2R blocker PD123319 (1 μM, n=9, green trace) or in the presence of the MasR blocker A779 (10 μM, n=5, purple trace).

(C) Peak constriction in (A) and (B) for each condition, showing that the AT1R blocker losartan significantly inhibited the Ang II-evoked pericyte contraction and the MasR blocker A779 significantly increased the Ang II-induced pericyte contraction. The AT2R blocker did not significantly increase the peak constriction.

6.3.4 The receptor binding domain of SAR-CoV-2 potentiates the Ang II-induced vasoconstriction

Because the RBD has been suggested to decrease ACE2 activity either through internalisation of ACE2 (Rothlin *et al.*, 2021) or obstructing the catalytic site of ACE2 (Castiglione *et al.*, 2021), the RBD might be able to increase the Ang II-evoked capillary constriction through decreased enzymatic breakdown of vasoconstricting Ang II. In physiological conditions, there is reported to be approximately 61 pg/g of Ang II in rat cortex (approximately 60 pM) (Phillips & Stenstrom, 1985; DiResta *et al.*, 1990).

To test whether the RBD alone evokes a change in capillary diameter, hamster brain capillaries were superfused with RBD (0.7 mg/l or 22.5 nM, which is ~5 times the EC_{50} for binding to ACE2 (Tai *et al.*, 2020)) and capillary diameters were imaged and analysed. Application of the RBD for 40 min evoked a statistically insignificant diameter decrease of 0.2 ± 2.2% (n=8, p=0.36 compared to aCSF applied for the same duration which evoked a diameter change of -2.4 ± 1.6%, n=8, Fig. 6.4A).

Application of a high concentration of Ang II (2 μM) for 15 min in the absence of RBD resulted in a small peak vasoconstriction of 6.3 ± 3.6% (n=6); however, after brain slices were incubated in RBD (0.7 mg/l) for 30 min, perfusing the same concentration of Ang II (2 μM) evoked a peak constriction of 31.5 ± 9.3% (n=4, significantly increased, p=0.019, Fig. 6.4B). Thus, the RBD potentiates the Ang II-evoked capillary constriction. The 30 min pre-incubation in the RBD was performed to allow the RBD to diffuse into the slices and bind to ACE2 (30 min incubation in aCSF was used as a control before application of Ang II in the absence of the RBD).

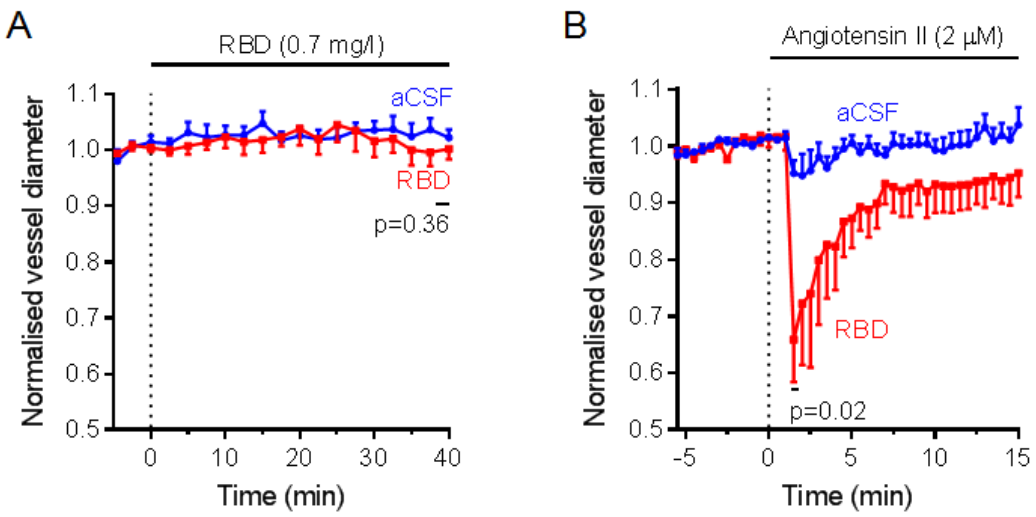

Figure 6.4: The RBD alone does not evoke capillary constriction but potentiates Ang II-evoked vasoconstriction.

(A) RBD (0.7 mg/l, n=8) did not significantly evoke a change of capillary diameter after 40 min when compared to aCSF.

(B) Applying a high concentration of Ang II (2 µM) after pre-incubating hamster brain slices in aCSF for 30 min evoked a small transient capillary constriction (n=6), while applying the same concentration of Ang II to brain slices pre-incubated with RBD (0.7 mg/l) evoked a ~5-fold larger response.

6.3.5 Potentiation of the Ang II-evoked capillary constriction by RBD is due to specific binding of the RBD by ACE2

To assess whether the potentiating effect of RBD is specific to the Ang II-evoked vasoconstriction, I incubated brain slices in the RBD or aCSF for 30 min and applied the thromboxane A_2 analogue U46619 (200 nM). The U46619-induced capillary constriction in the presence of the RBD (47.0 ± 16.0%, n=5) was not significantly different from that in the absence of the RBD (42.5 ± 12.3%, n=6, p=0.82, Fig. 6.5A), implying that the potentiating effect of the RBD is not a non-specific effect on the contractile machinery in pericytes.

To discover whether that the binding of the RBD to ACE2 is the process underlying the potentiating effect of the RBD on constriction, I used the fact that my collaborator, Professor Ray Owens, has identified the Y489R mutation of RBD as inhibiting the binding of the RBD to ACE2. This mutated RBD-Y489R showed ~94% less binding to ACE2, when measured with surface plasma resonance (Fig. 6.5B), but the molecular weight of the RBD and its glycosylation are expected to be similar to those of the normal RBD.

A lower concentration of Ang II (50 nM) than was used in Figure 6.4 evoked a transient capillary constriction of ~2% in the absence of the RBD, followed by a slowly increasing dilation, as was also seen when perfusing aCSF alone, resulting in a net dilation of 4.5 ± 3.0% (n=9) after 30 min (Fig. 6.5C). If the slices were incubated in the RBD (0.7 mg/l) for 30 min before the application of 50 nM Ang II, there was a larger initial capillary constriction (~7%) that was maintained to give a steady state constriction at 30 min of 7.8 ± 3.6% (n=9, p=0.02 compared to the diameter in the absence of RBD, Fig. 6.5C, D). Thus, the potentiating effect of the RBD also occurs with lower concentrations of Ang II. In contrast, when the slices were incubated in the

mutated RBD-Y489R (0.7 mg/l) for 30 min, perfusing Ang II (50 nM) evoked a capillary diameter change similar to that seen when applying aCSF (Fig. 6.5C, D). These experiments imply that binding of the RBD to ACE2 is essential for the potentiation of the Ang II-evoked capillary constriction by the RBD.

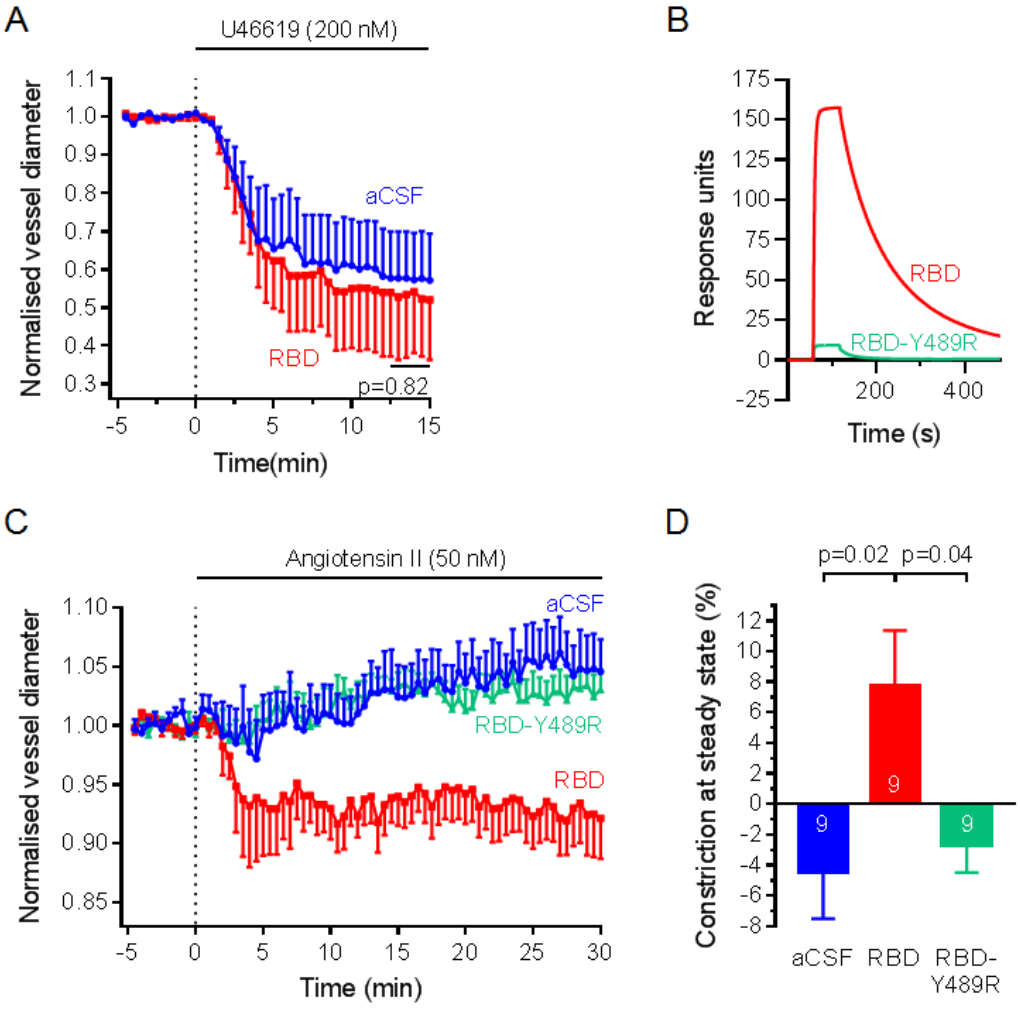

Figure 6.5: The potentiating effect of the RBD on Ang II-evoked capillary constriction results from binding of the RBD to ACE2.

(A) Pre-incubation of hamster brain slices in RBD (0.7 mg/l) did not affect the U46619-induced vasoconstriction (n=5 for RBD and n=6 for aCSF). (B) Surface plasmon resonance responses for binding of RBD and the mutated RBD-Y489R to immobilised human ACE2 (data provided by Prof Ray Owens, Oxford). (C) Time course of capillary diameter after application of Ang II (50 nM) to hamster brain slices pre-incubated for 30 min with aCSF (n=9), aCSF containing RBD (n=9) and aCSF containing the mutated RBD-Y489R (n=9). (D) Constriction in (C) at t=29.67-30.00 min (baseline drift seen in aCSF was represented as a dilation).

6.3.6 Potentiation by the RBD is equivalent to that of an ACE2 blocker

Because the potentiation of the Ang II-induced vasoconstriction is assumed to reflect binding of the RBD to ACE2 which reduces ACE2 activity, a similar potentiation should be observed in the presence of an ACE2 blocker.

The following experiment was performed in collaboration with my colleague, Dr. Greg James. To show that the potentiating effect of the RBD is comparable to that of an ACE2 blocker, I incubated hamster brain slices in the RBD (0.7 mg/l) or the ACE2 inhibitor MLN4760 (1 μM) for 30 min, before applying Ang II (50 nM). A capillary constriction of 9.7 ± 1.6% was seen in the ACE2 blocker (n=9, not significantly different from the Ang II-evoked vasoconstriction of 7.8 ± 3.6% seen in the presence of the RBD (p=0.63), but significantly larger than the Ang II-induced capillary constriction seen without the RBD (p=0.002; Fig. 6.6A, B). This experiment suggests that the ACE2 blocker has a potentiating effect similar to that of the RBD, consistent with the RBD mediating its effect through a reduction of ACE2 activity. However, further experiments perfusing the combination of these two drugs and observing whether their effects occlude each other might be needed to further clarify this point.

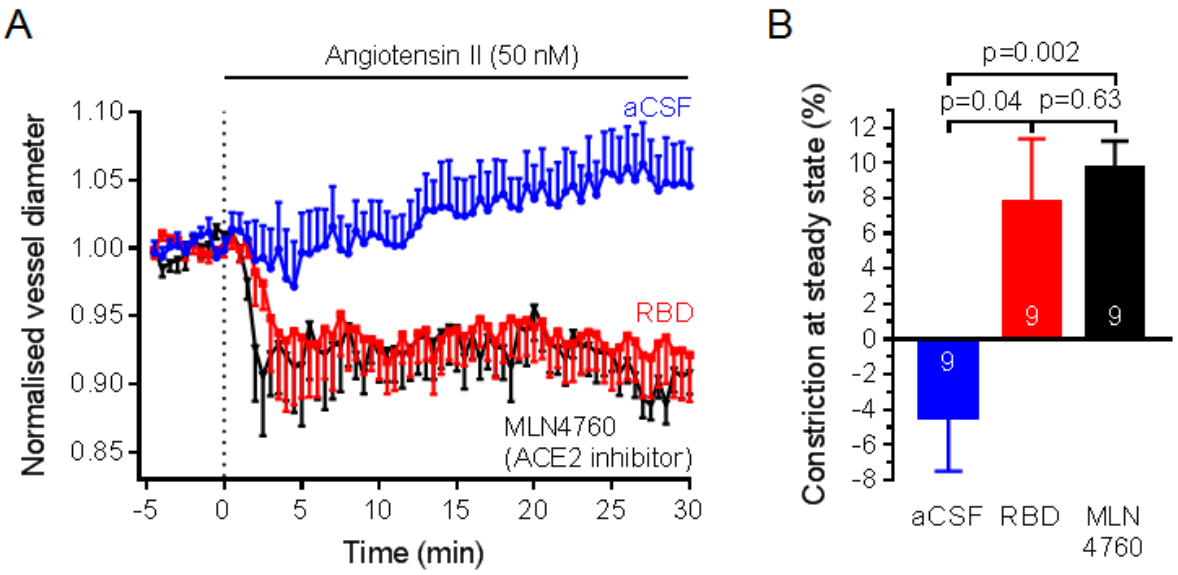

Figure 6.6: The potentiating effect of the RBD on Ang II-evoked vasoconstriction is mimicked by application of an ACE2 inhibitor.

(A) Time course of capillary diameter in response to Ang II (50 nM) in the absence and presence of the RBD (0.7 mg/l, reproduced from Fig. 6.5C) and in the presence of the ACE2 inhibitor MLN4760 (1 μM, n=9 for each).

(B) Mean capillary constriction at t=29.67-30 min in (A).

6.3.7 The Ang II-evoked vasoconstriction potentiated by the RBD is blocked by losartan

Since the Ang II-evoked capillary constriction was mediated via AT1Rs and the RBD is thought to potentiate this constriction by reducing the conversion of Ang II to Ang(1-7), it seems possible that AT1R blockers might prove to be useful in preventing the potentiation of the Ang II-induced pericyte constriction by the RBD.

I incubated hamster brain slices in the RBD (0.7 mg/l) with the AT1R blocker losartan (20 µM) for 30 min before applying Ang II (50 nM) to check whether losartan can block the constriction. In the presence of both the RBD and losartan, the Ang II-evoked vasoconstriction was inhibited, resulting in a capillary dilation of 2.5 ± 1.2% (n=10, significantly reduced, p=0.025, compared to the vasoconstriction of 7.8 ± 3.6% evoked by Ang II (50 nM) in the presence of the RBD (0.7 mg/l) without losartan, Fig. 6.7A, B). Thus losartan inhibits the potentiated vasoconstriction evoked by Ang II in the presence of the RBD.

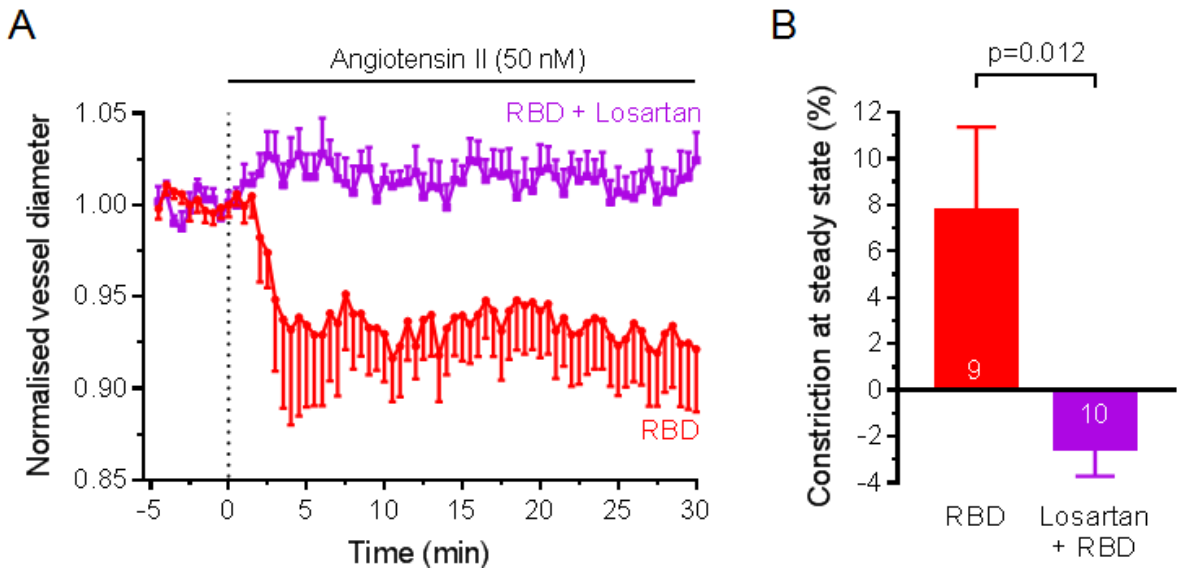

Figure 6.7: The AT1R blocker losartan prevents the RBD-potentiated Ang II-evoked capillary constriction.

(A) Capillary constriction at pericytes in response to Ang II (50 nM) in the presence of the RBD (0.7 mg/l, n=9, reproduced from Fig. 6.5C) alone or with the RBD plus the AT1R blocker losartan (20 μM, n=10), showing that losartan prevented the constriction.

(B) Constriction in (A) at t=29.67-30 min.

6.3.8 Pericyte death is not altered with application of RBD and/or Ang II

He *et al.* (2020) have suggested that one potential pathophysiological aspect of human SARS-CoV-2 infection is a virus infection induced loss of pericytes, which could lead to increased von Willebrand Factor (vWF) production in endothelial cells, resulting in a pro-thrombotic state and coagulopathy. The following experiment was performed in collaboration with my colleague, Dr. Felipe Freitas, to test whether the RBD causes pericyte loss. Hamster brain slices were exposed for 3 h to aCSF or RBD (0.7 mg/l), with or without Ang II (50 nM), in the presence of propidium iodide (7.5 μM) to monitor plasma membrane breakdown signifying necrotic cell death. The pericyte death occurring was evaluated by analysing the proportion of pericytes stained by propidium iodide. No significant effect on pericyte death was found in all conditions (Fig. 6.8), suggesting that binding of the RBD to ACE2, with or without Ang II being present, does not cause pericyte loss (p-value comparing with or without RBD=0.30, p-value comparing with or without Ang II=0.08, two-way ANOVA).

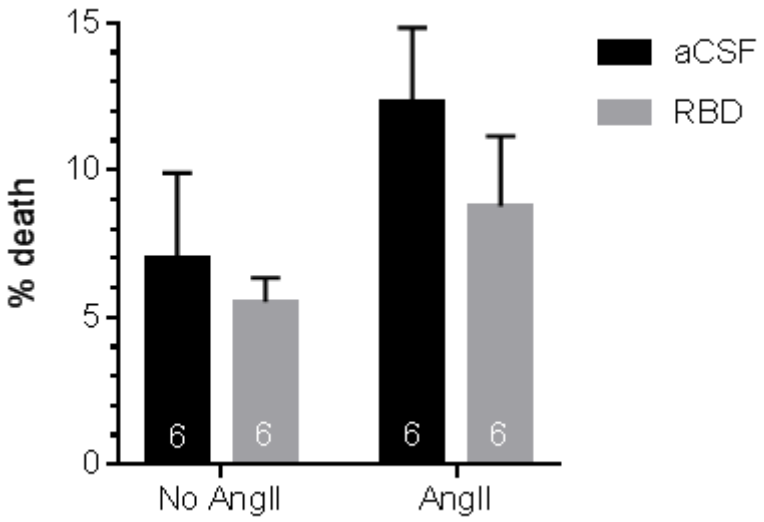

Figure 6.8: Application of the RBD and/or Ang II does not affect pericyte death. Percentage of pericytes that were dead (defined by propidium iodide staining) in hamster brain slices after incubation in aCSF, or in aCSF containing Ang II (50 nM) and/or RBD (0.7 mg/l), showing that application of Ang II and/or RBD did not significantly affect pericyte death. (p-value comparing with or without RBD=0.30, p-value comparing with or without Ang II=0.08, two-way ANOVA). Number of brain slices in each condition is shown on the bars.

6.3.9 Potentiation of Ang II-evoked vasoconstriction by the RBD also occurs in human tissue

To test whether the potentiating effect of the RBD on Ang II-evoked capillary constriction also happens in human capillaries, human brain slices were pre-incubated in aCSF or aCSF containing RBD (0.7 mg/l) for 30 min before being perfused with Ang II (50 nM) under a bright-field microscope. Ang II (50 nM) alone evoked a steady state capillary diameter constriction of -1.0 ± 1.1% (i.e. a small dilation, n=4) after 30 min, but in the presence of the RBD induced a constriction of 8.7 ± 1.7% (n=5, p=0.0027 compared with Ang II alone; Fig. 6.9A, B), implying a net constriction of 0.913/1.01 = 0.904 or 9.6% compared to Ang II alone. Thus, potentiation of Ang II-evoked capillary constriction by SARS-CoV-2 also occurs in human tissue.

To assess the possible implications of the RBD-evoked potentiation of Ang II-mediated capillary constriction, I calculated the flow change from the constriction evoked by the 50 nM Ang II, which is more physiological, in the presence of the RBD using the Poiseuille's law analysis in Section 2.3.4. As stated in Section 2.3.4, the capillary radius at the pericyte somata (r_2) with no exogenous drugs applied is approximately 1.1 times that between pericytes (r_1) in rodent capillaries, thus in the presence of the RBD and Ang II this ratio will be reduced by a multiplicative factor of 0.913 (from the constriction of 8.7% given above for human capillaries) giving a new value of r_2/r_1 for Ang II with RBD of 1.0043. Application of Ang II alone evoked a dilation of -1.0%, which will increase r_2/r_1 by a factor of 1.01, resulting in a new r_2/r_1 for Ang II alone of 1.111. By inserting these two values of r_2/r_1 into eqn. (1) of Section 2.3.4, I estimated the blood flow decrease when the capillaries were in the presence of both RBD and Ang II to be ~11.1% when compared to the blood flow in the presence of

Ang II alone. The corresponding value derived from the hamster data in Fig. 6.5 is 13.6%.

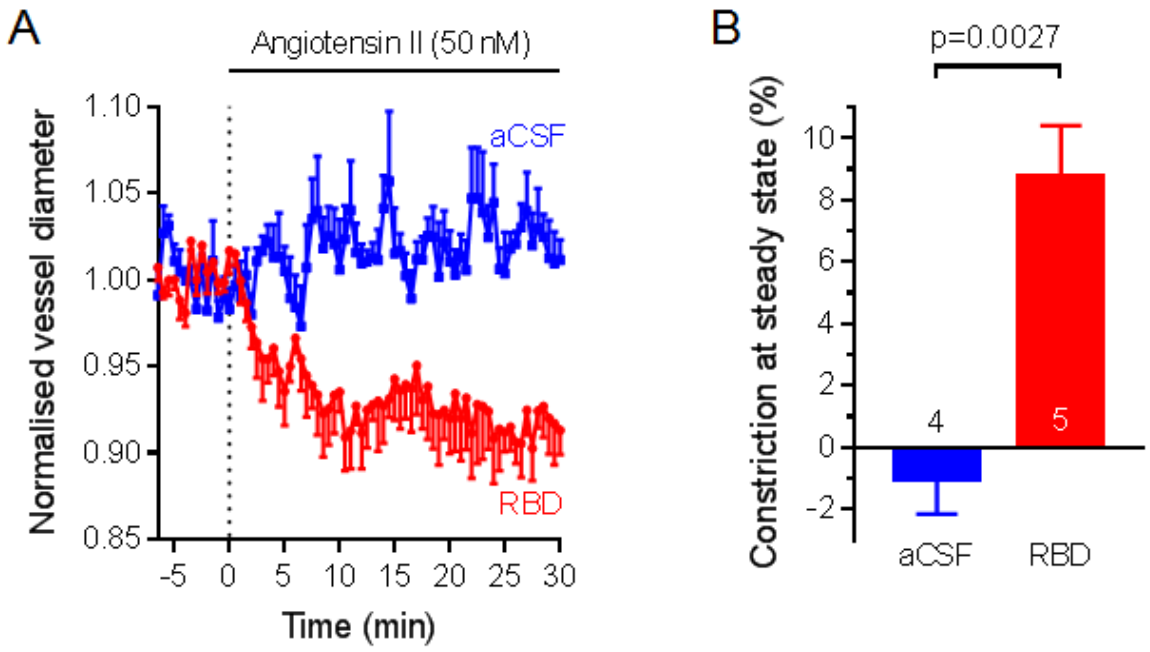

Figure 6.9: The potentiating effect of the RBD on Ang II-evoked capillary constriction also occurs in human brain tissue.

(A) Time course of capillary diameter measured at pericyte locations after application of Ang II (50 nM) in human brain slices pre-incubated with aCSF or aCSF containing RBD (0.7 mg/l).

(B) Mean capillary constriction at t=29.67-30 min in (A).

6.4 Discussion

My experiments provide three contributions to the understanding of how SARS-CoV-2 may affect brain pericytes and cerebral blood flow, as follows

(i) In the brain, the receptors for SARS-CoV-2, the ACE2 molecules, are present mostly on cerebral pericytes.

(ii) The RBD of SARS-CoV-2 potentiates Ang II-evoked capillary constriction both in human and in hamster tissue, through a reduction of ACE2 activity.

(iii) It is, in principle, possible to prevent the RBD-evoked potentiation of the Ang II-evoked pericyte contraction with AT1R blockers such as losartan.

Firstly, most of the ACE2 expression in the cortex was found in cerebral pericytes while a minority of the expression was found in arteriolar smooth muscle cells. This is similar to transcriptomic data, showing a high level of *ACE2* mRNA in pericytes and venous smooth muscle cells and a lower level of the mRNA in arterial smooth muscle cells (Zeisel *et al.*, 2018; He *et al.*, 2020). Immunofluorescence images of ACE2 in the mouse brain also support this finding (He *et al.*, 2020). The ACE2 positive cells that did not co-localise with PDGFRβ signals were not characterised in this work, but might be neurons in the cerebral cortex because small amounts of *ACE2* mRNA (Zeisel *et al.*, 2018) and ACE2 protein (Doobay *et al.*, 2007) were also detected in neurons.

The results in this chapter support the hypothesis that the RBD of SARS-CoV-2 binds to ACE2 on pericytes and decreases its activity, either through internalisation of ACE2 (Wang *et al.*, 2008) or obstruction of its catalytic site (Castiglione *et al.*, 2021) (Fig. 6.10). The importance of the binding of the RBD to ACE2 is emphasised by the fact that the mutated RBD-Y489R, which retains all the chemical properties of RBD except for its binding to ACE2, did not show the potentiating effect seen with the

normal RBD. The ACE2 blocker MLN4760 mimicked the potentiating effect of the RBD, supporting a role for reduced ACE2 activity in the potentiated Ang II-evoked capillary constriction in the presence of SARS-CoV-2. The possibility that the RBD acts non-specifically on the pericyte contractile apparatus to enhance contraction was excluded because (i) application of the RBD alone did not increase pericyte contractility; and (ii) the U46619-evoked vasoconstriction was unaffected by the presence of the RBD.

Reduced ACE2 activity will increase the level of vasoconstricting Ang II and decrease the level of vasodilating Ang(1-7) (Fig. 6.10). My results showed that Ang II-evoked capillary diameter changes were mediated through: (i) AT1Rs which constrict the capillaries; and (ii) MasRs that are activated by Ang(1-7), which is produced by ACE2-catalysed conversion from Ang II, and which oppose constriction. The net effect of Ang II is pericyte contraction, which is similar to what has been shown in the kidney (Pallone & Silldorff, 2001) and retina (Schönfelder *et al.*, 1998). In some experiments with high concentrations of Ang II (see Sections 6.3.3 and 6.3.4), Ang II evoked only a transient constriction. This might be caused by rapid desensitisation of the AT1Rs (Hunyady *et al.*, 2000) or a delayed effect of MasR activation. Because ACE2 is expressed mostly in cerebral pericytes, the disturbance of the local balance of Ang II and Ang(1-7) resulting from blockage of ACE2 by SARS-CoV-2 is expected to be maximised near pericytes.

For SARS-CoV-2 to induce cerebral pericyte contraction, the virus or the RBD need to be present on the abluminal surface of the vessels to be in contact with pericytes. Access to cerebral pericytes might occur through the spreading of the virus from the nasal mucosa to the olfactory nerve, thus bypassing the blood-brain barrier into the brain (Meinhardt *et al.*, 2021). Viral particles can also be carried by infected

monocytes across the endothelial cell layer (Zhang *et al.*, 2021) or pass through the leaky blood-brain barrier caused by cytokines released from lung inflammation (Kumar *et al.*, 2020). Endothelial dysfunction and vascular leakage may allow SARS-CoV-2 to reach pericytes and infect them (He *et al.*, 2020). Furthermore, the S1 portion of the spike protein, which includes the RBD, can travel across the the blood-brain barrier by transcytosis (Rhea *et al.*, 2021) and potentially reach cerebral pericytes to cause contraction.

Pericyte changes in COVID-19 might also contribute to reduced cerebral blood flow through thrombus formation (He *et al.*, 2020). Pericyte loss has been found in the hearts of hamsters infected with SARS-CoV-2 (Daems *et al.*, 2020) and in the lungs of COVID-19 patients (Cardot-Leccia *et al.*, 2020). It is known to increase vWF release from endothelial cells and induce pro-coagulation responses that could explain coagulopathy in COVID-19 patients (He *et al.*, 2020). Although application of the RBD with or without Ang II did not increase pericyte death in my experiments, suggesting that binding of the RBD to ACE2 does not explain the pericyte loss, entry of actual virus into the cells might activate other pathways to affect pericyte viability. SARS-CoV-2 has been shown to induce apoptosis via the ORF3a peptide of the virus and caspase-8, and inflammatory cell death such as pyroptosis and necroptosis of host cells through phosphorylation of pseudokinase mixed lineage kinese domain-like (MLKL) (Paolini *et al.*, 2021). Thus, more studies with actual virus or pseudovirus might be needed to study the mechanism of pericyte loss in COVID-19 and its contribution to the blood flow decrease and neurological symptoms occurring in this disease.

The combination of the potentiating effect of the RBD on the Ang II-evoked capillary constriction, and potentially thrombus formation from pericyte loss (He *et al.*, 2020), might be able to explain the cerebral blood flow deficit found in COVID-19

patients (Helms *et al.*, 2020; Soldatelli *et al.*, 2020; Qin *et al.*, 2021). This could possibly contribute to the neurological complications of COVID-19 (Taquet *et al.*, 2021) and the “long COVID” syndrome (Theoharides *et al.*, 2021).

My data also suggest a therapeutic approach for the reduced cerebral blood flow occurring in COVID-19, using AT1R blockers. Because the AT1R blocker losartan was able to block the vasoconstricting effect of Ang II even in the presence of the RBD, using losartan or other AT1R blockers might be useful in preventing or treating neurological complications of COVID-19. There were some concerns that chronic administration of inhibitors of the RAS might upregulate ACE2 expression and potentially contribute to an increased risk of SARS-CoV-2 infection (Ferrario *et al.*, 2005; Igase *et al.*, 2008); however, no significant increased risk of contracting COVID-19 disease nor increased risk of poorer outcomes from COVID-19 has been detected in chronic users of angiotensin-converting enzyme inhibitors (ACEIs) and/or AT1R blockers (ARBs) (Lopes *et al.*, 2021; Morales *et al.*, 2021). In fact, it has been shown that usage of ACEIs and/or ARBs results in a better prognosis in COVID-19 patients with reduced risk of critical disease and/or death (Pirola & Sookoian, 2020; Hippisley-Cox *et al.*, 2020). Currently, prospective trials studying the effect of AT1R blockers on the outcome of COVID-19 are being conducted (Rothlin *et al.*, 2021) and the results from these studies might provide more insight into using ARBs or ACEIs to treat COVID-19.

6.5 Suggestions for future work

Following on from the experiments done in this chapter, suggesting that the receptor binding domain of SARS-CoV-2 potentiates angiotensin II-induced pericyte

contraction via a decrease in angiotensin converting enzyme (ACE2) receptor activity (see Section 6.3.5-6.3.7), three main elements should be further clarified.

To test if the RBD definitely blocks ACE2 function, perfusing an ACE2 inhibitor onto RBD-treated capillaries and observing whether the effects of the RBD and of the ACE2 inhibitor occlude each other or not would be needed..

The process by which ACE2 receptor activity declines could be studied in more detail. ACE2 could be internalised along with the virus or the RBD (Wang *et al.*, 2008; Ou *et al.*, 2020), or the catalytic site of ACE2 might be blocked after binding to the RBD (Castiglione *et al.*, 2021). Brain slice biotinylation followed by immunoblotting (Gabriel, Wu & Melikian, 2014) could be used to compare the amount of ACE2 on the surface of pericytes in the presence and absence of the RBD.

The other key experiment that could be performed is investigating whether the application of RBD/spike protein or pseudovirus particles expressing the SARS-CoV-2 Spike protein can cause a CBF decrease *in vivo*, and also whether the process is mediated by a decreased activity of ACE2. This would help in relating the results of this chapter to the processes occurring in COVID-19 patients.

6.6 Conclusion

My data suggest that SARS-CoV-2 causes decreased cerebral blood flow in COVID-19 infection through the binding of the RBD to ACE2, resulting in reduced ACE2 activity to convert vasoconstricting Ang II to vasodilating Ang(1-7). This, in turn, increases the local concentration of Ang II, especially near pericytes, and leads to capillary constriction. The experiments also suggest that AT1R blockers are able to prevent the potentiated capillary constriction that results from the combination of Ang II and the RBD, implying that using AT1R blockers might be an interesting therapeutic

approach to preserving cerebral blood flow in COVID-19 patients that could potentially reduce the rate of neurological complications in these patients. It will be interesting to see the results of ongoing clinical trials using AT1R inhibitors (clinicaltrials.gov/ct2/show/NCT04312009 and clinicaltrials.gov/ct2/show/NCT04311177) on the neurological outcome of COVID-19 patients.

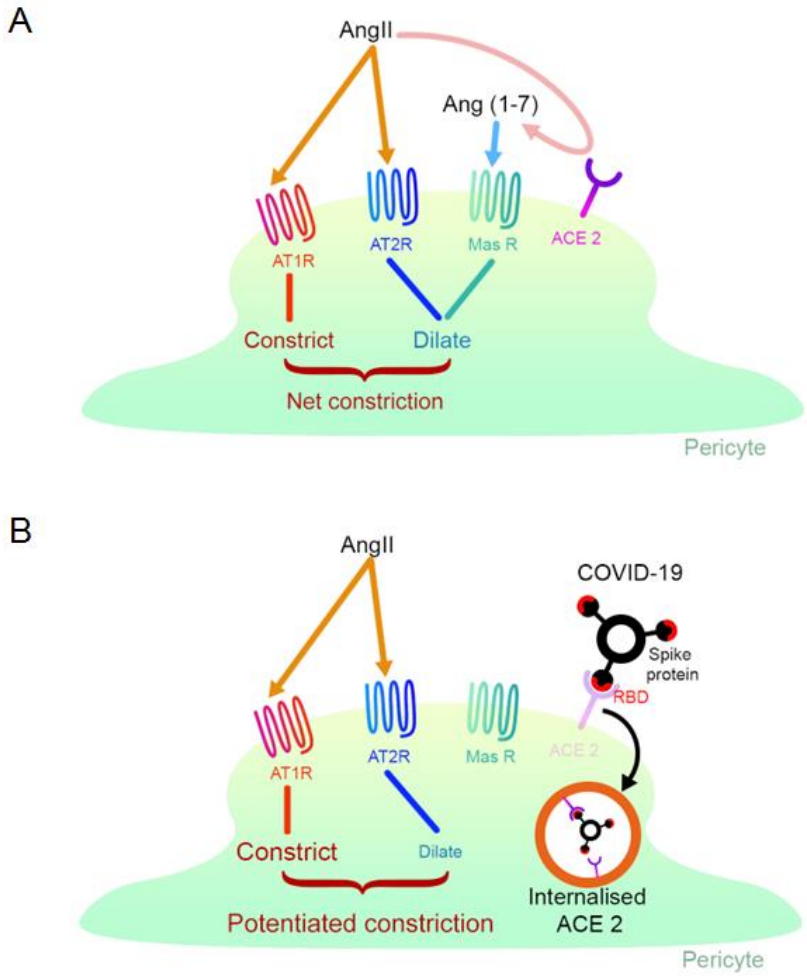

Figure 6.10: Schematic diagram of the mechanism of potentiation of Ang II-evoked pericyte contraction by the SARS-CoV-2 RBD.

(A) In normal physiology, Ang II acts on vasoconstricting AT1Rs and vasodilating AT2Rs to evoke capillary constriction. Ang II is also converted to Ang(1-7) by pericyte ACE2 and acts on MasRs to oppose the constriction/promote dilation of capillaries.

(B) In COVID-19 infection, SARS-CoV-2 binds to ACE2, causing internalisation of the virus-receptor complex or obstructing the catalytic site of ACE2. This leads to reduced conversion of Ang II to Ang(1-7), which will increase the local concentration of Ang II. As a result, capillary constriction is more pronounced in SARS-CoV-2 infection.

Chapter 7: Summary and final conclusion

7.1 Summary

The brain consumes as much as 20% of the resting body's oxygen utilisation while it weighs about 2% of the body's mass (Sokoloff, 1960; Rolfe & Brown, 1997), reflecting the very high metabolic rate of the brain. The energy consumption depends on brain regions and their activity (Hahn *et al.*, 2016; Yu *et al.*, 2018); however, the brain lacks energy substrate reserves, making it dependent heavily on continuous supply of glucose and oxygen from the blood to function (Iadecola, 2017). Thus precise control of cerebral blood flow is needed to match the energy supplied to the spatially and temporally dynamic metabolism of the brain (Iadecola, 2017).

In the intracranial circulation, the blood flow resistance in the cerebral arteries upstream of the pial network, pial arteries and arterioles, and microvasculature are 33-39%, 15-21% and 40-52% of the total respectively (De Silva & Faraci, 2016), suggesting that the microvasculature confers the most resistance to the intracerebral circulation; however, direct measurement of microvascular pressure and/or resistance is not feasible (Iadecola, 2017). Most models for investigating the resistance in cerebral arterioles and capillaries reveal that capillaries provide the most resistance to intracerebral blood flow (Boas *et al.*, 2008; Hall *et al.*, 2014; Gould *et al.*, 2017; Peyrounette *et al.*, 2018; Rungta *et al.*, 2018).

Regulation of capillary diameter, and hence the capillary resistance to blood flow, is performed by bump-on-a-log shaped cells called pericytes on the abluminal surface of the capillary and at capillary branch points (Hirschi & D'Amore, 1996; Armulik *et al.*, 2011; Cheng *et al.*, 2018). Many functions of pericytes have been identified, such as maintaining the blood-brain barrier, regulating leukocyte entry and modulating CBF (Cheng *et al.*, 2018). While most published studies support pericyte

contractility, a few studies disapprove of the idea (Hill *et al.*, 2015; Attwell *et al.*, 2016). This conflict might arise from drift in the definition of pericytes (Attwell *et al.*, 2016), difficulties in pericyte identification, measuring different locations in the vasculature and studying different subtypes of pericytes.

Pericyte dysfunction contributes significantly to various CNS conditions with CBF dysregulation (Cheng *et al.*, 2018). These diseases include ischaemic stroke (Hall *et al.*, 2014), cortical spreading depression (Khennouf *et al.*, 2018), epilepsy (Leal-Campanario *et al.*, 2017); however, the role of pericyte contractility in other neurological conditions with dysregulation of CBF has not yet been demonstrated.

In this thesis, I focused on addressing problems that might cause the controversies in pericyte contractility by investigating different pericyte identification methods, locations of capillary vasoconstriction in relation to pericyte locations and contractility in different pericyte subtypes. I also described a potential role for pericytes in causing CBF deficits in AD, hyperoxic conditions and COVID-19, and reviewed the effect of peripheral diseases such as hypertension, kidney disease and diabetes on cerebral pericytes.

I studied two methods of pericyte identification and found that (with practice) pericyte detection under live bright-field imaging is accurate and can be used for *ex vivo* studies of cerebral pericytes. Neurotrace 500/525, which is a novel dye claimed to specifically label non-contractile pericytes (Damisah *et al.*, 2017), is mostly taken up by live pericytes on higher capillary branch orders, which are usually not contractile. However, some pericytes stained by Neurotrace 500/525 expressed contractile proteins and were shown to constrict capillaries upon application of a vasoactive agent. Hence, using Neurotrace 500/525 might not be ideal for studying pericyte contractility because most of the pericytes stained by this dye are not contractile. I

found that capillary segments at pericyte soma locations show the maximal constriction, thus measuring capillary diameter changes to represent pericyte contractility should be performed at locations of pericyte somata. In terms of the contractility of different pericyte subtypes, I agree with other studies that support a larger contractility for proximal capillary pericytes. My measurements of mid-capillary distension during red blood cell passage suggest it is possible that contraction of mid-capillary pericytes will decrease the elasticity of capillaries, resulting in an alteration of CBF via an effect on the ease of passage of RBCs and leukocytes through the lumen (Lee *et al.*, 2010; Pini *et al.*, 2016). This model could be used for future experiments to measure changes in elasticity and RBC velocity after stimulating mid-capillary pericytes.

In AD, a CBF deficit is found early in the pathogenesis of AD and probably contributes to cognitive decline (de la Torre, 2002; Iturria-Medina *et al.*, 2016). In order to demonstrate an involvement of pericytes in the CBF decline in AD, Dr. Ross Nortley, Dr. Nils Korte and I observed pericyte contraction *ex vivo* after application of exogenous $A\beta_{1-40}$ and $A\beta_{1-42}$, and *in vivo* in the Aβ-plaque-laden cerebral cortex but not in the Aβ-plaque-sparing cerebellar cortex. Further investigation revealed that this process was mediated by ROS produced by NOX4 that underwent conversion to hydroxyl radicals, which evoked endothelin (ET) production. The ET acted on ET_A receptors on pericytes to cause pericyte contraction. I also showed that application of a combination of a NOX4 blocker and an ET_A receptor blocker or a strong vasodilator (C-type natriuretic peptide, CNP) could reverse the Aβ-induced pericyte contraction, suggesting a potential therapeutic approach to AD.

Because hyperoxic conditions cause significant cerebral vasoconstriction, I explored whether cerebral pericytes are affected in this condition. A high concentration

of oxygen in rat and human brain slices led to pericyte contraction, which was not readily restored to the baseline upon returning to a normoxic condition. Pericyte contraction was further confirmed by detecting an increase in intracellular calcium concentration, which is closely linked to actin-myosin coupling (Webb, 2003), in mouse brain pericytes. The hyperoxic vasoconstriction was mediated through production of 20-HETE at least in rats but was not mediated through increased ROS or ET, even though more ROS were produced. In human, 20-HETE generation might not contribute to the hyperoxic vasoconstriction.

I also investigated (with Drs. Greg James and Felipe Freitas) whether cerebral pericytes contribute to the CBF deficits found in COVID-19 patients and found that the SARS-CoV-2 RBD potentiated Ang II-induced pericyte contraction in both rats and human through a decrease in the enzymatic activity of ACE2 (the receptor for the virus), for which expression in the brain was mostly on pericytes. The RBD evoked potentiation of Ang II-activated capillary vasoconstriction could be inhibited by application of an AT1R blocker, suggesting a therapeutic approach to cerebral dysfunction in COVID-19.

7.2 Final conclusion

The work presented in this thesis describes the characteristics of cerebral pericytes and their roles in regulating CBF in physiological and pathological conditions, such as AD, brain hyperoxia and COVID-19. Although this thesis tries to explore pericyte contractility in both health and disease, much is still unknown about these cells despite their importance in CBF control, and this represents a vast research opportunity. For example, I have shown that a novel pericyte-specific dye Neurotrace 500/525 does not label all pericytes, especially those on proximal capillaries, thus new

pericyte identification methods might be needed to further advance research in this field. For this, pericyte-specific proteins, which might potentially be determined by novel techniques such as transcriptomic and single-cell analysis, are needed. These proteins could be potentially useful for developing pericyte-targeted therapy. Moreover, the contractility of each pericyte subtype and how it modulates CBF should be studied in more detail to provide more understanding of blood flow regulation at the microvascular level in the brain.

Despite all these knowledge gaps, evidence from my work supports the idea that pericytes could be involved in the pathogenesis of neurological manifestations of AD, hyperoxia and COVID-19, and that they are potentially an interesting therapeutic target. This is particularly important in AD, for which the current theurapeutic strategies fail to cure or significantly delay disease progression.

Aside from these pathologies, pericytes could potentially contribute to other brain pathologies with CBF disturbance. It would be interesting to see whether pericyte dysfunction is involved in the pathogenesis of such diseases and whether rescuing pericyte function could have an effect on disease progression, given that CBF is important in maintaining the normal function of the brain.

Thus, I hope that the knowledge from this thesis will be useful for understanding the contractile properties of pericytes and their roles in the pathogenesis of AD, brain hyperoxia and COVID-19 as well as for identifying molecular pathways governing pericyte contractility in those conditions, which could be useful to create novel therapeutic approaches to help patients.

Bibliography

Abadir, P.M., Periasamy, A., Carey, R.M. & Siragy, H.M. (2006) Angiotensin II type 2 receptor-bradykinin B2 receptor functional heterodimerization. *Hypertension*. 48 (2), 316–322.

Abassi, Z., Higazi, A.A.R., Kinaneh, S., Armaly, Z., et al. (2020a) ACE2, COVID-19 Infection, Inflammation, and Coagulopathy: Missing Pieces in the Puzzle. *Frontiers in Physiology*. 11 (3), 574753.

Abassi, Z., Skorecki, K., Heyman, S.N., Kinaneh, S., et al. (2020b) Covid-19 infection and mortality: a physiologist's perspective enlightening clinical features and plausible interventional strategies. *American journal of physiology. Lung cellular and molecular physiology*. 318 (5), L1020–L1022.

AbdAlla, S., Lother, H., Abdel-tawab, A.M. & Quitterer, U. (2001) The angiotensin II AT2 receptor is an AT1 receptor antagonist. *The Journal of biological chemistry*. 276 (43), 39721–39726.

Ago, T., Kitazono, T., Kuroda, J., Kumai, Y., et al. (2005) NAD(P)H oxidases in rat basilar arterial endothelial cells. *Stroke*. 36 (5), 1040–1046.

Alarcon-Martinez, L., Yilmaz-Ozcan, S., Yemisci, M., Schallek, J., et al. (2018) Capillary pericytes express α-smooth muscle actin, which requires prevention of filamentous-actin depolymerization for detection. *eLife*. 7.

Aliev, G., Seyidova, D., Neal, M.L., Shi, J., et al. (2002) Atherosclerotic lesions and mitochondria DNA deletions in brain microvessels as a central target for the development of human AD and AD-like pathology in aged transgenic mice. *Annals of the New York Academy of Sciences*. 977 (1), 45–64.

Aliyev, A., Chen, S.G., Seyidova, D., Smith, M.A., et al. (2005) Mitochondria DNA deletions in atherosclerotic hypoperfused brain microvessels as a primary target for the development of Alzheimer's disease. *Journal of the Neurological Sciences*. 229 (230), 285–292.

Allen, A.M., Zhuo, J. & Mendelsohn, F.A. (2000) Localization and function of angiotensin AT1 receptors. *American journal of hypertension*. 13 (1 Pt 2), 31S-38S.

Altenhöfer, S., Radermacher, K.A., Kleikers, P.W.M., Wingler, K., et al. (2015) Evolution of NADPH oxidase inhibitors: Selectivity and mechanisms for target engagement. *Antioxidants and Redox Signaling*.23 (5) pp.406–427.

Alzheimer, A. (1906) Uber einen eigenartigen schweren Erkrankungsprozess der Hirninde. *Neurologisches Centralblatt*. 25, 1134.

American College of Surgeons Committee on Trauma. (2018) *Advanced Trauma Life Support®, ATLS®. Student Course Manual*.

American Psychiatric Association (2013) *Diagnostic and Statistical Manual of Mental Disorders*. American Psychiatric Association.

Amirmansour, C., Vallance, P. & Bogle, R.G. (1999) Tyrosine nitration in blood vessels occurs with increasing nitric oxide concentration. *British Journal of Pharmacology*. 127 (3), 788–794.

Anon (2021) 2021 Alzheimer's disease facts and figures. 17 (3), 327–406.

Armstead, W.M. (1996) Role of endothelin in pial artery vasoconstriction and altered responses to vasopressin after brain injury. *Journal of Neurosurgery*. 85 (5),

901–907.

Armulik, A., Genové, G., Betsholtz, C., Genove, G., et al. (2011) Pericytes: Developmental, Physiological, and Pathological Perspectives, Problems, and Promises. *Developmental Cell*. 21 (2), 193–215.

Armulik, A., Genové, G., Mäe, M., Nisancioglu, M.H., et al. (2010) Pericytes regulate the blood-brain barrier. *Nature*. 468 (7323), 557–561.

Asano, T., Sasaki, T., Koide, T., Takakura, K., et al. (1984) Experimental evaluation of the beneficial effect of an antioxidant on cerebral vasospasm. *Neurological Research*. 6 (1–2), 49–53.

Asano, T., Takakura, K., Sano, K., Kikuchi, H., et al. (1996) Effects of a hydroxyl radical scavenger on delayed ischemic neurological deficits following aneurysmal subarachnoid hemorrhage: Results of a multicenter, placebo-controlled double-blind trial. *Journal of Neurosurgery*. 84 (5), 792–803.

Asllani, I., Habeck, C., Scarmeas, N., Borogovac, A., et al. (2008) Multivariate and univariate analysis of continuous arterial spin labeling perfusion MRI in Alzheimer's disease. *Journal of Cerebral Blood Flow and Metabolism*. 28 (4), 725–736.

Attwell, D., Buchan, A.M., Charpak, S., Lauritzen, M., et al. (2010) Glial and neuronal control of brain blood flow. *Nature*.468 (7321) pp.232–243.

Attwell, D., Mishra, A., Hall, C.N., O'Farrell, F.M., et al. (2016) What is a pericyte? *Journal of Cerebral Blood Flow & Metabolism*. 36 (2), 451–455.

Aubert, A., Costalat, R., Magistretti, P.J. & Pellerin, L. (2005) Brain lactate kinetics:

Modeling evidence for neuronal lactate uptake upon activation. *Proceedings of the National Academy of Sciences*. 102 (45), 16448–16453.

Augsburger, F., Filippova, A., Rasti, D., Seredenina, T., et al. (2019) Pharmacological characterization of the seven human NOX isoforms and their inhibitors. *Redox Biology*. 26.

Austin, S.A., Santhanam, A.V.R., D'Uscio, L. V. & Katusic, Z.S. (2015) Regional Heterogeneity of Cerebral Microvessels and Brain Susceptibility to Oxidative Stress Stephen D Ginsberg (ed.). *PLOS ONE*. 10 (12), e0144062.

Ayala, A., Muñoz, M.F. & Argüelles, S. (2014) Lipid Peroxidation: Production, Metabolism, and Signaling Mechanisms of Malondialdehyde and 4-Hydroxy-2-Nonenal. *Oxidative Medicine and Cellular Longevity*. 2014, 1–31.

Baig, A.M., Khaleeq, A., Ali, U. & Syeda, H. (2020) Evidence of the COVID-19 Virus Targeting the CNS: Tissue Distribution, Host-Virus Interaction, and Proposed Neurotropic Mechanisms. *ACS Chemical Neuroscience*.11 (7) pp.995–998.

Baleeiro, C.E.O., Wilcoxen, S.E., Morris, S.B., Standiford, T.J., et al. (2003) Sublethal Hyperoxia Impairs Pulmonary Innate Immunity. *The Journal of Immunology*. 171 (2), 955–963.

Bandopadhyay, R., Orte, C., Lawrenson, J.G., Reid, A.R., et al. (2001) Contractile proteins in pericytes at the blood-brain and blood-retinal barriers. *Journal of Neurocytology*. 30 (1), 35–44.

Barnes, D.E. & Yaffe, K. (2011) The projected effect of risk factor reduction on Alzheimer's disease prevalence. *Lancet Neurology*. 10 (9), 819–828.

Bärtsch, P. & Swenson, E.R. (2013) Acute High-Altitude Illnesses. *New England Journal of Medicine*. 368 (24), 2294–2302.

Basora, N., Boulay, G., Bilodeau, L., Rousseau, E., et al. (2003) 20-Hydroxyeicosatetraenoic acid (20-HETE) activates mouse TRPC6 channels expressed in HEK293 cells. *Journal of Biological Chemistry*. 278 (34), 31709–31716.

Bedard, K. & Krause, K.-H. (2007) The NOX family of ROS-generating NADPH oxidases: physiology and pathophysiology. *Physiological reviews*. 87 (1), 245–313.

Benilova, I., Karran, E. & De Strooper, B. (2012) The toxic Aβ oligomer and Alzheimer's disease: An emperor in need of clothes. *Nature Neuroscience*.15 (3) pp.349–357.

Berne, R.M., Levy, M.N. & Koeppen, B.M. (2008) *Berne & levy physiology*. Elsevier Brasil.

Berry, C., Hamilton, C.A., Brosnan, M.J., Magill, F.G., et al. (2000) Investigation Into the Sources of Superoxide in Human Blood Vessels. *Circulation*. 101 (18), 2206–2212.

Berthiaume, A.A., Grant, R.I., McDowell, K.P., Underly, R.G., et al. (2018) Dynamic Remodeling of Pericytes In Vivo Maintains Capillary Coverage in the Adult Mouse Brain. *Cell Reports*. 22 (1), 8–16.

Bertram, L. & Tanzi, R.E. (2004) Alzheimer's disease: one disorder, too many genes? *Human Molecular Genetics*. 13 (suppl_1), R135–R141.

Bianca, V.D., Dusi, S., Bianchini, E., Dal Prà, I., et al. (1999) beta-amyloid activates the O-2 forming NADPH oxidase in microglia, monocytes, and neutrophils. A possible inflammatory mechanism of neuronal damage in Alzheimer's disease. *The Journal of biological chemistry*. 274 (22), 15493–15499.

Bielski, B.H.J. & Cabelli, D.E. (1995) Superoxide and Hydroxyl Radical Chemistry in Aqueous Solution. In: *Active Oxygen in Chemistry*. Springer Netherlands. pp. 66–104.

Bin-Jaliah, I. & Haffor, A.-S. (2018) Ultrastructural Morphological Alterations during Hyperoxia Exposure in Relation to Glutathione Peroxidase Activity and Free Radicals Productions in the Mitochondria of the Cortical Brain Alteraciones Morfológicas Ultraestructurales durante la Exposición a. *Int. J. Morphol*.36 (4).

Binnewijzend, M.A.A., Benedictus, M.R., Kuijer, J.P.A., van der Flier, W.M., et al. (2016) Cerebral perfusion in the predementia stages of Alzheimer's disease. *European Radiology*. 26 (2), 506–514.

Blazey, T., Snyder, A.Z., Goyal, M.S., Vlassenko, A.G., et al. (2018) A systematic meta-analysis of oxygen-toglucose and oxygen-to-carbohydrate ratios in the resting human brain. *PLoS ONE*. 13 (9).

Boas, D.A., Jones, S.R., Devor, A., Huppert, T.J., et al. (2008) A vascular anatomical network model of the spatio-temporal response to brain activation. *NeuroImage*. 40 (3), 1116–1129.

Bocci, M., Oudenaarden, C., Xavier Sàenz-Sardà, †, Simrén, J., et al. (2021) Infection of brain pericytes underlying neuropathology of COVID-19 patients. *bioRxiv*. 2021.05.24.445532.

Braak, H. & Braak, E. (1991) Acta H ’ pathologica Neuropathological stageing of Alzheimer-related changes. *Acta Neuropathol*.82.

Brand, M.D. (2010) The sites and topology of mitochondrial superoxide production. *Experimental gerontology*. 45 (7–8), 466.

Brandes, R.P., Barton, M., Philippens, K.M., Schweitzer, G., et al. (1997) Endothelial-derived superoxide anions in pig coronary arteries: evidence from lucigenin chemiluminescence and histochemical techniques. *The Journal of Physiology*. 500 (Pt 2), 331.

Brann, D.H., Tsukahara, T., Weinreb, C., Lipovsek, M., et al. (2020) Non-neuronal expression of SARS-CoV-2 entry genes in the olfactory system suggests mechanisms underlying COVID-19-associated anosmia. *Science Advances*. 6 (31), 5801–5832.

Brian, D.A. & Baric, R.S. (2005) Coronavirus genome structure and replication. *Current Topics in Microbiology and Immunology*.287 pp.1–30.

Bruce-Keller, A.J., Gupta, S., Knight, A.G., Beckett, T.L., et al. (2011) Cognitive Impairment in Humanized APPxPS1 Mice is Linked to Aβ 1-42 and NOX Activation. *Neurobiol Dis*. 44 (3), 317–326.

Bruce-Keller, A.J., Gupta, S., Parrino, T.E., Knight, A.G., et al. (2010) NOX Activity Is Increased in Mild Cognitive Impairment. *Antioxidants & Redox Signaling*. 12 (12), 1371–1382.

Brueckl, C., Kaestle, S., Kerem, A., Habazettl, H., et al. (2006) Hyperoxia-induced reactive oxygen species formation in pulmonary capillary endothelial cells in situ. *American Journal of Respiratory Cell and Molecular Biology*. 34 (4), 453–

463.

Brugniaux, J.V., Coombs, G.B., Barak, O.F., Dujic, Z., et al. (2018) Highs and lows of hyperoxia: Physiological, performance, and clinical aspects. *American Journal of Physiology - Regulatory Integrative and Comparative Physiology*.315 (1) pp.R1-R27,.

Brunnström, H.R. & Englund, E.M. (2009) Cause of death in patients with dementia disorders. *European Journal of Neurology*. 16 (4), 488–492.

Burdyga, T. & Borysova, L. (2014) Calcium signalling in pericytes. *Journal of Vascular Research*.51 (3) pp.190–199.

Butterfield, D.A., Reed, T.T., Perluigi, M., De Marco, C., et al. (2007) Elevated levels of 3-nitrotyrosine in brain from subjects with amnestic mild cognitive impairment: Implications for the role of nitration in the progression of Alzheimer's disease. *Brain Research*. 1148, 243–248.

Cai, C., Fordsmann, J.C., Jensen, S.H., Gesslein, B., et al. (2018) Stimulation-induced increases in cerebral blood flow and local capillary vasoconstriction depend on conducted vascular responses. *Proceedings of the National Academy of Sciences of the United States of America*. 115 (25), E5796–E5804.

Cao, W., Fang, Z., Hou, G., Han, M., et al. (2020) The psychological impact of the COVID-19 epidemic on college students in China. *Psychiatry Research*. 287, 112934.

Cardot-Leccia, N., Hubiche, T., Dellamonica, J., Burel-Vandenbos, F., et al. (2020) Pericyte alteration sheds light on micro-vasculopathy in COVID-19 infection. *Intensive Care Medicine*.46 (9) pp.1777–1778.

Carnethon, M.R. (2009) Physical Activity and Cardiovascular Disease: How Much Is Enough? *American Journal of Lifestyle Medicine*. 3 (1_suppl), 44S-49S.

Caro, C.G., Pedley, T.J., Schroter, R.C., Seed, W.A., et al. (2011) *The Mechanics of the Circulation*. Cambridge, Cambridge University Press.

Carrano, A., Hoozemans, J.J.M., Van Der Vies, S.M., Rozemuller, A.J.M., et al. (2011) Amyloid beta induces oxidative stress-mediated blood-brain barrier changes in capillary amyloid angiopathy. *Antioxidants and Redox Signaling*. 15 (5), 1167–1178.

Carvalho, C., Machado, N., Mota, P.C., Correia, S.C., et al. (2013) Type 2 Diabetic and Alzheimer's Disease Mice Present Similar Behavioral, Cognitive, and Vascular Anomalies. *Journal of Alzheimer's Disease*. 35, 623–635.

Carvalho, C. & Moreira, P.I. (2018) Oxidative stress: A major player in cerebrovascular alterations associated to neurodegenerative events. *Frontiers in Physiology*.9 (JUL) p.806.

Cascella, M., Rajnik, M., Cuomo, A., Dulebohn, S.C., et al. (2020) *Features, Evaluation and Treatment Coronavirus (COVID-19)*. StatPearls Publishing.

Castiglione, G.M., Zhou, L., Xu, Z., Neiman, Z., et al. (2021) The ancient cardioprotective mechanisms of ACE2 bestow SARS-CoV-2 with a wide host range. *bioRxiv*.

Cavaliere, F., Urra, O., Alberdi, E. & Matute, C. (2012) Oligodendrocyte differentiation from adult multipotent stem cells is modulated by glutamate. *Cell Death & Disease*. 3 (2), e268–e268.

Chai, S.Y., Fernando, R., Peck, G., Ye, S.-Y., et al. (2004) The angiotensin IV/AT 4 receptor. *CMLS, Cell. Mol. Life Sci*. 61, 2728–2737.

Chakravarthy, U., Gardiner, T.A., Anderson, P., Archer, D.B., et al. (1992) The effect of endothelin 1 on the retinal microvascular pericyte. *Microvascular Research*. 43 (3), 241–254.

Chan, J.F.W., Zhang, A.J., Yuan, S., Poon, V.K.M., et al. (2020) Simulation of the Clinical and Pathological Manifestations of Coronavirus Disease 2019 (COVID-19) in a Golden Syrian Hamster Model: Implications for Disease Pathogenesis and Transmissibility. *Clinical Infectious Diseases*. 71 (9), 2428–2446.

Charles, A.C. & Baca, S.M. (2013) Cortical spreading depression and migraine. *Nature Reviews Neurology*.9 (11) pp.637–644.

Chasseigneaux, S., Moraca, Y., Cochois-Guégan, V., Boulay, A.C., et al. (2018) Isolation and differential transcriptome of vascular smooth muscle cells and mid-capillary pericytes from the rat brain. *Scientific Reports*. 8 (1), 12272.

Chen, F., Haigh, S., Barman, S.A. & Fulton, D.J.R. (2012) From form to function: the role of Nox4 in the cardiovascular system. *Frontiers in Physiology*. 412.

Chen, G.F., Xu, T.H., Yan, Y., Zhou, Y.R., et al. (2017) Amyloid beta: Structure, biology and structure-based therapeutic development. *Acta Pharmacologica Sinica*.38 (9) pp.1205–1235.

Chen, J., Wang, R., Wang, M. & Wei, G.W. (2020a) Mutations Strengthened SARS-CoV-2 Infectivity. *Journal of Molecular Biology*. 432 (19), 5212–5226.

Chen, L., Li, X., Chen, M., Feng, Y., et al. (2020b) The ACE2 expression in human

heart indicates new potential mechanism of heart injury among patients infected with SARS-CoV-2. *Cardiovascular Research*. 116 (6), 1097–1100.

Chen, Q., Wang, Q., Zhu, J., Xiao, Q., et al. (2018) Reactive oxygen species: key regulators in vascular health and diseases. *British journal of pharmacology*. 175 (8), 1279–1292.

Chen, Y.-R. & Glabe, C.G. (2006) Distinct early folding and aggregation properties of Alzheimer amyloid-beta peptides Abeta40 and Abeta42: stable trimer or tetramer formation by Abeta42. *The Journal of biological chemistry*. 281 (34), 24414–24422.

Cheng, G., Cao, Z., Xu, X., Meir, E.G.V., et al. (2001) Homologs of gp91phox: Cloning and tissue expression of Nox3, Nox4, and Nox5. *Gene*. 269 (1–2), 131–140.

Cheng, J., Korte, N., Nortley, R., Sethi, H., et al. (2018) Targeting pericytes for therapeutic approaches to neurological disorders. *Acta Neuropathologica*. 136 (4), 507–523.

Chih, C.P., He, J., Sly, T.S. & Roberts, E.L. (2001) Comparison of glucose and lactate as substrates during NMDA-induced activation of hippocampal slices. *Brain research*. 893 (1–2), 143–154.

Chiu, A.T., Dunscomb, J., Kosierowski, J., Burton, C.R.A., et al. (1993) The Ligand Binding Signatures of the Rat AT1A, AT1B and the Human AT1 Receptors Are Essentially Identical. *Biochemical and Biophysical Research Communications*. 197 (2), 440–449.

Choi, S.H., Aid, S., Kim, H.W., Jackson, S.H., et al. (2012) Inhibition of NADPH

oxidase promotes alternative and anti-inflammatory microglial activation during neuroinflammation. *Journal of Neurochemistry*. 120 (2), 292–301.

Chow, N., Bell, R.D., Deane, R., Streb, J.W., et al. (2007) Serum response factor and myocardin mediate arterial hypercontractility and cerebral blood flow dysregulation in Alzheimer's phenotype. *Proceedings of the National Academy of Sciences of the United States of America*. 104 (3), 823–828.

Chu, D.K., Kim, L.H.Y., Young, P.J., Zamiri, N., et al. (2018) Mortality and morbidity in acutely ill adults treated with liberal versus conservative oxygen therapy (IOTA): a systematic review and meta-analysis. *The Lancet*. 391 (10131), 1693–1705.

Ciarlone, G.E. & Dean, J.B. (2016) Normobaric hyperoxia stimulates superoxide and nitric oxide production in the caudal solitary complex of rat brain slices. *American Journal of Physiology - Cell Physiology*. 311 (6), C1014–C1026.

Ciarlone, G.E., Hinojo, C.M., Stavitzski, N.M. & Dean, J.B. (2019) CNS function and dysfunction during exposure to hyperbaric oxygen in operational and clinical settings. *Redox Biology*.27 p.101159.

Ciudad, S., Puig, E., Botzanowski, T., Meigooni, M., et al. (2020) Aβ(1-42) tetramer and octamer structures reveal edge conductivity pores as a mechanism for membrane damage. *Nature Communications*. 11 (1).

Claxton, S., Kostourou, V., Jadeja, S., Chambon, P., et al. (2008) Efficient, inducible Cre-recombinase activation in vascular endothelium. *genesis*. 46 (2), 74–80.

Cline, E.N., Bicca, M.A., Viola, K.L. & Klein, W.L. (2018) The Amyloid-β Oligomer Hypothesis: Beginning of the Third Decade. *Journal of Alzheimer's Disease*.64

(s1) pp.S567–S610.

Clozel, M., Gray, G.A., Breu, V., Löffler, B.M., et al. (1992) The endothelin ETB receptor mediates both vasodilation and vasoconstriction in vivo. *Biochemical and Biophysical Research Communications*. 186 (2), 867–873.

Cobley, J.N. (2020) Mechanisms of mitochondrial ros in assisted reproduction: The known, the unknown, and the intriguing. *Antioxidants*. 9 (10), 1–31.

Coelho-Santos, V., Shih, A.Y., Coelho-Santos, V. & Shih, A.Y. (2020) Postnatal development of cerebrovascular structure and the neurogliovascular unit. *Wiley Interdisciplinary Reviews: Developmental Biology*. 9 (2), 1–20.

Collin, F. (2019) Chemical basis of reactive oxygen species reactivity and involvement in neurodegenerative diseases. *International Journal of Molecular Sciences*.20 (10).

Conceicao, C., Thakur, N., Human, S., Kelly, J.T., et al. (2020) The SARS-CoV-2 Spike protein has a broad tropism for mammalian ACE2 proteins. *PLoS Biology*. 18 (12 December), e3001016.

Connolly, E.S., Rabinstein, A.A., Carhuapoma, J.R., Derdeyn, C.P., et al. (2012) Guidelines for the management of aneurysmal subarachnoid hemorrhage: A guideline for healthcare professionals from the american heart association/american stroke association. *Stroke*.43 (6) pp.1711–1737.

Cornish, D. & Owen-Williams, R. (2020) Deaths registered in England and Wales: 2019. *London: Office for National Statistics*.

Cosardereliogl u, C., Nidadavolu, L.S., George, C.J., Oh, E.S., et al. (2020) Brain

Renin–Angiotensin System at the Intersect of Physical and Cognitive Frailty. *Frontiers in Neuroscience*.14 p.981.

Cox, D.W.G. & Bachelard, H.S. (1988) Partial attenuation of dentate granule cell evoked activity by the alternative substrates, lactate and pyruvate: evidence for a postsynaptic action. *Experimental Brain Research 1988 69:2*. 69 (2), 368–372.

Crapper McLachlan, D.R., Dalton, A.J., Kruck, T.P., Bell, M.Y., et al. (1991) Intramuscular desferrioxamine in patients with Alzheimer's disease. *Lancet (London, England)*. 337 (8753), 1304–1308.

Cryer, P.E. (2007) Hypoglycemia, functional brain failure, and brain death. *Journal of Clinical Investigation*.117 (4) pp.868–870.

D'Agostino, D.P., Putnam, R.W. & Dean, J.B. (2007) Superoxide (•O2-) production in CA1 neurons of rat hippocampal slices exposed to graded levels of oxygen. *Journal of Neurophysiology*. 98 (2), 1030–1041.

Daems, M., Liesenborghs, L., Cuijpers, I., Boudewijns, R., et al. (2020) SARS-CoV-2 infection leads to cardiac pericyte loss, fibrosis, cardiomyocyte hypertrophy, and diastolic dysfunction. *Research Square*.

Dallinger, S., Dorner, G.T., Wenzel, R., Graselli, U., et al. (2000) Endothelin-1 contributes to hyperoxia-induced vasoconstriction in the human retina. *Investigative ophthalmology & visual science*. 41 (3), 864–869.

Damisah, E.C., Hill, R.A., Tong, L., Murray, K.N., et al. (2017) A fluoro-Nissl dye identifies pericytes as distinct vascular mural cells during in vivo brain imaging. *Nature Neuroscience*. 20 (7), 1023–1032.

Dasgupta, C. & Zhang, L. (2011) Angiotensin II receptors and drug discovery in cardiovascular disease. *Drug Discovery Today*. 16 (1–2), 22–34.

Davenport, A.P., Hyndman, K.A., Dhaun, N., Southan, C., et al. (2016) Endothelin. *Pharmacological Reviews*.68 (2) pp.357–418.

Davis, C.M., Liu, X. & Alkayed, N.J. (2017) Cytochrome P450 eicosanoids in cerebrovascular function and disease. *Pharmacology and Therapeutics*.179 pp.31–46.

Deane, R., Yan, S. Du, Submamaryan, R.K., LaRue, B., et al. (2003) RAGE mediates amyloid-β peptide transport across the blood-brain barrier and accumulation in brain. *Nature Medicine*. 9 (7), 907–913.

Dehouck, M.P., Vigne, P., Torpier, G., Breittmayer, J.P., et al. (1997) Endothelin-1 as a mediator of endothelial cell-pericyte interactions in bovine brain capillaries. *Journal of Cerebral Blood Flow and Metabolism*. 17 (4), 464–469.

Demchenko, I.T., Oury, T.D., Crapo, J.D. & Piantadosi, C.A. (2002) Regulation of the brain's vascular responses to oxygen. *Circulation Research*. 91 (11), 1031–1037.

Dessalles, C.A., Babataheri, A. & Barakat, A.I. (2021) *Pericyte mechanics and mechanobiology*.

Didion, S.P. & Faraci, F.M. (2002) Effects of NADH and NADPH on superoxide levels and cerebral vascular tone. *American Journal of Physiology-Heart and Circulatory Physiology*. 282 (2), H688–H695.

Dienel, G.A. (2019) Brain glucose metabolism: Integration of energetics with

function. *Physiological Reviews*. 99 (1), 949–1045.

Dienel, G.A. (2012) Fueling and imaging brain activation. *ASN Neuro*.4 (5) pp.267–321.

Dienel, G.A. & Hertz, L. (2001) Glucose and lactate metabolism during brain activation. *Journal of Neuroscience Research*. 66 (5), 824–838.

Dimitropoulou, C., White, R.E., Fuchs, L., Zhang, H., et al. (2001) Angiotensin II Relaxes Microvessels Via the AT 2 Receptor and Ca 2+ -Activated K + (BK Ca) Channels. *Hypertension*. 37 (2), 301–307.

Ding, J., Zhou, D., Sui, M., Meng, R., et al. (2018) The effect of normobaric oxygen in patients with acute stroke: a systematic review and meta-analysis. *Neurological Research*. 40 (6), 433–444.

DiNuzzo, M., Mangia, S., Maraviglia, B. & Giove, F. (2010) Glycogenolysis in Astrocytes Supports Blood-Borne Glucose Channeling Not Glycogen-Derived Lactate Shuttling to Neurons: Evidence from Mathematical Modeling. *Journal of Cerebral Blood Flow & Metabolism*. 30 (12), 1895–1904.

DiResta, G.R., Lee, J., Lau, N., Ali, F., et al. (1990) Measurement of Brain Tissue Density Using Pycnometry. In: *Brain Edema VIII*. Vienna, Springer Vienna. pp. 34–36.

Donahue, J.E., Flaherty, S.L., Johanson, C.E., Duncan, J.A., et al. (2006) RAGE, LRP-1, and amyloid-beta protein in Alzheimer's disease. *Acta Neuropathologica*. 112 (4), 405–415.

Dong, E., Du, H. & Gardner, L. (2020) An interactive web-based dashboard to track

COVID-19 in real time. *The Lancet Infectious Diseases*.20 (5) pp.533–534.

Doobay, M.F., Talman, L.S., Obr, T.D., Tian, X., et al. (2007) Differential expression of neuronal ACE2 in transgenic mice with overexpression of the brain renin-angiotensin system. *American journal of physiology. Regulatory, integrative and comparative physiology*. 292 (1), R373-81.

Dore-Duffy, P., Wang, S., Mehedi, A., Katyshev, V., et al. (2011) Pericyte-mediated vasoconstriction underlies TBI-induced hypoperfusion. *Neurological Research*. 33 (2), 176–184.

Drummond, E. & Wisniewski, T. (2017) Alzheimer's Disease: Experimental Models and Reality. *Acta neuropathologica*. 133 (2), 155.

Du, G., Huang, P., Liang, B.T. & Frohman, M.A. (2004) Phospholipase D2 Localizes to the Plasma Membrane and Regulates Angiotensin II Receptor Endocytosis. *Molecular Biology of the Cell*. 15 (3), 1024–1030.

Duvernoy, H.M., Delon, S. & Vannson, J.L. (1981) Cortical blood vessels of the human brain. *Brain Research Bulletin*. 7 (5), 519–579.

Dzau, V.J. (1988) Tissue renin-angiotensin system: physiologic and pharmacologic implications. Introduction. *Circulation*. 77 (6 Pt 2), I1-3.

Eberth, C.J. (1871) *Handbuch der Lehre von der Gewegen des Menschen und der Tiere (Vol. 1)*.

Edson, K. & Rettie, A. (2013) CYP4 Enzymes As Potential Drug Targets: Focus on Enzyme Multiplicity, Inducers and Inhibitors, and Therapeutic Modulation of 20-Hydroxyeicosatetraenoic Acid (20-HETE) Synthase and Fatty Acid ω-

Hydroxylase Activities. *Current Topics in Medicinal Chemistry*. 13 (12), 1429–1440.

Ellul, M.A., Benjamin, L., Singh, B., Lant, S., et al. (2020) Neurological associations of COVID-19. *The Lancet Neurology*.19 (9) pp.767–783.

Elshenawy, O.H., Shoieb, S.M., Mohamed, A. & El-Kadi, A.O.S. (2017) Clinical implications of 20-hydroxyeicosatetraenoic acid in the kidney, liver, lung and brain: An emerging therapeutic target. *Pharmaceutics*.9 (1).

Engl, E. & Attwell, D. (2015) Non-signalling energy use in the brain. *The Journal of Physiology*. 593 (Pt 16), 3417.

Esakandari, H., Nabi-Afjadi, M., Fakkari-Afjadi, J., Farahmandian, N., et al. (2020) A comprehensive review of COVID-19 characteristics. *Biological Procedures Online*.22 (1).

Esiri, M.M. & Wilcock, G.K. (1986) Cerebral amyloid angiopathy in dementia and old age. *Neurosurgery, and Psychiatry*. 49, 1221–1226.

Evans, M.L., Lindauer, M. & Farrell, M.E. (2020) A Pandemic within a Pandemic — Intimate Partner Violence during Covid-19. *New England Journal of Medicine*. 383 (24), 2302–2304.

Fan, F., Ge, Y., Lv, W., Elliott, M.R., et al. (2016) Molecular mechanisms and cell signaling of 20-hydroxyeicosatetraenoic acid in vascular pathophysiology. *Frontiers in Bioscience - Landmark*.21 (7) pp.1427–1463.

Faraci, F.M. (2006) Reactive oxygen species: Influence on cerebral vascular tone. *Journal of Applied Physiology*. 100 (2), 739–743.

Faraci, F.M., Lamping, K.G., Modrick, M.L., Ryan, M.J., et al. (2006) Cerebral vascular effects of angiotensin II: New insights from genetic models. *Journal of Cerebral Blood Flow and Metabolism*. 26 (4), 449–455.

Farkas, E. & Luiten, P.G.M. (2001) Cerebral microvascular pathology in aging and Alzheimer's disease. *Progress in Neurobiology*.64 (6) pp.575–611.

Ferrario, C.M., Jessup, J., Chappell, M.C., Averill, D.B., et al. (2005) Effect of angiotensin-converting enzyme inhibition and angiotensin II receptor blockers on cardiac angiotensin-converting enzyme 2. *Circulation*. 111 (20), 2605–2610.

Fordsmann, J.C., Ko, R.W.Y., Choi, H.B., Thomsen, K., et al. (2013) Increased 20-HETE synthesis explains reduced cerebral blood flow but not impaired neurovascular coupling after cortical spreading depression in rat cerebral cortex. *Journal of Neuroscience*. 33 (6), 2562–2570.

Fowler, J.C. (1993) Glucose Deprivation Results in a Lactate Preventable Increase in Adenosine and Depression of Synaptic Transmission in Rat Hippocampal Slices. *Journal of Neurochemistry*. 60 (2), 572–576.

Fox, P.T., Raichle, M.E., Mintun, M.A. & Dence, C. (1988) Nonoxidative glucose consumption during focal physiologic neural activity. *Science*. 241 (4864), 462–464.

Fraile, M.L., Conde, M. V, Sanz, L., Moreno, M.J., et al. (1994) Different influence of superoxide anions and hydrogen peroxide on endothelial function of isolated cat cerebral and pulmonary arteries. *General Pharmacology*. 25 (6), 1197–1205.

Frieman, M., Yount, B., Agnihothram, S., Page, C., et al. (2012) Molecular Determinants of Severe Acute Respiratory Syndrome Coronavirus Pathogenesis

and Virulence in Young and Aged Mouse Models of Human Disease. *Journal of Virology*. 86 (2), 884–897.

Frisbee, J.C., Krishna, U.M., Falck, J.R. & Lombard, J.H. (2001) Role of Prostanoids and 20-HETE in Mediating Oxygen-Induced Constriction of Skeletal Muscle Resistance Arteries. *Microvascular Research*. 62 (3), 271–283.

Fukuda, S., Koga, Y., Fujita, M., Suehiro, E., et al. (2019) Hyperoxemia during the hyperacute phase of aneurysmal subarachnoid hemorrhage is associated with delayed cerebral ischemia and poor outcome: a retrospective observational study. *Journal of Neurosurgery*. 1 (aop), 1–8.

Fuxe, K., Ganten, D., Hökfelt, T., Locatelli, V., et al. (1980) Renin-like immunocytochemical activity in the rat and mouse brain. *Neuroscience Letters*. 18 (3), 245–250.

Gabriel, L.R., Wu, S. & Melikian, H.E. (2014) Brain slice biotinylation: An ex vivo approach to measure region-specific plasma membrane protein trafficking in adult neurons. *Journal of Visualized Experiments*. (86), 51240.

Gainer, J. V., Bellamine, A., Dawson, E.P., Womble, K.E., et al. (2005) Functional variant of CYP4A11 20-hydroxyeicosatetraenoic acid synthase is associated with essential hypertension. *Circulation*. 111 (1), 63–69.

Ganz, W., Donoso, R., Marcus, H. & Swan, H.J. (1972) Coronary hemodynamics and myocardial oxygen metabolism during oxygen breathing in patients with and without coronary artery disease. *Circulation*. 45 (4), 763–768.

Garrido-Gil, P., Rodriguez-Perez, A.I., Fernandez-Rodriguez, P., Lanciego, J.L., et al. (2017) Expression of angiotensinogen and receptors for angiotensin and

prorenin in the rat and monkey striatal neurons and glial cells. *Brain Structure and Function*. 222 (6), 2559–2571.

Gee, J.M., Smith, N.A., Fernandez, F.R., Economo, M.N., et al. (2014) Imaging Activity in Neurons and Glia with a Polr2a-Based and Cre-Dependent GCaMP5G-IRES-tdTomato Reporter Mouse. *Neuron*. 83 (5), 1058–1072.

De Georgia, M.A. (2015) Brain Tissue Oxygen Monitoring in Neurocritical Care. *Journal of Intensive Care Medicine*.30 (8) pp.473–483.

Germanò, A., Imperatore, C., D'Avella, D., Costa, G., et al. (1998) Antivasospastic and brain-protective effects of a hydroxyl radical scavenger (AVS) after experimental subarachnoid hemorrhage. *Journal of Neurosurgery*. 88 (6), 1075–1081.

Ghebreyesus, T.A. (2020) *WHO Director-General's opening remarks at the media briefing on COVID-19-2020*.

Gironacci, M.M., Vatta, M., Rodriguez-Fermepín, M., Fernández, B.E., et al. (2000) Angiotensin-(1-7) reduces norepinephrine release through a nitric oxide mechanism in rat hypothalamus. *Hypertension*. 35 (6), 1248–1252.

Glabe, C.G. (2006) Common mechanisms of amyloid oligomer pathogenesis in degenerative disease. *Neurobiology of Aging*. 27, 570–575.

Gonzalez-Fernandez, E., Staursky, D., Lucas, K., Nguyen, B. V., et al. (2020) 20-HETE Enzymes and Receptors in the Neurovascular Unit: Implications in Cerebrovascular Disease. *Frontiers in Neurology*. 11, 983.

Gordon, G.R.J., Choi, H.B., Rungta, R.L., Ellis-Davies, G.C.R., et al. (2008) Brain

metabolism dictates the polarity of astrocyte control over arterioles. *Nature*. 456 (7223), 745–750.

Gould, I.G., Tsai, P., Kleinfeld, D. & Linninger, A. (2017) The capillary bed offers the largest hemodynamic resistance to the cortical blood supply. *Journal of Cerebral Blood Flow and Metabolism*. 37 (1), 52–68.

Govindpani, K., McNamara, L.G., Smith, N.R., Vinnakota, C., et al. (2019) Vascular Dysfunction in Alzheimer's Disease: A Prelude to the Pathological Process or a Consequence of It? *Journal of Clinical Medicine*. 8 (5), 651.

Grant, R.I., Hartmann, D.A., Underly, R.G., Berthiaume, A.A., et al. (2019) Organizational hierarchy and structural diversity of microvascular pericytes in adult mouse cortex. *Journal of Cerebral Blood Flow and Metabolism*. 39 (3), 411–425.

Green, S.P., Cairns, B., Rae, J., Errett-Baroncini, C., et al. (2001) Induction of gp91-phox, a component of the phagocyte NADPH oxidase, in microglial cells during central nervous system inflammation. *Journal of Cerebral Blood Flow and Metabolism*. 21 (4), 374–384.

Greenhalgh, T., Jimenez, J.L., Prather, K.A., Tufekci, Z., et al. (2021) Ten scientific reasons in support of airborne transmission of SARS-CoV-2. *The Lancet*.397 (10285) pp.1603–1605.

Griendling, K.K., Delafontaine, P., Rittenhouse, S.E., Gimbrone, M.A., et al. (1987) Correlation of receptor sequestration with sustained diacylglycerol accumulation in angiotensin II-stimulated cultured vascular smooth muscle cells. *Journal of Biological Chemistry*. 262 (30), 14555–14562.

Grobe, J.L., Xu, D. & Sigmund, C.D. (2008) An intracellular renin-angiotensin system in neurons: Fact, hypothesis, or fantasy. *Physiology*. 23 (4), 187–193.

Guensch, D.P., Fischer, K., Shie, N., Lebel, J., et al. (2015) Hyperoxia Exacerbates Myocardial Ischemia in the Presence of Acute Coronary Artery Stenosis in Swine. *Circulation: Cardiovascular Interventions*. 8 (10).

Guo, T., Zhang, D., Zeng, Y., Huang, T.Y., et al. (2020) Molecular and cellular mechanisms underlying the pathogenesis of Alzheimer's disease. *Molecular Neurodegeneration*.15 (1) pp.1–37.

Gutteridge, J.M.C. (1985a) Inhibition of the Fenton reaction by the protein caeruloplasmin and other copper complexes. Assessment of ferroxidase and radical scavenging activities. *Chemico-Biological Interactions*. 56 (1), 113–120.

Gutteridge, J.M.C. (1985b) Superoxide dismutase inhibits the superoxide-driven Fenton reaction at two different levels. *FEBS Letters*. 185 (1), 19–23.

Gutteridge, J.M.C., Maidt, L. & Poyer, L. (1990) Superoxide dismutase and Fenton chemistry. Reaction of ferric-EDTA complex and ferric-bipyridyl complex with hydrogen peroxide without the apparent formation of iron(II). *Biochemical Journal*. 269 (1), 169–174.

Guzik, T.J., West, N.E.J., Black, E., McDonald, D., et al. (2000) Vascular Superoxide Production by NAD(P)H Oxidase. *Circulation Research*. 86 (9).

Ha, J.S., Lee, J.E., Lee, J.R., Lee, C.S., et al. (2010) Nox4-dependent H2O2 production contributes to chronic glutamate toxicity in primary cortical neurons. *Experimental Cell Research*. 316 (10), 1651–1661.

Hafen, B.B. & Sharma, S. (2021) *Oxygen Saturation*. StatPearls Publishing.

Hahn, A., Gryglewski, G., Nics, L., Hienert, M., et al. (2016) Quantification of task-specific glucose metabolism with constant infusion of 18F-FDG. *Journal of Nuclear Medicine*.

Hall, C.N. & Attwell, D. (2008) Assessing the physiological concentration and targets of nitric oxide in brain tissue. *Journal of Physiology*. 586 (15), 3597–3615.

Hall, C.N., Klein-Flügge, M.C., Howarth, C. & Attwell, D. (2012) Oxidative phosphorylation, not glycolysis, powers presynaptic and postsynaptic mechanisms underlying brain information processing. *Journal of Neuroscience*. 32 (26), 8940–8951.

Hall, C.N., Reynell, C., Gesslein, B., Hamilton, N.B., et al. (2014) Capillary pericytes regulate cerebral blood flow in health and disease. *Nature*. 508 (1), 55–60.

Hama-Tomioka, K., Kinoshita, H., Azma, T., Nakahata, K., et al. (2009) The role of 20-hydroxyeicosatetraenoic acid in cerebral arteriolar constriction and the inhibitory effect of propofol. *Anesthesia and Analgesia*. 109 (6), 1935–1942.

Hamilton, N.B., Attwell, D. & Hall, C.N. (2010) Pericyte-mediated regulation of capillary diameter: a component of neurovascular coupling in health and disease. *Frontiers in neuroenergetics*. 2, 5.

Harder, D.R., Gebremedhin, D., Narayanan, J., Jefcoat, C., et al. (1994) Formation and action of a P-450 4A metabolite of arachidonic acid in cat cerebral microvessels. *American Journal of Physiology - Heart and Circulatory Physiology*. 266 (5 35-5).

Harder, D.R., Lange, A.R., Gebremedhin, D., Birks, E.K., et al. (1997) Cytochrome P450 metabolites of arachidonic acid as intracellular signaling molecules in vascular tissue. *Journal of Vascular Research*. 34 (3), 237–243.

Harder, D.R., Narayanan, J., Birks, E.K., Liard, J.F., et al. (1996) Identification of a putative microvascular oxygen sensor. *Circulation Research*. 79 (1), 54–61.

Hardy, J.A. & Higgins, G.A. (1992) Alzheimer's disease: The amyloid cascade hypothesis. *Science*.256 (5054) pp.184–185.

Harland, S.P., Kuc, R.E., Pickard, J.D. & Davenport, A.P. (1995) Characterization of endothelin receptors in human brain cortex, gliomas, and meningiomas. *Journal of cardiovascular pharmacology*. 26 Suppl 3, S408-11.

Hartings, J.A., Watanabe, T., Bullock, M.R., Okonkwo, D.O., et al. (2011) Spreading depolarizations have prolonged direct current shifts and are associated with poor outcome in brain trauma. *Brain*. 134 (5), 1529–1540.

Hartmann, D.A., Berthiaume, A.A., Grant, R.I., Harrill, S.A., et al. (2021) Brain capillary pericytes exert a substantial but slow influence on blood flow. *Nature Neuroscience*. 24 (5), 633–645.

Hartmann, D.A., Underly, R.G., Grant, R.I., Watson, A.N., et al. (2015) Pericyte structure and distribution in the cerebral cortex revealed by high-resolution imaging of transgenic mice. *Neurophotonics*. 2 (4), 041402.

Hashimura, T., Kimura, T. & Miyakawa, T. (1991) Morphological Changes of Blood Vessels in the Brain with Alzheimer's Disease. *Psychiatry and Clinical Neurosciences*. 45 (3), 661–665.

Hauck, E.F., Apostel, S., Hoffmann, J.F., Heimann, A., et al. (2004) Capillary Flow and Diameter Changes during Reperfusion after Global Cerebral Ischemia Studied by Intravital Video Microscopy. *Journal of Cerebral Blood Flow and Metabolism*. 24 (4), 383–391.

Hays, C.C., Zlatar, Z.Z. & Wierenga, C.E. (2016) The Utility of Cerebral Blood Flow as a Biomarker of Preclinical Alzheimer's Disease. *Cellular and Molecular Neurobiology*.36 (2) pp.167–179.

He, L., Mäe, M.A., Muhl, L., Sun, Y., et al. (2020) Pericyte-specific vascular expression of SARS-CoV-2 receptor ACE2 – implications for microvascular inflammation and hypercoagulopathy in COVID-19. *bioRxiv*. 2020.05.11.088500.

He, L., Vanlandewijck, M., Mäe, M.A., Andrae, J., et al. (2018) Data descriptor: Single-cell RNA sequencing of mouse brain and lung vascular and vessel-associated cell types. *Scientific Data*. 5 (1), 1–11.

Hein, L., Meinel, L., Pratt, R.E., Dzau, V.J., et al. (1997) Intracellular trafficking of angiotensin II and its AT1 and AT2 receptors: Evidence for selective sorting of receptor and ligand. *Molecular Endocrinology*. 11 (9), 1266–1277.

Helms, J., Kremer, S., Merdji, H., Clere-Jehl, R., et al. (2020) Neurologic Features in Severe SARS-CoV-2 Infection. *New England Journal of Medicine*. 382 (23), 2268–2270.

Hermann, K., Raizada, M.K., Summers, C. & Phillips, M.I. (1987) Presence of renin in primary neuronal and glial cells from rat brain. *Brain Research*. 437 (2), 205–213.

Hernandes, M.S. & Britto, L.R.G. (2012) NADPH oxidase and neurodegeneration.

Current neuropharmacology. 10 (4), 321–327.

Hernández, J.C.C., Bracko, O., Kersbergen, C.J., Muse, V., et al. (2019) Neutrophil adhesion in brain capillaries reduces cortical blood flow and impairs memory function in Alzheimer's disease mouse models. *Nature neuroscience*. 22 (3), 413.

Herzog, R.I., Jiang, L., Herman, P., Zhao, C., et al. (2013) Lactate preserves neuronal metabolism and function following antecedent recurrent hypoglycemia. *The Journal of Clinical Investigation*. 123 (5), 1988–1998.

Higgins, R.D., Hendricks-Munoz, K.D., Caines, V. V., Gerrets, R.P., et al. (1998) Hyperoxia stimulates endothelin-1 secretion from endothelial cells; modulation by captopril and nifedipine. *Current Eye Research*. 17 (5), 487–493.

Hilenski, L.L., Clempus, R.E., Quinn, M.T., Lambeth, J.D., et al. (2004) Distinct Subcellular Localizations of Nox1 and Nox4 in Vascular Smooth Muscle Cells. *Arteriosclerosis, Thrombosis, and Vascular Biology*. 24 (4), 677–683.

Hilgers, R.H.P.P. & Webb, R.C. (2005) Molecular aspects of arterial smooth muscle contraction: focus on Rho. *Experimental biology and medicine (Maywood, N.J.)*. 230 (11), 829–835.

Hill, R.A., Tong, L., Yuan, P., Murikinati, S., et al. (2015) Regional Blood Flow in the Normal and Ischemic Brain Is Controlled by Arteriolar Smooth Muscle Cell Contractility and Not by Capillary Pericytes. *Neuron*. 87 (1), 95–110.

Hindenes, L.B., Håberg, A.K., Johnsen, L.H., Mathiesen, E.B., et al. (2020) Variations in the Circle of Willis in a large population sample using 3D TOF angiography: The Tromsø Study. *PLOS ONE*. 15 (11), e0241373.

Hippisley-Cox, J., Young, D., Coupland, C., Channon, K.M., et al. (2020) Risk of severe COVID-19 disease with ACE inhibitors and angiotensin receptor blockers: Cohort study including 8.3 million people. *Heart*. 106 (19), 1503–1511.

Hirschi, K.K. & D'Amore, P.A. (1996) Pericytes in the microvasculature. *Cardiovascular research*. 32 (4), 687–698.

Hirunpattarasilp, C., Attwell, D. & Freitas, F. (2019) The role of pericytes in brain disorders: from the periphery to the brain. *Journal of Neurochemistry*. 150 (6), 648–665.

Hlatky, R., Valadka, A.B., Gopinath, S.P. & Robertson, C.S. (2008) Brain tissue oxygen tension response to induced hyperoxia reduced in hypoperfused brain. *Journal of Neurosurgery*. 108 (1), 53–58.

Hoffmann, M., Kleine-Weber, H., Schroeder, S., Krüger, N., et al. (2020) SARS-CoV-2 Cell Entry Depends on ACE2 and TMPRSS2 and Is Blocked by a Clinically Proven Protease Inhibitor. *Cell*. 181 (2), 271-280.e8.

Hoopes, S.L., Garcia, V., Edin, M.L., Schwartzman, M.L., et al. (2015) Vascular actions of 20-HETE. *Prostaglandins and Other Lipid Mediators*.120 pp.9–16.

Horinouchi, T., Terada, K., Higashi, T. & Miwa, S. (2013) Endothelin Receptor Signaling: New Insight Into Its Regulatory Mechanisms. *Journal of Pharmacological Sciences*. 123 (2), 85–101.

Hu, B., Guo, H., Zhou, P. & Shi, Z.L. (2021) Characteristics of SARS-CoV-2 and COVID-19. *Nature Reviews Microbiology*.19 (3) pp.141–154.

Huang, W., Zhao, N., Bai, X., Karram, K., et al. (2014) Novel NG2-CreERT2 knock-in

mice demonstrate heterogeneous differentiation potential of NG2 glia during development. *Glia*. 62 (6), 896–913.

Hunyady, L., Catt, K.J., Clark, A.J.L. & Gáborik, Z. (2000) Mechanisms and functions of AT1 angiotensin receptor internalization. *Regulatory Peptides*. 91 (1–3), 29–44.

Huo, J., Le Bas, A., Ruza, R.R., Duyvesteyn, H.M.E., et al. (2020) Neutralizing nanobodies bind SARS-CoV-2 spike RBD and block interaction with ACE2. *Nature Structural and Molecular Biology*. 27 (9), 846–854.

Iadecola, C. (2004) Neurovascular regulation in the normal brain and in Alzheimer's disease. *Nature Reviews Neuroscience*.5 (5) pp.347–360.

Iadecola, C. (2017) The Neurovascular Unit Coming of Age: A Journey through Neurovascular Coupling in Health and Disease. *Neuron*.96 (1) pp.17–42.

Iadecola, C., Duering, M., Hachinski, V., Joutel, A., et al. (2019) Vascular Cognitive Impairment and Dementia: JACC Scientific Expert Panel. *Journal of the American College of Cardiology*.73 (25) pp.3326–3344.

Igase, M., Kohara, K., Nagai, T., Miki, T., et al. (2008) Increased expression of angiotensin converting enzyme 2 in conjunction with reduction of neointima by angiotensin II type 1 receptor blockade. *Hypertension Research*. 31 (3), 553–559.

Iida, Y., Katusic, Z.S. & Wei, E.P. (2000) Mechanisms of cerebral arterial relaxations to hydrogen peroxide. *Stroke*. 31 (9), 2224–2230.

Infanger, D.W., Sharma, R. V. & Davisson, R.L. (2006) NADPH Oxidases of the

Brain: Distribution, Regulation, and Function. *Antioxidants & Redox Signaling*. 8 (9–10), 1583–1596.

Ishii, A., Kurosawa, A., Saito, S. & Adachi, N. (2014) Analysis of the role of homology arms in gene-targeting vectors in human cells. *PLoS ONE*. 9 (9), 108236.

Ishizaka, N., Griendling, K.K., Lassègue, B. & Alexander, R.W. (1998) Angiotensin II type 1 receptor: Relationship with caveolae and caveolin after initial agonist stimulation. *Hypertension*. 32 (3), 459–466.

Iturria-Medina, Y., Sotero, R.C., Toussaint, P.J., Mateos-Pérez, J.M., et al. (2016) Early role of vascular dysregulation on late-onset Alzheimer's disease based on multifactorial data-driven analysis. *Nature Communications*. 7 (1), 11934.

Ivanov, K.P., Kalinina, M.K. & Levkovich, Y.I. (1981) Blood flow velocity in capillaries of brain and muscles and its physiological significance. *Microvascular Research*. 22 (2), 143–155.

Jackson, L., Eldahshan, W., Fagan, S.C. & Ergul, A. (2018) Within the Brain: The Renin Angiotensin System. *International Journal of Molecular Sciences*. 19 (3).

Jaeschke, H. (2010) Antioxidant Defense Mechanisms. *Comprehensive Toxicology, Second Edition*. 9, 319–337.

Jamali, A. El, Valente, A.J. & Clark, R.A. (2010) Regulation of Phagocyte NADPH Oxidase by Hydrogen Peroxide through a Ca2+/c-Abl Signaling Pathway. *Free radical biology & medicine*. 48 (6), 798.

Jan, A., Hartley, D.M. & Lashuel, H.A. (2010) Preparation and characterization of toxic aβ aggregates for structural and functional studies in alzheimer's disease

research. *Nature Protocols*. 5 (6), 1186–1209.

Jana, M.K., Cappai, R., Pham, C.L.L. & Ciccotosto, G.D. (2016) Membrane-bound tetramer and trimer Aβ oligomeric species correlate with toxicity towards cultured neurons. *Journal of Neurochemistry*. 136 (3), 594–608.

Janz, D.R., Hollenbeck, R.D., Pollock, J.S., McPherson, J.A., et al. (2012) Hyperoxia is associated with increased mortality in patients treated with mild therapeutic hypothermia after sudden cardiac arrest*. *Critical Care Medicine*. 40 (12), 3135–3139.

Jerison, H.J. (1973) *Evolution of the brain and intelligence*. Academic Press New York.

Johnson, K.A. & Albert, M.S. (2000) Perfusion abnormalities in prodromal AD. In: *Neurobiology of Aging*. March 2000 Neurobiol Aging. pp. 289–292.

Johnstone, J.T., Morton, P.D., Jayakumar, A.R., Johnstone, A.L., et al. (2013) Inhibition of NADPH oxidase activation in oligodendrocytes reduces cytotoxicity following trauma. *PLoS ONE*. 8 (11).

Johren, O., Inagami, T. & Saavedra, J.M. (1995) AT1A, AT1B, and AT2 angiotensin ii receptor subtype gene expression in rat brain. *NeuroReport*. 6 (18), 2549–2552.

Jones, R.T., Faas, G.C. & Mody, I. (2014) Intracellular bicarbonate regulates action potential generation via KCNQ channel modulation. *Journal of Neuroscience*. 34 (12), 4409–4417.

Kai, H., Griendling, K.K., Lassegue, B., Ollerenshaw, J.D., et al. (1994) Agonist-

induced phosphorylation of the vascular type 1 angiotensin II receptor. *Hypertension*. 24 (4), 523–527.

Kalaria, R.N. (2000) The role of cerebral ischemia in Alzheimer's disease. In: *Neurobiology of Aging*. 1 March 2000 Elsevier. pp. 321–330.

Kamenetz, F., Tomita, T., Hsieh, H., Seabrook, G., et al. (2003) APP Processing and Synaptic Function. *Neuron*. 37 (6), 925–937.

Kamouchi, M., Kitazono, T., Ago, T., Wakisaka, M., et al. (2007) Hydrogen peroxide-induced Ca 2+ responses in CNS pericytes. *Neuroscience Letters*. 416, 12–16.

Kaptoge, S., Pennells, L., De Bacquer, D., Cooney, M.T., et al. (2019) World Health Organization cardiovascular disease risk charts: revised models to estimate risk in 21 global regions. *The Lancet Global Health*. 7 (10), e1332–e1345.

Kaschina, E. & Unger, T. (2003) Angiotensin AT1/AT2 receptors: regulation, signalling and function. *Blood pressure*. 12 (2), 70–88.

Katusic, Z.S., Schugel, J., Cosentino, F. & Vanhoutte, P.M. (1993) Endothelium-dependent contractions to oxygen-derived free radicals in the canine basilar artery. *American Journal of Physiology - Heart and Circulatory Physiology*. 264 (3 33-3).

Kawamura, H., Kobayashi, M., Li, Q., Yamanishi, S., et al. (2004) Effects of angiotensin II on the pericyte-containing microvasculature of the rat retina. *Journal of Physiology-London*. 561 (3), 671–683.

Kawanabe, Y. & Nauli, S.M. (2011) Endothelin. *Cellular and Molecular Life Sciences*.68 (2) pp.195–203.

Kawasaki, T., Marumo, T., Shirakami, K., Mori, T., et al. (2012) Increase of 20-HETE synthase after brain ischemia in rats revealed by PET study with 11 C-labeled 20-HETE synthase-specific inhibitor. *Journal of Cerebral Blood Flow and Metabolism*. 32 (9), 1737–1746.

Kehl, F., Cambj-Sapunar, L., Maier, K.G., Miyata, N., et al. (2002) 20-HETE contributes to the acute fall in cerebral blood flow after subarachnoid hemorrhage in the rat. *American Journal of Physiology - Heart and Circulatory Physiology*. 282 (4 51-4).

Khalil, R.A. (2010) Rho Kinase in Vascular Smooth Muscle. In: *Regulation of Vascular Smooth Muscle Function*. San Rafael (CA), Morgan & Claypool Life Sciences. p.

Khennouf, L., Gesslein, B., Brazhe, A., Octeau, J.C., et al. (2018) Active role of capillary pericytes during stimulation-induced activity and spreading depolarization. *Brain*. 141 (7), 2032–2046.

Kikuchi, Y., Tateda, K., Fuse, E.T., Matsumoto, T., et al. (2009) Hyperoxia exaggerates bacterial dissemination and lethality in Pseudomonas aeruginosa pneumonia. *Pulmonary Pharmacology and Therapeutics*. 22 (4), 333–339.

Kim, S., Ong, P.K., Yalcin, O., Intaglietta, M., et al. (2009) The cell-free layer in microvascular blood flow. *Biorheology*. 46 (3), 181–189.

Kimura, T., Hashimura, T. & Miyakawa, T. (1991) Observations of Microvessels in the Brain with Alzheimer's Disease by the Scanning Electron Microscopy. *Psychiatry and Clinical Neurosciences*. 45 (3), 671–676.

King, P., Kong, M.-F., Parkin, H., MacDonald, I.A., et al. (1998) Intravenous Lactate

Prevents Cerebral Dysfunction during Hypoglycaemia in Insulin-Dependent Diabetes Mellitus. *Clinical Science*. 94 (2), 157–163.

Kisler, K., Nelson, A.R., Montagne, A. & Zlokovic, B. V. (2017a) Cerebral blood flow regulation and neurovascular dysfunction in Alzheimer disease. *Nature Reviews Neuroscience*.18 (7) pp.419–434.

Kisler, K., Nelson, A.R., Rege, S. V., Ramanathan, A., et al. (2017b) Pericyte degeneration leads to neurovascular uncoupling and limits oxygen supply to brain. *Nature neuroscience*. 20 (3), 406–416.

de Kloet, A.D., Liu, M., Rodriguez, V., Krause, E.G., et al. (2015) Role of neurons and glia in the CNS actions of the renin-angiotensin system in cardiovascular control. *American Journal of Physiology-Regulatory Integrative and Comparative Physiology*. 309 (5), R444–R458.

Koffie, R.M., Meyer-Luehmann, M., Hashimoto, T., Adams, K.W., et al. (2009) Oligomeric amyloid β associates with postsynaptic densities and correlates with excitatory synapse loss near senile plaques. *Proceedings of the National Academy of Sciences of the United States of America*. 106 (10), 4012–4017.

Kontos, H.A. (2001) Oxygen radicals in cerebral ischemia: The 2001 Willis lecture. *Stroke*. 32 (11), 2712–2716.

Kontos, H.A. & Wei, E.P. (1993) Hydroxyl radical-dependent inactivation of guanylate cyclase in cerebral arterioles by methylene blue and by LY83583. *Stroke*. 24 (3), 427–434.

Korte, N., Nortley, R. & Attwell, D. (2020) Cerebral blood flow decrease as an early pathological mechanism in Alzheimer's disease. *Acta Neuropathologica*.140 (6)

pp.793–810.

Kovacs-Oller, T., Ivanova, E., Bianchimano, P. & Sagdullaev, B.T. (2020) The pericyte connectome: spatial precision of neurovascular coupling is driven by selective connectivity maps of pericytes and endothelial cells and is disrupted in diabetes. *Cell Discovery*. 6 (1), 39.

Koyama, Y. (2013) Endothelin systems in the brain: Involvement in pathophysiological responses of damaged nerve tissues. *Biomolecular Concepts*.4 (4) pp.335–347.

Kramár, E.A., Harding, J.W. & Wright, J.W. (1997) Angiotensin II- and IV-induced changes in cerebral blood flow roles of AT1 AT2, and AT4 receptor subtypes. *Regulatory Peptides*. 68 (2), 131–138.

Kramár, E.A., Krishnan, R., Harding, J.W. & Wright, J.W. (1998) Role of nitric oxide in angiotensin IV-induced increases in cerebral blood flow. *Regulatory Peptides*. 74 (2–3), 185–192.

Krumova, K. & Cosa, G. (2016) *Chapter 1. Overview of Reactive Oxygen Species*. In: pp. 1–21.

Kucharski, A.J., Klepac, P., Conlan, A.J.K., Kissler, S.M., et al. (2020) Effectiveness of isolation, testing, contact tracing, and physical distancing on reducing transmission of SARS-CoV-2 in different settings: a mathematical modelling study. *The Lancet Infectious Diseases*. 20 (10), 1151–1160.

Kumar, A., Pareek, V., Prasoon, P., Faiq, M.A., et al. (2020) Possible routes of SARS-CoV-2 invasion in brain: In context of neurological symptoms in COVID-19 patients. *Journal of Neuroscience Research*.98 (12) pp.2376–2383.

Kureli, G., Yilmaz-Ozcan, S., Erdener, S.E., Donmez-Demir, B., et al. (2020) *F-actin polymerization contributes to pericyte contractility in retinal capillaries*.

Kuroda, J., Ago, T., Nishimura, A., Nakamura, K., et al. (2014) Nox4 Is a Major Source of Superoxide Production in Human Brain Pericytes. *Journal of Vascular Research*. 51 (6), 429–438.

de la Torre, J. (2018) The Vascular Hypothesis of Alzheimer's Disease: A Key to Preclinical Prediction of Dementia Using Neuroimaging. Patrizia Mecocci (ed.). *Journal of Alzheimer's disease : JAD*. 63 (1), 35–52.

de la Torre, J.C. (2002) Alzheimer disease as a vascular disorder: nosological evidence. *Stroke*. 33 (4), 1152–1162.

de la Torre, J.C. & Mussivan, T. (1993) Can disturbed brain microcirculation cause Alzheimer's disease? *Neurological Research*. 15 (3), 146–153.

Lakhkar, A., Dhagia, V., Joshi, S.R., Gotlinger, K., et al. (2016) 20-hete-induced mitochondrial superoxide production and inflammatory phenotype in vascular smooth muscle is prevented by glucose-6-phosphate dehydrogenase inhibition. *American Journal of Physiology - Heart and Circulatory Physiology*. 310 (9), H1107–H1117.

Lamers, M.M., Beumer, J., Vaart, J. Van Der, Knoops, K., et al. (2020) SARS-CoV-2 productively infects human gut enterocytes. *Science*. 369 (6499), 50–54.

Lan, J., Ge, J., Yu, J., Shan, S., et al. (2020) Structure of the SARS-CoV-2 spike receptor-binding domain bound to the ACE2 receptor. *Nature*. 581 (7807), 215–220.

Lange, A., Gebremedhin, D., Narayanan, J. & Harder, D. (1997) 20-Hydroxyeicosatetraenoic acid-induced vasoconstriction and inhibition of potassium current in cerebral vascular smooth muscle is dependent on activation of protein kinase C. *Journal of Biological Chemistry*. 272 (43), 27345–27352.

Lautner, R.Q., Villela, D.C., Fraga-Silva, R.A., Silva, N., et al. (2013) Discovery and characterization of alamandine: A novel component of the renin-angiotensin system. *Circulation Research*. 112 (8), 1104–1111.

Leal-Campanario, R., Alarcon-Martinez, L., Rieiro, H., Martinez-Conde, S., et al. (2017) Abnormal Capillary Vasodynamics Contribute to Ictal Neurodegeneration in Epilepsy. *Scientific Reports*. 7 (1), 1–14.

Lebeux, Y.J. & Willemot, J. (1978) Actin- and myosin-like filaments in rat brain pericytes. *The Anatomical Record*. 190 (4), 811–826.

Lee, J.M., Grabb, M.C., Zipfel, G.J. & Choi, D.W. (2000) Brain tissue responses to ischemia. *Journal of Clinical Investigation*.106 (6) pp.723–731.

Lee, M.-H., Perl, D.P., Nair, G., Li, W., et al. (2021) Microvascular Injury in the Brains of Patients with Covid-19. *The New England journal of medicine*. 384 (5), 481–483.

Lee, S., Zeiger, A., Maloney, J.M., Kotecki, M., et al. (2010) Pericyte actomyosin-mediated contraction at the cell–material interface can modulate the microvascular niche. *Journal of Physics: Condensed Matter*. 22 (19), 194115.

Leffler, C.W., Busija, D.W., Armstead, W.M. & Mirro, R. (1990) H2O2 effects on cerebral prostanoids and pial arteriolar diameter in piglets. *American Journal of*

Physiology - Heart and Circulatory Physiology. 258 (5 27-5).

Lenkei, Z., Palkovits, M., Corvol, P. & Llorens-Cortès, C. (1997) Expression of angiotensin type-1 (AT1) and type-2 (AT2) receptor mRNAs in the adult rat brain: A functional neuroanatomical review. *Frontiers in Neuroendocrinology*. 18 (4), 383–439.

Lescure, F.X., Bouadma, L., Nguyen, D., Parisey, M., et al. (2020) Clinical and virological data of the first cases of COVID-19 in Europe: a case series. *The Lancet Infectious Diseases*. 20 (6), 697–706.

Li, K.C., Tam, C.W.Y., Shum, H.P. & Yan, W.W. (2019) Impact of hyperoxia and hypocapnia on neurological outcome in patients with aneurysmal subarachnoid haemorrha...20th Congress of Asia Pacific Association of Critical Care Medicine and Annual Scientific Meeting of Hong Kong SCCM 2018, 15-16 December 2018, . *Critical Care & Shock*. 22 (1), 63.

Li, Q. & Puro, D.G. (2001) Adenosine activates ATP-sensitive K+ currents in pericytes of rat retinal microvessels: role of A1 and A2a receptors. *Brain Research*. 907 (1–2), 93–99.

Li, Y. & Pagano, P.J. (2017) Microvascular NADPH oxidase in health and disease. *Free Radical Biology and Medicine*.109 pp.33–47.

Lighthill, M.J. (1968) Pressure-forcing of tightly fitting pellets along fluid-filled elastic tubes. *Journal of Fluid Mechanics*. 34 (1), 113–143.

Lima, M., Siokas, V., Aloizou, A.M., Liampas, I., et al. (2020) Unraveling the Possible Routes of SARS-COV-2 Invasion into the Central Nervous System. *Current Treatment Options in Neurology*.22 (11) p.37.

Liu, R., Gao, M., Qiang, G.-F., Zhang, T.-T., et al. (2009) The anti-amnesic effects of luteolin against amyloid β25–35 peptide-induced toxicity in mice involve the protection of neurovascular unit. *NSC*. 162, 1232–1243.

Liu, Y., Zhang, H., Wu, C.Y., Yu, T., et al. (2021) 20-HETE-promoted cerebral blood flow autoregulation is associated with enhanced pericyte contractility. *Prostaglandins and Other Lipid Mediators*. 154, 106548.

Long, J.M. & Holtzman, D.M. (2019) Alzheimer Disease: An Update on Pathobiology and Treatment Strategies. *Cell*.179 (2) pp.312–339.

Lopes, R.D., Macedo, A.V.S., De Barros E Silva, P.G.M., Moll-Bernardes, R.J., et al. (2021) Effect of Discontinuing vs Continuing Angiotensin-Converting Enzyme Inhibitors and Angiotensin II Receptor Blockers on Days Alive and out of the Hospital in Patients Admitted with COVID-19: A Randomized Clinical Trial. *JAMA - Journal of the American Medical Association*. 325 (3), 254–264.

López, H.V., Vivas, M.F., Ruiz, R.N., Martínez, J.R., et al. (2019) Association between post-procedural hyperoxia and poor functional outcome after mechanical thrombectomy for ischemic stroke: an observational study. *Annals of Intensive Care*. 9 (1), 59.

Lu, R., Zhao, X., Li, J., Niu, P., et al. (2020) Genomic characterisation and epidemiology of 2019 novel coronavirus: implications for virus origins and receptor binding. *The Lancet*. 395 (10224), 565–574.

Lubow, J.M., Piñón, I.G., Avogaro, A., Cobelli, C., et al. (2006) Brain oxygen utilization is unchanged by hypoglycemia in normal humans: lactate, alanine, and leucine uptake are not sufficient to offset energy deficit. *American Journal of*

Physiology-Endocrinology and Metabolism. 290 (1), E149–E153.

Lumb, A.B. & Pearl, R.G. (2017) *Respiratory Physiology Nunn ' S Applied Respiratory*.

Ma, D., Chen, C.B., Jhanji, V., Xu, C., et al. (2020) Expression of SARS-CoV-2 receptor ACE2 and TMPRSS2 in human primary conjunctival and pterygium cell lines and in mouse cornea. *Eye (Basingstoke)*. 34 (7), 1212–1219.

Maas, A.I., Fleckenstein, W., de Jong, D.A. & van Santbrink, H. (1993) Monitoring cerebral oxygenation: experimental studies and preliminary clinical results of continuous monitoring of cerebrospinal fluid and brain tissue oxygen tension. *Acta neurochirurgica. Supplementum*. 59, 50–57.

Mach, W.J., Thimmesch, A.R., Pierce, J.T. & Pierce, J.D. (2011) Consequences of Hyperoxia and the Toxicity of Oxygen in the Lung. *Nursing Research and Practice*. 2011, 1–7.

Maeda, N., Suzuki, Y., Tanaka, J. & Tateishi, N.-H. (1996) Erythrocyte flow and elasticity of microvessels evaluated by marginal cell-free layer and flow resistance. *American Journal of Physiology-Heart and Circulatory Physiology*. 271 (6), H2454–H2461.

Magistretti, P.J. & Pellerin, L. (1999) Astrocytes Couple Synaptic Activity to Glucose Utilization in the Brain. *Physiology*. 14 (5), 177–182.

Mahley, R.W. (2016) Apolipoprotein E: from cardiovascular disease to neurodegenerative disorders. *Journal of Molecular Medicine*.94 (7) pp.739–746.

Mangia, S., Garreffa, G., Bianciardi, M., Giove, F., et al. (2003) The aerobic brain:

lactate decrease at the onset of neural activity. *Neuroscience*. 118 (1), 7–10.

Maran, A., Crepaldi, C., Trupiani, S., Lucca, T., et al. (2000) Brain function rescue effect of lactate following hypoglycaemia is not an adaptation process in both normal and Type I diabetic subjects. *Diabetologia 2000 43:6*. 43 (6), 733–741.

Marshall, J.J., Wei, E.P. & Kontos, H.A. (1988) Independent blockade of cerebral vasodilation from acetylcholine and nitric oxide. *American Journal of Physiology-Heart and Circulatory Physiology*. 255 (4), H847–H854.

Mason, S. (2017) Lactate Shuttles in Neuroenergetics—Homeostasis, Allostasis and Beyond. *Frontiers in Neuroscience*. 0 (FEB), 43.

Massaad, C.A., Amin, S.K., Hu, L., Mei, Y., et al. (2010) Mitochondrial superoxide contributes to blood flow and axonal transport deficits in the Tg2576 mouse model of Alzheimer's disease. *PLoS ONE*. 5 (5).

Matrougui, K., Loufrani, L., Heymes, C., Lévy, B.I., et al. (1999) Activation of AT2 Receptors by Endogenous Angiotensin II Is Involved in Flow-Induced Dilation in Rat Resistance Arteries. *Hypertension*. 34 (4), 659–665.

Matschke, J., Lütgehetmann, M., Hagel, C., Sperhake, J.P., et al. (2020) Neuropathology of patients with COVID-19 in Germany: a post-mortem case series. *The Lancet Neurology*. 19 (11), 919–929.

Matsuo, Y., Mihara, S.I., Ninomiya, M. & Fujimoto, M. (2001) Protective effect of endothelin type A receptor antagonist on brain edema and injury after transient middle cerebral artery occlusion in rats. *Stroke*. 32 (9), 2143–2148.

Matsusaka, T., Niimura, F., Shimizu, A., Pastan, I., et al. (2012) Liver

angiotensinogen is the primary source of renal angiotensin II. *Journal of the American Society of Nephrology*. 23 (7), 1181–1189.

Mattos, J.D., Campos, M.O., Rocha, M.P., Mansur, D.E., et al. (2019) Human brain blood flow and metabolism during isocapnic hyperoxia: the role of reactive oxygen species. *The Journal of Physiology*. 597 (3), 741–755.

McCord, J.M. (2008) Superoxide dismutase, lipid peroxidation, and bell-shaped dose response curves. *Dose-response : a publication of International Hormesis Society*. 6 (3), 223–238.

McNulty, P.H., King, N., Scott, S., Hartman, G., et al. (2005) Effects of supplemental oxygen administration on coronary blood flow in patients undergoing cardiac catheterization. *American Journal of Physiology - Heart and Circulatory Physiology*. 288 (3 57-3), 1057–1062.

Mehta, P.K. & Griendling, K.K. (2007) Angiotensin II cell signaling: physiological and pathological effects in the cardiovascular system. *American journal of physiology. Cell physiology*. 292 (1), C82-97.

Meinhardt, J., Radke, J., Dittmayer, C., Franz, J., et al. (2021) Olfactory transmucosal SARS-CoV-2 invasion as a port of central nervous system entry in individuals with COVID-19. *Nature Neuroscience*. 24 (2), 168–175.

Meng, X., Li, T., Wang, X., Lv, X., et al. (2019) Association between increased levels of amyloid-β oligomers in plasma and episodic memory loss in Alzheimer's disease. *Alzheimer's Research and Therapy*. 11 (1), 1–10.

Merdzo, I., Rutkai, I., Sure, V.N.L.R., McNulty, C.A., et al. (2017) Impaired Mitochondrial Respiration in Large Cerebral Arteries of Rats with Type 2

Diabetes. *Journal of Vascular Research*. 54 (1), 1–12.

Miller, A.A., Drummond, G.R., Schmidt, H.H.H.W. & Sobey, C.G. (2005) NADPH oxidase activity and function are profoundly greater in cerebral versus systemic arteries. *Circulation Research*. 97 (10), 1055–1062.

Minami, M., Kimura, M., Iwamoto, N. & Arai, H. (1995) Endothelin-1-like immunoreactivity in cerebral cortex of Alzheimer-type dementia. *Progress in Neuropsychopharmacology and Biological Psychiatry*. 19 (3), 509–513.

Miners, J.S., Palmer, J.C. & Love, S. (2016) Pathophysiology of Hypoperfusion of the Precuneus in Early Alzheimer's Disease. *Brain Pathology*. 26 (4), 533–541.

Mishra, A., Hamid, A. & Newman, E.A. (2011) Oxygen modulation of neurovascular coupling in the retina. *Proceedings of the National Academy of Sciences of the United States of America*. 108 (43), 17827–17831.

Mishra, A., O'Farrell, F.M., Reynell, C., Hamilton, N.B., et al. (2014) Imaging pericytes and capillary diameter in brain slices and isolated retinae. *Nature Protocols*. 9 (2), 323–336.

Mishra, A., Reynolds, J.P., Chen, Y., Gourine, A. V., et al. (2016) Astrocytes mediate neurovascular signaling to capillary pericytes but not to arterioles. *Nature Neuroscience*. 19 (12), 1619–1627.

Miura, S., Imaizumi, S. & Saku, K. (2013) Recent Progress in Molecular Mechanisms of Angiotensin II Type 1 and 2 Receptors. *Current Pharmaceutical Design*. 19 (17), 2981–2987.

Miyata, N., Taniguchi, K., Seki, T., Ishimoto, T., et al. (2001) HET0016, a potent and

selective inhibitor of 20-HETE synthesizing enzyme. *British Journal of Pharmacology*. 133 (3), 325–329.

Mizuno, Y., Isotani, E., Huang, J., Ding, H., et al. (2008) Myosin light chain kinase activation and calcium sensitization in smooth muscle in vivo. *American Journal of Physiology - Cell Physiology*. 295 (2), C358.

Mogi, M., Iwanami, J. & Horiuchi, M. (2012) Roles of brain angiotensin II in cognitive function and dementia. *International Journal of Hypertension*.2012.

Mohamed, R. (2013) *Effect Of Oxidative Stress On Human Brain Vascular Pericytes*. North Carolina Agricultural and Technical State University.

Morales, D.R., Conover, M.M., You, S.C., Pratt, N., et al. (2021) Renin–angiotensin system blockers and susceptibility to COVID-19: an international, open science, cohort analysis. *The Lancet Digital Health*. 3 (2), e98–e114.

Morishima-Kawashima, M. (2014) Molecular mechanism of the intramembrane cleavage of the β-carboxyl terminal fragment of amyloid precursor protein by γ-Secretase. *Frontiers in Physiology*. 5 (Nov).

Mount, C.A. & Das, J.M. (2021) *Cerebral Perfusion Pressure*. StatPearls Publishing.

Mu, Y., Klamerus, M.M., Miller, T.M., Rohan, L.C., et al. (2008) Intravenous formulation of N-hydroxy-N′-(4-n-butyl-2-methylphenyl) formamidine (HET0016) for inhibition of rat brain 20-hydroxyeicosatetraenoic acid formation. *Drug Metabolism and Disposition*. 36 (11), 2324–2330.

Mumbengegwi, D.R., Li, Q., Li, C., Bear, C.E., et al. (2008) Evidence for a Superoxide Permeability Pathway in Endosomal Membranes. *Molecular and*

Cellular Biology. 28 (11), 3700.

Murgolo, N., Therien, A.G., Howell, B., Klein, D., et al. (2021) SARS-CoV-2 tropism, entry, replication, and propagation: Considerations for drug discovery and development. *PLoS Pathogens*.17 (2) p.e1009225.

Nakamura, K., Kamouchi, M., Kitazono, T., Kuroda, J., et al. (2009) Amiloride inhibits hydrogen peroxide-induced Ca2+ responses in human CNS pericytes. *Microvascular Research*. 77 (3), 327–334.

Nakane, M. (2020) Biological effects of the oxygen molecule in critically ill patients. *Journal of Intensive Care*.8 (1) pp.1–12.

Näveri, L., Strömberg, C. & Saavedra, J.M. (1994) Angiotensin II AT1 receptor mediated contraction of the perfused rat cerebral artery. *Neuroreport*. 5 (17), 2278–2280.

Nayernia, Z., Jaquet, V. & Krause, K.H. (2014) New insights on NOX enzymes in the central nervous system. *Antioxidants and Redox Signaling*.20 (17) pp.2815–2837.

Nelson, A.R., Sagare, M.A., Wang, Y., Kisler, K., et al. (2020) Channelrhodopsin Excitation Contracts Brain Pericytes and Reduces Blood Flow in the Aging Mouse Brain in vivo. *Frontiers in Aging Neuroscience*. 12.

Nelson, C.W., Wei, E.P., Povlishock, J.T., Kontos, H.A., et al. (1992) Oxygen radicals in cerebral ischemia. *Heart Circ. Physiol*.263.

Nelson, P.T., Alafuzoff, I., Bigio, E.H., Bouras, C., et al. (2012) Correlation of alzheimer disease neuropathologic changes with cognitive status: A review of

the literature. *Journal of Neuropathology and Experimental Neurology*.71 (5) pp.362–381.

Netland, J., Meyerholz, D.K., Moore, S., Cassell, M., et al. (2008) Severe Acute Respiratory Syndrome Coronavirus Infection Causes Neuronal Death in the Absence of Encephalitis in Mice Transgenic for Human ACE2. *Journal of Virology*. 82 (15), 7264–7275.

Netter, F.H. (Frank H. (2014) Includes bibliographical references and index. *Atlas of human anatomy*. 6th ed. Philadelphia, PA, Saunders/Elsevier.

Nettleship, J.E., Watson, P.J., Rahman-Huq, N., Fairall, L., et al. (2015) Transient expression in HEK 293 cells: An alternative to E. coli for the production of secreted and intracellular mammalian proteins. *Methods in Molecular Biology*. 1258, 209–222.

Neuhaus, A.A., Couch, Y., Sutherland, B.A. & Buchan, A.M. (2017) Novel method to study pericyte contractility and responses to ischaemia in vitro using electrical impedance. *Journal of Cerebral Blood Flow and Metabolism*. 37 (6), 2013–2024.

Ng, S.Y. & Lee, A.Y.W. (2019) Traumatic Brain Injuries: Pathophysiology and Potential Therapeutic Targets. *Frontiers in Cellular Neuroscience*. 13, 528.

Ngo, A.T., Riemann, M., Holstein-Rathlou, N.H., Torp-Pedersen, C., et al. (2013) Significance of KATP channels, L-type Ca2+ channels and CYP450-4A enzymes in oxygen sensing in mouse cremaster muscle arterioles in vivo. *BMC Physiology*. 13 (1), 8.

Ni, W., Yang, X., Yang, D., Bao, J., et al. (2020) Role of angiotensin-converting enzyme 2 (ACE2) in COVID-19. *Critical Care*.24 (1) pp.1–10.

Ni, Y.-N., Wang, Y.-M., Liang, B.-M. & Liang, Z.-A. (2019) The effect of hyperoxia on mortality in critically ill patients: a systematic review and meta analysis. *BMC pulmonary medicine*. 19 (1), 53.

Nichols, E., Szoeke, C.E.I., Vollset, S.E., Abbasi, N., et al. (2019) Global, regional, and national burden of Alzheimer's disease and other dementias, 1990–2016: a systematic analysis for the Global Burden of Disease Study 2016. *The Lancet Neurology*. 18 (1), 88–106.

Nicola, M., Alsafi, Z., Sohrabi, C., Kerwan, A., et al. (2020) The socio-economic implications of the coronavirus pandemic (COVID-19): A review. *International Journal of Surgery*.78 pp.185–193.

Nicolakakis, N., Aboulkassim, T., Ongali, B., Lecrux, C., et al. (2008) Complete rescue of cerebrovascular function in aged Alzheimer's disease transgenic mice by antioxidants and pioglitazone, a peroxisome proliferator-activated receptor γ agonist. *Journal of Neuroscience*. 28 (37), 9287–9296.

Nilsson, D., Wackenfors, A., Gustafsson, L., Edvinsson, L., et al. (2008) Increased ETA and ETB receptor contraction in the left internal mammary artery from patients with hypertension. *Journal of Human Hypertension*. 22 (3), 226–229.

Nisimoto, Y., Diebold, B.A., Constentino-Gomes, D. & Lambeth, J.D. (2014) Nox4: A hydrogen peroxide-generating oxygen sensor. *Biochemistry*. 53 (31), 5111–5120.

Niwa, K., Kazama, K., Younkin, L., Younkin, S.G., et al. (2002a) Cerebrovascular autoregulation is profoundly impaired in mice overexpressing amyloid precursor protein. *American Journal of Physiology - Heart and Circulatory Physiology*. 283

(1 52-1).

Niwa, K., Kazama, K., Younkin, S.G., Carlson, G.A., et al. (2002b) Alterations in cerebral blood flow and glucose utilization in mice overexpressing the amyloid precursor protein. *Neurobiology of Disease*. 9 (1), 61–68.

Niwa, K., Porter, V.A., Kazama, K.E.N., Cornfield, D., et al. (2001) Aβ-peptides enhance vasoconstriction in cerebral circulation. *American Journal of Physiology - Heart and Circulatory Physiology*. 281 (6 50-6), 2417–2424.

Niwa, K., Younkin, L., Ebeling, C., Turner, S.K., et al. (2000) Aβ1-40-related reduction in functional hyperemia in mouse neocortex during somatosensory activation. *Proceedings of the National Academy of Sciences of the United States of America*. 97 (17), 9735–9740.

Nora, E.H., Munzenmaier, D.H., Hansen-Smith, F.M., Lombard, J.H., et al. (1998) Localization of the ANG II type 2 receptor in the microcirculation of skeletal muscle. *American Journal of Physiology - Heart and Circulatory Physiology*. 275 (4 44-4).

Nortley, R., Korte, N., Izquierdo, P., Hirunpattarasilp, C., et al. (2019) Amyloid b oligomers constrict human capillaries in Alzheimer's disease via signaling to pericytes. *Science*. 365 (6450).

O'Brien, R.J. & Wong, P.C. (2011) Amyloid precursor protein processing and alzheimer's disease. *Annual Review of Neuroscience*. 34, 185–204.

O'Connell, K.E., Mikkola, A.M., Stepanek, A.M., Vernet, A., et al. (2015) Practical murine hematopathology: a comparative review and implications for research. *Comparative medicine*. 65 (2), 96–113.

O’Driscoll, B.R., Howard, L.S. & Davison, A.G. (2011) Emergency oxygen use in adult patients: Concise guidance. *Clinical Medicine, Journal of the Royal College of Physicians of London*. 11 (4), 372–375.

O’Farrell, F.M., Mastitskaya, S., Hammond-Haley, M., Freitas, F., et al. (2017) Capillary pericytes mediate coronary no-reflow after myocardial ischaemia. *eLife*. 6.

Okada, Y. & Lipton, P. (2007) Glucose, Oxidative Energy Metabolism, and Neural Function in Brain Slices—Glycolysis Plays a Key Role in Neural Activity BT - Handbook of Neurochemistry and Molecular Neurobiology: Brain Energetics. Integration of Molecular and Cellular Processes. *Handbook of Neurochemistry and Molecular Neurobiology: Brain Energetics. Integration of Molecular and Cellular Processes*. (1.2), 1–23.

Örd, M., Faustova, I. & Loog, M. (2020) The sequence at Spike S1/S2 site enables cleavage by furin and phospho-regulation in SARS-CoV2 but not in SARS-CoV1 or MERS-CoV. *Scientific Reports*. 10 (1), 1–10.

Ortiz-Prado, E., Dunn, J.F., Vasconez, J., Castillo, D., et al. (2019) Partial pressure of oxygen in the human body: a general review. *American journal of blood research*. 9 (1), 1–14.

Østergaard, L. (2021) SARS CoV-2 related microvascular damage and symptoms during and after COVID-19: Consequences of capillary transit-time changes, tissue hypoxia and inflammation. *Physiological Reports*. 9 (3), 1–12.

Ou, X., Liu, Y., Lei, X., Li, P., et al. (2020) Characterization of spike glycoprotein of SARS-CoV-2 on virus entry and its immune cross-reactivity with SARS-CoV.

Nature Communications. 11 (1), 1–12.

Pacher, P., Beckman, J.S. & Liaudet, L. (2007) Nitric oxide and peroxynitrite in health and disease. *Physiological Reviews*.87 (1) pp.315–424.

Pala Cifci, S., Urcan Tapan, Y., Turemis Erkul, B., Savran, Y., et al. (2020) The Impact of Hyperoxia on Outcome of Patients Treated with Noninvasive Respiratory Support. *Canadian respiratory journal*. 2020, 3953280.

Pallone, T.L. & Silldorff, E.P. (2001) Pericyte regulation of renal medullary blood flow. *Experimental Nephrology*.9 (3) pp.165–170.

Palmer, J. & Love, S. (2011) Endothelin receptor antagonists: Potential in Alzheimer's disease. *Pharmacological Research*. 63, 525–531.

Palmer, J.C., Barker, R., Kehoe, P.G. & Love, S. (2012) Endothelin-1 is Elevated in Alzheimer's Disease and Upregulated by Amyloid-β. *Journal of Alzheimer's Disease*. 29 (4), 853–861.

Palmer, J.C., Tayler, H.M. & Love, S. (2013) Endothelin-Converting Enzyme-1 Activity, Endothelin-1 Production, and Free Radical-Dependent Vasoconstriction in Alzheimer's Disease. *Journal of Alzheimer's Disease*. 36, 577–587.

Pannu, S. (2016) Too Much Oxygen: Hyperoxia and Oxygen Management in Mechanically Ventilated Patients. *Seminars in Respiratory and Critical Care Medicine*. 37 (01), 016–022.

Paolini, A., Borella, R., De Biasi, S., Neroni, A., et al. (2021) Cell death in coronavirus infections: Uncovering its role during COVID-19. *Cells*. 10 (7).

Paravicini, T.M. & Touyz, R.M. (2008) NADPH oxidases, reactive oxygen species,

and hypertension: clinical implications and therapeutic possibilities. *Diabetes care*.31 Suppl 2 (Supplement 2) pp.S170–S180.

Paris, D., Humphrey, J., Quadros, A., Patel, N., et al. (2003) Vasoactive effects of Aβ in isolated human cerebrovessels and in a transgenic mouse model of Alzheimer's disease: Role of inflammation. *Neurological Research*.25 (6) pp.642–651.

Park, L., Anrather, J., Zhou, P., Frys, K., et al. (2004) Exogenous NADPH Increases Cerebral Blood Flow Through NADPH Oxidase–Dependent and –Independent Mechanisms. *Arteriosclerosis, Thrombosis, and Vascular Biology*. 24 (10), 1860–1865.

Park, L., Uekawa, K., Garcia-Bonilla, L., Koizumi, K., et al. (2017) Brain Perivascular Macrophages Initiate the Neurovascular Dysfunction of Alzheimer Aβ Peptides. *Circulation Research*. 121 (3), 258–269.

Park, L., Wang, G., Moore, J., Girouard, H., et al. (2014) The key role of transient receptor potential melastatin-2 channels in amyloid-β-induced neurovascular dysfunction. *Nature Communications*. 5 (1), 1–12.

Park, L., Wang, G., Zhou, P., Zhou, J., et al. (2011) Scavenger receptor CD36 is essential for the cerebrovascular oxidative stress and neurovascular dysfunction induced by amyloid-β. *Proceedings of the National Academy of Sciences of the United States of America*. 108 (12), 5063–5068.

Paul, M., Mehr, A.P. & Kreutz, R. (2006) Physiology of local renin-angiotensin systems. *Physiological Reviews*.86 (3) pp.747–803.

Pavlovic, R. & Santaniello, E. (2007) Peroxynitrite and nitrosoperoxycarbonate, a

tightly connected oxidizing-nitrating couple in the reactive nitrogen-oxygen species family: new perspectives for protection from radical-promoted injury by flavonoids. *JPP*. 59, 1687–1695.

Pendyala, S., Gorshkova, I.A., Usatyuk, P. V., He, D., et al. (2009) Role of Nox4 and Nox2 in hyperoxia-induced reactive oxygen species generation and migration of human lung endothelial cells. *Antioxidants and Redox Signaling*. 11 (4), 747–764.

Peppiatt, C.M., Howarth, C., Mobbs, P. & Attwell, D. (2006) Bidirectional control of CNS capillary diameter by pericytes. *Nature*. 443 (7112), 700–704.

Peyrounette, M., Davit, Y., Quintard, M. & Lorthois, S. (2018) Multiscale modelling of blood flow in cerebral microcirculation: Details at capillary scale control accuracy at the level of the cortex. *PLoS ONE*. 13 (1), e0189474.

Phaniendra, A., Jestadi, D.B. & Periyasamy, L. (2015) Free Radicals: Properties, Sources, Targets, and Their Implication in Various Diseases. *Indian Journal of Clinical Biochemistry*.30 (1) pp.11–26.

Phillips, M.I. & Stenstrom, B. (1985) Angiotensin II in rat brain comigrates with authentic angiotensin II in high pressure liquid chromatography. *Circulation Research*. 56 (2), 212–219.

Pietromonaco, P.R. & Overall, N.C. (2020) Applying Relationship Science to Evaluate How the COVID-19 Pandemic May Impact Couples' Relationships. *American Psychologist*.

Pilcher, J., Weatherall, M., Shirtcliffe, P., Bellomo, R., et al. (2012) The effect of hyperoxia following cardiac arrest: A systematic review and meta-analysis of

animal trials. *Resuscitation*. 83 (4), 417–422.

Pini, L., Pievani, M., Bocchetta, M., Altomare, D., et al. (2016) Brain atrophy in Alzheimer's Disease and aging. *Ageing Research Reviews*. 30, 25–48.

Pirola, C.J. & Sookoian, S. (2020) Estimation of Renin-Angiotensin-Aldosterone-System (RAAS)-Inhibitor effect on COVID-19 outcome: A Meta-analysis. *Journal of Infection*. 81 (2), 276–281.

Poloyac, S.M., Reynolds, R.B., Yonas, H. & Kerr, M.E. (2005) Identification and quantification of the hydroxyeicosatetraenoic acids, 20-HETE and 12-HETE, in the cerebrospinal fluid after subarachnoid hemorrhage. *Journal of Neuroscience Methods*. 144 (2), 257–263.

Prasad, M. (1991) Release of endothelin from cultured bovine endothelial cells. *Journal of Molecular and Cellular Cardiology*. 23 (6), 655–658.

Qin, Y., Wu, J., Chen, T., Li, J., et al. (2021) Long-term microstructure and cerebral blood flow changes in patients recovered from COVID-19 without neurological manifestations. *Journal of Clinical Investigation*. 131 (8).

Qiu, T., Liu, Q., Chen, Y.X., Zhao, Y.F., et al. (2015) Aβ42 and Aβ40: similarities and differences. *Journal of Peptide Science*. 21 (7), 522–529.

Raad, H., Paclet, M.H., Boussetta, T., Kroviarski, Y., et al. (2009) Regulation of the phagocyte NADPH oxidase activity: Phosphorylation of gp91phox/NOX2 by protein kinase C enhances its diaphorase activity and binding to Rac2, p67phox, and p47phox. *FASEB Journal*. 23 (4), 1011–1022.

Rafols, J.A. & Kreipke, C.W. (2011) Current brain endothelin research: a pathway to

novel approaches impacting clinical trials. *Neurological Research*. 33 (2), 115–118.

Randriamboavonjy, V., Busse, R. & Fleming, I. (2003) 20-HETE-induced contraction of small coronary arteries depends on the activation of Rho-kinase. In: *Hypertension*. 1 March 2003 Lippincott Williams & Wilkins. pp. 801–806.

Ray, P.D., Huang, B.-W. & Tsuji, Y. (2012) *Reactive oxygen species (ROS) homeostasis and redox regulation in cellular signaling*.

Reeson, P., Choi, K. & Brown, C.E. (2018) VEGF signaling regulates the fate of obstructed capillaries in mouse cortex. *eLife*. 7.

Renic, M., Klaus, J.A., Omura, T., Kawashima, N., et al. (2009) Effect of 20-HETE inhibition on infarct volume and cerebral blood flow after transient middle cerebral artery occlusion. *Journal of Cerebral Blood Flow and Metabolism*. 29 (3), 629–639.

Rhea, E.M., Logsdon, A.F., Hansen, K.M., Williams, L.M., et al. (2021) The S1 protein of SARS-CoV-2 crosses the blood–brain barrier in mice. *Nature Neuroscience*. 24 (3), 368–378.

Rice, M.E. (2011) H2O2: A Dynamic Neuromodulator. *The Neuroscientist*. 17 (4), 389.

Rich, L.R., Harris, W. & Brown, A.M. (2019) The Role of Brain Glycogen in Supporting Physiological Function. *Frontiers in Neuroscience*. 13, 1176.

Riganti, C., Gazzano, E., Polimeni, M., Costamagna, C., et al. (2004) Diphenyleneiodonium inhibits the cell redox metabolism and induces oxidative

stress. *The Journal of biological chemistry*. 279 (46), 47726–47731.

Rigutto, S., Hoste, C., Grasberger, H., Milenkovic, M., et al. (2009) Activation of dual oxidases Duox1 and Duox2: Differential regulation mediated by cAMP-dependent protein kinase and protein kinase C-dependent phosphorylation. *Journal of Biological Chemistry*. 284 (11), 6725–6734.

Robinson, K.M., Janes, M.S., Pehar, M., Monette, J.S., et al. (2006) Selective fluorescent imaging of superoxide in vivo using ethidium-based probes. *Proceedings of the National Academy of Sciences of the United States of America*. 103 (41), 15038–15043.

Rockswold, S.B., Rockswold, G.L., Zaun, D.A., Zhang, X., et al. (2010) A prospective, randomized clinical trial to compare the effect of hyperbaric to normobaric hyperoxia on cerebral metabolism, intracranial pressure, and oxygen toxicity in severe traumatic brain injury: Clinical article. *Journal of Neurosurgery*. 112 (5), 1080–1094.

Rodiño-Janeiro, B.K., Paradela-Dobarro, B., Castiñeiras-Landeira, M.I., Raposeiras-Roubín, S., et al. (2013) Current status of NADPH oxidase researchin cardiovascular pharmacology. *Vascular Health and Risk Management*.9 (1) pp.401–428.

Rodríguez-González, R., Martín-Barrasa, J.L., Ramos-Nuez, Á., Cañas-Pedrosa, A.M., et al. (2014) Multiple system organ response induced by Hyperoxia in a clinically relevant animal model of sepsis. *Shock*. 42 (2), 148–153.

Rogers, S.D., Peters, C.M., Pomonis, J.D., Hagiwara, H., et al. (2003) Endothelin B receptors are expressed by astrocytes and regulate astrocyte hypertrophy in the

normal and injured CNS. *GLIA*. 41 (2), 180–190.

Rolfe, D.F.S. & Brown, G.C. (1997) Cellular Energy Utilization and Molecular Origin of Standard Metabolic Rate in Mammals. *REVIEWS*.77 (3).

Roman, R.J. (2002) P-450 metabolites of arachidonic acid in the control of cardiovascular function. *Physiological Reviews*.82 (1) pp.131–185.

Rosenblum, W.I. (1987) Hydroxyl radical mediates the endothelium-dependent relaxation produced by bradykinin in mouse cerebral arterioles. *Circulation Research*. 61 (4), 601–603.

Rossi, P., Tauzin, L., Weiss, M., Rostain, J.-C., et al. (2007) Could hyperoxic ventilation impair oxygen delivery in septic patients? *Clinical Physiology and Functional Imaging*. 27 (3), 180–184.

Rothlin, R.P., Duarte, M., Pelorosso, F.G., Nicolosi, L., et al. (2021) Angiotensin Receptor Blockers for COVID-19: Pathophysiological and Pharmacological Considerations About Ongoing and Future Prospective Clinical Trials. *Frontiers in pharmacology*. 12, 603736.

Rouget, C. (1873) Memoire sur le develloppment, la structure et les propietes physiologiques des capillaries senguins et lymphatiques. *Arch. Physiol. Norm. Pathol.* 5, 603–663.

Rudinskiy, N., Grishchuk, Y., Vaslin, A., Puyal, J., et al. (2009) Calpain hydrolysis of α- and β2-adaptins decreases clathrin-dependent endocytosis and may promote neurodegeneration. *Journal of Biological Chemistry*. 284 (18), 12447–12458.

Ruitenberg, A., Den Heijer, T., Bakker, S.L.M., Van Swieten, J.C., et al. (2005)

Cerebral hypoperfusion and clinical onset of dementia: The Rotterdam Study. *Annals of Neurology*. 57 (6), 789–794.

Rungta, R.L., Chaigneau, E., Osmanski, B.F. & Charpak, S. (2018) Vascular Compartmentalization of Functional Hyperemia from the Synapse to the Pia. *Neuron*. 99 (2), 362-375.e4.

Saito, T., Matsuba, Y., Mihira, N., Takano, J., et al. (2014) Single App knock-in mouse models of Alzheimer's disease. *Nature Neuroscience*. 17 (5), 661–663.

Sampaio, W.O., Dos Santos, R.A.S., Faria-Silva, R., Da Mata Machado, L.T., et al. (2007) Angiotensin-(1-7) through receptor Mas mediates endothelial nitric oxide synthase activation via Akt-dependent pathways. *Hypertension*. 49 (1), 185–192.

Sampol, D., Ostrofet, E., Jobin, M.-L., Raffard, G., et al. (2013) Glucose and lactate metabolism in the awake and stimulated rat: a 13C-NMR study. *Frontiers in Neuroenergetics*. 0 (MAY), 5.

Sangaralingham, S.J. & Burnett, J.C. (2018) Relaxing with c-type natriuretic peptide, the guanylyl cyclase b receptor, and pericytes. *Circulation*. 138 (5), 509–512.

Santos, A.N., Ewers, M., Minthon, L., Simm, A., et al. (2012) Amyloid-β oligomers in cerebrospinal fluid are associated with cognitive decline in patients with Alzheimer's disease. *Journal of Alzheimer's Disease*. 29 (1), 171–176.

Santos, R.A.S., Sampaio, W.O., Alzamora, A.C., Motta-Santos, D., et al. (2018) The ACE2/Angiotensin-(1-7)/Mas axis of the renin-angiotensin system: Focus on Angiotensin-(1-7). *Physiological Reviews*.98 (1) pp.505–553.

Sarma, B.K. & Mugesh, G. (2008) Antioxidant Activity of the Anti-Inflammatory Compound Ebselen: A Reversible Cyclization Pathway via Selenenic and Seleninic Acid Intermediates. *Chemistry - A European Journal*. 14 (34), 10603–10614.

Schaffranietz, L., Vetter, B., Rudolph, C. & König, F. (2001) [Hyperoxia-induced liberation of big-endothelin into jugular venous blood of electric neurosurgical patients]. *Anaesthesiologie und Reanimation*. 26 (5), 123–132.

Schindler, C., Bramlage, P., Kirch, W. & Ferrario, C.M. (2007) Role of the vasodilator peptide angiotensin-(1-7) in cardiovascular drug therapy. *Vascular Health and Risk Management*.3 (1) pp.125–137.

Schmid, F., Tsai, P.S., Kleinfeld, D., Jenny, P., et al. (2017) Depth-dependent flow and pressure characteristics in cortical microvascular networks. *PLoS Computational Biology*. 13 (2), e1005392.

Schneider, M.P., Boesen, E.I. & Pollock, D.M. (2007) Contrasting actions of endothelin ETA and ETB receptors in cardiovascular disease. *Annual Review of Pharmacology and Toxicology*.47 pp.731–759.

Schönfelder, U., Hofer, A., Paul, M. & Funk, R.H.W. (1998) In situ observation of living pericytes in rat retinal capillaries. *Microvascular Research*. 56 (1), 22–29.

Schuff, N., Matsumoto, S., Kmiecik, J., Studholme, C., et al. (2009) Cerebral Blood Flow in Ischemic Vascular Dementia and Alzheimer's Disease By Arterial Spin Labeling MRI. *Alzheimers Dement*. 5 (6), 454–462.

Schurr, A., West, C.A. & Rigor, B.M. (1988) Lactate-supported synaptic function in the rat hippocampal slice preparation. *Science Science*. 240 (4857), 1326–1328.

Secomb, T.W. (2016) Hemodynamics. *Comprehensive Physiology*. 6 (2), 975–1003.

Selkoe, D.J. & Hardy, J. (2016) The amyloid hypothesis of Alzheimer's disease at 25 years. *EMBO Molecular Medicine*. 8 (6), 595–608.

Sengupta, U., Nilson, A.N. & Kayed, R. (2016) The Role of Amyloid-β Oligomers in Toxicity, Propagation, and Immunotherapy. *EBioMedicine*.6 pp.42–49.

Seo, B., Oemar, B.S., Siebenmann, R., Von Segesser, L., et al. (1994) Both ET(A) and ET(B) receptors mediate contraction to endothelin-1 in human blood vessels. *Circulation*. 89 (3), 1203–1208.

Serrano, F., Kolluri, N.S., Wientjes, F.B., Card, J.P., et al. (2003) NADPH oxidase immunoreactivity in the mouse brain. *Brain Research*. 988 (1–2), 193–198.

Shafafy, R., Suresh, S., Afolayan, J.O., Vaccaro, A.R., et al. (2017) Blunt vertebral vascular injury in trauma patients: ATLS® recommendations and review of current evidence. *Journal of Spine Surgery*. 3 (2), 217–225.

Shah, R.S. & Jeyaretna, D.S. (2018) Cerebral vascular anatomy and physiology. *Surgery (United Kingdom)*.36 (11) pp.606–612.

Shang, J., Wan, Y., Luo, C., Ye, G., et al. (2020) Cell entry mechanisms of SARS-CoV-2. *Proceedings of the National Academy of Sciences of the United States of America*. 117 (21), 11727–11734.

Shaw, K., Bell, L., Boyd, K., Grijseels, D.M., et al. (2021) Neurovascular coupling and oxygenation are decreased in hippocampus compared to neocortex because of microvascular differences. *Nature Communications 2021 12:1*. 12 (1), 1–16.

Sheng, Y., Abreu, I.A., Cabelli, D.E., Maroney, M.J., et al. (2014) Superoxide dismutases and superoxide reductases. *Chemical Reviews*.114 (7) pp.3854–3918.

Sher, L. (2020) The impact of the COVID-19 pandemic on suicide rates. *QJM*.113 (10) pp.707–712.

Shimada, I., Kubota, A., Katoh, M. & Suzuki, F. (2016) Hyperoxia causes diffuse alveolar damage through mechanisms involving upregulation of c-Myc/Bax and enhanced production of reactive oxygen species. *Respiratory Investigation*. 54 (1), 59–68.

Shimohama, S., Tanino, H., Kawakami, N., Okamura, N., et al. (2000) Activation of NADPH Oxidase in Alzheimer's Disease Brains. *Biochemical and Biophysical Research Communications*. 273 (1), 5–9.

Shinohara, K., Nakagawa, P., Gomez, J., Morgan, D.A., et al. (2017) Selective Deletion of Renin-b in the Brain Alters Drinking and Metabolism. *Hypertension*. 70 (5), 990–997.

Shipman, C. (1969) Evaluation of 4-(2-Hydroxyethyl)-1-piperazineëthanesulfonic Acid (HEPES) as a Tissue Culture Buffer. *Proceedings of the Society for Experimental Biology and Medicine*. 130 (1), 305–310.

Shojaee, N., Patton, W.F., Hechtman, H.B. & Shepro, D. (1999) Myosin translocation in retinal pericytes during free-radical induced apoptosis. *Journal of Cellular Biochemistry*. 75 (1), 118–129.

Silva, T.M. De, Brait, V.H., Drummond, G.R., Sobey, C.G., et al. (2011) Nox2 Oxidase Activity Accounts for the Oxidative Stress and Vasomotor Dysfunction

in Mouse Cerebral Arteries following Ischemic Stroke. *PLoS ONE*. 6 (12).

De Silva, T.M. & Faraci, F.M. (2013) Effects of angiotensin II on the cerebral circulation: role of oxidative stress. *Frontiers in Physiology*. 3.

De Silva, T.M. & Faraci, F.M. (2016) Microvascular Dysfunction and Cognitive Impairment. *Cellular and Molecular Neurobiology*.36 (2) pp.241–258.

Sims, D.E. (1986) The pericyte-A review. *Tissue and Cell*.18 (2) pp.153–174.

Smaje, L.H., Fraser, P.A. & Clough, G. (1980) The distensibility of single capillaries and venules in the cat mesentery. *Microvascular Research*. 20 (3), 358–370.

Smit, B., Smulders, Y.M., Eringa, E.C., Gelissen, H.P.M.M., et al. (2018a) Hyperoxia does not affect oxygen delivery in healthy volunteers while causing a decrease in sublingual perfusion. *Microcirculation*. 25 (2), e12433.

Smit, B., Smulders, Y.M., van der Wouden, J.C., Oudemans-van Straaten, H.M., et al. (2018b) Hemodynamic effects of acute hyperoxia: systematic review and meta-analysis. *Critical care (London, England)*. 22 (1), 45.

Smith, M.A., Richey Harris, P.L., Sayre, L.M., Beckman, J.S., et al. (1997) Widespread peroxynitrite-mediated damage in Alzheimer's disease. *Journal of Neuroscience*. 17 (8), 2653–2657.

Smythe, E. & Ayscough, K.R. (2006) Actin regulation in endocytosis. *Journal of Cell Science*. 119 (22), 4589–4598.

Snowdon, D.A., Greiner, L.H., Mortimer, J.A., Riley, K.P., et al. (1997) Brain infarction and the clinical expression of Alzheimer disease. The Nun Study. *JAMA*. 277 (10), 813–817.

Sokoloff, L. (1996) Cerebral Metabolism and Visualization of Cerebral Activity. *Comprehensive Human Physiology*. 579–602.

Sokoloff, L. (1960) Handbook of Physiology, Section I, Neurophysiology. *Amer. Physiol. Soc.*3 p.1846.

Soldatelli, M.D., Amaral, L.F. do, Veiga, V.C., Rojas, S.S.O., et al. (2020) Neurovascular and perfusion imaging findings in coronavirus disease 2019: Case report and literature review. *Neuroradiology Journal*. 33 (5), 368–373.

Song, Y., Nagaoka, T., Yoshioka, T., Ono, S., et al. (2016) Glial endothelin-1 regulates retinal blood flow during hyperoxia in cats. *Investigative Ophthalmology and Visual Science*. 57 (11), 4962–4969.

Sorce, S. & Krause, K.H. (2009) NOX enzymes in the central nervous system: From signaling to disease. *Antioxidants and Redox Signaling*. 11 (10), 2481–2504.

Špiranec, K., Chen, W., Werner, F.K.A., Nikolaev, V.O., et al. (2018) Endothelial C-type natriuretic peptide acts on pericytes to regulate microcirculatory flow and blood pressure. *Circulation*. 138 (5), 494–508.

Steinman, J., Koletar, M.M., Stefanovic, B. & Sled, J.G. (2017) 3D morphological analysis of the mouse cerebral vasculature: Comparison of in vivo and ex vivo methods Timothy W. Secomb (ed.). *PLOS ONE*. 12 (10), e0186676.

Stolmeijer, R., Bouma, H.R., Zijlstra, J.G., Drost-de Klerck, A.M., et al. (2018) A Systematic Review of the Effects of Hyperoxia in Acutely Ill Patients: Should We Aim for Less? *BioMed Research International*. 2018, 1–9.

Stornetta, R.L., Hawelu-Johnson, C.L., Guyenet, P.G. & Lynch, K.R. (1988)

Astrocytes synthesize angiotensinogen in brain. *Science*. 242 (4884), 1444–1446.

Strickland, S. (2018) Blood will out: Vascular contributions to Alzheimer's disease. *Journal of Clinical Investigation*.128 (2) pp.556–563.

Stromberg, D.D. & Fox, J.R. (1972) Pressures in the Plal Arterial Microcirculation of the Cat during Changes in Systemic Arterial Blood Pressure. *Circulation Rtsttrcb*.XXXI.

De Strooper, B. (2007) Loss-of-function presenilin mutations in Alzheimer disease. Talking Point on the role of presenilin mutations in Alzheimer disease. *EMBO Reports*.8 (2) pp.141–146.

Sun, C., Sellers, K.W., Sumners, C. & Raizada, M.K. (2005) NAD(P)H Oxidase Inhibition Attenuates Neuronal Chronotropic Actions of Angiotensin II. *Circulation Research*. 96 (6), 659–666.

Sun, X., He, G., Qing, H., Zhou, W., et al. (2006) Hypoxia facilitates Alzheimer's disease pathogenesis by up-regulating BACE1 gene expession. *Proceedings of the National Academy of Sciences of the United States of America*. 103 (49), 18727–18732.

Suzuki, S., Eastwood, G.M., Peck, L., Glassford, N.J., et al. (2013) Current oxygen management in mechanically ventilated patients: A prospective observational cohort study. *Journal of Critical Care*. 28 (5), 647–654.

Sweeney, M.D., Ayyadurai, S. & Zlokovic, B. V. (2016) Pericytes of the neurovascular unit: key functions and signaling pathways. *Nature Neuroscience*. 19 (6), 771–783.

Sweeney, P.W., Walker-Samuel, S. & Shipley, R.J. (2018) Insights into cerebral haemodynamics and oxygenation utilising in vivo mural cell imaging and mathematical modelling. *Scientific Reports*. 8 (1), 1–15.

Szok, D., Hansen-Schwartz, J. & Edvinsson, L. (2001) In depth pharmacological characterization of endothelin B receptors in the rat middle cerebral artery. *Neuroscience Letters*. 314 (1–2), 69–72.

Tai, W., He, L., Zhang, X., Pu, J., et al. (2020) Characterization of the receptor-binding domain (RBD) of 2019 novel coronavirus: implication for development of RBD protein as a viral attachment inhibitor and vaccine. *Cellular and Molecular Immunology*. 17 (6), 613–620.

Tallant, E.A. & Clark, M.A. (2003) Molecular mechanisms of inhibition of vascular growth by angiotensin-(1-7). *Hypertension*. 42 (4 I), 574–579.

Taquet, M., Geddes, J.R., Husain, M., Luciano, S., et al. (2021) 6-month neurological and psychiatric outcomes in 236 379 survivors of COVID-19: a retrospective cohort study using electronic health records. *The Lancet Psychiatry*. 8 (5), 416–443.

Tateda, K., Deng, J.C., Moore, T.A., Newstead, M.W., et al. (2003) Hyperoxia Mediates Acute Lung Injury and Increased Lethality in Murine Legionella Pneumonia: The Role of Apoptosis . *The Journal of Immunology*. 170 (8), 4209–4216.

Tcw, J. & Goate, A.M. (2017) Genetics of β-Amyloid Precursor Protein in Alzheimer's Disease. *Cold Spring Harbor perspectives in medicine*. 7 (6), a024539.

Thampatty, B.P., Sherwood, P.R., Gallek, M.J., Crago, E.A., et al. (2011) Role of

Endothelin-1 in human aneurysmal subarachnoid hemorrhage: Associations with vasospasm and delayed cerebral ischemia. *Neurocritical Care*. 15 (1), 19–27.

Theoharides, T.C., Cholevas, C., Polyzoidis, K. & Politis, A. (2021) Long-COVID syndrome -associated brain fog and chemofog : Luteolin to the rescue . *BioFactors*. 47 (2), 232–241.

Thomas, T., Thomas, G., McLendon, C., Sutton, T., et al. (1996) β-Amyloid-mediated vasoactivity and vascular endothelial damage. *Nature*. 380 (6570), 168–171.

Tigerstedt, R. & Bergman, P.Q. (1898) Niere und Kreislauf. *Skandinavisches Archiv Für Physiologie*. 8 (1), 223–271.

Toedebusch, R., Belenchia, A. & Pulakat, L. (2018) Cell-specific protective signaling induced by the novel AT2R-agonist NP-6A4 on human endothelial and smooth muscle cells. *Frontiers in Pharmacology*. 9 (AUG), 928.

Toksvang, L.N. & Berg, R.M.G. (2013) Using a classic paper by Robin Fåhraeus and Torsten Lindqvist to teach basic hemorheology. *American Journal of Physiology - Advances in Physiology Education*. 37 (2), 129–133.

Török, O., Schreiner, B., Schaffenrath, J., Tsai, H.C., et al. (2021) Pericytes regulate vascular immune homeostasis in the CNS. *Proceedings of the National Academy of Sciences of the United States of America*. 118 (10).

Touyz, R.M., Alves-Lopes, R., Rios, F.J., Camargo, L.L., et al. (2018) Vascular smooth muscle contraction in hypertension. *Cardiovascular Research*.114 (4) pp.529–539.

Trost, A., Lange, S., Schroedl, F., Bruckner, D., et al. (2016) Brain and retinal pericytes: Origin, function and role. *Frontiers in Cellular Neuroscience*.10 (FEB).

Turrens, J.F. (2003) Mitochondrial formation of reactive oxygen species. *The Journal of physiology*. 552 (Pt 2), 335–344.

Turrens, J.F., Freeman, B.A., Levitt, J.G. & Crapo, J.D. (1982) The effect of hyperoxia on superoxide production by lung submitochondrial particles. *Archives of biochemistry and biophysics*. 217 (2), 401–410.

Uemura, M.T., Maki, T., Ihara, M., Lee, V.M.Y., et al. (2020) Brain Microvascular Pericytes in Vascular Cognitive Impairment and Dementia. *Frontiers in Aging Neuroscience*.12 p.80.

Vallet, P., Charnay, Y., Steger, K., Ogier-Denis, E., et al. (2005) Neuronal expression of the NADPH oxidase NOX4, and its regulation in mouse experimental brain ischemia. *Neuroscience*. 132 (2), 233–238.

Vanlandewijck, M., He, L., Mäe, M.A., Andrae, J., et al. (2018) A molecular atlas of cell types and zonation in the brain vasculature. *Nature*. 554 (7693), 475-+.

Veneman, T., Mitrakou, A., Mokan, M., Cryer, P., et al. (1994) Effect of Hyperketonemia and Hyperlacticacidemia on Symptoms, Cognitive Dysfunction, and Counterregulatory Hormone Responses During Hypoglycemia in Normal Humans. *Diabetes*. 43 (11), 1311–1317.

Vincent, J.M., Kwan, Y.W., Chan, S.L., Perrin-Sarrado, C., et al. (2005) Constrictor and dilator effects of angiotensin II on cerebral arterioles. *Stroke*. 36 (12), 2691–2695.

Voutsinos-Porche, B., Bonvento, G., Tanaka, K., Steiner, P., et al. (2003) Glial Glutamate Transporters Mediate a Functional Metabolic Crosstalk between Neurons and Astrocytes in the Mouse Developing Cortex. *Neuron*. 37 (2), 275–286.

Waggoner, W.G., Genova, S.L. & Rash, V.A. (1992) Kinetic analyses demonstrate that the equilibrium assumption does not apply to [125I]endothelin-1 binding data. *Life Sciences*. 51 (24), 1869–1876.

Wang, J., Zohar, R. & McCulloch, C.A. (2006) Multiple roles of α-smooth muscle actin in mechanotransduction. *Experimental Cell Research*. 312 (3), 205–214.

Wang, M.Y., Zhao, R., Gao, L.J., Gao, X.F., et al. (2020) SARS-CoV-2: Structure, Biology, and Structure-Based Therapeutics Development. *Frontiers in Cellular and Infection Microbiology*.10 p.724.

Wang, S., Guo, F., Liu, K., Wang, H., et al. (2008) Endocytosis of the receptor-binding domain of SARS-CoV spike protein together with virus receptor ACE2. *Virus Research*. 136 (1–2), 8–15.

Wang, Y., Branicky, R., Noë, A. & Hekimi, S. (2018) Superoxide dismutases: Dual roles in controlling ROS damage and regulating ROS signaling. *Journal of Cell Biology*.217 (6) pp.1915–1928.

Wang, Z., Yang, D., Zhang, X., Li, T., et al. (2011) Hypoxia-induced Down-regulation of Neprilysin by histone modification in mouse primary cortical and Hippocampal neurons. *PLoS ONE*. 6 (4), e19229.

Ward, N.C., Croft, K.D., Blacker, D., Hankey, G.J., et al. (2011) Cytochrome P450 metabolites of arachidonic acid are elevated in stroke patients compared with

healthy controls. *Clinical Science*. 121 (11), 501–507.

Wardman, P. (1989) Reduction Potentials of One Electron Couples Involving Free Radicals in Aqueous Solution. *Journal of Physical and Chemical Reference Data*. 18 (4), 1637–1755.

Warner, T.D., Allcock, G.H. & Vane, J.R. (1994) Reversal of established responses to endothelin-1 in vivo and in vitro by the endothelin receptor antagonists, BQ-123 and PD 145065. *British Journal of Pharmacology*. 112 (1), 207–213.

Watson, N.A., Beards, S.C., Altaf, N., Kassner, A., et al. (2000) The effect of hyperoxia on cerebral blood flow: a study in healthy volunteers using magnetic resonance phase-contrast angiography. *European Journal of Anaesthesiology*. 17 (3), 152–159.

Webb, R.C. (2003) Smooth muscle contraction and relaxation. In: *American Journal of Physiology - Advances in Physiology Education*. 2003 American Physiological Society. pp. 201–206.

Wei, E.P. & Kontos, H.A. (1990) H2O2 and endothelium-dependent cerebral arteriolar dilation: Implications for the identity of endothelium-derived relaxing factor generated by acetylcholine. *Hypertension*. 16 (2), 162–169.

Wei, E.P., Kontos, H.A. & Beckman, J.S. (1996) Mechanisms of cerebral vasodilation by superoxide, hydrogen peroxide, and peroxynitrite. *American Journal of Physiology-Heart and Circulatory Physiology*. 271 (3), H1262–H1266.

Welches, W.R., Bridget Brosnihan, K. & Ferrario, C.M. (1993) A comparison of the properties and enzymatic activities of three angiotensin processing enzymes: Angiotensin converting enzyme, prolyl endopeptidase and neutral

endopeptidase 24.11. *Life Sciences*.52 (18) pp.1461–1480.

Wen, H., Östman, J., Bubb, K.J., Panayiotou, C., et al. (2012) 20-Hydroxyeicosatetraenoic acid (20-HETE) is a novel activator of transient receptor potential vanilloid 1 (TRPV1) channel. *Journal of Biological Chemistry*. 287 (17), 13868–13876.

Wiesmann, M., Zerbi, V., Jansen, D., Lütjohann, D., et al. (2017) Hypertension, cerebrovascular impairment, and cognitive decline in aged AβPP/PS1 mice. *Theranostics*. 7 (5), 1277–1289.

Wildwing, T. & Holt, N. (2021) The neurological symptoms of COVID-19: a systematic overview of systematic reviews, comparison with other neurological conditions and implications for healthcare services. *Therapeutic advances in chronic disease*. 12, 2040622320976979.

Williamson, K.S., Prasad Gabbita, S., Mou, S., West, M., et al. (2002) The Nitration Product 5-Nitro-γ-tocopherol Is Increased in the Alzheimer Brain. *Nitric Oxide*. 6 (2), 221–227.

Winegrad, S., Henrion, D., Rappaport, L. & Samuel, J.L. (1999) Self-protection by cardiac myocytes against hypoxia and hyperoxia. *Circulation Research*. 85 (8), 690–698.

Wittenberg, R., Hu, B., Barraza-Araiza, L., Funder, A.R., et al. (2019) *Projections of older people with dementia and costs of dementia care in the United Kingdom, 2019--2040*.

World Health Organization (2017) *Global action plan on the public health response to dementia 2017--2025*.

Wright, J.W. & Harding, J.W. (2011) Brain renin-angiotensin-A new look at an old system. *Progress in Neurobiology*.95 (1) pp.49–67.

Wright, J.W. & Harding, J.W. (2013) The brain renin-angiotensin system: A diversity of functions and implications for CNS diseases. *Pflugers Archiv European Journal of Physiology*.465 (1) pp.133–151.

Wu, Z. & McGoogan, J.M. (2020) Characteristics of and Important Lessons from the Coronavirus Disease 2019 (COVID-19) Outbreak in China: Summary of a Report of 72314 Cases from the Chinese Center for Disease Control and Prevention. *JAMA - Journal of the American Medical Association*.323 (13) pp.1239–1242.

Xiong, J., Lipsitz, O., Nasri, F., Lui, L.M.W., et al. (2020) Impact of COVID-19 pandemic on mental health in the general population: A systematic review. *Journal of Affective Disorders*.277 pp.55–64.

Xu, Q., Jensen, D.D., Peng, H. & Feng, Y. (2016) The critical role of the central nervous system (pro)renin receptor in regulating systemic blood pressure. *Pharmacology & Therapeutics*. 164, 126–134.

Yamada, M., Hayashi, H., Suzuki, K., Sato, S., et al. (2019) Furin-mediated cleavage of LRP1 and increase in ICD of LRP1 after cerebral ischemia and after exposure of cultured neurons to NMDA. *Scientific Reports*. 9 (1).

Yamamoto, S., Teng, W., Nishizawa, S., Kakiuchi, T., et al. (2000) Improvement in cerebral blood flow and metabolism following subarachnoid hemorrhage in response to prophylactic administration of the hydroxyl radical scavenger, AVS, (±)-N,N'-propylenedinicotinamide: A positron emission tomography study in rats.

Journal of Neurosurgery. 92 (6), 1009–1015.

Yang, S., Jin, H., Zhu, Y., Wan, Y., et al. (2017) Diverse Functions and Mechanisms of Pericytes in Ischemic Stroke. *Current Neuropharmacology*. 15 (6), 892–905.

Yang, Z.W., Zhang, A., Altura, B.T. & Altura, B.M. (1998) Endothelium-dependent relaxation to hydrogen peroxide in canine basilar artery: A potential new cerebral dilator mechanism. *Brain Research Bulletin*. 47 (3), 257–263.

Yemisci, M., Gursoy-Ozdemir, Y., Vural, A., Can, A., et al. (2009) Pericyte contraction induced by oxidative-nitrative stress impairs capillary reflow despite successful opening of an occluded cerebral artery. *Nature Medicine*. 15 (9), 1031-U82.

Yew, B. & Nation, D.A. (2017) Cerebrovascular resistance: Effects on cognitive decline, cortical atrophy, and progression to dementia. *Brain*. 140 (7), 1987–2001.

Ying, Z., Xin, W., Jin-Sheng, H., Fu-Xiang, B., et al. (2009) Preparation and Characterization of a Monoclonal Antibody with High Affinity for Soluble Aβ Oligomers. *Hybridoma*. 28 (5), 349–354.

Yokoyama, S., Hifumi, T., Kawakita, K., Tamiya, T., et al. (2019) Early Hyperoxia in The Intensive Care Unit is Significantly Associated With Unfavorable Neurological Outcomes in Patients With Mild-to-Moderate Aneurysmal Subarachnoid Hemorrhage. *SHOCK*. 51 (5), 593–598.

You, J., Golding, E.M. & Bryan, R.M. (2005) Arachidonic acid metabolites, hydrogen peroxide, and EDHF in cerebral arteries. *American Journal of Physiology - Heart and Circulatory Physiology*. 289 (3 58-3), 1077–1083.

Yu, L., Zheng, M., Wang, W., Rozanski, G.J., et al. (2010) Developmental changes in AT1 and AT2 receptor-protein expression in rats. *JRAAS - Journal of the Renin-Angiotensin-Aldosterone System*. 11 (4), 214–221.

Yu, Y., Herman, P., Rothman, D.L., Agarwal, D., et al. (2018) Evaluating the gray and white matter energy budgets of human brain function. *Journal of Cerebral Blood Flow and Metabolism*. 38 (8), 1339–1353.

Yuki, K., Fujiogi, M. & Koutsogiannaki, S. (2020) COVID-19 pathophysiology: A review. *Clinical Immunology*.215 p.108427.

Zambach, S.A., Cai, C., Cederberg Helms, H.C., Hald, B.O., et al. (2020) Nitric oxide, K ATP channels and endothelin-1 modulate brain pericyte function, vascular tone and neurovascular coupling. *bioRxiv*. 2020.06.07.138875.

Zeisel, A., Hochgerner, H., Lönnerberg, P., Johnsson, A., et al. (2018) Molecular Architecture of the Mouse Nervous System. *Cell*. 174 (4), 999-1014.e22.

Zeng, X., Ren, H., Zhu, Y., Zhang, R., et al. (2018) Gp91phox (NOX2) in Activated Microglia Exacerbates Neuronal Damage Induced by Oxygen Glucose Deprivation and Hyperglycemia in an in Vitro Model. *Cellular Physiology and Biochemistry*. 50 (2), 783–797.

Zhang, D., Guo, R., Lei, L., Liu, H., et al. (2021) Frontline Science: COVID-19 infection induces readily detectable morphologic and inflammation-related phenotypic changes in peripheral blood monocytes. *Journal of Leukocyte Biology*. 109 (1), 13–22.

Zhang, X., Zhou, K., Wang, R., Cui, J., et al. (2007) Hypoxia-inducible factor 1α (HIF-1α)-mediated hypoxia increases BACE1 expression and β-amyloid generation.

Journal of Biological Chemistry. 282 (15), 10873–10880.

Zhang, Y., Chen, K., Sloan, S.A., Bennett, M.L., et al. (2014) An RNA-sequencing transcriptome and splicing database of glia, neurons, and vascular cells of the cerebral cortex. *Journal of Neuroscience*. 34 (36), 11929–11947.

Zhao, R.Z., Jiang, S., Zhang, L. & Yu, Z. Bin (2019) Mitochondrial electron transport chain, ROS generation and uncoupling (Review). *International Journal of Molecular Medicine*.44 (1) pp.3–15.

Zhilyaev, S.Y., Moskvin, A.N., Platonova, T.F., Gutsaeva, D.R., et al. (2003) Hyperoxic Vasoconstriction in the Brain Is Mediated by Inactivation of Nitric Oxide by Superoxide Anions. *Neuroscience and Behavioral Physiology*. 33 (8), 783–787.

Zhiyou, C., Yong, Y., Shanquan, S., Jun, Z., et al. (2009) Upregulation of BACE1 and β-amyloid protein mediated by chronic cerebral hypoperfusion contributes to cognitive impairment and pathogenesis of alzheimer's disease. *Neurochemical Research*. 34 (7), 1226–1235.

Zhu, N., Zhang, D., Wang, W., Li, X., et al. (2020) A Novel Coronavirus from Patients with Pneumonia in China, 2019. *New England Journal of Medicine*. 382 (8), 727–733.

Zhu, X., Bergles, D.E. & Nishiyama, A. (2008) NG2 cells generate both oligodendrocytes and gray matter astrocytes. *Development*. 135 (1), 145–157.

Zhu, X., Smith, M.A., Perry, G. & Aliev, G. (2004) Mitochondrial failures in Alzheimer's disease. *American Journal of Alzheimer's Disease and other Dementias*.19 (6) pp.345–352.

Zhu, Y., Park, T.S. & Gidday, J.M. (1998) Mechanisms of hyperoxia-induced reductions in retinal blood flow in newborn pig. *Experimental Eye Research*. 67 (3), 357–369.

Zimmermann, K.W. & Zimmermann, K.W. (1923) Die Endothelzellen. In: *Der Feinere Bau der Blutcapillaren*. Springer Berlin Heidelberg. pp. 2–20.

Zlokovic, B. V. (2011) Neurovascular pathways to neurodegeneration in Alzheimer's disease and other disorders. *Nature Reviews Neuroscience*.12 (12) pp.723–738.

Zott, B., Simon, M.M., Hong, W., Unger, F., et al. (2019) A vicious cycle of β amyloid−dependent neuronal hyperactivation. *Science*. 365 (6453), 559–565.